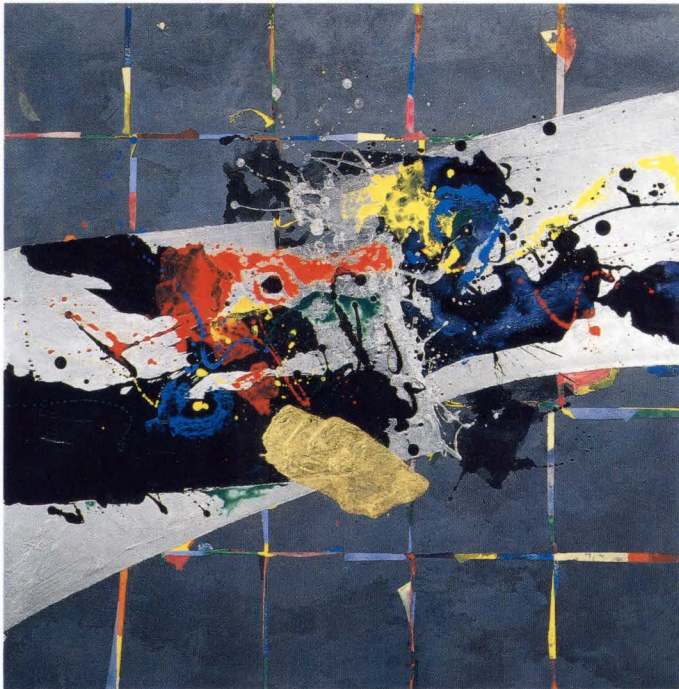


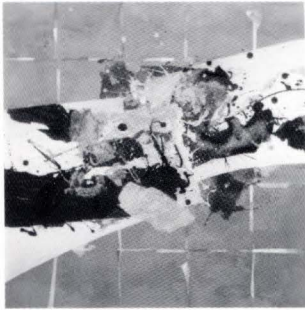
FUJITSU

SCIENTIFIC & TECHNICAL JOURNAL

Spring 1990 VOL.26, NO.1

Special Issue on Production Engineering Technologies





This Issue's Cover:

Conversations by Yukinobu Kudo

Telecommunications is one means of conversing. The development of telecommunications has greatly contributed to the advancement of human beings.

At Fujitsu Limited, we are promoting telecommunications R&D in such areas as broad-band ISDN, image communications, ultra-high-speed optical communications and satellite communications, all for the next generation. We are devoting ourselves to enabling more conversations to be transferred faster over a wider area.

In addition, we have developed automatic translation systems to break down language barriers all around the world. We are helping to contribute to the advancement of human beings by achieving smoother and richer conversations around the world.

FUJITSU Scientific & Technical Journal is published quarterly by FUJITSU LIMITED of Japan to report the results of research conducted by FUJITSU LIMITED, FUJITSU LABORATORIES LTD., and their associated companies in communications, electronics, and related fields. It is the publisher's intent that FSTJ will promote the international exchange of such information, and we encourage the distribution of FSTJ on an exchange basis. All correspondence concerning the exchange of periodicals should be addressed to the editor.

FSTJ can be purchased through KINOKUNIYA COMPANY LTD., 3-17-7 Shinjuku, Shinjuku-ku, Tokyo 160-91, (Telex No. 2424344, answerback KINOKUNI J).

The price is US \$7.00 per copy, without consumption tax, excluding postage.

FUJITSU LIMITED reserves all rights concerning the republication and publication after translation into other languages of articles appearing herein.

Permission to publish these articles may be obtained by contacting the editor.

FUJITSU LIMITED

Takuma Yamamoto, *President*

FUJITSU LABORATORIES LTD.

Masaka Ogi, *President*

Editorial Board

Editor Takahiko Misugi

Associated Editors Yukio Fukukawa Shigeru Sato

Editorial Representatives

Kunihiko Asama	Masakazu Fujita	Tatsuzumi Furukawa
Kazuhisa Kobayashi	Masaaki Kobayashi	Yoshimasa Miura
Makoto Mukai	Seiya Ogawa	Shinji Ohkawa
Shinya Okuda	Hirofumi Okuyama	Tohru Sato
Yoshio Tago	Shozo Taguchi	Jyun'ichi Tanahashi
Hirobumi Takanashi	Mitsuhiko Toda	Toru Tsuda
Akira Yoshida		

Editorial Coordinator

Kazuo Yono

FUJITSU LIMITED 1015 Kamikodanaka, Nakahara-ku,
Kawasaki 211, Japan

Cable Address: FUJITSULIMITED KAWASAKI

Telephone: +81-44-777-1111

Telex: 3842122, 3842221, 3842802, 3842803,

Answerback FTWKAW J

Printed by MIZUNO PRITECH Co., Ltd. in Japan

© 1990 FUJITSU LIMITED (April 25, 1990)

CONTENTS

Featuring Papers

- 1 Preface ● Takefumi Inagaki
- 3 Laser Welding of Thermocouple to Molybdenum Heating Tip
● Naohisa Matsushita ● Kazuo Yokoi
- 8 Automated Optical Pattern Inspection for High-Density Printed Wiring Boards
● Moritoshi Ando ● Hiroshi Oka ● Satoshi Iwata
- 16 High-Speed, Wide Area 3-D Vision System for PWB Inspection
● Tetsuo Koezuka ● Yoshikazu Kaikinoki ● Masato Nakashima
- 26 Sensory Pattern Inspection System for Print Quality of Dot-Matrix Printer
● Masato Nakashima ● Tetsuo Koezuka
- 35 Surface Flatness Measurement System
● Shin-ichi Wakana ● Yoshiro Goto
- 41 Six-Axis Force/Torque Sensor for Assembly Robots
● Akihiko Yabuki
- 48 High-Speed Force Controller for SCARA Robots
● Yutaka Yoshida ● Akihiko Yabuki ● Yasuyuki Nakata
- 55 Simulator for a Coordinated Two-Arm Robot
● Hiroshi Wada ● Mitsuo Kamimura ● Sadao Fujii
- 65 A Logic State Measurement Technique Using Multi-Stroboscopic Sampling for
the Electron Beam Tester
● Akio Ito ● Kazuo Okubo ● Akifumi Muto
- 71 Electron Beam Tester for VLSI Diagnosis
● Masaaki Kawabata ● Akifumi Muto ● Tetsuya Mukunoki

Papers

- 78 Phase-Shifted Gratings for DFB Lasers
● Manabu Matsuda ● Shouichi Ogita ● Yuji Kotaki
- 86 Overview of an Experimental Reflective Programming System: ExReps
● Jiro Tanaka ● Yukiko Ohta ● Fumio Matono
- 98 Unified Hardware Description Language (UHDL) and Its Support Tools
● Masahiro Fujita ● Hisanori Fujisawa ● Nobuaki Kawato
- 107 Approximation for the Rate of Short Circuit in Electronic Devices Caused
by Whisker Growth on Zn Electroplated Steel
● Takeshi Nagai ● Katsuhide Natori ● Takashi Furusawa

UDC 621.791.35:621.375.823:669.018.57
FUJITSU Sci. Tech. J., **26**, 1, pp. 3-7(1990)

Laser Welding of Thermocouple to Molybdenum Heating Tip

• Naohisa Matsushita • Kazuo Yokoi

This paper presents a new method of attaching a thermocouple to a heating tip using a pulsed YAG laser.

This heating tip is used in reflow soldering of Surface Mount components on printed wiring boards. The thermocouple is attached to the heating tip to control the soldering temperature.

The heating tip is made of molybdenum and the thermocouple is made of chromel and constantan wires. These wires are so thin that their heat capacity is far less than that of the heating tip. It is therefore difficult to attach the thermocouple to the heating tip using brazing or conventional laser welding.

UDC 53.084.87:621.3.049.75
FUJITSU Sci. Tech. J., **26**, 1, pp. 8-15(1990)

Automated Optical Pattern Inspection for High-Density Printed Wiring Boards

• Moritoshi Ando • Hiroshi Oka • Satoshi Iwata

A new technique for the automated optical inspection of printed wiring boards (PWBs) has been developed. It uses black-line sensing and a radial-matching algorithm. The black-line sensing detects copper patterns as shadows. Color and roughness do not affect the sensing.

The radial-matching algorithm converts patterns into 16-bit binary codes, and compares them with a code dictionary. The algorithm can inspect various kinds of patterns by changing the contents of the dictionary.

An inspection system using these techniques was constructed. It has a resolution of 5 μm and can inspect a 490 x 540 mm area in five minutes.

UDC 53.084.87:621.3.049.75
FUJITSU Sci. Tech. J., **26**, 1, pp. 16-25(1990)

High-Speed, Wide Area 3-D Vision System for PWB Inspection

• Tetsuo Koezuka • Yoshikazu Kakinoki • Masato Nakashima

This paper describes a three-dimensional (3-D) vision system developed for factory automation. The system is based on a newly developed 3-D imager. This imager uses a laser diode beam to scan the object area and obtains range and intensity data simultaneously.

Range measurement is based on triangulation. For inspecting printed wiring boards (PWBs), the system was capable of detecting missing, shifted, and floating components.

The inspection resolution is 125 μm along the X and Y axes and 30 μm along the Z axis.

A PWB 250 mm by 330 mm can be measured in 14 s.

UDC 53.084.87:681.327.5
FUJITSU Sci. Tech. J., **26**, 1, pp. 26-34(1990)

Sensory Pattern Inspection System for Print Quality of Dot-Matrix Printer

• Masato Nakashima • Tetsuo Koezuka

A print quality evaluation method has been developed and applied to the inspection of wire dot-matrix printers. A new algorithm has been developed that has characteristics of human vision, such as the edge emphasis and logarithmic sensitivity of the optic nerve, and accumulative evaluation. Experimental results shows that the print quality inspection system can perform at the same level as expert inspectors and that reproducibility is three times higher.

UDC 53.084.85:681.327.634
FUJITSU Sci. Tech. J., **26**, 1, pp. 35-40(1990)

Surface Flatness Measurement System

• Shin-ichi Wakana • Yoshiro Goto

An optical non-contact and non-destructive measurement system has been developed for surface flatness inspection. It is based on a new measurement principle, and is applicable to highly reflective flat planes, such as aluminum magnetic disk substrates and semiconductor wafers. It measures angular displacement at a fixed pitch, then calculates the surface profile by totaling the angular data multiplied by the measurement pitch. When it is calibrated with a reference flat mirror, the system has a measurement accuracy better than 0.01 μm . In addition, another calibration algorithm using a Fast Fourier Transform (FFT) for the direction of rotation was developed.

UDC 62-52:681.2-5
FUJITSU Sci. Tech. J., **26**, 1, pp. 41-47(1990)

Six-Axis Force/Torque Sensor for Assembly Robots

• Akihiko Yabuki

Force control assembly robots require a six-axis force/torque sensor to detect the forces applied to the robot arm. A new force/torque sensor has been developed which mounts on the wrist of the robot and detects strains exerted on a bit deformable elastic body caused by contact of the end-effector with the assembly. Force/torque detection is performed in real time and in six-degrees-of-freedom in a Cartesian coordinate system. The elastic body consists of eight parallel leaf springs and has excellent noninterference and output linearity.

The sensor has an internal overload protector for impact tolerance.

UDC 62-52:681.5
FUJITSU Sci. Tech. J., **26**, 1, pp. 48-54(1990)

High-Speed Force Controller for SCARA Robots

• Yutaka Yoshida • Akihiko Yabuki • Yasuyuki Nakata

The SCARA (Selective Compliance Assembly Robot Arm) robot has horizontal compliance. However, the amount and direction of compliance must be controlled before the robot can be used in actual applications. An active compliance controller has been developed that uses force sensors on the wrists of the robot to determine the contact force acting on the end effector. The sensors feed this information to the trajectory generator of the robot controller. The controller achieves high-speed control (sampling rate: 1 kHz) by performing all control operations in parallel using two Fujitsu MB8764 digital signal processors (DSPs).

UDC 681.3.06:681.51
FUJITSU Sci. Tech. J., **26**, 1, pp. 55-64(1990)

Simulator for a Coordinated Two-Arm Robot

• Hiroshi Wada • Mitsuo Kamimura • Sadao Fujii

Fujitsu is developing a general-purpose assembly robot consisting of two coordinated multi-jointed arms modeled on their human counterpart. Fujitsu is also developing software to deal with assembly problems such as the layout of work, assembly procedures, and path generation; and to deal with operation problems such as representation and implementation of coordinated operation. The robot language TACL: Two Arm Cooperation Language and simulator for the robot was developed to help solve these problems. A task-level robot language ASL: Assembly Sequence Language and a method of generating TACL from ASL have also been developed. This paper describes TACL, the simulator, ASL, and how TACL is generated.

UDC 53.084.87:771.448.6

FUJITSU Sci. Tech. J., 26, 1, pp. 65-70(1990)

A Logic State Measurement Technique Using Multi-Stroboscopic Sampling for the Electron Beam Tester

• Akio Ito • Kazuo Okubo • Akifumi Muto

A multi-stroboscopic sampling (MSS) technique was devised for electron beam tester logic state measurement. In this technique, electron beam pulses are shot and secondary electron signals are sampled m times in each cycle of LSI device operation. In addition, s-curve interpolation (SCI) is combined with MSS for quantitative voltage measurement. Using this combination, the measurement time required for 1 024 logic states was reduced to 1/70 the time required for stroboscopic waveform measurement.

UDC 53.084.87:621.3.049.771.14

FUJITSU Sci. Tech. J., 26, 1, pp. 71-77(1990)

Electron Beam Tester for VLSI Diagnosis

• Masaaki Kawabata • Akifumi Muto • Tetsuya Mukunoki

An electron beam tester for design verification and fault diagnosis of large-scale high-density ICs was developed.

The tester can measure voltage waveforms of fine electrodes in VLSI circuits by using an electron beam. The measurement time resolution is 100 ps and the voltage resolution is better than 0.1 V.

The electron beam tester is directly connected to an LSI tester to reduce the propagation delay and waveform distortion. It can measure through the insulation film and can test a logic circuit with a long repetition frequency in a short time.

UDC 621.375.823:621.391.6

FUJITSU Sci. Tech. J., 26, 1, pp. 78-85(1990)

Phase-Shifted Gratings for DFB Lasers

• Manabu Matsuda • Shouichi Ogita • Yuji Kotaki

The introduction of phase shifts in the grating for distributed feedback (DFB) lasers gives additional freedom in DFB laser design to realize various kinds of advanced performance. Here, a technology of fabricating a multiple-phase-shifted grating for long-cavity DFB lasers for coherent optical communication systems has been developed. This new technology is based on a method using a phase-shifting mask. A new phase-shifting mask with three steps in the height has been developed and uniform gratings with the three phase shifts of 0.8π have been fabricated. This method can provide not only an arbitrary phase shift, but also an arbitrary combination of phase shifts at arbitrary locations.

UDC 681.32:800.92

FUJITSU Sci. Tech. J., 26, 1, pp. 98-106(1990)

Unified Hardware Description Language (UHDL) and Its Support Tools

• Masahiro Fujita • Hisanori Fujisawa • Nobuaki Kawato

A lot of effort has been devoted to improving the efficiency of designing ASICs, and many new hardware description languages have been developed. However they have serious drawbacks. They are designed for use only in limited areas, and their semantics are constructed in rather an *ad hoc* manner. To overcome these drawbacks, UHDL, which has a multiple view mechanism and whose semantics are based on mathematical logic, is being developed. Using UHDL realizes high-quality synthesis, and there is no ambiguity in the interpretation of design descriptions. This paper summarizes the important features of UHDL and its support tools.

UDC 681.3.06:681.326.3

FUJITSU Sci. Tech. J., 26, 1, pp. 86-97(1990)

Overview of an Experimental Reflective Programming System: ExReps

• Jiro Tanaka • Yukiko Ohta • Fumio Matono

This paper presents an overview of an experimental reflective programming system (ExReps). ExReps is an environment in which one can input programs and execute goals. It consists of two layers: the abstract machine layer and the execution system layer. Both layers are based on an enhanced metacall mechanism. Reflective operations are implemented on these metacalls. This paper shows examples of program execution on ExReps and examples of reflective programming.

UDC 538.975:539.4.016:669-122:669.587

FUJITSU Sci. Tech. J., 26, 1, pp. 107-113(1990)

Approximation for the Rate of Short Circuit in Electronic Devices Caused by Whisker Growth on Zn Electroplated Steel

• Takeshi Nagai • Katsuhide Natori • Takashi Furusawa

Specimens of electroplated cold-rolled steel plate were exposed for approximately six years. Nucleation and growth of Zn whisker on specimens were observed, and the number of days before whiskers were detected was recorded. A correlation was found between the number of days before whisker detection and the macro internal stress measured using the bending strain method.

The number and length of whiskers was counted and measured, and an approximation for the projected rate of short circuit caused by whiskers was obtained.

An approximate rate of short circuit by whisker growth was of about nine fit was obtained.

Preface

Special Issue on Production Engineering Technologies

● Takefumi Inagaki

Electronic Systems Division, Fujitsu Laboratories Ltd.

For Fujitsu Limited, a company having annual gross sales of more than two trillion yen, it is becoming essential to develop high-grade production technologies that can be integrated with all company activities.

Fujitsu is now developing its next generation of key products. Some examples of these products are VLSIs (very large scale integrated circuits) PWBs (printed wiring boards) for tomorrow's large-scale computers and magnetic disks. To develop these products, it is becoming increasingly necessary to use technologies of measurement, recognition, and mechanical control that simulate functions of the human brain, eye, and hand. Therefore, Fujitsu's business divisions anticipate increasing activity in the development of these technologies.

This special issue focusses on production technology. It presents some examples of technologies for inspection and measurement, assembly, and test and diagnosis which have been developed at Fujitsu Laboratories and at Fujitsu's Corporate Production Engineering Group.

The first section of this special issue covers manufacturing technology. In recent years, surface mounting technology has frequently been applied to PWBs. Reflow soldering is used to solder surface mounted components, and the heating tip that controls the solder temperature plays a key role in the reliability of the soldered junctions. The first section presents a paper on the development of a laser welding method that bonds a thermocouple to this type of heating tip.

The second section of this special issue presents four papers on inspection and measurement technology. The first of these papers describes an automated optical pattern inspection system for high-density PWBs. (Pattern inspection is a very important stage in the production of the high quality PWBs used in Fujitsu's large-scale computers). The equipment developed using this technology is now operating at the Nagano Plant.

Most of the components of PWBs are surface mounted, and are becoming smaller and more densely mounted. The second paper describes a high-speed wide area 3-D vision system that uses range and intensity images. This system inspects surface mounted components at high speed in three dimensions.

The demand for printers is expanding with the advance of OA. Fujitsu also produces printers and therefore has a strong interest in automated inspection of print quality. Previously, print quality inspection was performed by skilled personnel and could not be automated. The third paper discusses a sensory pattern inspection system that assesses the print quality of dot-matrix printers by simulating human vision.

The fourth paper describes a surface flatness measurement system for magnetic disks. High-density magnetic disks are constantly being improved and their flatness has a strong influence on their recording characteristics. To measure the flatness of these disks, Fujitsu has developed a non-contact high-precision flatness measuring system that uses a laser beam.

The third section of this special issue covers assembly technology. Robots are essential tools for the automation of assembly work in wide-variety small-quantity production. This section presents three papers that discuss sensor, force control, and simulator technologies for robots. Force,

as can be seen by observing humans performing manual work, is indispensable when assembling a product. To detect the forces exerted on a robot from the workpieces and environment and to control the forces generated by the robot, a six-axes force-torque sensor is required. The first paper in this section describes the development of a six-axes force/torque sensor for assembly robots. The second paper describes a high-speed force controller for SCARA (Selective Compliance Assembly Robot Arm) robots. This controller performs active-compliance control by using force/torque signals obtained from a sensor installed on the wrist of a SCARA robot. The last paper of this section describes a simulation to coordinate the operation of a two-arm articulated robot.

The last section of this special issue presents two papers on test and diagnosis technology. These two papers describe the advanced technology and equipment required to develop VLSIs. To diagnose VLSIs, the logic waveforms on the VLSIs' internal wiring must be measured at high speed. To achieve this, Fujitsu has developed a logic state measurement technique that uses multi-stroboscopic sampling for the Electron Beam Tester. Fujitsu has also developed an electron beam tester that uses this measurement technique for VLSIs. The second paper describes the development of an electron beam tester for VLSI diagnosis that has a time resolution of 100 ps and a voltage resolution of better than -0.1 V. This tester is now operating at the Kawasaki Plant.

Fujitsu is continually improving its product planning and production technology to produce advanced high-quality products. Competition in the electronic equipment field is growing more intense, and in the near future, production technology will become a key to success. Fujitsu will continue to develop new technologies and equipment to maintain its position as a world leader.

Laser Welding of Thermocouple to Molybdenum Heating Tip

• Naohisa Matsushita • Kazuo Yokoi (Manuscript received December 18, 1989)

This paper presents a new method of attaching a thermocouple to a heating tip using a pulsed YAG laser.

This heating tip is used in reflow soldering of Surface Mount components on printed wiring boards. The thermocouple is attached to the heating tip to control the soldering temperature.

The heating tip is made of molybdenum and the thermocouple is made of chromel and constantan wires. These wires are so thin that their heat capacity is far less than that of the heating tip. It is therefore difficult to attach the thermocouple to the heating tip using brazing or conventional laser welding.

1. Introduction

Reflow soldering is a technique used in Surface Mount Technology (SMT). There are two types of reflow soldering. One involves heating the entire printed circuit board, and the other involves heating the soldering point only. The heating tip described in this paper is used for local heating. To achieve good reflow soldering, it is essential to keep the temperature of the tip constant at about 300 °C.

The heating tip is made of molybdenum and the thermocouple is made of chromel and constantan wires. It is difficult to attach these thermocouple wires to the molybdenum tip because they are made of two different metals each having a high melting point. Also, the thermocouple wires are thin (0.2 mm or 0.3 mm) and have very different thermal capacities from that of the molybdenum tip.

To solve these problems, a pulsed YAG laser that provides a high energy density was used¹⁾.

2. Welding using a pulsed YAG laser

The essential point of laser welding is how to melt the molybdenum tip sufficiently without

thinning the thermocouple wires placed on the heating tip²⁾.

Figure 1 shows the multi-point laser irradiation method that is normally used. This method irradiates the thermocouple and tip with a large number of low energy pulsed lasers.

This method has the following disadvantages:

- 1) The strength of the weld is low (tensile strength is only about 1.2 kgf) because the molybdenum tip is not sufficiently melted,
- 2) Accurate temperature measurement is impossible (measurement accuracy is ± 5 °C) because the bonding between the chromel and constantan wires is poor,
- 3) The welding takes a long time because multi-point laser irradiation is used.

To overcome these problems and to achieve sufficient welding, the following objectives were established:

- 1) Improvements in weld strength
 - i) Tensile strength: 3 kgf or more
 - ii) Peel strength: 1.5 kgf or more
 - iii) Cycle bending fatigue strength:
 - Welds must be able to withstand at least

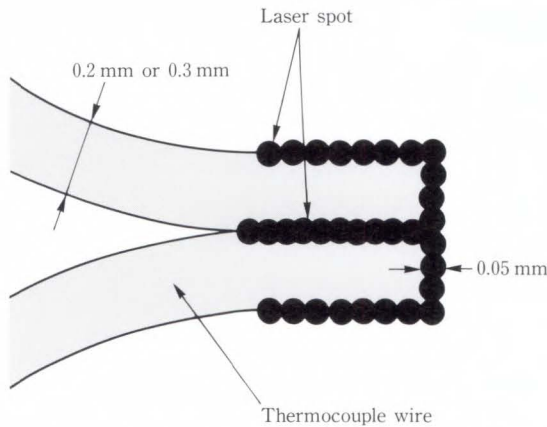


Fig. 1—Multi-point laser irradiation.

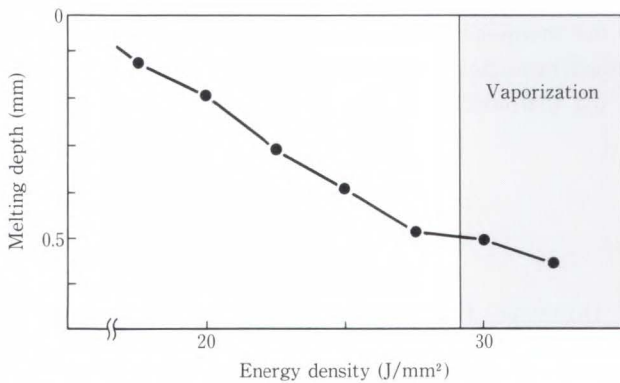


Fig. 2—Relationship between laser irradiation energy density and melting depth.

30 000 bending cycles.

- 2) Improvements in temperature measurement accuracy
 - i) Temperature measurement accuracy:
Within $\pm 2^\circ\text{C}$
- 3) Improvements in welding
 - i) Welding with one shot laser irradiation.

2.1 Conditions for optimum melting of the tip and wires

Experiments were carried out to determine the conditions required for optimum melting of the molybdenum tip and thermocouple wires.

2.1.1 Conditions for optimum melting of the molybdenum tip

In welding using a pulsed YAG laser, the pulse width and energy density (energy irradiated per unit area) are essential parameters^{2),3)}. To ensure sufficient melting, a laser

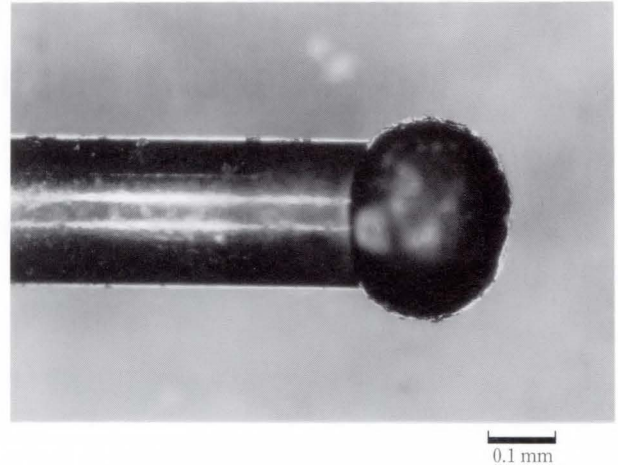


Fig. 3—End of a chromel wire irradiated by laser beam: Irradiation has made the end spherical.

beam with a long pulse width must be used. Figure 2 shows the relationship between the irradiation energy and melting depth observed when the pulse width was between 7 ms and 9 ms and the spot diameter was 0.5 mm.

The following observations were made: At pulse widths between 7 ms and 9 ms, the melting depth was 0.2 mm or less when the energy density was 20 J/mm² or less, and was 0.3 mm to 0.5 mm at 25 J/mm²: Holes were formed in the tip by vaporization when the energy density was 30 J/mm² or more. Therefore the irradiated energy density of the molybdenum tip was fixed to about 25 J/mm².

2.1.2 Conditions for optimum melting of the thermocouple wires

Figure 3 shows the end of a chromel wire that was irradiated by a laser beam. As can be seen, the laser has made the end spherical. It is therefore possible to melt the wires without thinning them by utilizing these spheres. The laser irradiation conditions required to make the ends of the wires spherical were therefore sought.

Figure 4 shows the relationship between the laser irradiation position (L mm) and the resultant shape of the wire end. At a pulse width of 7 ms and an irradiation spot diameter of 0.5 mm, the ends became stably spherical when the irradiated energy density was 18 J/mm² to 25 J/mm². The shapes obtained

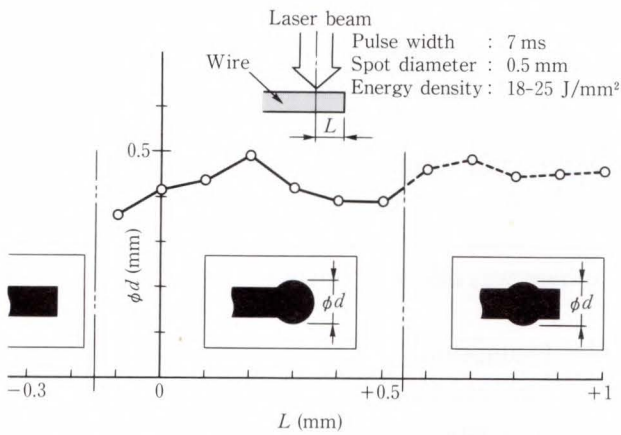


Fig. 4—Relationship between laser irradiation position and the shape of wire ends.

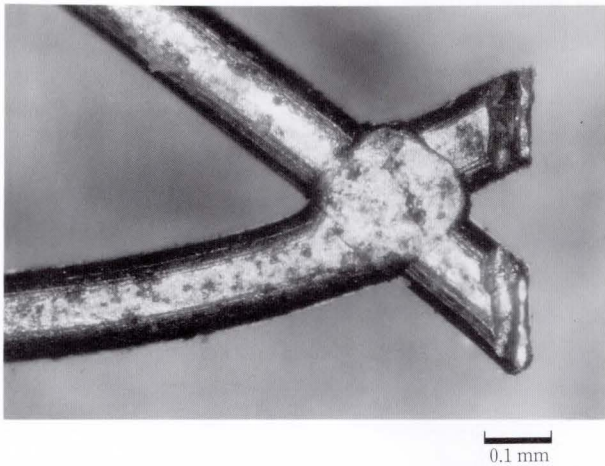


Fig. 5—Preforming of thermocouple wires: Two wires are crossed near their end to form an X and then welded together using an electric spot welder.

at $L = -0.2$ mm to $+0.5$ mm are suitable for welding the thermocouple. In particular, when $L = +0.2$ mm the diameter of the spheres was 0.5 mm, which satisfied the objective.

To improve the temperature measurement accuracy and one shot laser irradiation, the wires were preformed (see Fig. 5). The two wires were crossed to form at X near their ends and were when welded together using an electric spot welder.

2.2 Tip and thermocouple wire welding technique

As mentioned above, the optimum laser irradiation conditions required for the various

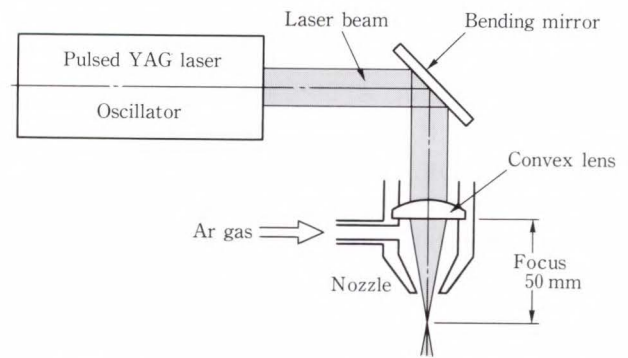


Fig. 6—Configuration of pulsed YAG laser welding system.

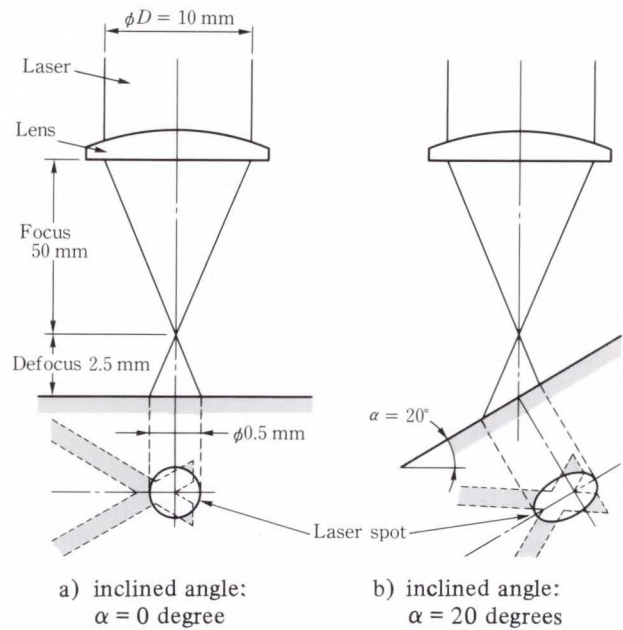


Fig. 7—Oblique laser beam irradiation.

materials (molybdenum tip, chromel and constantan wire) were determined. However, the energy density irradiating the molybdenum tip must be about 25 J/mm^2 , but must be slightly lower at about 22 J/mm^2 for the thermocouple wires.

2.2.1 Configuration of the pulsed YAG laser welding system

This system includes a pulsed YAG laser oscillator, a convex lens having a focus of 50 mm, and a jet of inert gas (see Fig. 6). The inert gas prevents metal oxidation and is argon gas in this system.

2.2.2 Oblique irradiation of laser beam

To satisfy the requirement of different

irradiation energy densities, an oblique irradiation technique was devised (see Fig. 7). The laser beam is focused by a convex lens into a cone. If the workpieces are set obliquely, the irradiation density at the top of the oblique slope is greater than the density at the bottom. If the molybdenum tip is placed at an appropriately higher position on the slope than the thermocouple wires, the tip and thermocouple wires will be subjected to the correct proportion of irradiation energy densities.

The following configuration was used. The laser beam diameter was 10 mm, and was condensed by a convex lens having a focal length of 50 mm and a defocus of 2.5 mm. The spot diameter was 0.5 mm. The workpieces were inclined at 20 degrees and were irradiated at an energy density that would have been 24 J/mm^2 if directed perpendicularly. Calculations for this configuration gave an energy density at the molybdenum tip of about 25 J/mm^2 and about 22 J/mm^2 at the thermocouple wires.

3. Results and evaluation

3.1 Results

The thermocouple wires were preformed and placed on the molybdenum tip. The assembly was and then irradiated with one pulse at the position shown Fig. 8. The result is

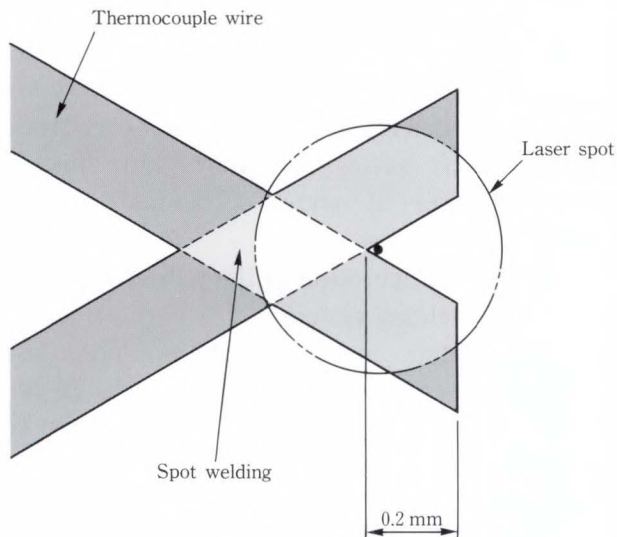


Fig. 8—Laser irradiation position.

shown in Fig. 9. The wires were melted without thinning because of the spherical portions that formed near the ends. The laser beam also passed through the gap between the crossed wires and irradiated the molybdenum tip. Therefore, the materials were welded together at a small spot. (The diameter of the weld sphere was about 0.5 mm.)

3.2 Evaluation

The mechanical strength and thermometric characteristics of the thermocouples are described below.

3.2.1 Mechanical strength

Figure 10 compares the mechanical strength of welds formed by multi-point laser irradiation with that of welds formed by our technique

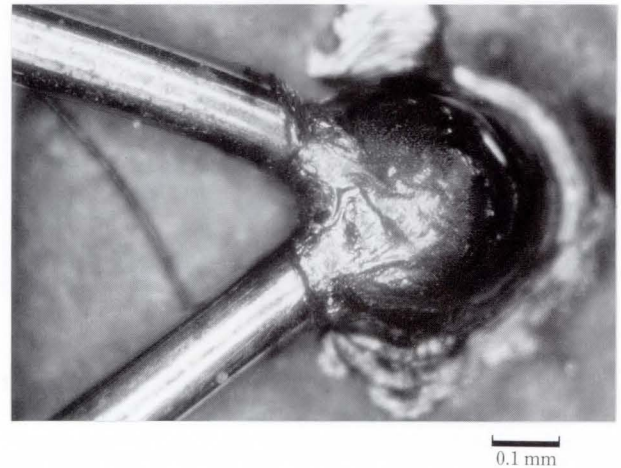


Fig. 9—Shape of welded section: thermocouple wires are melted without thinning.

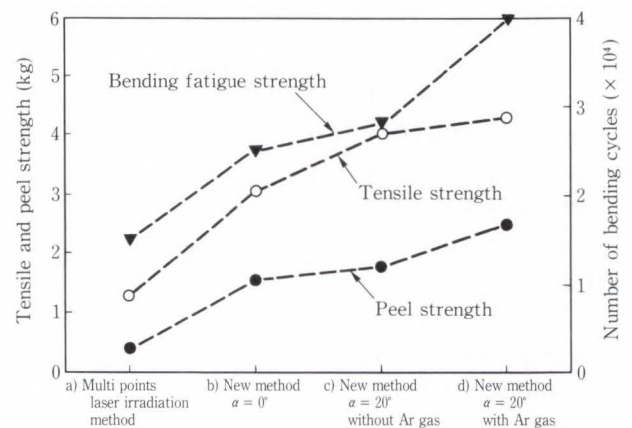


Fig. 10—Comparison of mechanical strengths.

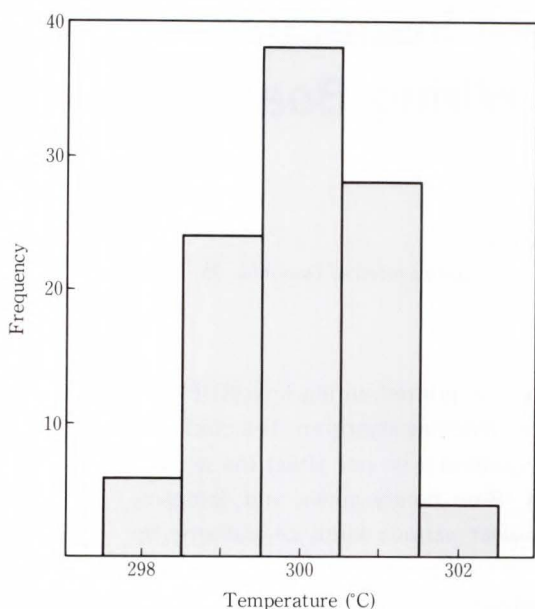


Fig. 11—Distribution of indicated temperature at 300 °C.

of preforming and one shot laser irradiation.

Three types of welds formed by the new method were evaluated: welds formed with the workpiece inclined at 0 degrees, welds formed with the workpiece inclined at 20 degrees, and welds formed with the workpiece inclined at 20 degrees and sprayed with argon gas.

The results of this evaluation show that welds formed by the new method have up to three times more strength than welds formed by multi-point laser irradiation. In addition, the welds formed by oblique irradiation have about 30 percent more tensile strength than welds formed by perpendicular laser irradiation. The use of argon gas increased the peel strength by about 25 percent and more than doubled the cycle bending fatigue strength.

3.2.2 Thermometric accuracy

Figure 11 shows the distribution of indicated temperature at 300 °C.

The accuracy of thermocouples attached by the new method was ± 2 °C at this temperature.

4. Conclusion

This paper discussed a new method of using a pulsed YAG laser to attach a thermocouple to the heating tip used in Surface Mounting Technology reflow soldering.

The results are summarized below.

- 1) The thermocouple wires are crossed (preformed) to form an X and then bonded to the heating tip. The bonded wires and tip are tilted at about 20 degrees. One pulse of a YAG laser beam at an energy density which would be 24 J/mm² if irradiated perpendicularly is irradiated onto a 0.45 mm diameter spot to perform small-diameter spot welding.
- 2) The use of an inert gas (argon) and a radiator helps to increase the weld strength.
- 3) Although this technique involves preforming, the overall processing time is short because the wires are attached using a single laser pulse.

References

- 1) John, F. Ready: Material Processing-An Overview. *Proc. IEEE*, **70**, 6, pp. 533-544 (1982).
- 2) Watanabe, T., and Shimo, C.: Melting and Removing Process of Stainless by YAG Laser Irradiation. *JSPE*, **51**, 5, pp. 1007-1012 (1985).
- 3) Matsunawa, A., and Katayama, S.: Fusion and solidification process of pulsed YAG laser spot weld. *Proc. 5th Int. Cong. Appl. Laser Electro-optics*, 1986, Arlington, Va., pp. 81-87.



Naohisa Matsushita

Corporate Production Engineering Group
Production Engineering Div.
FUJITSU LIMITED
Bachelor of Mechanical Eng.
Meiji University 1976
Master of Mechanical Eng.
Meiji University 1978
Specializing in Materials Processing



Kazuo Yokoi

Corporate Production Engineering Group
Production Engineering Div.
FUJITSU LIMITED
Bachelor of Mechanical Eng.
The University of Tokyo 1971
Specializing in Materials Processing

Automated Optical Pattern Inspection for High-Density Printed Wiring Boards

• Moritoshi Ando • Hiroshi Oka • Satoshi Iwata

(Manuscript received December 28, 1989)

A new technique for the automated optical inspection of printed wiring boards (PWBs) has been developed. It uses black-line sensing and a radial-matching algorithm. The black-line sensing detects copper patterns as shadows. Color and roughness do not affect the sensing. The radial-matching algorithm converts patterns into 16-bit binary codes, and compares them with a code dictionary. The algorithm can inspect various kinds of patterns by changing the contents of the dictionary.

An inspection system using these techniques was constructed. It has a resolution of 5 μm and can inspect a 490 x 540 mm area in five minutes.

1. Introduction

The automated optical inspection of the patterns of printed wiring boards (PWB) is indispensable in the production of high-density PWBs. This is because PWBs have become too large and complex for manual inspection. For example, a PWB used in Fujitsu's FACOM M-780 mainframe is 540 x 490 mm, and the pattern line width is 60 μm . The PWB has 42 inner layers, and is one of the densest ever made.

The defects on inner layer patterns that must be detected are breaks, bridges, residues, narrow tracks, and poor spacing. Breaks and shorts cause the electrical circuit to malfunction immediately. Residues, narrow tracks, and poor spacing do not cause immediate problems, but might deteriorate into serious defects. All these defects have to be detected and repaired before lamination, after which repair is impossible.

PWBs are inspected both electrically and visually. The electrical tester checks the electrical conductivity and detects breaks and bridges. However, it cannot detect residues, narrow traces, and poor spacing. The visual inspection measures pattern widths and detects

the defects not detected by the electrical tester. Visual inspection of a single inner layer takes hours. Automated inspection reduces inspection time and ensures reliability.

Automated inspection is conducted through pattern sensing and defect detection algorithms. A new method using a black-line sensing¹⁾ and radial-matching²⁾ algorithm has been developed for the inspection of the inner high-density PWB layers.

2. Requirements for the pattern inspection system

The most important requirements for PWB pattern inspection are high-speed pattern processing and wide adaptability.

High-speed processing is needed because a PWB may have ten gigapixels of picture information which must be inspected within several minutes. An example of PWB patterns is shown in Fig. 1. The system must have a processing speed of several tens of megapixels per second. A special-purpose hardware circuit must be implemented to achieve this speed.

The system has to be able to be adapted both to the pattern design variety and the surface conditions of copper patterns. PWB

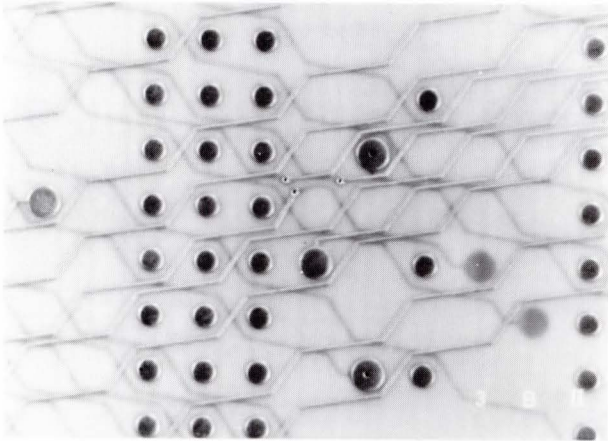


Fig. 1—Inner PWB layer.

patterns differ in width, direction, and shape, depending on design rules. In a factory, various kinds of PWB patterns are produced in the same production line. The system must adapt to the production environment. The system must also adapt to the fluctuations in surface conditions such as copper color and surface roughness. The color of copper is changed by a chemical process and becomes darker when exposed to air. Copper surface roughness is also changed by a chemical process. These fluctuations have little effect on the electrical characteristics, and must be allowed for. The system has to detect copper patterns without being affected by these fluctuations.

First, the pattern sensing system is discussed.

3. Pattern sensing system

3.1 Requirements for pattern sensing

There are two requirements for pattern sensing. The first is the stable detection of the pattern. Copper easily becomes dark, as is shown in Fig. 2. The dark area is often mistaken for nicks or pinholes when light reflected from the surface is sensed. The effect becomes most serious when the pattern width is only $60\ \mu\text{m}$, because a small dark spot on a line is often perceived as a break. This increases the false error rate. Conventional systems mainly use reflected light sensing³⁾. This method cannot distinguish between dark spots and breaks and is not satisfactory for high-density PWB inspection. To construct a practical inspection

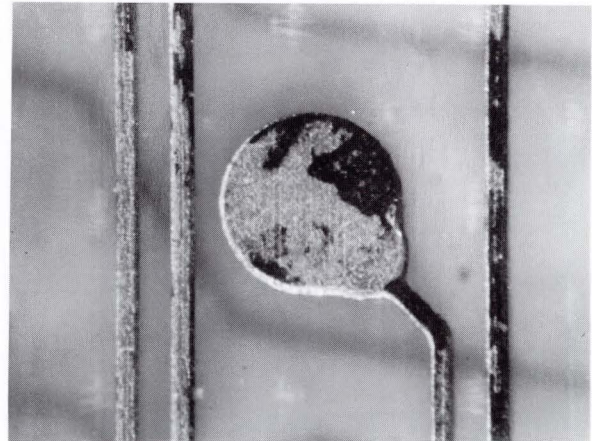


Fig. 2—Copper pattern.

system, a rule of thumb says the S/N ratio should be greater than three. This could only be achieved by making the sensing so that it is not affected by the copper color.

The second requirement is high resolution. To measure the pattern width, the resolution should be within one-tenth of the pattern width. Since the pattern is only $60\ \mu\text{m}$ wide, the resolution must be within $5\ \mu\text{m}$.

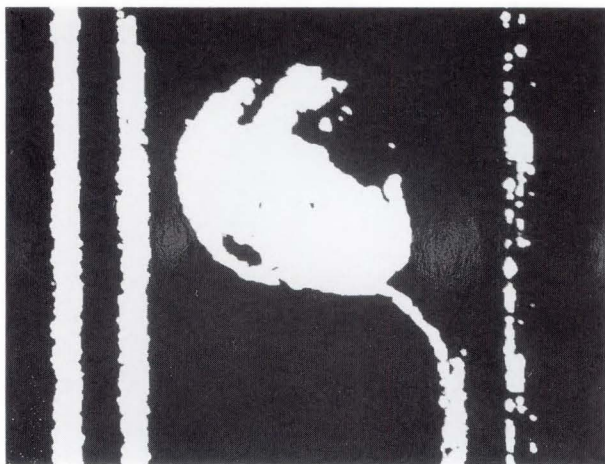
3.2 Conventional pattern sensing

There are two conventional sensing methods: Reflected light sensing and transmitted light sensing³⁾. Neither is well suited for detecting fine PWB patterns.

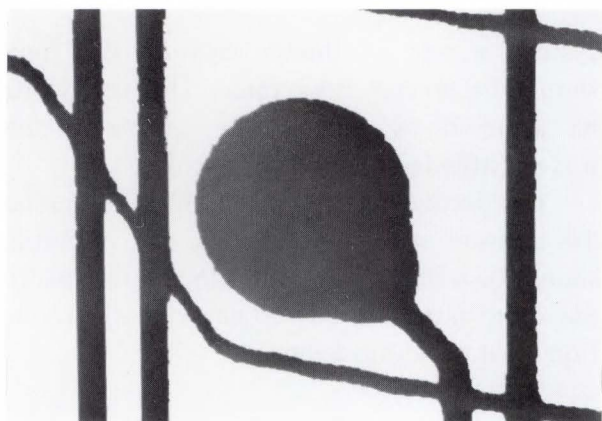
Reflected light sensing detects the copper patterns as shining regions and the substrate as a dark region. If the copper is dark, sensing is affected as shown in Fig. 3 a). This method cannot be used for pattern sensing.

Transmitted light sensing detects the copper patterns as shadows and the substrate as a bright region. Sensing is not affected by the copper color, but it does erroneously detect patterns etched on the other side of the substrate, as is shown in Fig. 3 b). In the figure, the narrow diagonal lines are noise patterns from the other side.

A new method is needed, with the advantages of transmitted light sensing, but without the drawbacks.



a) Reflected light sensing



b) Transmitted light sensing

Fig. 3—Results of conventional sensing.

3.3 Black line sensing

3.3.1 Principle

Figure 4 shows the black line sensing system. A xenon lamp light source illuminates a line filter, which has a black line in the center. The line pattern is focused onto the printed wiring board and the area around the line is illuminated brightly. The illuminance is about one million lux. Because the substrate is translucent, the light diffuses into the substrate before being reflected back. The image is sensed by a CCD line sensor. The sensor detects the substrate as a bright area and detects the copper patterns as shadows because they do not transmit light. This method detects the pattern regardless of the surface conditions of the copper, and can detect only surface patterns

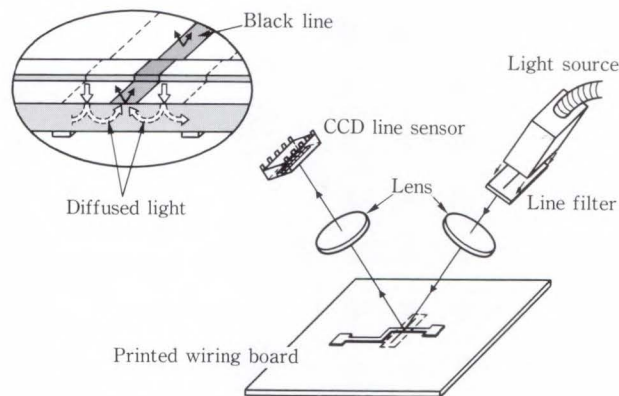


Fig. 4—Black line sensing system.

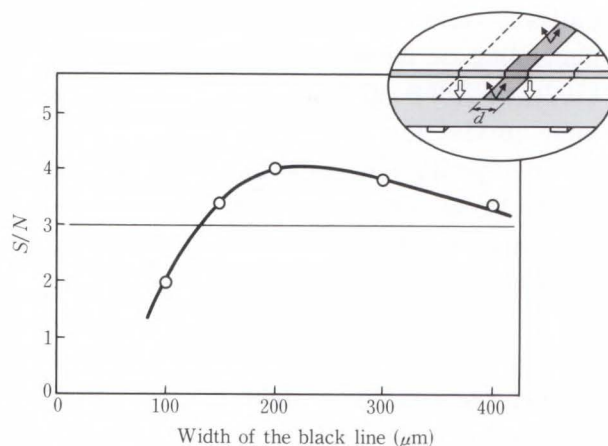


Fig. 5— S/N ratio of the black line sensing.

without detecting patterns on the other side.

3.3.2 S/N of black line sensing

Figure 5 shows the effectiveness of the black line sensing system. The horizontal axis is the width of the black line, d . The S/N ratio is defined as the ratio of the signal intensities of the substrate and the copper pattern that are within the black line area. Figure 5 shows that the S/N ratio deteriorates at greater line widths. This is because the farther the light must diffuse, the less its intensity. At widths of less than $100 \mu\text{m}$, the S/N ratio decreases as the line becomes brighter due to diffraction. A range of $200 \mu\text{m}$ to $250 \mu\text{m}$ gives the optimum value of around four for the S/N ratio.

3.4 Result of the sensing

Figure 6 shows the result of black line

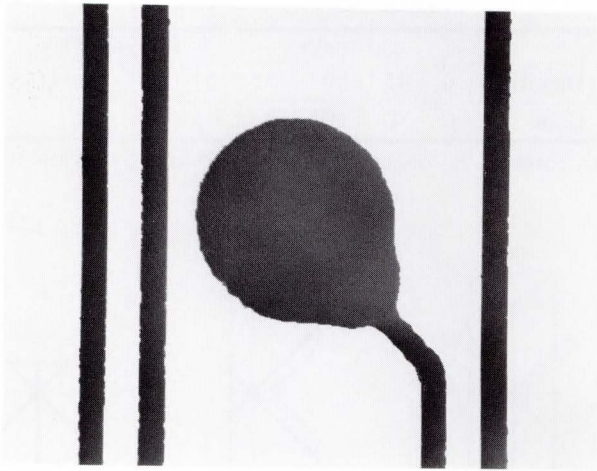


Fig. 6—Black line sensing.

sensing. The surface color does not affect the result and the patterns on the other side of the substrate are not detected.

4. Pattern inspection algorithm

4.1 Requirements for an algorithm

Printed wiring patterns consist of pads and lines. However, the pattern width, pattern direction, and pad size vary depending on PWB design. There are two pattern inspection algorithms: design rule⁴⁾ and data reference⁵⁾. The design rule algorithm detects pattern features such as width, length, and spacing, and compares them with predetermined standard values. The algorithm is simple and easily implemented with hardware circuits. However, hardware implementation requires a specific circuit for each type of defect, and is not easily adapted to new patterns or new inspection rules.

The data reference algorithm stores all pattern data such as pattern width, direction, and positions generated by CAD, and compares them with the detected patterns. The method is adaptable to any pattern and extracts all defects that differ from the design. However, storing and updating the pattern data is difficult and time-consuming. Loading reference data into the system when testing a different PWB is also slow. This algorithm cannot be used for high-density PWB inspection.

A new method is needed, that can easily adapt to a new patterns and inspect various patterns without having to store the entire design. A new method, called radial-matching, is proposed. In radial-matching, pattern data is expressed by code and can adapt to various kinds of patterns.

4.2 Radial-matching

4.2.1 Principle

A new algorithm describes PWB patterns with a minimum amount of information. The essential features that define the PWB line pattern are width, direction, and symmetry. The new algorithm measures these features and encodes them into subclasses. The resulting codes are 16-bit binary codes and can represent 65 536 patterns.

Inspection is performed by checking the obtained pattern codes in a look-up dictionary. The dictionary tells whether the code represents a good or a bad pattern. The contents of the dictionary are changed according to the pattern and the definitions of the defects. Data is loaded into the dictionary automatically before inspection, using a good pattern.

This algorithm inspects various kinds of patterns using a minimum amount of memory.

The inspection algorithm follows the procedures described below.

1) Detection of a pattern center

The algorithm first finds certain points called the pattern centers. Pattern centers correspond to points on the center-lines of printed wires, as well as to certain other points on the boards.

If a point is on a printed wire, the corresponding pixel lies in a dark region. Each pixel is tested to determine whether it is a pattern center. This is done by measuring the distance of the region edge from the pixel in 16 radial directions. Figure 7 shows the sensors used to perform this measurement.

Two length-measuring sensors which point in opposite directions form a measuring pair, of which there are eight. When both sensors in a measuring pair calculate equal distances from the region edge, the pixel is said to have

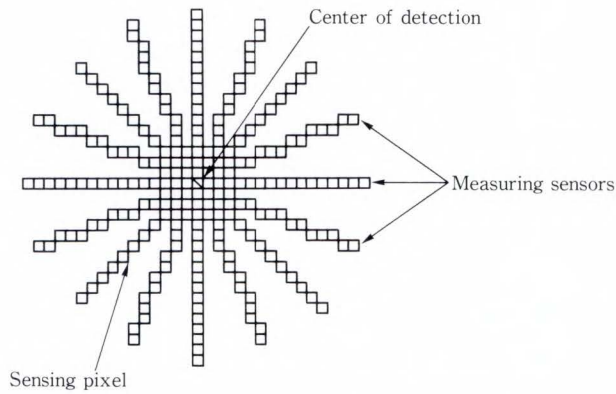


Fig. 7—Measuring sensors for radial matching.

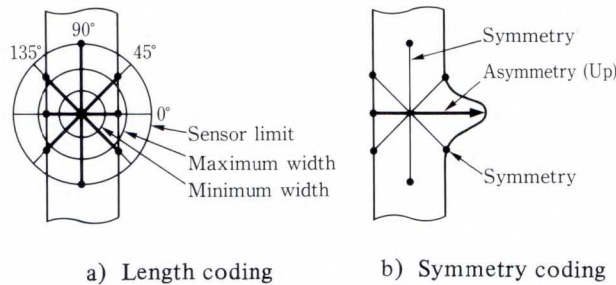


Fig. 8—Elements of coding.

symmetry in that direction. If the number of pairs that indicate symmetry exceeds a threshold value, the pixel is a pattern center.

Only information on the pattern center is used in coding the pattern.

2) Classifying the patterns

Information on each pattern center is used to generate a binary code for that center. First, the lengths are calculated by the measuring pairs in the 0°, 45°, 90°, and 135° directions, as shown in Fig. 8 a). The pattern length for each direction is the sum of the length calculated by the two measuring sensors of the pair for that direction. Each pattern length is then compared with three threshold values. The threshold values are the minimum allowable line width, the maximum allowable line width, and the maximum length of a measuring sensor. A pattern length that is shorter than the minimum line width is classified as shorter (S), one between the maximum width and the sensor limit is classified as longer (L), and one over the sensor length is classified as over (OV). The classified results are represented as codes.

Table 1. Examples of coding

Direction	a) Length				b) Symmetry			
	0°	45°	90°	135°	0°	45°	90°	135°
Code	C	L	OV	L	Up	Sy		

C: correct L: longer OV: over Up: up Sy: symmetry

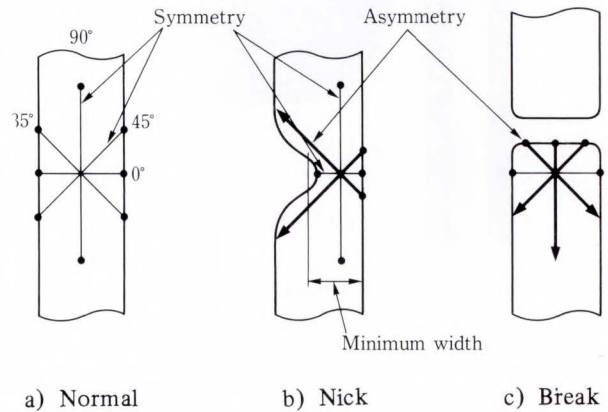


Fig. 9—Examples of coding.

Results for a line pattern center are shown in Table 1 a).

Symmetry is also classified as follows: When the lengths of the paired sensors are equal, the pattern center has symmetry (Sy). When the length of the upper sensor is longer, it is called up (Up). When the length of the lower sensor is longer, it is classified as lower (Lw). An example of symmetry classification is shown in Table 1 b). Here, only the 0° direction does not have symmetry. When the length of the sensor on the right side is longer, it is classified as Up.

Both the length classes and the symmetry classes are expressed by two bits. The total number of binary bits are calculated as follows, $(2 + 2) \times 4 = 16$, giving a total number of 16 bits. The total number of classes are 65 536 patterns. Each 16-bit binary number corresponds to a specific pattern, and the number is called the code of the pattern.

3) Distinguishing between good and bad patterns

The 16-bit code for each pattern center is looked up in the look-up dictionary. The dictionary determines whether each code is defined as good or 'bad. A bad code indicates a defect. The contents of the look-up dictionary

Table 2. Exmaples of codes

	a) Normal				b) Nick				c) Break			
Direction	0°	45°	90°	135°	0°	45°	90°	135°	0°	45°	90°	135°
Code	C	L	OV	L	S	L	OV	L	C		OV	C
Symmetry	Sy				Sy	Lw	Sy	Up	Sy	Lw		

Lw: lower
Up

can be changed according to the inspected patterns.

Figure 9 shows how binary codes describe the pattern features, and Table 2 shows the results of coding. Figure 9 a) shows a normal pattern. This pattern center has symmetry in all four directions. The length in the 90° direction is equal to the maximum sensor length, and indicates the direction of the printed wire. The direction perpendicular to the direction of the printed wire indicates the pattern width.

Figure 9 b) shows an example of a nick. This pattern has a shorter value at 0° and has an OV code at 90°. It indicates the presence of a narrow line pattern in the 90° direction. Symmetry investigation shows that this pattern has symmetry at 0° and 90°, but not at 45° or 135°. Here, arrows mark the larger parts of the asymmetry pairs. Table 2 b) shows the code of the nick. The codes show not only that the defect is a nick, but also that the nick is on the left side.

Figure 9 c) shows an example of a break. The 0° measurement has symmetry and is within the line-width tolerance. However, 45°, 90°, and 135° are all asymmetric and have longer lengths on the lower sides. The greatest length is at 270°. These results indicate a break. Table 2 c) shows the code of the break.

4.2.2 Generation of a dictionary

Using this encoding method, a code dictionary is generated. The results are shown in Fig. 10. The horizontal axis shows the inspection area, and the vertical axis shows the number of extracted good pattern codes. The black dotted line shows the number of good codes made from the line pattern, and the white dotted line shows the number of good codes extracted from the pattern gaps. Because the

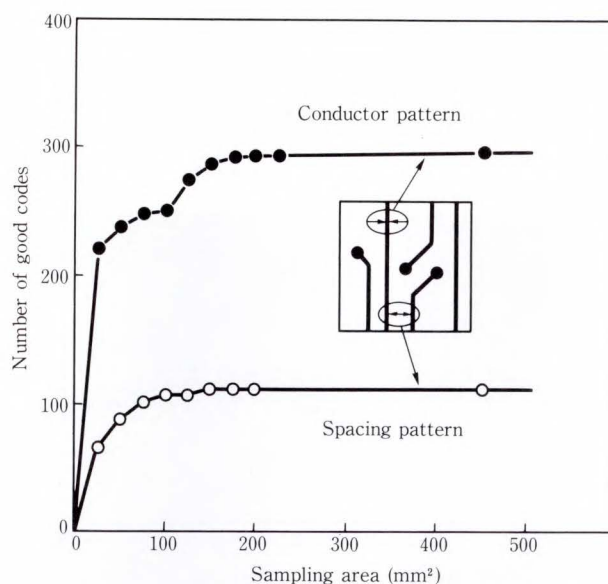
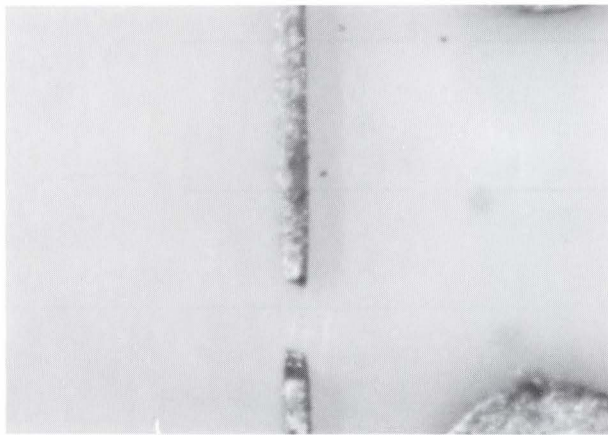


Fig. 10—Generation of good-code dictionary.

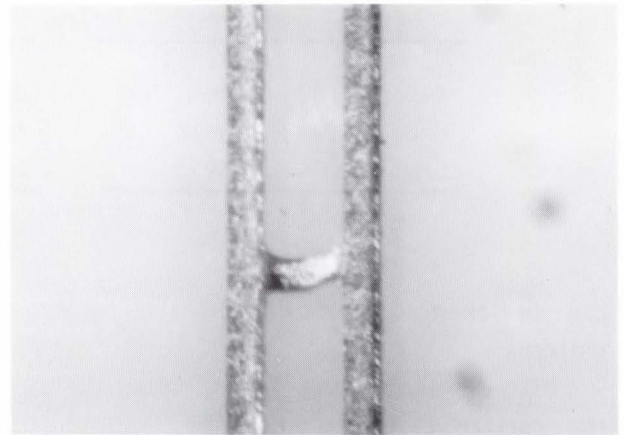
PWB patterns are basically repetitive, the number of good codes in the dictionary stops increasing for a sampling area over 200 mm².

4.2.3 Example of defect detection

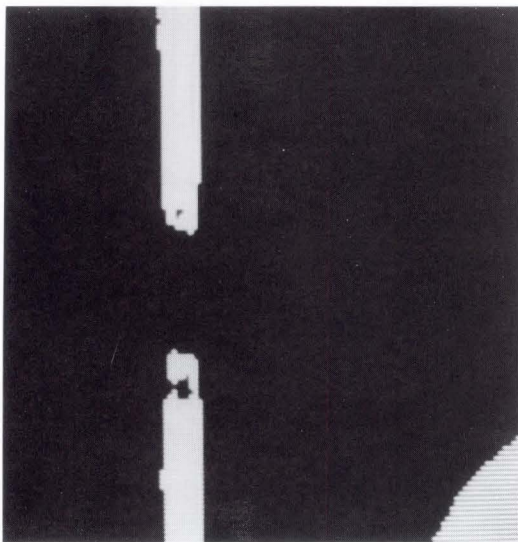
Based on this algorithm, a practical inspection system has been constructed. The system can inspect a 540 × 490 mm area within five minutes with a resolution of 5 μm. Figure 11 shows an example of a break. Figure 11 a) shows the copper pattern. Figure 11 b) shows the result of copper pattern detection. The white area is the copper pattern, and the black spots in the break patterns indicate that defective pattern codes are detected at the area. Figure 12 shows the result of bridge detection. In Fig. 12 b), the black spots also indicate that defective codes are detected at the crossing points of the pattern. Clearly, the algorithm can detect a bridge which has the same width as the normal printed wire. Figure 12 c) shows the result of pattern gap inspection. The algorithm is effective for spaces between copper patterns, i.e.



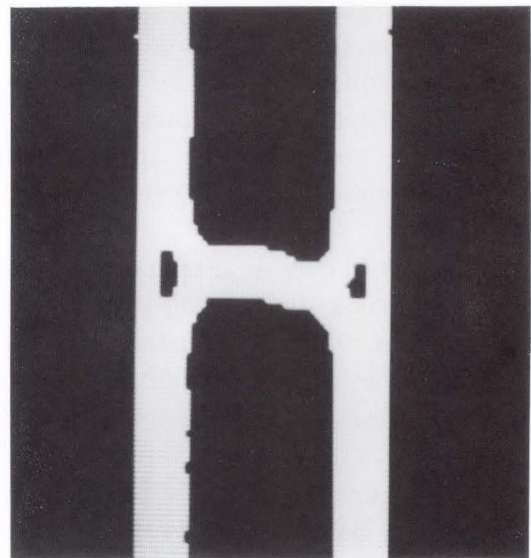
a) Inner layer pattern



a) Inner layer pattern



b) Copper pattern inspection



b) Copper pattern inspection

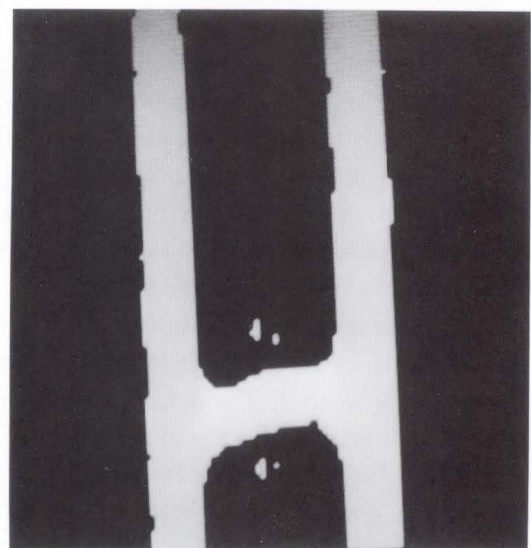
Fig. 11—Example of detected break defect.

the black area in Fig. 12 c). White spots indicate that defective codes are detected there. Near the bridge, Up codes which correspond to a short defect are detected.

As shown in Figs. 11 and 12, the inspection algorithm works both for patterns and pattern gaps, and ensures high-precision inspection.

5. Conclusion

A new black line sensing method that is not affected by surface color and radial-matching algorithm for inspecting various patterns have been developed. Practical inspection systems based on these methods have been developed. They are now operating in the Fujitsu factory.



c) Space inspection

Fig. 12—Example of detected bridge defect.

References

- 1) Ando, M., Oka, H., Iwata, S., and Inagaki, T.: Automated optical pattern inspection for high-density printed wiring boards. Proc. SPIE, Automated Inspection and High Speed Vision Architecture II, **1004**, pp. 135-141 (1988).
- 2) Iwata, S., Ando, M., and Inagaki, T.: Versatile Printed Wiring Board Pattern Inspection Algorithm: Radial Matching. Proc. SPIE, Applications of Artificial Intelligence VII, **1095**, pp. 1142-1150 (1980).
- 3) Spitz, S.L.: AOI "Sees Better, Users Say". *Electron. Package. Prod.*, **6**, pp. 48-53 (1987).
- 4) Ando, M., Nakashima, M., Inagaki, T.: Automated Visual Inspection for Printed Circuit Boards. *FUJITSU Sci. Tech. J.*, **24**, 1, pp. 1-23 (1988).
- 5) Ninomiya, T., and Nakagawa, Y.: Automated pattern Inspection for Unbaked Layers of Multi-Layer Ceramic Substrate. Proc. Int. Workshop on Industrial Applications of Machine Vision and Intelligence, pp. 346-351 (1987).



Moritoshi Ando

Sensing Technology and Robotics
Laboratory
FUJITSU LABORATORIES, ATSUGI
Bachelor of Physical Electronic Eng.
Tokyo Institute of Technology 1971
Specializing in Sensing Technology
and Laser Application Systems



Satoshi Iwata

Sensing Technology and Robotics
Laboratory
FUJITSU LABORATORIES, ATSUGI
Bachelor of Electrical Eng.
Keio University 1983
Master of Electrical Eng.
Keio University 1985
Specializing in Sensing Technology
and Laser Application Systems



Hiroshi Oka

Sensing Technology and Robotics
Laboratory
FUJITSU LABORATORIES, ATSUGI
Bachelor of Electronic Eng.
Kyushu Institute of Technology 1984
Specializing in Sensing Technology
and Laser Application Systems

High-Speed, Wide Area 3-D Vision System for PWB Inspection

• Tetsuo Koezuka • Yoshikazu Kakinoki • Masato Nakashima

(Manuscript received December 28, 1989).

This paper describes a three-dimensional (3-D) vision system developed for factory automation. The system is based on a newly developed 3-D imager. This imager uses a laser diode beam to scan the object area and obtains range and intensity data simultaneously. Range measurement is based on triangulation. For inspecting printed wiring boards (PWBs), the system was capable of detecting missing, shifted, and floating components. The inspection resolution is 125 μm along the X and Y axes and 30 μm along the Z axis. A PWB 250 mm by 330 mm can be measured in 14 s.

1. Introduction

Object recognition in three dimensions has become increasingly important in factory automation (FA). For example, an automatic assembly line requires 3-D vision to pick up and manipulate target objects. 3-D vision is also used to detect incorrectly assembled components on PWBs. For FA use, the 3-D vision system must be fast to keep up with the assembly line.

In earlier projects, the slit-light technique using a TV camera¹⁾ has been favored over other systems, such as time-of-flight technique²⁾ and laser triangulation^{3),4)}. The slit-light techniques, however, have a limited measurement area, take too long to accept input images, and cannot produce range and intensity images simultaneously.

The authors developed a 3-D imager and a vision system based on it. The 3-D imager uses a laser diode beam to scan the measured area and obtains range and intensity data at all points on the scan line. Range measurement is based on triangulation. The vision system, which uses a 32-bit MPU (MC68030) and 12 Mbytes of image memory, has three main features.

1) Wide area sensing

3-D measurement covers 2048 by 3076 pixels formed in one image input sequence.

2) Quick measurement

The system produces data for an entire six-million-pixel area in just 14 s.

3) Simultaneous measurement of range and intensity

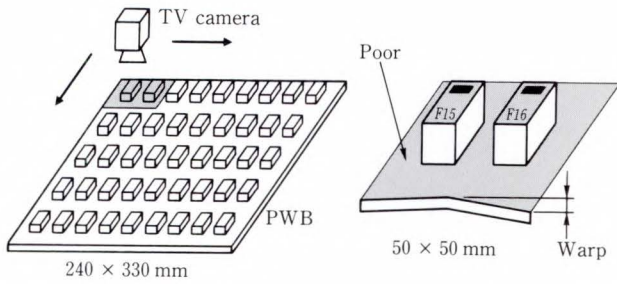
The 256 height level range image is used to determine an object's shape, and the 256 gray level intensity image to determine the surface texture, markings, and other features.

When used to inspect PWBs, the system detected missing, shifted, and floating components. Inspection resolution is 125 μm along the X and Y axes and 30 μm along the Z axis.

2. Requirements for FA 3-D vision

Figure 1 shows the requirements for an FA 3-D vision system.

- 1) It must be fast enough to keep up with the assembly line. For this purpose, the system's measurement area must be wide and the image capture time short { Fig. 1 a) }. To inspect a 250 mm by 330 mm PWB, a system with an ordinary TV camera, however, has a narrow 50 mm by 50 mm viewing area, so that it requires 35 image input sequences to image the entire PWB. It also needs an X - Y moving stage for board scanning. Stage movement alone increases the required



- a) High speed:
 - Wide area sensing
 - High speed image capture
- b) High recognition rate:
 - Segmentation by range
 - Identification by intensity

Fig. 1—Requirements for FA vision.

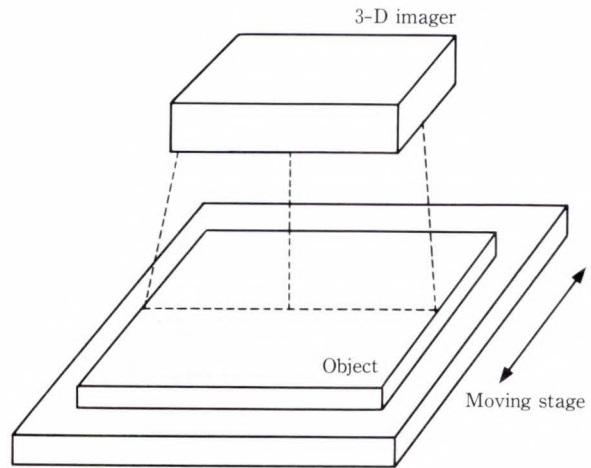


Fig. 2—3-D imager.

image input time too much.

- 2) The system's recognition rate must be high. For this purpose, the system must use both range and intensity data. Objects can be positioned, even on poor backgrounds, using range data alone, but identifying the object requires intensity data to read the object's surface. Range data is also useful to correct for board warp { Fig. 1 b) } .

To meet the above requirements, the authors have developed a high-speed, wide-area 3-D imager and a system based on it.

3. 3-D imager

This section describes the developed 3-D imager. The 3-D imager's two main features are the wide area telecentric laser scanning system and the retroreflection optics. Laser scanning triangulation was adopted for high-speed range measurement.

3.1 Principle of 3-D imager

The 3-D imager scans a focused laser diode beam on an object along the *X* axis (see Fig. 2) to obtain range and intensity data. The maximum scan length is 256 mm. An object is scanned along the *Y* axis by the conveyor or moving stage to enable the 3-D imager to sample the entire surface. The 3-D imager is based on the triangulation principle (see Fig. 3). The image of the incident laser beam is focused on a position-sensitive detector (PSD) located at the detected

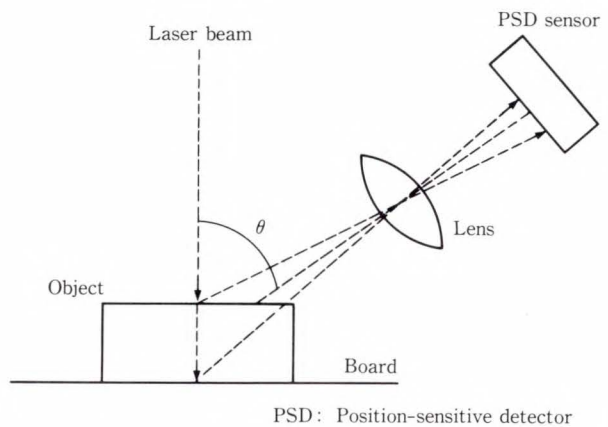


Fig. 3—Triangulation principle.

angle (θ) from the incident laser beam. This beam position on the PSD indicates an object's range or height, and the power of the detected beam determines the object's intensity.

3.2 Wide area telecentric laser scanning system

For wide-area, high-speed measurement, the authors designed a laser beam scanning system which uses a polygonal mirror and a parabolic mirror. The source is a laser diode with a 40-mW output. The focal length of the parabolic mirror is 300 mm. Constant-speed scanning is achieved by arranging the polygonal and parabolic mirrors so that the distance between the reflecting surfaces of the mirrors is two thirds of the focal length of the parabolic mirror (200 mm)⁵⁾.

The effective scanning length is 256 mm and the irradiation angle at the end of the scan is 8°.

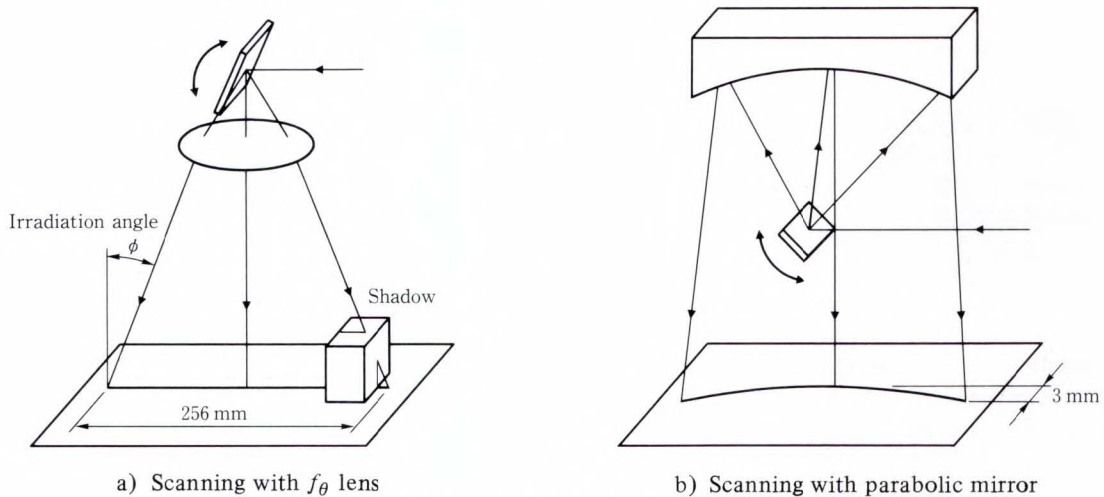


Fig. 4—Comparison of laser scanning system between f_{θ} lens and parabolic mirror.

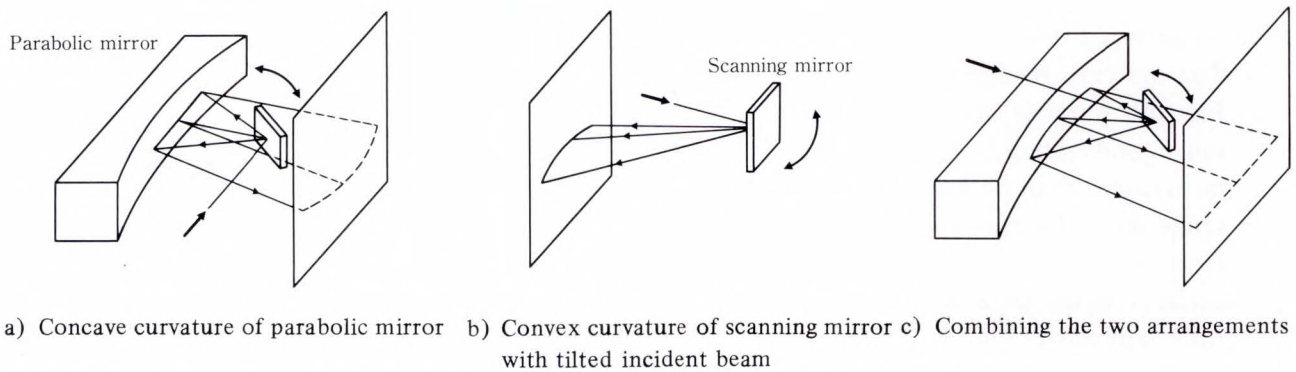


Fig. 5—The compensation principle for scanning curvature.

The spot beam diameter is $200\ \mu\text{m}$ or less in $1/e^2$ representation for the required X - Y sampling resolution of $125\ \mu\text{m}$.

Usually, an f_{θ} lens is used for laser scanning. However, a parabolic mirror was used instead. Figure 4 shows how these scanning methods differ. Telecentric scanning over a great distance is difficult with an f_{θ} lens. In contrast, scanning with a parabolic mirror makes it possible to reduce the irradiation angle (ϕ) over a long scan distance. In this system, ϕ is 8° or less. This angle is permissible, because the maximum positional error of a typical chip $1\ \text{mm}$ high is within $140\ \mu\text{m}$, nearly equal to the sampling resolution of $125\ \mu\text{m}$.

For 3-D sensing, a small irradiation angle gives the following advantages:

- 1) High intensity of reflected light can be produced, independently of the scanning position.

- 2) The variation in the scanning direction depending on the height of the object ($H \tan \phi$) is small.
- 3) The shadows in the scanning direction ($H \tan \phi$) are small.
- 4) The reflected light can be focused, as will be explained later. The rotation of the resulting image is low, which means that errors in height measurement are small.

3.3 Compensation for scanning curvature

As discussed earlier, the parabolic mirror is better than the f_{θ} lens in that the irradiation angle is smaller even when the scanning length is great. Unfortunately, conventional parabolic mirror scanning poses another problem. As is shown in Fig. 4, the scanning path is curved⁵⁾ because the incident plane and the reflecting plane do not coincide. The angle between these two surfaces is called the off-axis angle (α). A

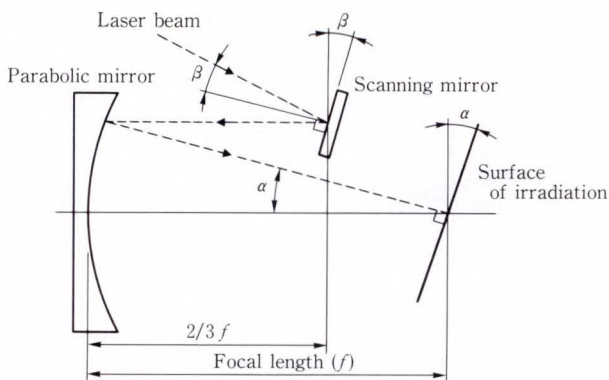


Fig. 6—Optical arrangement for scanning curvature compensation (side view).

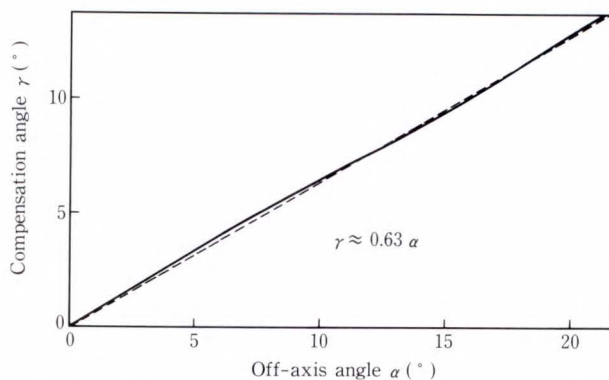


Fig. 8—Off-axis and compensation angle (optimized incident angle).

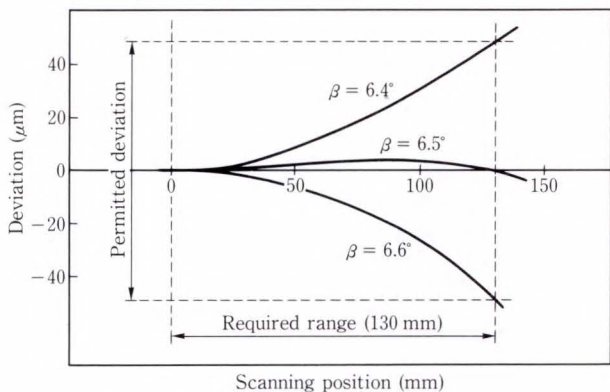


Fig. 7—Compensation characteristics of scanning path deviation.

method was devised for compensating for this curvature.

The principle of compensation developed is explained in Fig. 5. The normal arrangement of parabolic mirror scanning is shown in Fig. 5a). The incident beam is perpendicular to the rotation axis of the scanning mirror. In this arrangement, the parabolic mirror produces a concave scanning curvature.

In arrangement Fig. 5b), if the incident beam is tilted to the rotation axis of the scanning mirror, the reflected beam has a convex curvature. This phenomenon can be used to cancel the curvature caused by the parabolic mirror. Combining these two arrangements and optimizing the incident angle makes a straight scanning line, as shown in Fig. 5c). The path of the beam can then be calculated geometrically.

Figure 6 shows the arrangement of the scanning optics developed. Figure 7 is a sample

scanning path calculation. Assume that the focal length of the parabolic mirror is 300 mm, the off-axis angle is 10° , and the angle of the beam incident to the polygon (β) is 6.5° . When the scanning length in one direction is 130 mm (260 mm for a complete pass in both directions), the scanning path deviates less than $\pm 5 \mu\text{m}$ from a straight line. If β varies by $\pm 0.1^\circ$, the deviation is up to $\pm 50 \mu\text{m}$. This is within the permitted range for deviation, that is, half of the desired resolution of $125 \mu\text{m}$. If compensation is not used, the curvature deviation reaches 3 mm at the end of the scan.

Figure 8 shows the relationship between the optimal angle of incidence to the polygon (γ) and the two varying parameters, off-axis angle (α), and scanning length. The relationship between the optimal angle of incidence to the polygon (γ) and the off-axis angle of the parabolic mirror (α) which causes the scanning path to lie on a straight line is given by the following equation, regardless of the scanning length:

$$\gamma = 0.63\alpha. \dots \dots \dots (1)$$

3.4 Retroreflection optics for range measurement

For the range to be measured by triangulation, the reflected laser beam must be detected in an oblique direction. Since the scanning length is 256 mm for this system, ordinary focusing optics fail to achieve the necessary range resolution of $30 \mu\text{m}$.

To solve this problem, retroreflection optics

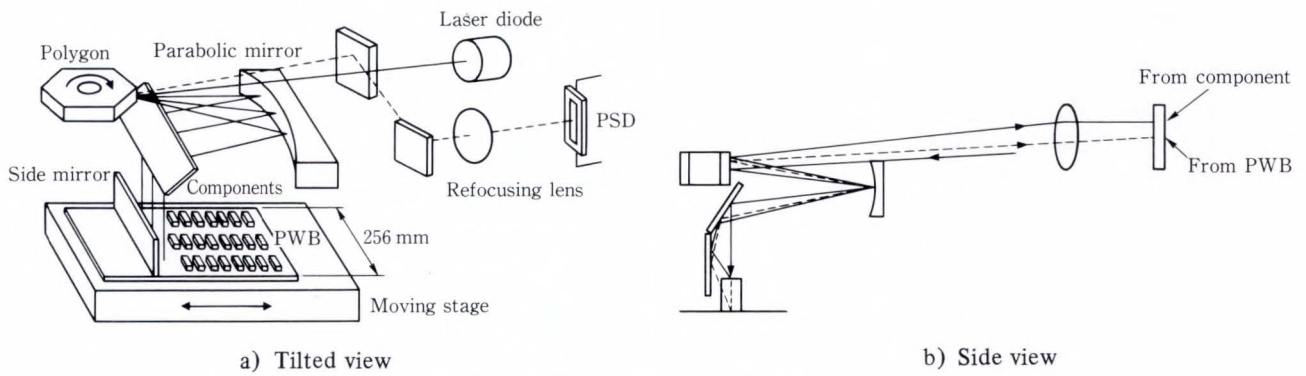


Fig. 9—Configuration of retroreflective triangulation optics.

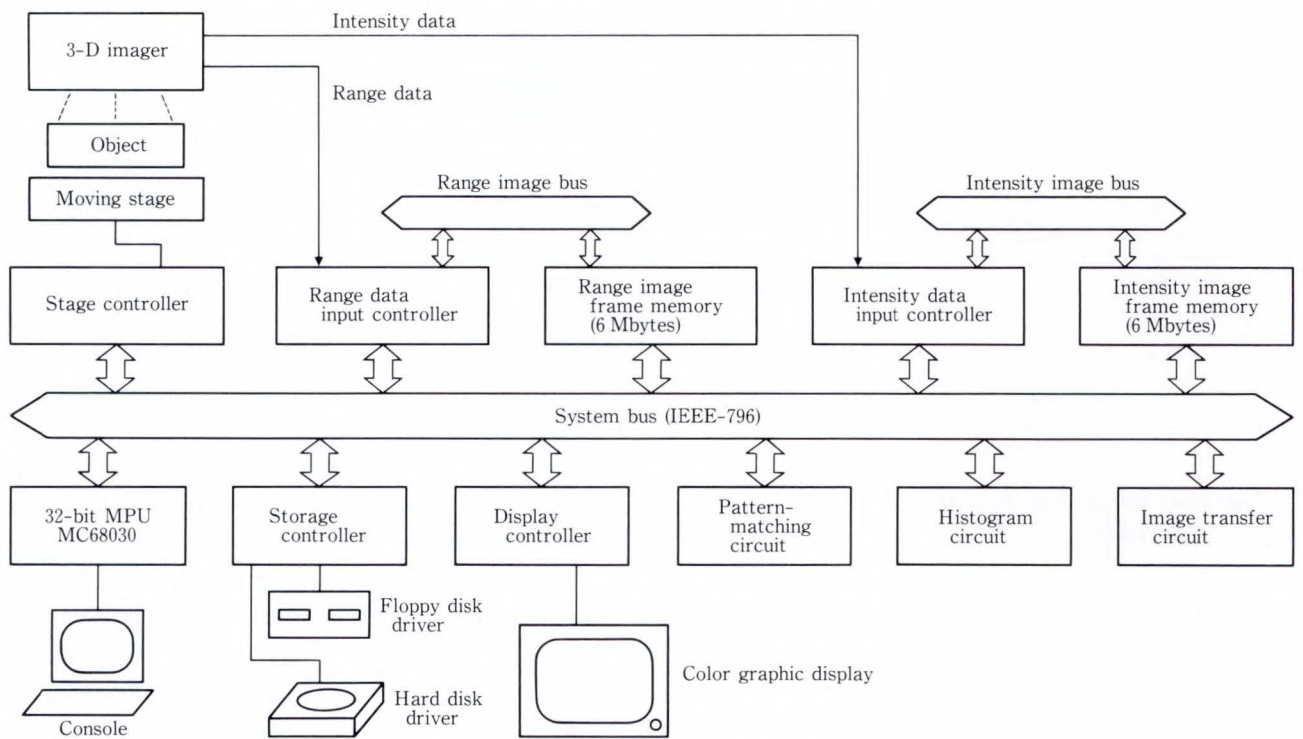


Fig. 10—System configuration.

were used. Figure 9 shows the configuration of the range measurement optics. A mirror is provided close to and parallel to the scanning beam, and nearly perpendicular to the board. The reflected light of the object is returned to the side mirror, the parabolic mirror, and the polygonal mirror, and is refocused on the PSD through a lens. The refocused beam traces a single line on the PSD, regardless of the scanning position on the PWB. In addition, the position of the focused beam corresponds linearly to the height of the object. Retroreflective triangulation measurement is thus achieved.

4. System configuration

The 3-D vision system (see Fig. 10) uses an IEEE-796 system bus and consists of a 32-bit MPU MC68030 board, range and intensity data input controllers, 6 Mbytes of memory for each image, a pattern matching circuit, a histogram circuit, and an image transfer circuit. Intensity and range data are obtained simultaneously and stored separately in frame, range image, and intensity image memory via special image buses. Images are formed by the image input controllers.

To reduce the time required for image input,

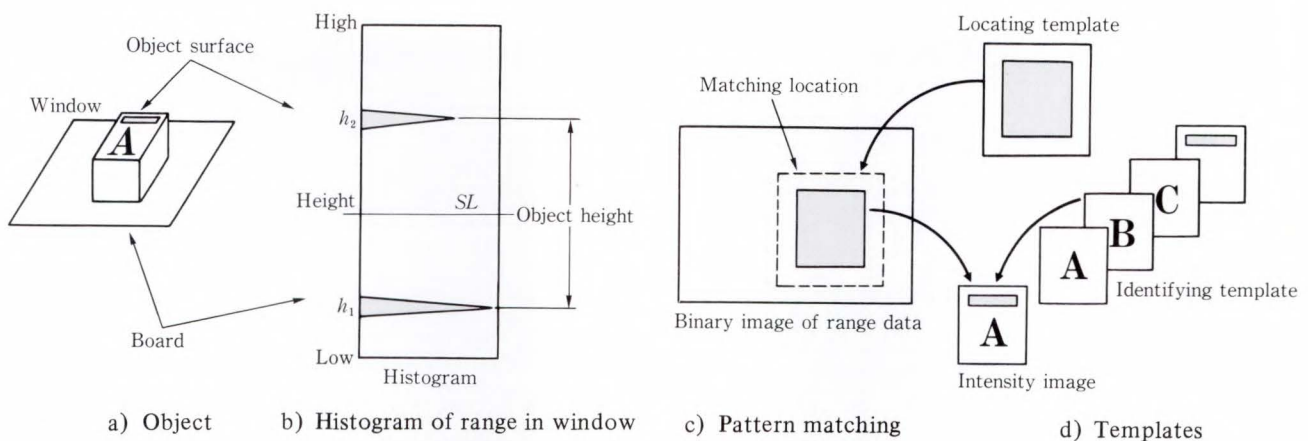


Fig. 11—Image processing algorithms.

each image memory is segmented. Each segment is opened to the system bus immediately after image data for that segment is stored.

This enables the system to start recognition or inspection in the first segment. The system compiles the processing windows sequence and resequences them so that the first window is in the first segment of image memory and the last window in the last. When the area is equal to 256 mm by 350 mm, the X-Y sampling resolution is 125 μm, the sampling rate is 1 Mpixel/s, and the effective scan rate (sampling time/scanning time) is 40 percent, the image input time is 14 s.

5. Image-processing algorithms

Figure 11 shows the image-processing algorithms. An object on the board is extracted by the processing window {Fig. 11a}. Figure 11b) indicates the range histogram in the window. The histogram of range data in the window has two peaks. The upper one (h_2) indicates the relative height of the object surface and the lower one (h_1) indicates the board height. The object height calculated by ($h_2 - h_1$) is accurate even if the board is warped.

Obtaining the histogram makes it possible to determine the threshold level, SL , converting range data to binary. SL is typically set at the center of the two peaks.

The binary image of range data and the locating template for pattern matching are shown in Fig. 11c). The template is scanned over the binary image window and the best matching



Fig. 12—PWB components inspection system.

location is detected. Next, the intensity image corresponding to the matching location is digitized and matched with the identifying templates.

Range image processing, histogram output, and pattern matching enable the system to determine the following:

1) Missing object

When the number of peaks in the range histogram is one, no object is in the window.

2) Floating or erroneous object

When the measured height of the object ($h_2 - h_1$) exceeds the height of the desired object, it indicates a floating object or erroneous object.

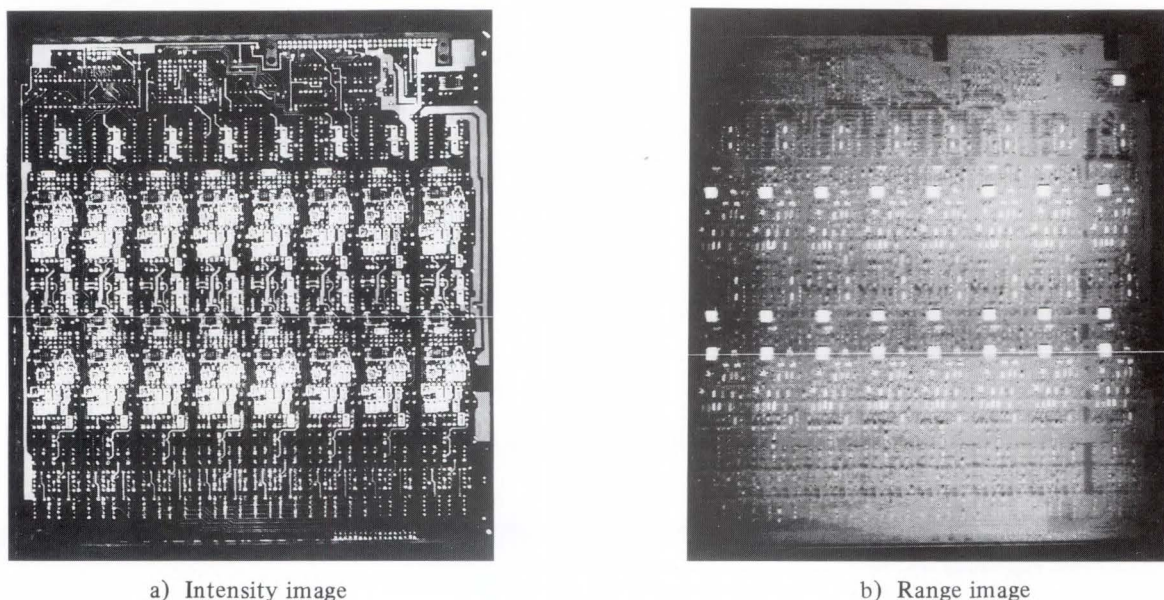


Fig. 13—Captured range and intensity images of overall PWB.

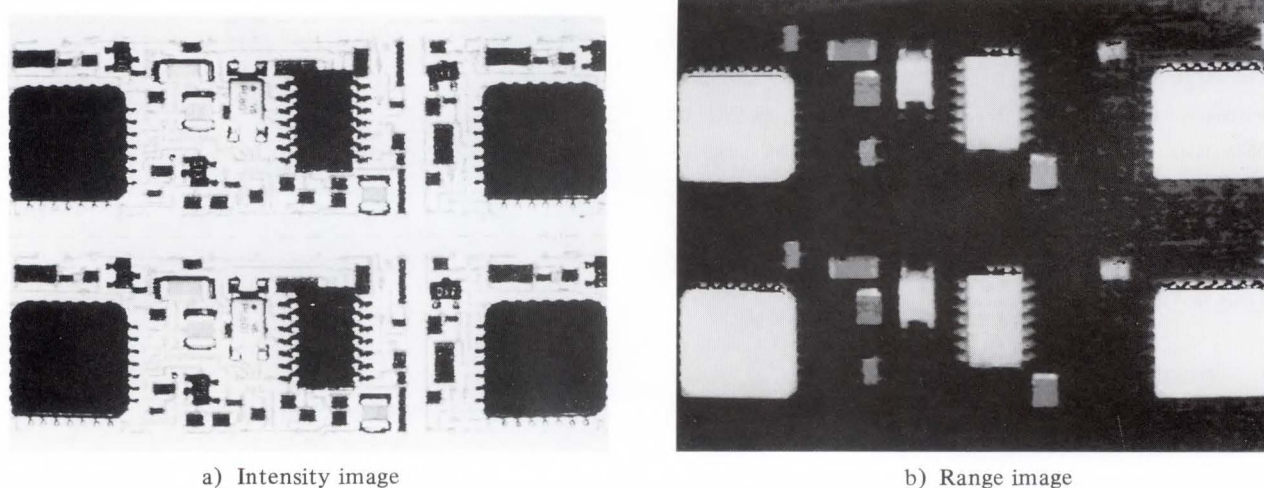


Fig. 14—Details of an input image.

3) Positioning error

If the best matched position shifts from that desired, the position of the object shifts.

4) Cracks or erroneous object

If the pattern matching degree is smaller than expected, the object is broken or cracked, or is of a different size.

6. System performance

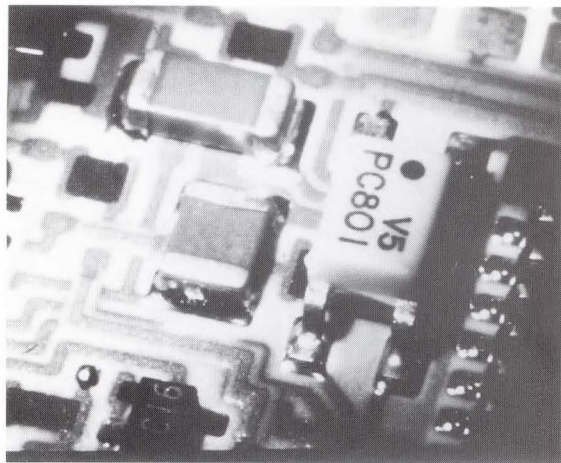
The practical 3-D vision system (see Fig. 12) is used in PWB component inspection⁶⁾. The 3-D imager is above and the inspection units are in the lower cabinet. The color CRT displays the

image of the inspected board and results.

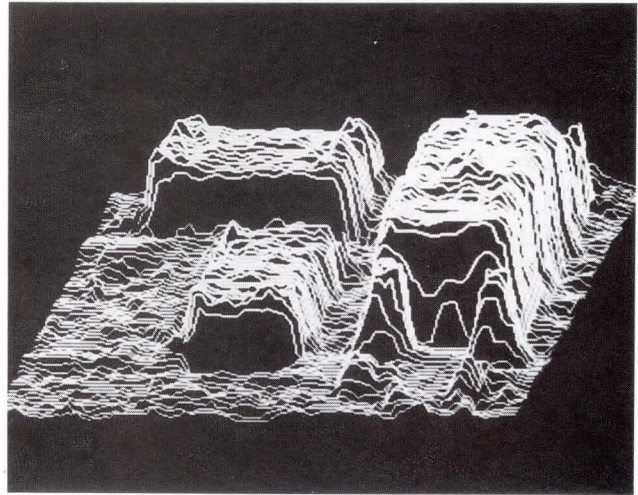
6.1 Range and intensity images

Figure 13 shows range and intensity images representing a 250 mm by 330 mm PWB. Each image is 2 048 pixels by 2 640 pixels. The range image represents the height in intensity gradations. With this system 12 Mbytes of the range and intensity images can be input in 14 s.

Figure 14 shows details of the images. Horizontal resolution is 125 μm . The board is populated with ICs, capacitors, and transistors. Note that the range image faithfully reproduces



a) Photograph of board



b) Measured 3-D image

Fig. 15—3-D display of measured range image.

the shape of each component independently of surface brightness, markings, and letters.

Figure 15 shows a 3-D representation of the partial range image shown in Fig. 14. The objects measured are a $4.5 \times 3 \times 2$ mm photocoupler and two $3 \times 2.5 \times 0.8$ mm capacitors.

6.2 Range measurement accuracy

Chip height is measured by the histogram circuit (see Fig. 16). The horizontal axis indicates the location on the X axis for each chip. Black rectangles show the chip height and white circles show the board height for surrounding chips. The board is warped about 1 mm along the X axis, 256-mm. Despite this, we can obtain the exact chip height which is around 0.7 mm. This is shown by black circles, by subtracting the board height from the chip surface height.

The range measurement accuracy is shown in Fig. 17a). The horizontal axis indicates chip height and the vertical axis data measured by the system. Measurement accuracy is within $\pm 100 \mu\text{m}$ over the full scanning length 256 mm. The distance between the two peaks in the three examples of the range histogram in Fig. 17b) indicates the chip height. Experiments showed the range measurement accuracy to be $100 \mu\text{m}$ with resolution $30 \mu\text{m}$ and the full measurement range to be 7.6 mm for range data with 256 levels. Table 1 lists the performance of the 3-D imager.

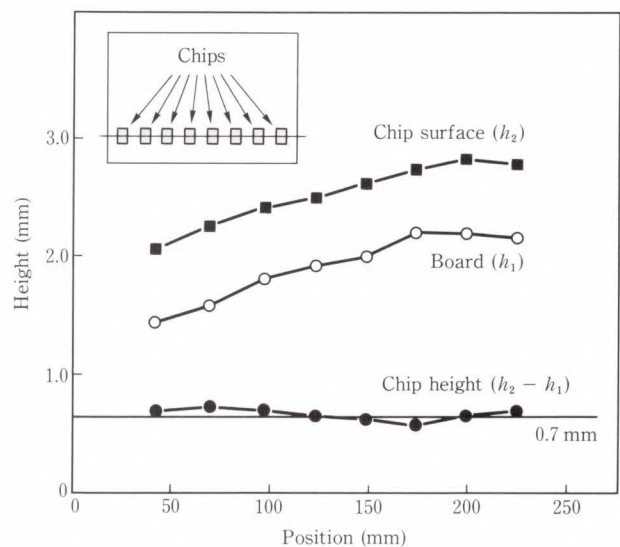


Fig. 16—Measured chip height.

This system attained the following objectives:

- 1) Wide area of measurement
2048 pixels by 3076 pixels per imaging frame.
- 2) High-speed image capture
A 14 s per frame of six million points.
- 3) Simultaneous range and intensity image processing

Shape recognition for range data and feature recognition for intensity data.

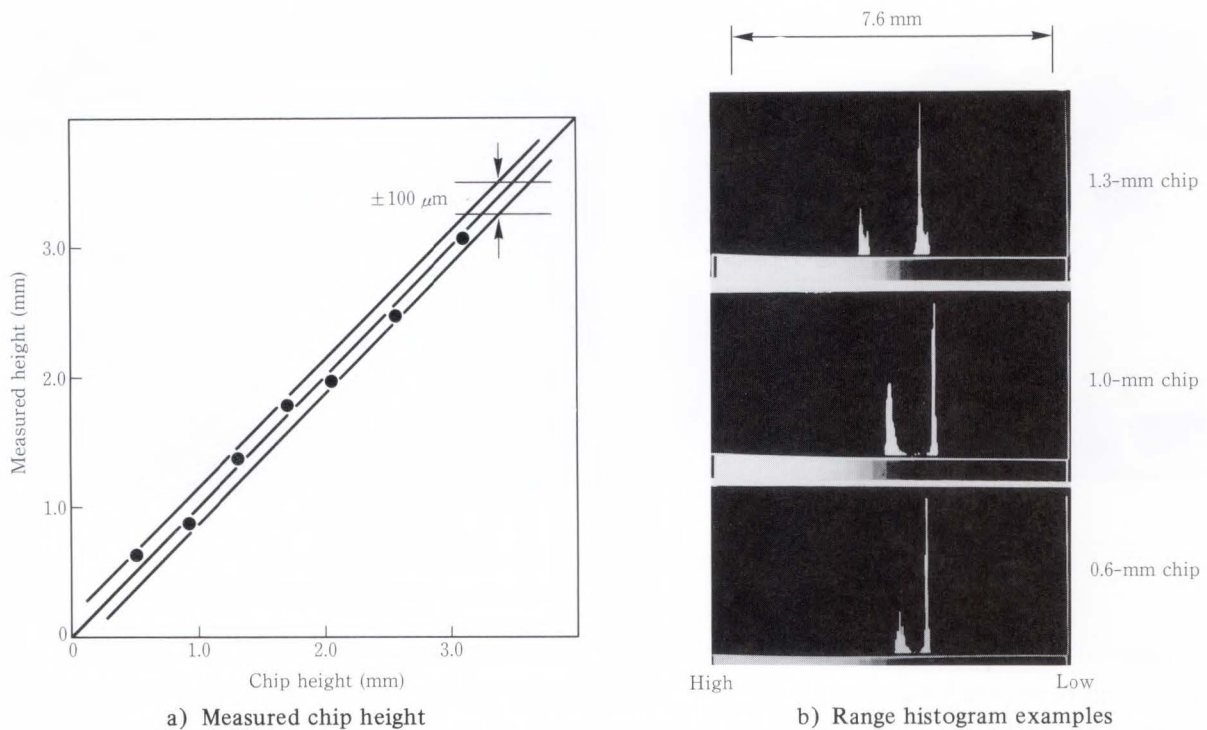


Fig. 17—Range measurement accuracy.

Table 1. Performance of the 3-D imager

Item	Performance
Measuring range	Horizontal: 256 × 330 mm Vertical: 7.6 mm
Image resolution	Horizontal: 125 μm Vertical: 30 μm
Image-capturing speed	0.4 M pixels/s
Light intensity dynamic range	10 ⁴

Table 2. Apparatus performance

Item	Performance
Detectable defects	Components missing, position errors, floating polarity errors, cracks, rotations, and reversals
Inspection time	0.1 s/component
Undetected defect rate	~ 0%
Detection error rate	~ 0.03%

7. Conclusion

The 3-D vision system we developed meets two major requirements for use in industry:

- 1) The system generates a range map of a wide area and accepts high-speed image input.
- 2) The system processes intensity and range

data simultaneously to locate and identify objects in a viewed area.

Table 2 lists the principal performance parameters for when the system is used to inspect PWB components. Defects such as missing parts, position error, and floating parts are detected at a rate of 0.1 s/component. A PWB with about 300 components can be inspected in 30 s. The system's performance thus meets the design requirements.

References

- 1) Landman, M., and Robertson, S.: A Flexible Industrial System for Automated Three-Dimensional Inspection. Proc. SPIE, Optics, Illumination, and Sensing for Machine Vision, **728**, pp. 203-209 (1986).
- 2) Hebert, M., and Kanade, T.: 3-D Vision for Autonomous Vehicle. Int. Workshop Indust. Appl. Machine Vision Machine Intell., Proc. Seiken Sympo, Tokyo, 1987, pp. 375-380.
- 3) Rioux, M.: Laser Range-Finder Based on Synchronized Scanners. *Appl. Opt.*, **23**, 21, pp. 3837-3844 (1984).
- 4) Donahue, J.: Intensity and Range Artifacts in Electronic Inspection. Top. Meet. Machine Vision,

Technical Digest Series, 12, Nevada, 1987, ThC6-1-ThC6-4.

- 5) Abe, F., and Matsuda, T.: The Correcting Method of Beam Scanning Distortion Using the Parabolic Mirror. *FUJITSU Sci. Tech. J.*, 14, 3, pp. 91-106 (1978).

- 6) Koezuka, T., Kakinoki, Y., Suto, Y., Nakashima, M., and Inagaki, T.: High-Speed 3-D Vision Using Range and Intensity Images Covering a Wide Area. *Proc. SPIE, Applications of Artificial Intelligence VII*, 1095, pp. 1134-1141 (1989).



Tetsuo Koezuka

Sensing Technology and Robotics
Laboratory
FUJITSU LABORATORIES, ATSUGI
Bachelor of Electrical Eng.
Saitama University 1979
Specializing in Sensing Technology
and Image Processing



Masato Nakashima

Holography and Color-Imaging
Laboratory
FUJITSU LABORATORIES, ATSUGI
Bachelor of Chemistry
Tohoku University 1969
Specializing in Sensing Technology
and Image Processing



Yoshikazu Kakinoki

Sensing Technology and Robotics
Laboratory
FUJITSU LABORATORIES, ATSUGI
Ishikawa Technical College 1980
Specializing in Sensing Technology
and Image Processing

53.084.87:681.327.5

Sensory Pattern Inspection System for Print Quality of Dot-Matrix Printer

• Masato Nakashima • Tetsuo Koezuka (Manuscript received December 21, 1989)

A print quality evaluation method has been developed and applied to the inspection of wire dot-matrix printers. A new algorithm has been developed that has characteristics of human vision, such as the edge emphasis and logarithmic sensitivity of the optic nerve, and accumulative evaluation. Experimental results shows that the print quality inspection system can perform at the same level as expert inspectors and that reproducibility is three times higher.

1. Introduction

Humans recognize images in two stages: meaning recognition, and sensory recognition. The functions of images can be promptly understood, but the image quality cannot be evaluated quantitatively.

In the last ten years, pattern recognition techniques in the area of character recognition and object recognition have advanced remarkably. However, in sensory recognition, there are still difficulties to overcome in the quantitative evaluation of human sensation. Many researchers have been studying sensory recognition in the three areas of sensory optics, psychophysics, and cognitive science¹⁾. But, at present there is no sensory pattern evaluation system for practical use.

Print quality inspection is a sensory operation. Up to now, print quality has been visually inspected by expert operators in the final process of manufacturing. However, reproducible and quantitative results using the human eye are difficult to obtain. Conventional inspection systems²⁾ only measure the reflectance of printed characters and do not consider human eye characteristics. Therefore, they cannot inspect print quality as well as expert operators.

We wanted to develop a sensory pattern

inspection system that simulated human vision using conventional image processing techniques. This paper presents an analysis of human inspection and a new sensory pattern recognition system³⁾ which can be used in the evaluation of dot-matrix print quality.

2. Analysis of print quality

Figure 1 is an example of a print test sheet for a wire dot-matrix printer. It has both good and defective characters. The print test sheet measures 380 mm by 300 mm. There are 18 lines per sheet and each line contains about 100 characters. Each character is 3.4 mm square and consists of 24 dots by 24 dots. The diameter of each dot is about 0.3 mm, and the test sheet consists of about one million dots. The three black circles in Fig. 1 show one good and two defective (edge blur and inner blur) printed characters.

Table 1 lists the types of defects. Print defects are divided into two groups: macroscopic, and microscopic. Macroscopic defects are caused by character or line irregularities in the print head and include inner blur and edge blur. The typical size of inner blur is 0.6 mm and the blur density is usually more than 0.1 times the optical density (OD). The typical size of edge blur is 0.2 mm and the

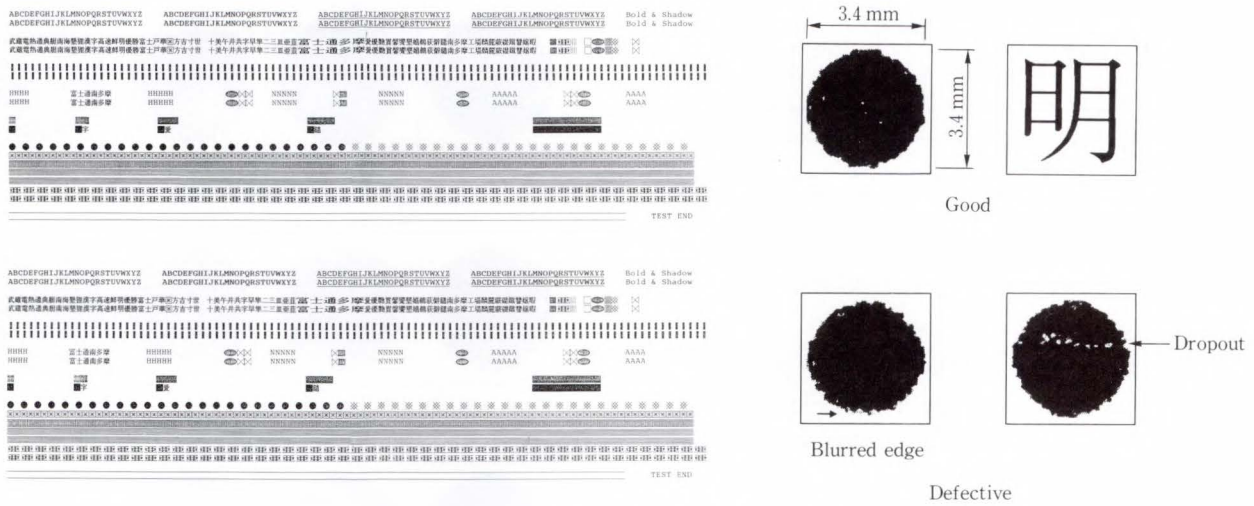


Fig. 1—Print test sheet for dot-matrix printer.

Table 1. Classification of defects

Classification		Examples	
Macroscopic	Position	<ul style="list-style-type: none"> Character pitch irregularity (p) Line interval irregularity (l) Waving 	
	Density	Non-uniformity	Dark, Light
		Inner blur	Blur
Edge blur		Blur	

Table 2. Sensory functions of image quality evaluation

Sensory function		Tasks
Eye optics	Sensor	Central/peripheral vision
	Light sensitivity Color sensitivity	Non-linear sensitivity Color contrast effect
Sensory nerve	Differentiation	Contour extraction
	Angularity detection	Detection of direction
Evaluation	Space perception	Space, depth, balance
	Feature detection	Irregularity, texture
	Quality sensing	Detection of image quality

density is also about 0.1 times the OD. These two types of blur usually appear horizontally because this is the direction of print head

movement.

3. Development aims

We wanted to develop a sensory pattern recognition system that simulated the sensory characteristics of human vision. Our system uses sensing algorithms for image processing to simulate human vision. The system also uses recognition algorithms to simulate human judgment.

Sensory recognition is divided into three functions: eye optics, sensory nerves, and human evaluation (see Table 2).

A sensory pattern recognition system can be constructed that simulates these sensory functions.

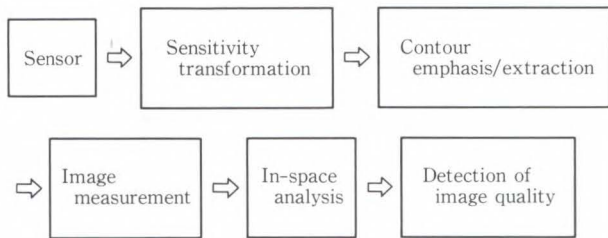


Fig. 2—Image quality recognition.

The flowchart of the sensory pattern recognition system is shown in Fig. 2. This is used to evaluate the print quality of a wire-dot printer.

4. Sensory evaluation of print quality

Print quality is usually evaluated by trained (expert) inspectors. Print quality is determined by subjective human judgment instead of by absolute physical values. It takes from three to six months to train an inspector.

4.1 Sensory characteristics of human vision

The functions of sensory decision making are explained using Fig. 3. Figure 3 a) shows random white-noise defects. These defects are permissible because they are unnoticed by human eye. In contrast, Fig. 3 b) shows an example of defect regularity. This figure shows several tint defects in the same area. These defects are easily detected by human eye and their detectability depends on the regularity of defects. Figure 3 c) shows an example of neighboring contrast. The defect in the circles in c) is perceived as enormous in contrast with the neighboring good images. Even though, the amount of white noise in the four circles in c) is the same as the amount in a) and b), the defect intensity is emphasized by human eye. In other words, the sensitivity of the human vision to print defects is non-linear.

The sensory characteristics of human vision include following factors:

4.1.1 Defect position

A specific defect may appear in a specific area of a specific character. A trained inspector therefore searches for a specific character and looks for the same defect in a specific area.

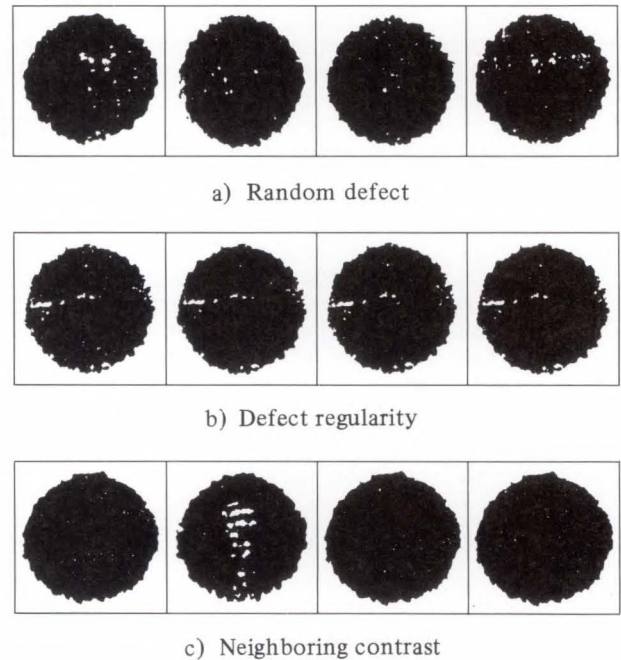


Fig. 3—Examples of sensory evaluation.

An inspector considers these specific defects to be more serious than other defects.

4.1.2 Defect regularity

A set of several defects are easily detected by the human eye. However, random defects are usually permissible because they are not easily detected by the human eye.

4.1.3 Neighboring contrast

To the human eye, defective images are conspicuous because they contrast with neighboring good images.

4.1.4 Accumulative sensitivity of human evaluation

Human evaluation of defects is not linear but is accumulatively proportional to defect intensity. The degree of defect determined by human judgment is exponentially proportional to the physical value of defect intensity.

4.2 Sensory functions of print quality inspection

There are four sensory functions of print quality inspection. These are: logarithmic sensitivity of the human eye, Mach phenomenon in edge enhancement, accumulative sensitivity of the regularity of image quality, and exponential sensitivity of defect intensity evaluation.

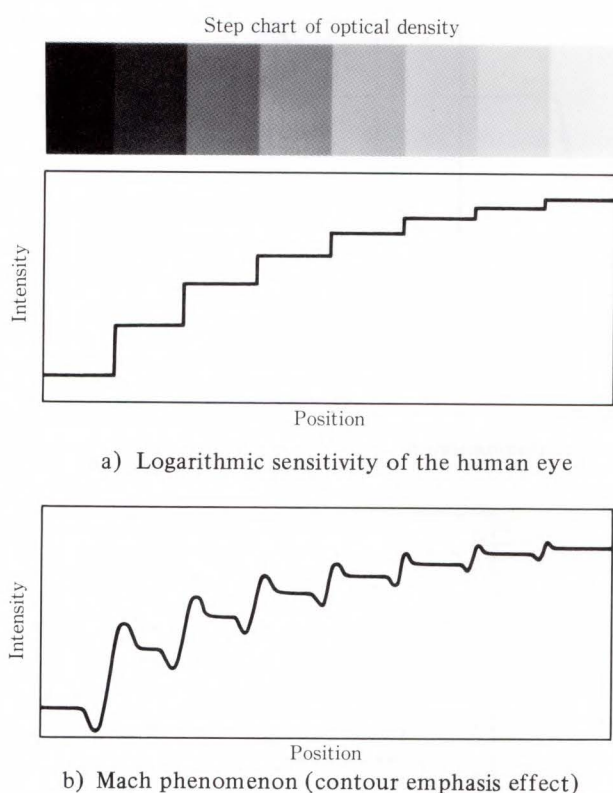


Fig. 4—Logarithmic sensitivity and Mach phenomenon phenomenon of the human eye.

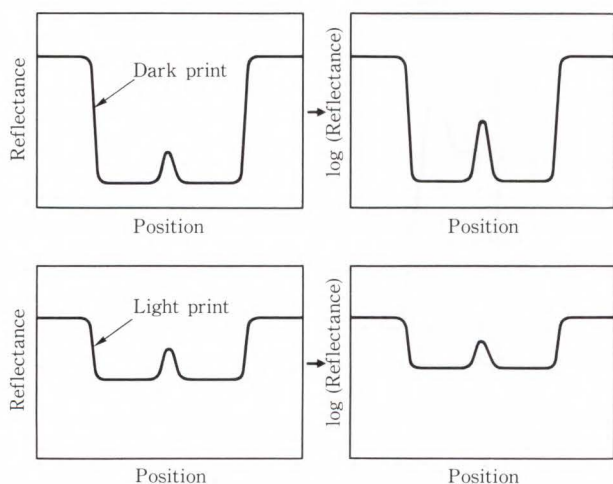


Fig. 5—Effect of logarithmic sensitivity.

4.2.1 Logarithmic sensitivity of the human eye

Figure 4 a) shows the logarithmic sensitivity of the human eye. The output of the human optic nerve $u(x, y)$ is not directly but logarithmically proportional to light intensity. The output is given by:

$$u(x, y) = \log \{d(x, y)\}, \quad \dots \dots \dots (1)$$

where $d(x, y)$ is the light intensity of the input reflectance.

Figure 5 shows the effects of logarithmic sensitivity. Inner blur in the dark print is emphasized by this effect. However, the blur in the light print is suppressed.

4.2.2 Mach phenomenon (Counter Emphasis Effect) of the human eye

Human sensory nerves have a contour emphasis effect called the Mach phenomenon⁴⁾. Figure 4 b) illustrates the Mach phenomenon. This effect is represented by Equation (2), using the linear-operator M ⁴⁾.

$$M \{d(x, y)\} = [1 + C_m \{ (\partial^2 / \partial x^2) + (\partial^2 / \partial y^2) \}] u(x, y). \quad (2)$$

Here C_m is a coefficient which represents the degree of emphasis on strength.

Figure 6 a) shows a two-dimensional Mach filter which simulates the Mach phenomenon. The central positive value is the stimulated area; the surrounding negative values make up the lateral inhibited area. This Mach filter simulates the function of the human optic nerve. As shown in Figs. 6 b) and c), the inner blur is emphasized. In the edge area, the normal edge is markedly emphasized, but the blurred edge is less emphasized.

4.2.3 Accumulative sensitivity of human evaluation

The degree of defect determined by human evaluation depends on the regularity of defect shape and the defect continuity. Therefore, accumulative summation is required in sensory print quality evaluation.

4.2.4 Exponential sensitivity of human evaluation

Human evaluation of quality is exponentially proportional to the physical value of defect intensity.

5. Print quality evaluation method

A new method for evaluating print quality has been developed. This method consists

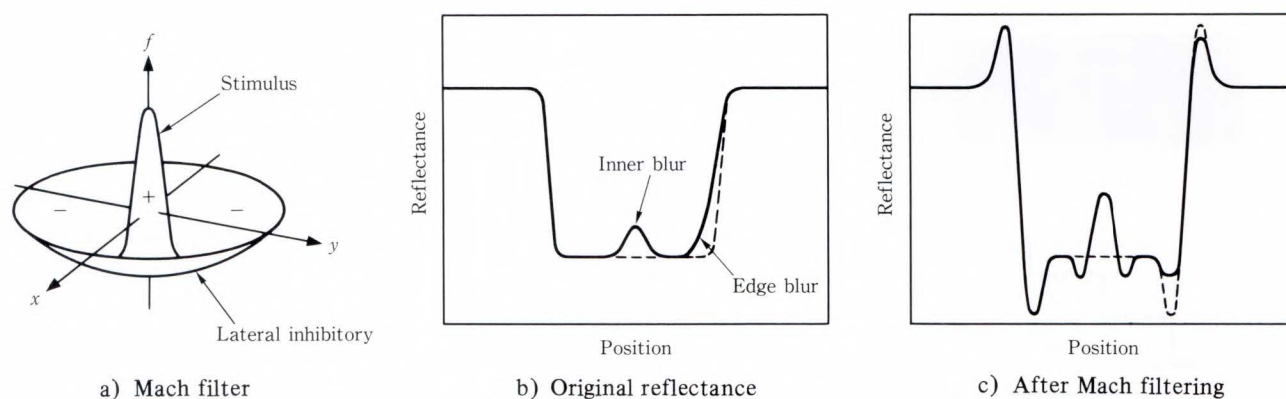


Fig. 6—Emphasis effect of Mach phenomenon.

of character position detection, print density measurement, and quality evaluation.

5.1 Character position detection

Character positions are detected using a pattern matching procedure. In this procedure, the template is 51 × 51 pixels, the object image is a maximum of 256 × 256 pixels, and the whole sheet is 5 120 × 4 096 pixels. Experimental results show that the accuracy of character position detection is within 75 microns (standard deviation).

5.2 Density measurement

After the character position has been detected, the defect density is evaluated.

First, the average reflectance D_{av} is calculated using Equation (3).

$$D_{av} = \{ \Sigma d(x, y) \} / S, \quad \dots \dots (3)$$

where the summation is performed over the inner area of a character and S is the area of the character. Density non-uniformity is evaluated from the variance of average reflectance.

Next, density blur is measured. Figure 7 shows the blur measurement procedure. Image data is projected horizontally. The projection value, $P(x)$, is calculated using the following equation:

$$P(x) = \Sigma_y d(x, y). \quad \dots \dots (4)$$

Blur density is emphasized by this projection because it usually appears horizontally.

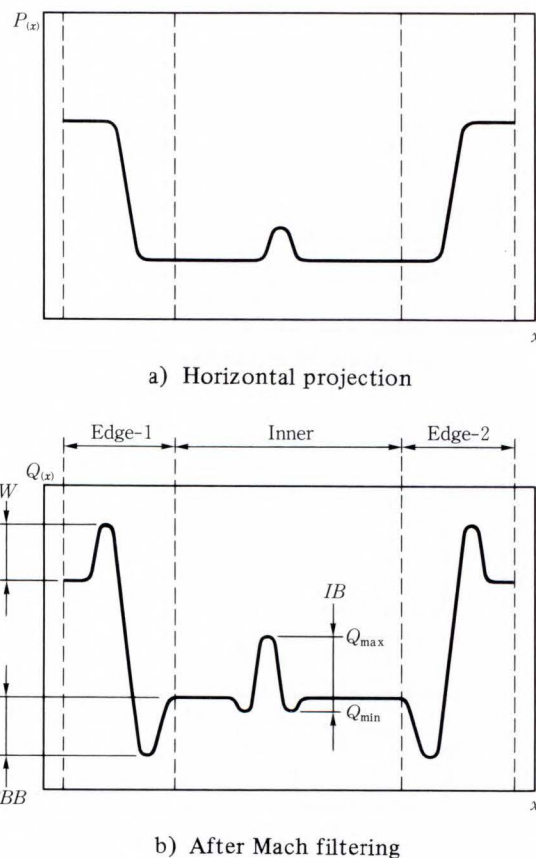


Fig. 7—Calculation procedure for blur inspection.

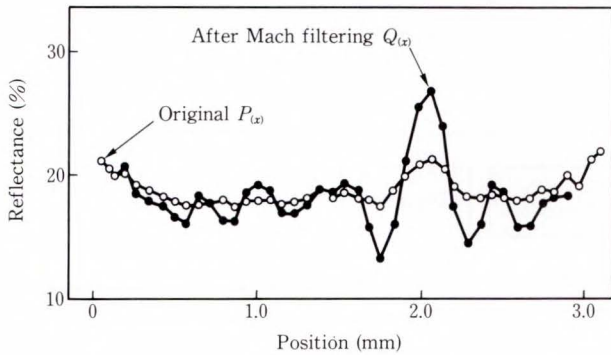
Next, a one-dimensional Mach filter is applied to the projection value.

$$Q(x) = M \{ P(x) \}. \quad \dots \dots (5)$$

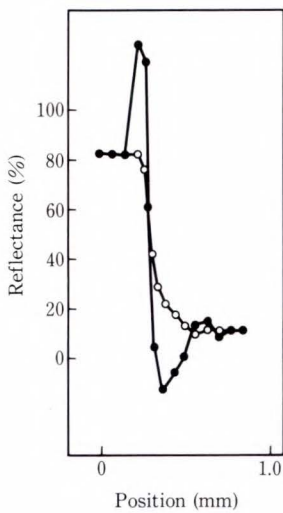
Three types of blur evaluation functions are defined: one inner blur evaluation function IB , and two edge blur evaluation functions EBW and EBB .

These are as follows:

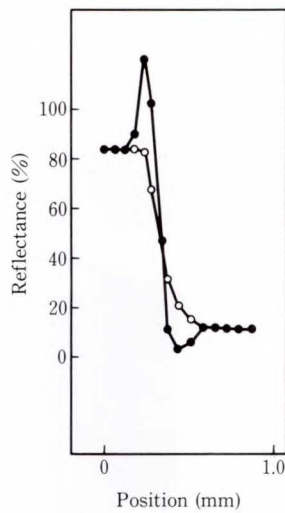
$$\left. \begin{aligned} IB(D_{av}, Q_{max}, Q_{min}) &= (Q_{max} - Q_{min}) / \{A_h \times \log(D_{av}) + B_h\} \\ EBW(W_{av}, Q_w) &= 1 / [(Q_w - W_{av}) / \{A_h \times \log(W_{av}) + B_h\}] \\ EBB(D_{av}, Q_b) &= 1 / [D_{av} - Q_b] / \{A_h \times \log(D_{av}) + B_h\} \end{aligned} \right\} \dots\dots\dots (6)$$



a) Inner blur



b) Normal edge



c) Blurred edge

Fig. 8—Experimental results of Mach filtering.

The values are shown in Fig. 7. A_h and B_h are coefficients that represent human eye characteristics. W_{av} is the average reflectance of white paper, and Q_w and Q_b are the maximum and minimum values in the edge area. *EBW* evaluates character bolt out and *EBB* evaluates character blur.

These functions are reciprocals, so the values increase with decreasing print quality.

Figure 8 shows the effect of one-dimensional Mach filtering. Figure 8 a) shows an example in which the inner blur is emphasized by a factor of about three. Figures 8 b) and c) show examples in which the normal edge is emphasized twice as much as the blurred edge.

The emphasis rate depends on the relationship between edge gradient and the filter size. Figure 9 shows their inter-relationship. The emphasis rate of the normal edge is maximum when the filter size is twice the size of the edge gradient. The rate is maximum when the filter size is equal to the size of inner blur.

5.3 Quality evaluation

A new algorithm has been developed to evaluate the total print quality *PWE*. The total print quality is an evaluation equipment to the evaluation. This equipment is made by the sensory decision making functions of human

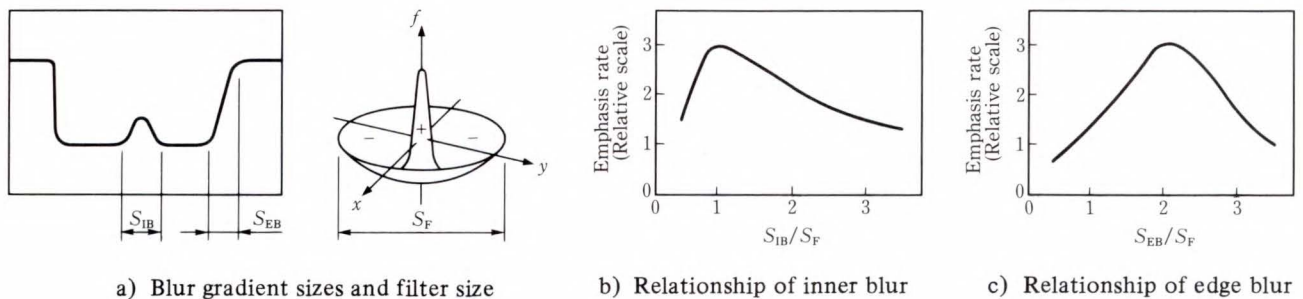


Fig. 9—Relationship between filter size and blur function.

vision such as defect regularity, neighboring contrast, and other characteristics.

This algorithm uses a weight function $w(B)$ as follows:

$$PWE = \frac{\sum \{w(IB) \times IB + w(EBW) \times EBW + w(EBB) \times EBB\}}{\sum \{w(IB) + w(EBW) + w(EBB)\}} \dots \dots \dots (7)$$

where $w(B) = B^\alpha$. Here, α is an exponential coefficient that represents human sensitivity. In Equation (7), the total print quality PWE progressively and accumulatively depends on blur evaluation functions.

The summation is calculated over the entire area of the test sheet being inspected.

6. Print quality inspection system

The decision levels of our sensory recognition system are based on the experience of trained inspectors. The system requires stability, reproducibility, and quantitative accuracy and was designed to simulate a trained inspectors' knowledge and experience.

6.1 Requirements for a print quality evaluation system

There are two requirements for a practical print quality inspection system:

- 1) High resolution image processing
The minimum size of a defect is 150 microns. This is about half the size of a dot. The resolution of an image pixel is therefore 75 microns. It requires 5120×4056 pixels to cover an entire sheet. To detect errors in print density, a resolution of 0.03 optical density (OD) is required.
- 2) Evaluation performance equivalent to human inspection

The Mach phenomenon and exponential sensitivity are important human inspection factors. Inspection algorithms must therefore include these factors. Total quality is assessed using the accumulative weighting method.

6.2 Inspection system

A new inspection system has been developed which satisfies these requirements. Figure 10

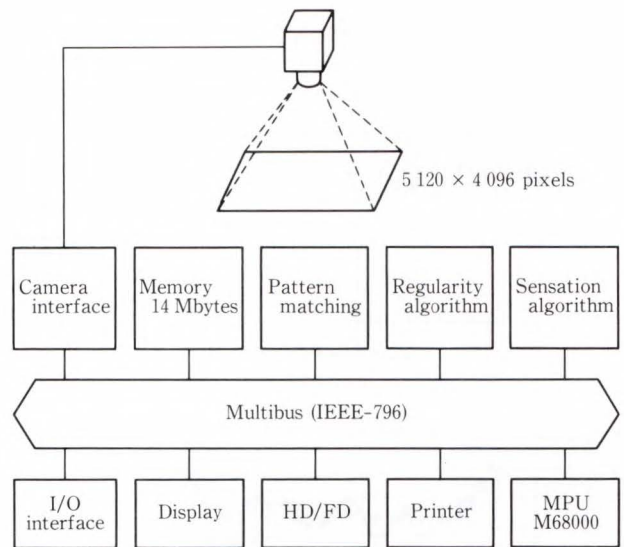


Fig. 10—System configuration.

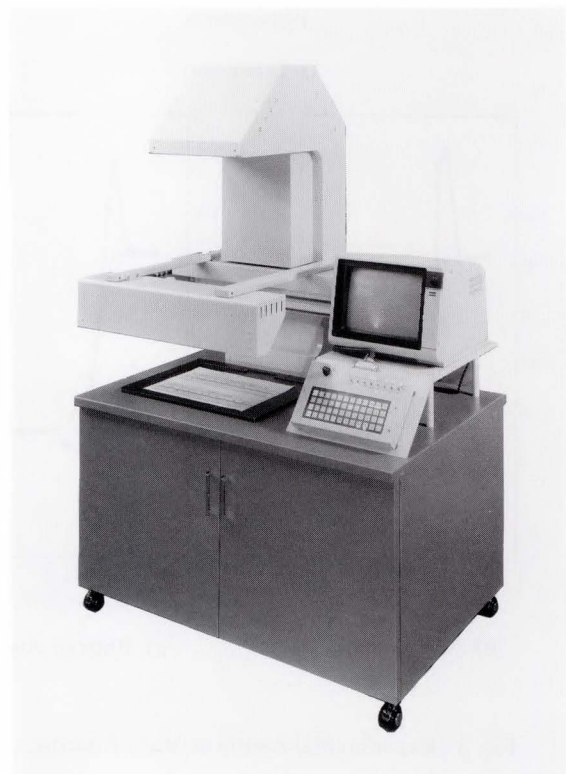


Fig. 11—Print quality evaluation system.

shows the system configuration. Figure 11 is a photograph of the system.

The system is based on a high-resolution camera with an object image capacity of 20 megabytes, a M68000 microprocessor, and a 10 megabyte image processing unit with an

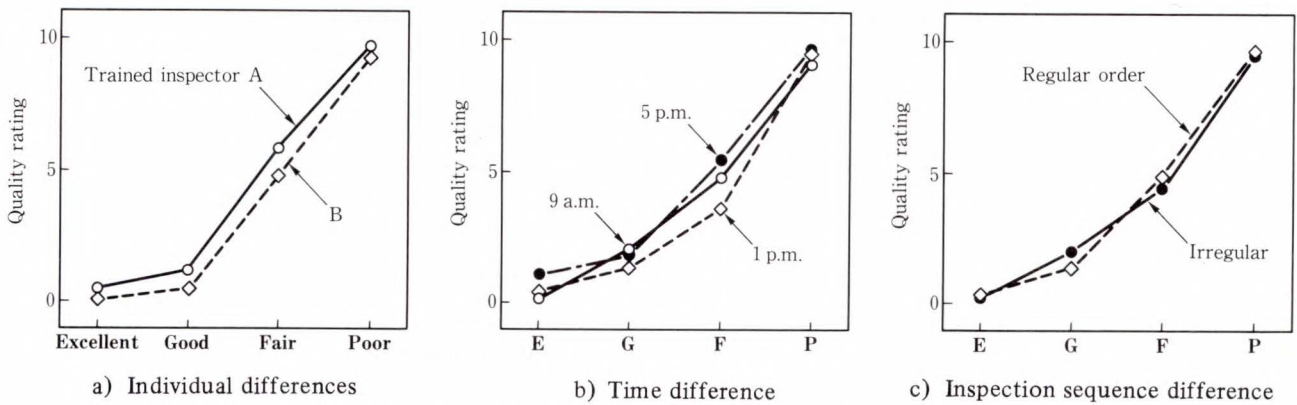


Fig. 12—Stability of human inspection (0 = excellent, 10 = poor).

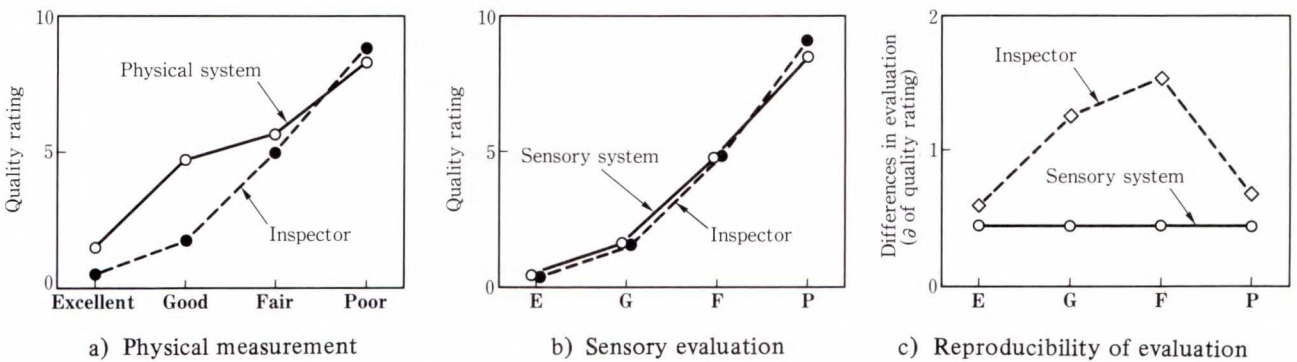


Fig. 13—Performance of our system (0 = excellent, 10 = poor).

illumination correction circuit and a pattern matching circuit.

6.2.1 Imaging system

An object image is formed by mechanically moving a 4096-element line CCD sensor perpendicular to the sensor. This system can produce an entire test sheet image (384 × 307 mm) at a resolution of 75 microns.

6.2.2 Illumination correction

The object is illuminated by ten 30 watt fluorescent lamps, and the illumination non-uniformity on the sheet is ±20%. To accurately estimate print density, the illumination non-uniformity must be corrected to within ±3%. A correction circuit is used for this purpose. The illumination non-uniformity is calculated using 256 × 256 bytes of data for each sheet and the result is stored as a reciprocal function. The analog data is multiplied by the correction function during image scanning.

Experimental results show that this technique corrects illumination non-uniformity to

within ±3%.

7. Experimental results

7.1 Accuracy of human evaluation

Figure 12 shows the results of print quality evaluation by trained inspectors on a scale of 0 to 10. A perfect sample is given 0 points and the worst sample is given ten points. Forty sheets of samples were divided into four groups by trained inspectors before examination. The four groups were: excellent (average of one point), good (average of two points), fair (average of five points), and poor (average of nine points).

The results in Fig. 12 indicate that the stability and reproducibility of evaluations by trained inspectors are high. However, untrained inspectors could not correctly evaluate the degree of defects. The reason for this is that beginners do not completely understand the evaluation rules.

7.2 Accuracy of evaluation by our system

The performance of our system is shown in Fig. 13. The evaluations of excellent and poor samples are well matched to the evaluations of trained inspectors {see Fig. 13 a)}. However, the evaluations of the good and fair samples are not well matched. In this case, exponential coefficient α in section 5.3 is 0.0. (This means that the sensory characteristics of human vision is not used for evaluation.)

Our sensory pattern recognition system can evaluate print quality as well as a trained inspector {see Fig. 13 b)}. In this case, the exponential coefficient α is 1.0. (This means that the sensory characteristics of human vision is used.)

The results in Fig. 13 c) indicate that the evaluation reproductibility of our system is better than that of trained inspectors.

8. Conclusion

We have developed a sensory pattern recognition system based on the characteristics of human vision. The system simulates characteristics of the human eye such as sensitivity transformation, the Mach phenomenon, and other characteristics of human vision such as accumulative evaluation and exponential sensitivity.

This system was used to evaluate the print quality of a dot-matrix printer. Its sensory recognition capability was compared to that

of trained inspectors. Experimental results indicate that the evaluation quality is on the same level as that of trained inspectors. This means that the sensory algorithms used are capable of simulating human vision.

Our system can therefore be used for sensory pattern recognition in specific applications, for example, print quality evaluation.

9. Acknowledgement

We are grateful to Messrs. S. Umezawa, T. Igarashi, and E. Aoyama of Fujitsu for their help with system development, and Messrs. Y. Ishikawa and H. Anbe of Fujitsu Isotec Limited for their help with the system development and evaluation.

References

- 1) Marr, D.: Vision. New York, W.H. Freeman, 1982, 431p.
- 2) Crawford, J.L., Elizinga, C.D., and Yudico, R.: Print quality measurements for high-speed electrophotographic printers. *IBM J. Res. Develop.*, **28**, 3, pp. 276-284 (1984).
- 3) Hiraoka, N., Uzumaki, T., Koezuka, T., Nakashima, M., and Inagaki, T.: Print quality inspection system based on human-eye response for a dot-matrix printer. Proc. SPIE, IECON'87, Automated Design and Manufacturing, **857**, pp. 870-877 (1987).
- 4) Lowry, E.M., and Palma, J.J.: Sine-wave response of the visual system. I, The Mach phenomenon. *J. Opt. Soc. Am.*, **51**, 7, pp. 740-746 (1961).



Masato Nakashima
Holography and Color-Imaging
Laboratory
FUJITSU LABORATORIES, ATSUGI
Bachelor of Chemistry
Tohoku University 1969
Specializing in Sensing Technology
and Image Processing



Tetsuo Koezuka
Sensing Technology and Robotics
Laboratory
FUJITSU LABORATORIES, ATSUGI
Bachelor of Electrical Eng.
Saitama University 1979
Specializing in Sensing Technology
and Image Processing

Surface Flatness Measurement System

• Shin-ichi Wakana • Yoshiro Goto

(Manuscript received December 15, 1989)

An optical non-contact and non-destructive measurement system has been developed for surface flatness inspection. It is based on a new measurement principle, and is applicable to highly reflective flat planes, such as aluminum magnetic disk substrates and semiconductor wafers. It measures angular displacement at a fixed pitch, then calculates the surface profile by totaling the angular data multiplied by the measurement pitch. When it is calibrated with a reference flat mirror, the system has a measurement accuracy better than $0.01 \mu\text{m}$. In addition, another calibration algorithm using a Fast Fourier Transform (FFT) for the direction of rotation was developed.

1. Introduction

The manufacture and evaluation of flat planes are important in many fields. For example, a magnetic disk substrate must be flat because of the decreasing gap between the magnetic head and the disk surface resulting from increased recording density. Semiconductor wafers must also be flat to eliminate loss of sharpness in the circuit patterns. Although surface undulation as well as surface roughness must be measured to ensure device integrity, a measurement standard for undulation does not exist. A surface roughness measuring instrument was used to measure surface undulation.

To inspect surface flatness, there are some requirements for a measurement system. The first is accuracy. Measurement accuracy must be better than $0.01 \mu\text{m}$. Other requirements are a wide working distance margin of $\pm 3 \text{ mm}$ for easy operation, and a measurement span of at least 5 inches. The final requirement is a measurement speed exceeding 1 mm/s for high throughput.

There are two conventional non-contact measuring methods. Surface scanning with an optical stylus can accurately measure surface undulation and roughness, but it is slow, and the measurement span is small¹⁾. Phase measurement using interferometric optics is fast and

has a wide span, but its accuracy is not sufficient^{2),3)}. Furthermore, the working distances for both methods are too small. A new measuring instrument is necessary.

The authors developed an instrument for measuring surface flatness using a laser, with an accuracy of $0.01 \mu\text{m}$. It can measure one dimensional surface undulation in the radial direction or direction of rotation, like an optical surface roughness tester. In this paper, the authors' measurement algorithm, calibration algorithm, and system configuration is described in detail, and the measurement results are given to show the system performance.

2. System elements

Three new elements were developed for the measurement system. The first is a micro-angle displacement sensor, which measures the angular displacement between points. The second is an algorithm for converting the measured angle data to surface height data. The third is a calibration algorithm, which corrects system errors.

2.1 Microangle displacement sensor

Figure 1 is a diagram of the microangle displacement sensor. Its optics are very similar to the reading head of a compact disc player. A semiconductor laser emits a divergent beam

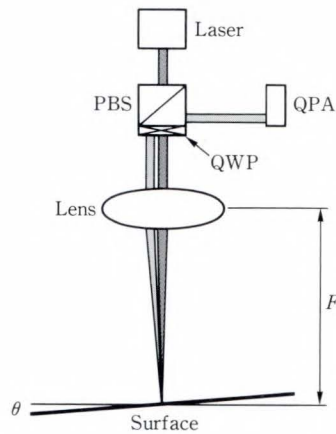


Fig. 1—Microangle displacement sensor.

that is collimated into a parallel light beam 1 mm in diameter. This beam passes through a polarization beam splitter (PBS), and a quarter-wave plate (QWP), and is then focused by a lens onto the surface to be measured. The spot diameter is about 50 μm. The focused beam is reflected by the surface at an angle of 2θ, twice the surface inclination angle θ. The reflected beam is recollimated by the focusing lens and guided through the QWP and PBS to a quadrant photodiode array (QPA). The incident position on the QPA deviates based on the surface inclination angle θ. The displacement from the center of the QPA is calculated from the focal length of the lens by:

$$D = F \tan(2\theta) \quad \dots \dots \dots (1)$$

The QPA outputs four different voltages on four lines according to the incident beam position. If the exact relationship between the voltage difference and displacement is known, the surface angle is determined using the inverse of Equation (1).

Figure 2 shows the relationship between the surface angle and the output voltage. In this figure, the output voltage was normalized by the total optical power input to the QPA. The dynamic range of the sensor is about ±0.3 degrees. Its resolution, calculated from the dynamic range of the sensor and the resolution of an analog-to-digital converter, is about 0.000 1 degrees.

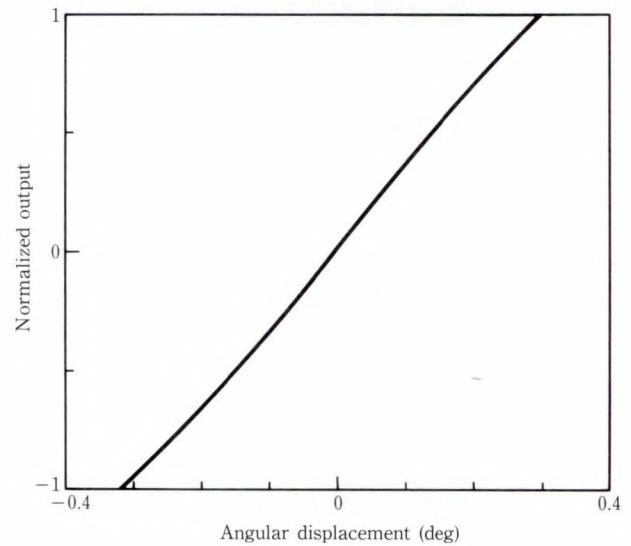


Fig. 2—Normalized output.

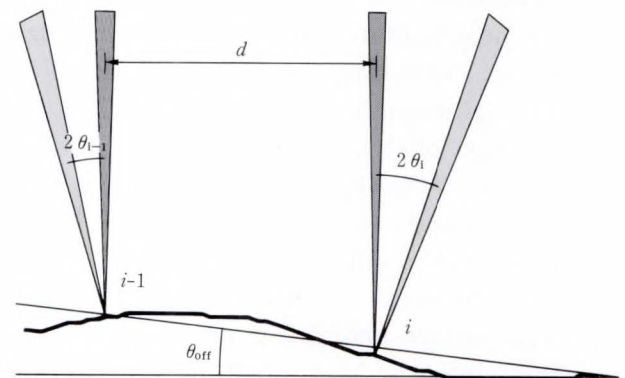


Fig. 3—Calculation algorithm.

2.2 Calculation algorithm

The surface height deviation is calculated from the angular displacement data. The surface height means the distance from a virtual zero level. In this system, the virtual zero level is defined at the start point.

The thick uneven line in Fig. 3 represents the surface profile. The vertical hatched lines are the vertically incident laser beam for measuring angular displacement. The measurement distance, *d*, is set to 10 μm. At the *i*-th measurement point, the surface angle is θ_{*i*}, and the reflection angle is 2θ_{*i*}. The surface height deviation is the sum of the angular differences multiplied by *d*. If the surface is inclined, the

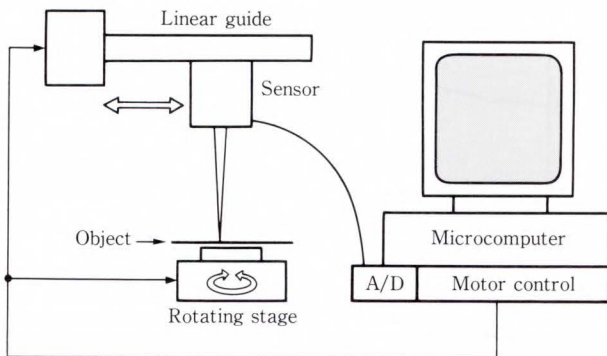


Fig. 4—Block diagram.

inclination angle θ_{off} is included in θ_i , and must be subtracted before totaling.

The conversion algorithm is summarized as

$$H_j = \sum_{i=1}^j \tan(\theta_i - \theta_{\text{off}}) \times d, \quad \dots \dots (2)$$

where H_j is the surface height deviation at the measurement point.

2.3 System configuration

The microangle displacement sensor and the conversion algorithm were used to construct the measurement system. Figure 4 is a block diagram of the system.

The sensor is moved above the object along a linear guide, and measures the angular displacements at discrete points. The position is controlled by the rotating stage. The microcomputer (FM R-50HD) contains an analog-to-digital converter and a motor controller. It controls the system and calculates the surface height deviation.

2.4 Calibration

Two error factors were discovered in the system. The first error occurred in radial measurement, and was caused by a bend in the linear guide. The guide sagged under its own weight near full extension, causing the sensor to detect excessive angular displacement. The second error occurred in rotational direction measurement, and was caused by the inclination of the rotating stage. The rotating stage is subject to tilting for a number of reasons,

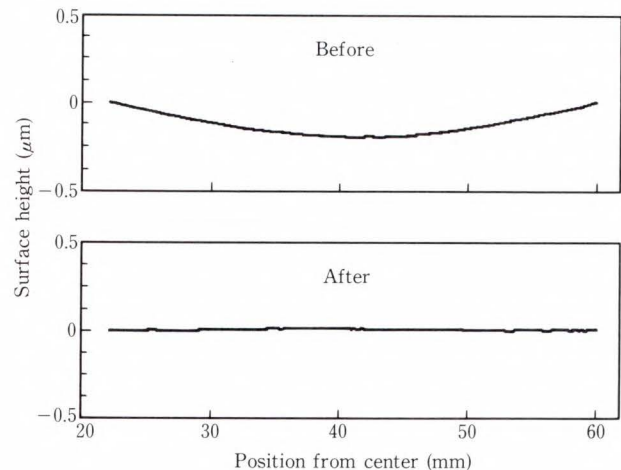


Fig. 5—Calibration effect in radial direction.

including loose bearings.

To compensate for these errors, two calibration algorithms were developed. The first algorithm corrects errors in the radial direction. The second corrects errors in the direction of rotation.

A third calibration algorithm was also developed to eliminate the effects of cracks and dust on the object.

2.4.1 Calibration algorithm for radial measurement

The first calibration algorithm uses reference angle data to determine the excess angle deviation caused by the sag of the driving guide. This data is acquired using a flat mirror before measurement, and is stored in memory. The data is then subtracted from the measured data by the conversion algorithm.

Figure 5 shows the effect of calibration. The measured object was a mirror with a surface flatness within $\lambda/20$, as measured by an interferometer. In the upper graph, the surface appears concave, deviating by about $0.25 \mu\text{m}$ at the center. After calibration, the concavity at the center disappears.

2.4.2 Calibration algorithm for measurement in the rotation direction

There are some error factors in the rotating stage mechanism as mentioned above. At first, the effects of these error factors were estimated theoretically.

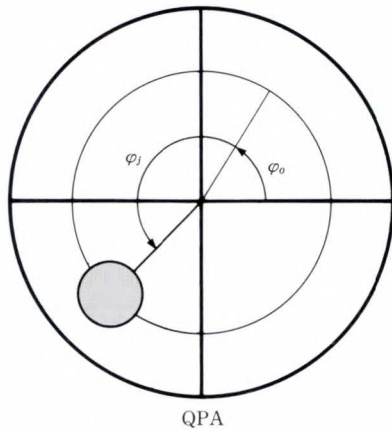


Fig. 6—Rotation of stage.

If the rotating stage is tilted on its axis, the result of measuring an ideally flat plane indicates a sinusoidal curve, instead of a flat line. The incident position of the reflected beam moves around a circle on the QPA according to the stage rotation, as shown in Fig. 6. The radius of the circle depends on the stage axis inclination angle ψ_{ax} . The j th incident beam position on the QPA can be described as

$$F \tan(2\psi_{ax}) \times \cos(\varphi_j + \varphi_0), \dots\dots (3)$$

φ_j is the angle of the incident position and φ_0 is the initial angle on the QPA. Then, the surface measurement result can be expressed as

$$H_i = \sum_{j=1}^i C \times F \tan(2\psi_{ax}) \times d \times \cos(\varphi_j + \varphi_0), \dots\dots (4)$$

C is a conversion constant. When the summation is converted to integral notation, the expression becomes

$$H = A \sin(\varphi + \varphi_0), \dots\dots (5)$$

In a real system, there are many error factors due to mechanical imperfections. Each error affects the measurement result independently. The cumulative error effect can be summarized by the equation

$$H = \sum_{i=1}^m A_i \sin(\varphi_i + \varphi_{0i}), \dots\dots (6)$$

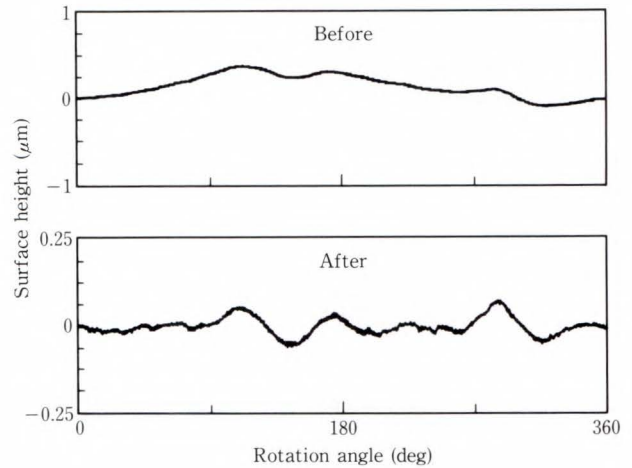


Fig. 7—Calibration effect in direction of rotation.

where m is the number of error factors.

To compensate for the inclination of the stage axis, spectral filtering was used. First, the microcomputer calculates the Fourier transform of Equation (6), and cuts off the power spectral values of less than a fixed order. Then it calculates the inverse Fourier transform of the filtered spectrum, to determine the calibrated surface profile. In this experiment, a Fast Fourier Transform (FFT) was used to calculate the power spectra of the measured profile. After that, all spectral values less than the 5th order were cut off. Figure 7 shows the effect of calibration. Before calibration, the surface profile has several orders of undulation. With calibration, the low-frequency large-amplitude component disappears and the fine surface profile becomes visible. There are some notches on the curve due to insufficient calculation accuracy.

This calibration algorithm may give a false surface profile because of the error correction. If the measured surface actually has low-frequency components, this calibration also cuts off them. Then the surface profile is distorted. However, in practice it is no problem. Because, for example, such a low-frequency undulation component does not affect the disk head in the magnetic storage system. This calibration is therefore useful for revealing



Fig. 8—Measurement system.

the fine surface profiles hidden by large components.

This calibration algorithm is very slow because of the large number of calculations, slow CPU (i80286 & i80287) speed, and programming language. (BASIC was used.) Therefore, the FFT calculation is applied to extracted data, not to all measured data. To make this algorithm faster, the authors plan to use a digital signal processor (DSP) as a FFT processor in the measurement system.

2.4.3 Calibration algorithm for obstructions

A separate algorithm was used to eliminate the influence of cracks and dust. When the laser beam strikes these obstructions, the light is scattered and the angular displacement cannot be measured correctly. When laser light is scattered by an obstruction, an extra photodiode in the sensor head detects the scattered light and reports the scattering to the controller. The controller then ignores the measured angle data for that point and interpolates the data as part of the calculation routine.

Figure 8 shows the measurement system. The small black box hanging from the carriage on the left is the microangle displacement

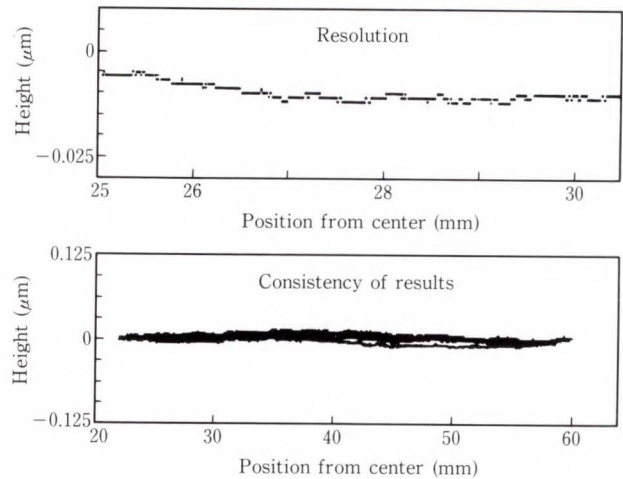


Fig. 9—System's performance.

sensor. The object under the sensor is an aluminum magnetic disk substrate 5.25 inches in diameter.

3. Experiment

This system's measurement results were almost the same as that of a surface roughness tester using a stylus. As there is no measurement standard for surface undulation, this system's performance was evaluated using the methods described below. All test measurements were made in the radial direction.

3.1 Resolution and consistency of results

The measurement resolution of the system was tested. Theoretically, measurement resolution depends on the angular resolution of the microangle displacement sensor, the conversion resolution of the analog-to-digital converter, and the calculation accuracy of the microcomputer. In this system, the conversion resolution of the analog-to-digital converter limits the measurement resolution. The upper graph in Fig. 9 is the magnified result of the flat mirror measurement. This shows that the surface height can be measured to within $0.001 \mu\text{m}$.

We tested result consistency by measuring the same profile 50 times. The lower graph shows the traces of the multiple measurements. We calculated the average value of the standard deviation of the height data for all of the

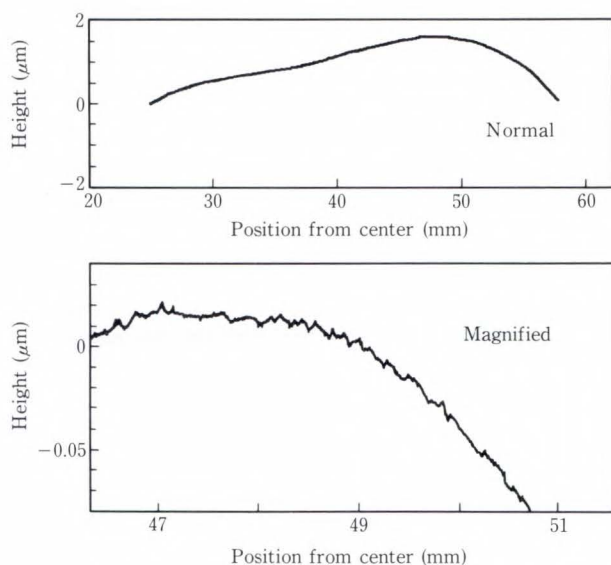


Fig. 10—Typical measurement result.

measurement points. The average standard deviation was within $0.01 \mu\text{m}$.

The system's tolerance to variation in height positioning was tested and it was confirmed that even if the working distance is changed by up to 3 mm, the results remain within the range of consistency.

Measurement time which contained calculation time was 30 s for 30-mm measurement in the radial direction. Then the measurement speed of this system is about 1 mm/s. This speed is faster than the conventional surface roughness tester.

3.2 Results of Al disk measurement

Figure 10 shows measurements of a 5.25-inch aluminum magnetic disk substrate. The disk had a surface undulation of about $1.6 \mu\text{m}$. The lower graph is a magnification of the range from 47 mm to 51 mm. There are many notches on the curve that seem to be caused by the diamond turning process.

4. Conclusion

The authors have developed a surface flatness measurement system based on three newly developed elements, a microangle displacement sensor, a calculation algorithm, and a calibration algorithm. The system measures surface undula-

tion with a resolution of $0.001 \mu\text{m}$ and an accuracy of $0.01 \mu\text{m}$, as estimated from the standard deviation of repeated tests. The vertically incident optics and the angular detection method give this system a working distance margin of about $\pm 3 \text{ mm}$. This system does not require fine height positioning or fine angle adjustment, and measures about 1 mm/s.

At this time, the calculation speed of the CPU (i80286) is too low, especially for the calibration routine. It is therefore necessary to use a special calculation system such as DSP to refine the measurement system.

The system can be used to measure magnetic disk substrate and semiconductor wafers, and other highly reflective objects. The measurement principle can be used in other measurement systems as well.

References

- 1) Kohno, T., Ozawa, N., Miyamoto, K., and Musha, T.: High-precision optical surface sensor. *Appl. Opt.*, **27**, 1, pp. 103-108 (1988).
- 2) Perry, D.M., Robinson, G.M., and Peterson, R.W.: Measurement of Surface Topography of Magnetic Recording Materials Through Computer-Analyzed Microscopic Interferometry. *IEEE Trans. Magnetics*, **MAG-19**, 5, pp. 1656-1657 (1983).
- 3) Zienlinski, R.J.: Unequal Path Interferometer Alignment and Use. *Opt. Eng.*, **18**, 5, pp. 479-482 (1979).



Shin-ichi Wakana

Sensing Technology and Robotics Laboratory
FUJITSU LABORATORIES, ATSUGI
Bachelor of Electric Eng.
Waseda University 1982
Master of Electric Eng.
Waseda University 1984
Specializing in Laser Application and Optical Sensing Technology



Yoshiro Goto

Sensing Technology and Robotics Laboratory
FUJITSU LABORATORIES, ATSUGI
Bachelor of Electric Eng.
Kyushu University 1969
Specializing in Optical Sensing and Electron Beam Technology

Six-Axis Force/Torque Sensor for Assembly Robots

● Akihiko Yabuki (Manuscript received December 19, 1989)

Force control assembly robots require a six-axis force/torque sensor to detect the forces applied to the robot arm. A new force/torque sensor has been developed which mounts on the wrist of the robot and detects strains exerted on a bit deformable elastic body caused by contact of the end-effector with the assembly. Force/torque detection is performed in real time and in six-degrees-of-freedom in a Cartesian coordinate system. The elastic body consists of eight parallel leaf springs and has excellent noninterference and output linearity. The sensor has an internal overload protector for impact tolerance.

1. Introduction

Precise positioning of two bodies in assembly work is difficult. Collision or jamming can occur during the assembly process in position control type assembly robots which require very high precision. For automated assembly, engineers have concentrated on improving robot functions by force or impedance control. Precise robot force/torque control generally takes the form of force/torque feedback control. This requires a six-axis force/torque sensor that can detect the force and torque (until Chap. 2, these will be collectively referred to as "the force") exerted on the end-effector.

Force sensor design should take the following three factors into account:

- 1) To accurately measure the force, the relationship between the load and force sensor outputs must be highly linear and the matrix which describes this relationship must have excellent noninterference.
- 2) The stiffness of the force sensor must be determined taking the robot control system into account. When the end-effector comes into contact with the assembly, a closed link system is formed which includes the robot arm. To increase the gain of the robot control system for a fast response and to reduce

the difference between the actual force and the target force, a compliant wrist may be beneficial¹⁾. A compliant force sensor may lower the natural frequency of the robot arm if the mass of the end-effector is large. Therefore, a force sensor should have a structure that permits a stiffness that suits the mass-spring system of the link.

- 3) A force sensor mounted on the wrist of a robot arm is subjected to forces due to end-effector contact or collision with the assembly. To maintain control of the robot, the detection time must be reduced and the sensor must be protected against potentially damaging loads.

We have developed a force sensor that satisfies these requirements. The detector section is a bit deformable elastic body consisting of eight parallel leaf springs and a mechanical stopper²⁾. This paper describes the structure, characteristics, and operating principle of this sensor.

2. Force detection method

Figure 1 shows how the force applied to an end-effector can be detected using a force sensor attached to an N-degree-of-freedom robot arm.

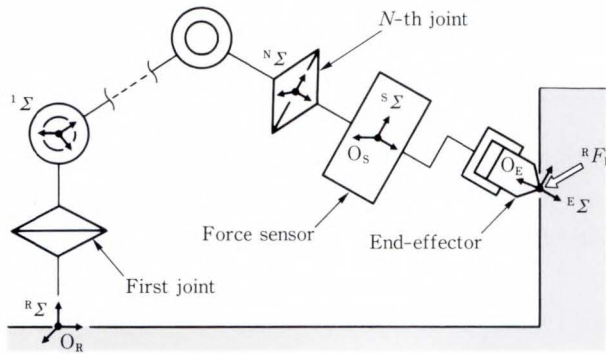


Fig. 1—Force measurement using the force sensor.

In Fig. 1, $R\Sigma$ is the reference coordinate system, $i\Sigma$ ($i = 1, 2, \dots, N$) is the coordinate system of each joint of the robot, $S\Sigma$ is the coordinate system of the force sensor, and $E\Sigma$ is the coordinate system of the end-effector. The 4×4 coordinate transformation matrix A_E between $S\Sigma$ and $E\Sigma$ is given by

$$A_E = \begin{bmatrix} R_{E/S} & r \\ 0 & 1 \end{bmatrix}, \quad \dots \dots \dots (1)$$

where $R_{E/S}$ is the 3×3 rotation matrix between $S\Sigma$ and $E\Sigma$, and r is the vector from the origin O_S of $S\Sigma$ to the origin O_E of $E\Sigma$ a vector in the $S\Sigma$ coordinate system.

If the coupling of the sensor to the robot hand/end-effector can be regarded as a rigid body, the force $E F_E$ exerted on O_E in the $E\Sigma$ coordinate system can be transformed into the equivalent force $S F_S$ exerted on O_S in the $S\Sigma$ coordinate system using Equation (2):

$$S F_S = U E F_E, \quad \dots \dots \dots (2)$$

where U is given by

$$U = \begin{bmatrix} R_{E/S} & 0 \\ D R_{E/S} & R_{E/S} \end{bmatrix}, \quad \dots \dots \dots (3)$$

and D is the 3×3 matrix given by Equation (4) which gives the exterior products between vector r and each row vector of a 3×3 matrix.

$$D = \begin{bmatrix} 0 & -r_Z & r_Y \\ r_Z & 0 & -r_X \\ -r_Y & r_X & 0 \end{bmatrix}, \quad \dots \dots \dots (4)$$

$$r = [r_X \ r_Y \ r_Z]^T. \quad \dots \dots \dots (5)$$

Where suffix T denotes a transposed matrix. The coordinate transformation matrix T_E

from $R\Sigma$ to $E\Sigma$ is given by Equation (6) which is obtained by multiplying the coordinate transformation matrices (A_i, A_S, A_E) between the coordinate systems before and after each link in the order of the series link shown in Fig. 1.

$$T_E = A_1 A_2 \dots A_N A_S A_E. \quad \dots \dots \dots (6)$$

Equation (7) indicates the elements of T_E . Where $R_{E/R}$ is the 3×3 rotation matrix between $R\Sigma$ and $E\Sigma$, and h is the vector from the origin O_R of $R\Sigma$ to the origin O_E of $E\Sigma$ a vector in the $R\Sigma$ coordinate system. Matrix $R_{E/R}$ can be obtained from the relationship between Equations (6) and (7).

$$T_E = \begin{bmatrix} R_{E/R} & h \\ 0 & 1 \end{bmatrix}. \quad \dots \dots \dots (7)$$

When force $S F_S$ is detected by the force sensor, force $R F_E$ exerted on O_E in the $R\Sigma$ coordinate system is given by

$$R F_E = R_{E/R} U^{-1} S F_S. \quad \dots \dots \dots (8)$$

In force measurement, the elastic strain caused by $S F_S$ is detected using strain gauges. The strain is so small that its effect on Equation (2) is negligible.

Assume that strain vector ϵ consisting of six components satisfies Equation (9) below

$$\epsilon = C_S S F_S. \quad \dots \dots \dots (9)$$

where C_S is a 6×6 matrix which corresponds to the sensor's strain compliance matrix defined by Uchiyama et al³⁾. The force $R F_E$ is then given by Equation (10) derived from Equations (8) and (9).

$$R F_E = R_{E/R} U^{-1} C_S^{-1} \epsilon. \quad \dots \dots \dots (10)$$

If the elements of ϵ appear to have no interference, that is, they correspond one-to-one with the six elements of $S F_S$, the operation for strain-to-force transformation can be simplified.

3. Force/torque sensor

3.1 Structure and deformation of an elastic body

Parallel leaf springs can be used for force

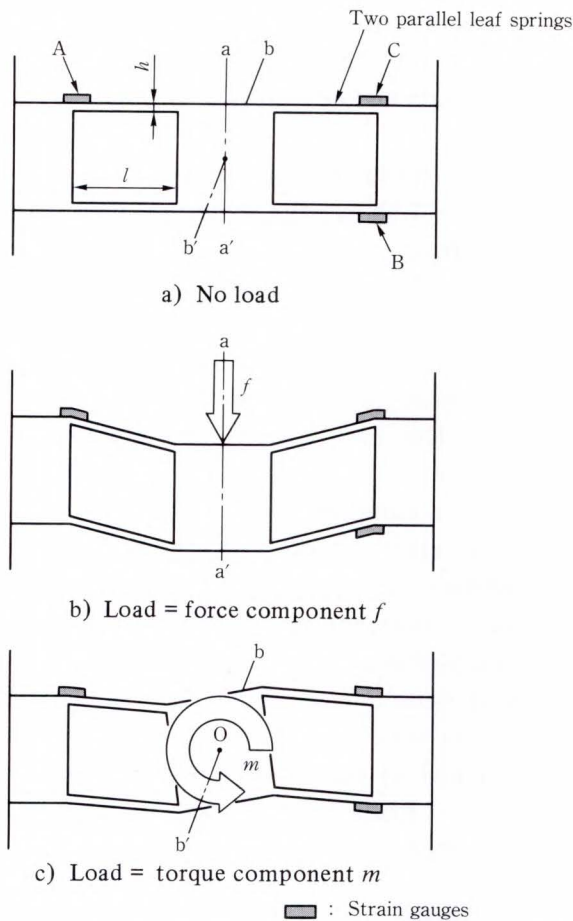


Fig. 2—Basic components and deformation of the elastic body.

detection⁴⁾ because of their deformation characteristics in the axis parallel to the direction of shear force. In this study, these characteristics were used to measure multi-axis force and torque. The elastic body consists of two beams (called basic beams) of parallel leaf springs { Fig. 2a }. These beams are symmetrical to the (a-a') axis in Fig. 2.

When a force (f) is applied to the beam along the (a-a') axis, the two parallel leaf springs are deformed symmetrically about that axis as shown in Fig. 2 b).

When a torque (m) is applied to the beam around axis (b-b') [at a right angle to axis (a-a') and at a right angle to the longitudinal axis of the beam], the parallel leaf springs deform symmetrically to point O as shown in Fig. 2 c).

The force components in the other two axes and the torque components around the axes only slightly deform the springs because of the

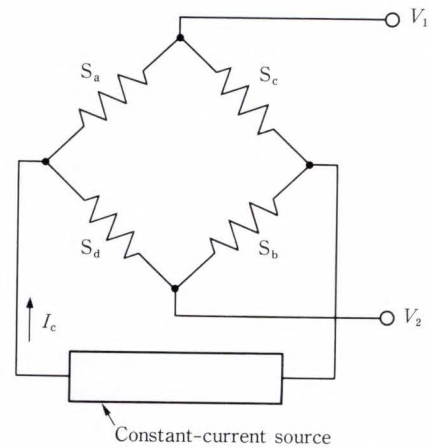


Fig. 3—Wheatstone bridge circuit.

high beam stiffness.

Components f and m therefore cause different deformations of the beam. This characteristic enables the force and torque components to be independently detected by detecting the strain in the beam. If three beams are combined so that they are mutually at right angles, three force and three torque components can be detected.

The basic beam's stiffness k_f and the maximum strain ϵ_{fmax} due to f were calculated using Equations (11) and (12). The torsional stiffness and maximum strain due to m were measured.

$$k_f = 4Bh^3E/l^3, \quad \dots \dots \dots (11)$$

$$\epsilon_{fmax} = 3lf/(4Bh^2E), \quad \dots \dots \dots (12)$$

where h , B , and l are the thickness, width, and length of the parallel leaf spring and E is the modulus of longitudinal elasticity of the beam. Stiffness k_f can be set to a desired value by changing h , B , and l .

3.2 Strain detection using a Wheatstone bridge

Strain vector ϵ is detected using six Wheatstone bridges each having four strain gauges (see Fig. 3). The circuits are temperature compensated and supplied by a constant current source I_c . The four gauges are connected in such a way that when the resistance of both gauges in either of the two opposing limbs (S_a and S_b , or S_c and S_d) changes in the same direction a voltage ($V_2 - V_1$) proportional to the change in resistance appears across the bridge.

To detect force component f in the basic beam shown in Fig. 2, S_a and S_b are attached to position A, and S_c and S_d are attached to position B. To detect the torque component m , S_a and S_b are attached to position A, and S_c and S_d are attached to position C.

The changes in gauge resistance caused by f and m are: r_{f1} and r_{m1} at position A, r_{f2} and r_{m1} at position B, and r_{f1} and r_{m2} at position C. If f and m are applied at the same time, the output voltage V_f of the f -detection bridge and the output voltage V_m of the m -detection bridge are given by Equations (13) and (14), and f and m can be independently detected.

$$V_f = (r_{f1} - r_{f2})I_c/2, \dots\dots\dots (13)$$

$$V_m = (r_{m1} - r_{m2})I_c/2. \dots\dots\dots (14)$$

Tensile and compressive strains of different polarity can be detected. Each of the detected

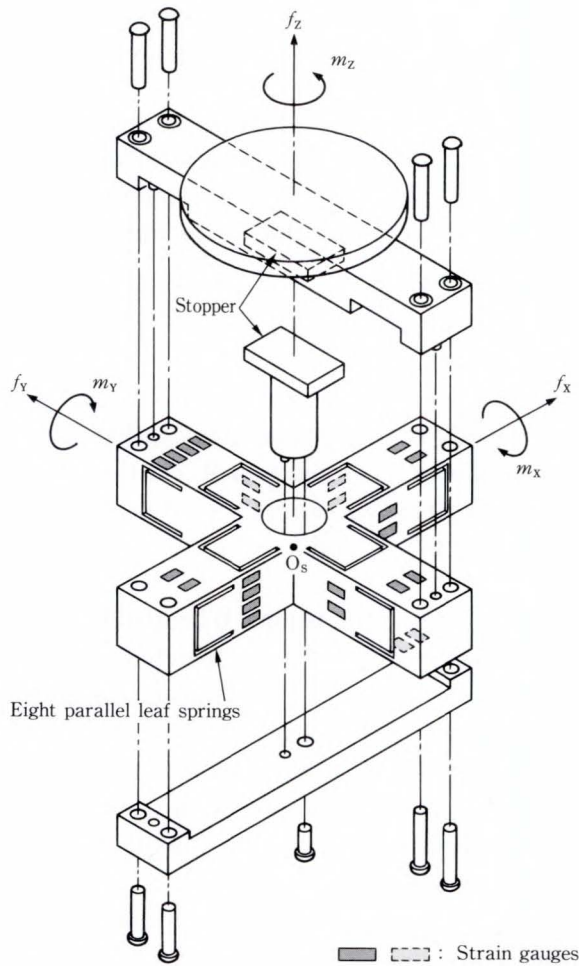


Fig. 4—Structure of the six-axis force/torque sensor.

components of strain vector ϵ are given as the mean value between the amplitudes of the tensile strain and compressive strain.

3.3 Force/torque sensor structure

Figure 4 shows the structure of our six-axis force/torque sensor and the strain gauge positions. The elastic body has a crossed-beam structure of basic beams. The basic beams for detecting the X and Y components of a force can be used to detect the Z component of a torque. The basic beam for detecting the Z component of a force can be used to detect the X or Y component of a torque.

The eight parallel leaf springs (material: Aluminum alloy) for detecting six force and torque components are formed by wire-cut electrodischarge machining. Because they are formed from a monolithic material, the elastic body has excellent output linearity. A stopper is attached to the crossed beams to prevent an excessive load from deforming the beams outside their linear range.

3.4 Force/torque sensor characteristics

Figure 5 shows the relationship between the load and output voltages (V_{fX} , V_{fY} , V_{fZ} , V_{mX} , V_{mY} , and V_{mZ}) of the prototype force/torque sensor when the Z component of a

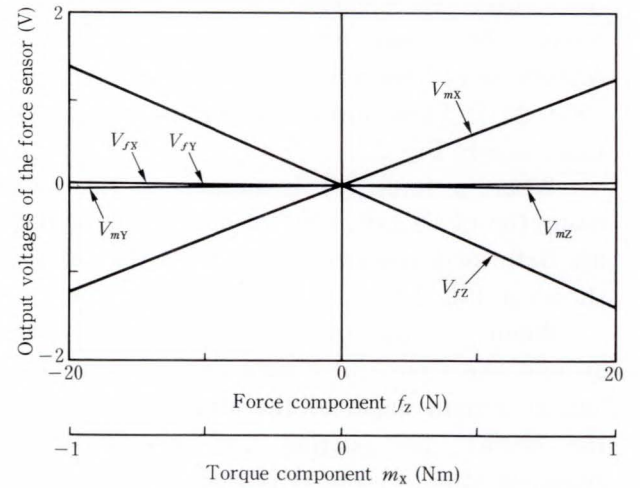


Fig. 5—Relationship between load and force/torque sensor output voltages when f_z and m_x are applied at the same time.

Table 1. Force/torque sensor specifications

	Force component	Torque component
Load range	20 N	2 Nm
Accuracy	2% of full scale	X, Y: 3%, Z: 5% of full scale
Stiffness	X	1.0×10^6 N/m
	Y	1.0×10^6 N/m
	Z	5.0×10^5 N/m

force and the X component of a torque are applied at the same time. The data shows that the output has excellent linearity and noninterference. Equation (15) gives the sensor's strain compliance matrix C_S obtained when the center O_S of the crossed-beam elastic body is regarded

$$C_S = \begin{bmatrix} -18.38 & -0.01 & -0.03 & 3.06 & 26.50 & 2.04 \\ 0.36 & 16.69 & 0.00 & 1.02 & 2.04 & 1.02 \\ -0.76 & 0.24 & -17.92 & 3.06 & 9.17 & 3.06 \\ -0.29 & -1.51 & -2.15 & 371.05 & 20.39 & 0.00 \\ -3.09 & -0.24 & -0.06 & 13.25 & 363.91 & -3.06 \\ 0.37 & 0.81 & 0.11 & 3.06 & 1.02 & -252.80 \end{bmatrix} (\mu/N, \mu/Nm). \quad \dots (15)$$

Using Equation (12), the diagonal elements c_{Sii} ($i = 1, 2, 3$) were designed to be $19.30 \mu/N$. Equation (15) shows that the actual values approximately match the design values. Elements other than the diagonal elements indicate the strains that have not been converted to noninterference strains. The operation described by Equation (10) can be simplified by setting negligible elements to zero.

As indicated in Equation (10), the necessary force/torque information includes a coordinate transformation that depends on the change in robot posture. Therefore, a real time detection system including coordinate transformation has been built by passing the force/torque data through a digital signal processor for high-speed operation. A prototype of the force/torque sensor satisfied the specifications listed in Table 1.

Figure 6 shows the prototype of the force/torque sensor and its circuit board. The board



Fig. 6—Six-axis force/torque sensor and circuit board.

as the origin of the ${}^S\Sigma$ coordinate system (see Appendix).

contains two hybrid ICs, and each IC has constant-current drive and amplifier circuits for the Wheatstone bridges (three channels).

4. Conclusion

A new six-axis force/torque sensor for assembly robots has been developed. For this sensor, a sensor structure using eight parallel leaf springs, a method of strain detection using Wheatstone bridges, and an overload protector in the sensor's body for impact protection were developed. This sensor has the characteristics necessary to control assembly robots.

Appendix

Force/torque sensor calibration

This appendix explains an example of calibrating the force/torque sensor. In this example, the method of calculating the sensor's strain compliance matrix C_S uses the relationship between the multi-axis load and the out-

put⁵⁾.

Here, Fig. A-1 is regarded as the coupling of the sensor to the end-effector. The calibration load is applied to origin O_E of the ${}^E\Sigma$ coordinate system. T_E is given by

$$T_E = A_S A_E, \quad \dots\dots\dots (A-1)$$

where

$$A_E = \begin{bmatrix} I & r \\ 0 & 1 \end{bmatrix}, \quad \dots\dots\dots (A-2)$$

and

$$A_S = \begin{bmatrix} R_{S/R} & 0 \\ 0 & 1 \end{bmatrix}, \quad \dots\dots\dots (A-3)$$

where I and $R_{S/R}$ are the 3×3 unit matrix and rotation matrix between ${}^R\Sigma$ and ${}^S\Sigma$. Using Equations (8) and (9), the relationship between the calibration load ${}^R F_E$ and the strain vector ϵ is given by

$$\epsilon = C_S U (R_{E/R})^T ({}^R F_E + {}^R \Xi_E), \quad (A-4)$$

where ${}^R \Xi_E$ is the force exerted on the strain detector due to the weight of the sensor and end-effector.

The calibration was performed using the system shown in Fig. A-1. A single-axis loading machine applies the calibration load ${}^R F_E$ given by Equation (A-5).

$${}^R F_E = [0 \ 0 \ f_z \ 0 \ 0 \ 0]^T. \quad \dots\dots\dots (A-5)$$

Because the linear and rotational stages change the position and orientation of the sensor, the loading point O_E can be fixed at any point of the cross-beam-shaped end-effector.

The calibration is performed by six loading experiments in which the loading point and sensor orientation are changed as shown below in articles 1)-6).

In the orientation of the ${}^S\Sigma$ coordinate system corresponding to the ${}^R\Sigma$ coordinate system given by

$$R_{S/R} = I, \quad \dots\dots\dots (A-6)$$

each position of O_E is given by

$$1) \ r = [0 \ 0 \ r_a]^T, \quad \dots\dots\dots (A-7)$$

$$2) \ r = [r_b \ 0 \ r_a]^T, \quad \dots\dots\dots (A-8)$$

$$3) \ r = [0 \ r_b \ r_a]^T. \quad \dots\dots\dots (A-9)$$

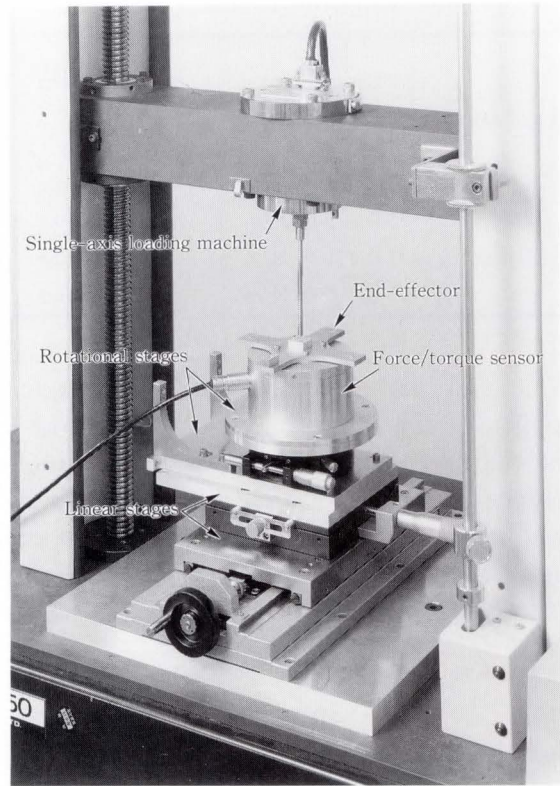


Fig. A-1—Force/torque sensor calibration system.

In the orientation of the ${}^S\Sigma$ coordinate system rotating at a right angle to the X -axis of the ${}^R\Sigma$ coordinate system given by

$$R_{S/R} = \begin{bmatrix} 1 & 0 & 0 \\ 0 & 0 & -1 \\ 0 & 1 & 0 \end{bmatrix}, \quad \dots\dots\dots (A-10)$$

each position of O_E is given by

$$4) \ r = [0 \ 0 \ r_a]^T, \quad \dots\dots\dots (A-11)$$

$$5) \ r = [r_b \ 0 \ r_a]^T. \quad \dots\dots\dots (A-12)$$

In the orientation of the ${}^S\Sigma$ coordinate system rotating at a right angle to the Y -axis of the ${}^R\Sigma$ coordinate system given by

$$R_{S/R} = \begin{bmatrix} 0 & 0 & 1 \\ 0 & 1 & 0 \\ -1 & 0 & 0 \end{bmatrix}, \quad \dots\dots\dots (A-13)$$

the position of O_E is given by

$$6) \ r = [0 \ 0 \ r_a]^T. \quad \dots\dots\dots (A-14)$$

The strain ζ caused by ${}^R \Xi_E$ is equivalent to the strain when load f_z was zero in each loading

experiment. If δ_i denotes the remainder of the strain ϵ_i after ζ_i has been subtracted, the strain δ_i is given by

$$\begin{aligned} \delta_i &= \epsilon_i - \zeta_i, \\ &= C_S \tilde{U}_i^R F_E, \end{aligned} \quad \dots\dots\dots (A-15)$$

where

$$\tilde{U}_i = U_i (R_{E/R_i})^T, \quad \dots\dots\dots (A-16)$$

and suffix i denotes the experiment number.

To calculate C_S statistically, the relationship between the load f_{zk} and the strain vector δ_{ik} is required when f_{zk} is varied within the rated load range and is applied as the k -th load in the experiment-(i). Figure 5 shows the relationship between the load $\tilde{U}_3^R F_{E_k}$ and the strain vector δ_{3k} in the loading experiment-(3).

If the regression line of Δ_i on W is assumed to be

$$\Delta_i = [\alpha_i \beta_i] W, \quad \dots\dots\dots (A-17)$$

where

$$\Delta_i = [\delta_{i1} \ \delta_{i2} \ \dots \ \delta_{ik} \ \dots \ \delta_{il}], \quad (A-18)$$

$$W = \begin{bmatrix} f_{z1} & f_{z2} & \dots & f_{zk} & \dots & f_{zl} \\ 1 & 1 & \dots & 1 & \dots & 1 \end{bmatrix}, \quad (A-19)$$

the least squares estimators $\hat{\alpha}_i$ and $\hat{\beta}_i$ are given by

$$[\hat{\alpha}_i \ \hat{\beta}_i] = \Delta_i W^\#, \quad \dots\dots\dots (A-20)$$

where $W^\#$ is the pseudo-inverse matrix of W .

An estimation of the sensor's strain compliance matrix \hat{C}_S is given by Equation (A-21) from Equations (A-22) and (A-23).

$$\hat{C}_S = A\Omega^{-1}, \quad \dots\dots\dots (A-21)$$

$$A = [\hat{\alpha}_1 \ \hat{\alpha}_2 \ \dots \ \hat{\alpha}_6], \quad \dots\dots\dots (A-22)$$

$$\Omega = [\tilde{U}_1^R F_E \ \tilde{U}_2^R F_E \ \dots \ \tilde{U}_6^R F_E], \quad (A-23)$$

where

$${}^R F_E = [0 \ 0 \ \pm 1 \ 0 \ 0 \ 0]^T. \quad \dots\dots\dots (A-24)$$

Each position of O_E and the orientation of the sensor in loading experiments must be determined so that Equation (A-25) can be satisfied.

$$\text{rank}(\Omega) = 6. \quad \dots\dots\dots (A-25)$$

If $\hat{\beta}_i$ s are negligible and the regression lines have excellent correlation, the sensor will be suitable for use.

References

- 1) Xu, Y., and Paul, R.P.: On Position Compensation and Force Control Stability of a Robot with a Compliant Wrist. IEEE Proc. Int. Conf. Robotics Autom., pp. 1173-1178 (1988).
- 2) Yabuki, A., and Asakawa, K.: 6 Axes Force/Torque Sensors for Assembly Robots. (in Japanese), 4th Ann. Conf. Robotics Soc. Jpn., pp. 133-134 (1986).
- 3) Uchiyama, M., Nakamura, Y., and Hakomori, K.: Evaluation of Robot Force Sensor Structure Using Singular Value Decomposition. (in Japanese), J. Robotics Soc., Jpn., 5, 1, pp. 4-10 (1987).
- 4) Asakawa, K., Akiya, F., and Yabuki, A.: Variable Compliance Robot with Tactile Sensory Feedback. FUJITSU Sci. Tech. J., 23, 3, pp. 188-197 (1986).
- 5) Uchiyama, M.: Design of Force Sensing System for a Robot. Syst. Contr., 31, 2, pp. 103-112 (1987).



Akihiko Yabuki
 Sensing Technology and Robotics
 Laboratory
 FUJITSU LABORATORIES, ASTUGI
 Bachelor of Mechanical Eng.
 Doshisha University 1983
 Master of Mechanical Eng.
 Osaka University 1985
 Specializing in Sensors and
 Mechanisms of Robots

High-Speed Force Controller for SCARA Robots

• Yutaka Yoshida • Akihiko Yabuki • Yasuyuki Nakata

(Manuscript received January 9, 1990)

The SCARA (Selective Compliance Assembly Robot Arm) robot has horizontal compliance. However, the amount and direction of compliance must be controlled before the robot can be used in actual applications. An active compliance controller has been developed that uses force sensors on the wrists of the robot to determine the contact force acting on the end effector. The sensors feed this information to the trajectory generator of the robot controller. The controller achieves high-speed control (sampling rate: 1 kHz) by performing all control operations in parallel using two Fujitsu MB8764 digital signal processors (DSPs).

1. Introduction

Industrial robots have been used to weld, paint, and handle mechanical parts and are now required to perform more complicated tasks such as assembly. Conventional robots are not suitable for these tasks because only their positions are controlled. When assembling mechanical parts or electronic device, there is a contact force between the end effector of the robot and the environment. Therefore, position control and force control are necessary to perform assembly tasks well. The RCC (Remote Center Compliance) device can sometimes be used, but the direction and amount of compliance are hard to change and the displacement is small. It therefore becomes necessary to control the contact force by manipulating the robot arm^{1),2)}.

We have developed an active force (compliance) controller for the SCARA robot. Force control is executed indirectly to feed the inverse Jacobian of the detected force vector to the reference joint velocity vector. To realize stable force control in such a control scheme, a high-gain wide-band joint servo is needed. Also force sensing, signal processing, and calculations of inverse kinematics must be

executed at high speed. We used two DSPs (digital signal processors) operating in parallel as the main controller to achieve a 1 kHz sampling rate.

One of these DSPs performs calculations for the joint servo and the joint reference function generator. The other performs calculations for position/force control and the inverse Jacobian.

The SCARA robot has ordinary joints and a speed reduction mechanism. Since the flexibility of such joints affects the stability of the controller³⁾, we analyzed the controller stability using a simplified robot arm model.

In this paper we describe the force and servo control configurations, the results of stability simulation, and the results of force control experiments.

2. Robot system

Figure 1 shows the SCARA robot with a force sensor attached to the wrist. Figure 2 shows the four degrees of freedom of the SCARA robot. The force sensor detects the contact forces acting on the end effector in the X , Y , and Z directions and detects the torque around the Z axis.

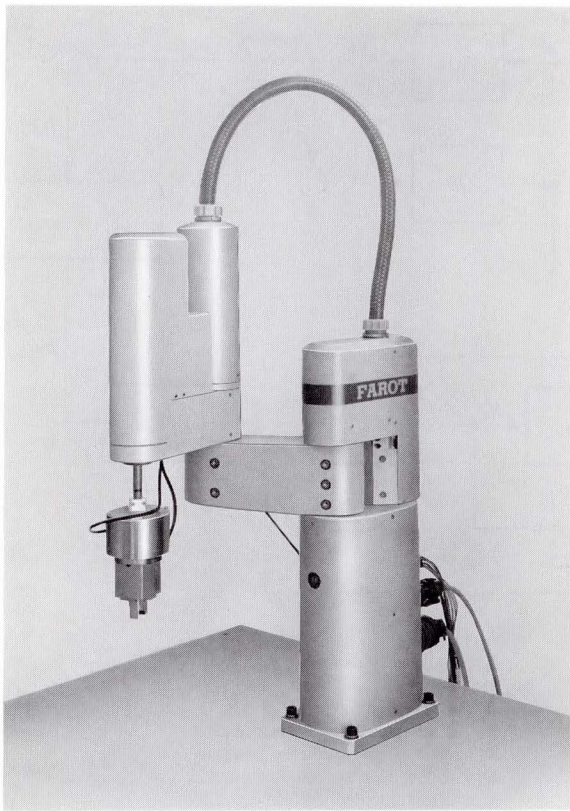


Fig. 1—SCARA robot.

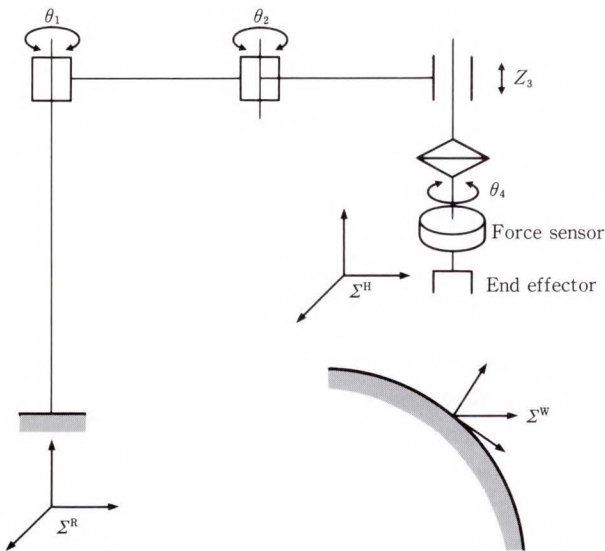


Fig. 2—SCARA robot configuration.

Figure 3 shows the configuration of the digital force and servo controller. The digital controller consists of two Fujitsu MB8764 16-bit fixed-point digital signal processors (DSPs) and an I80286 microprocessor that serves as the host computer. Table 1 lists the

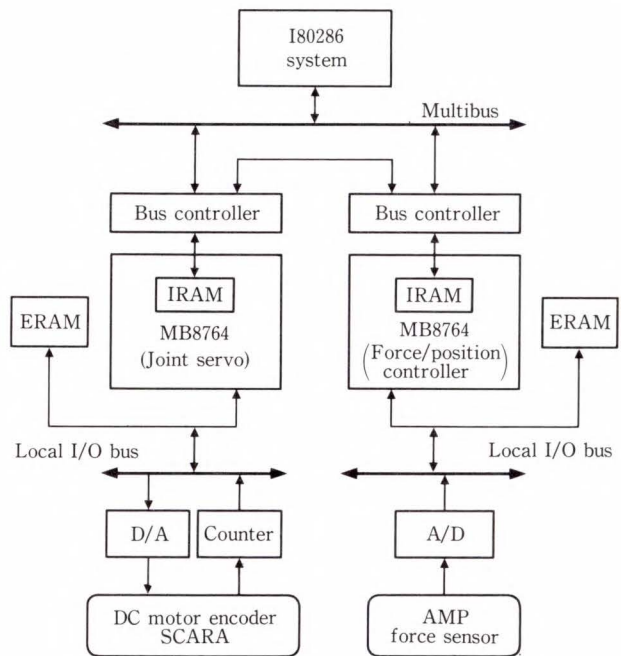


Fig. 3—Robot control system.

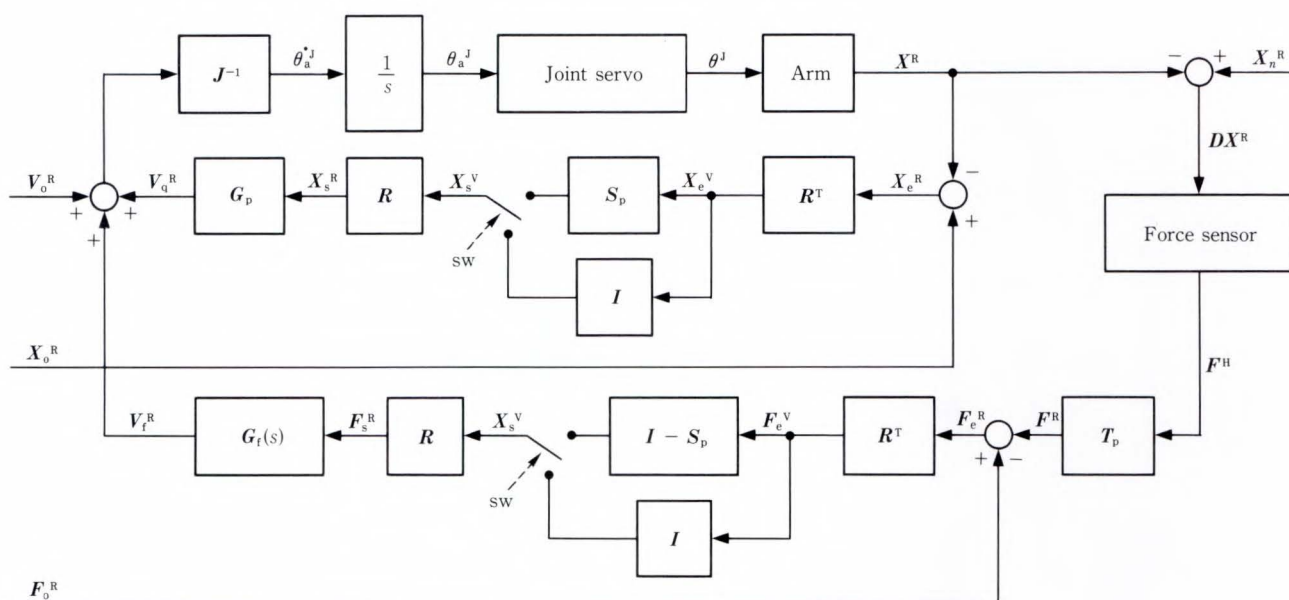
Table 1. MB8764 specifications

Clock rate	20 MHz
Word size (instruction)	24 bits
Word size (data)	16 bits
Multiplier	16 × 16 → 26 bits
Addition time	100 ns
Multiplication time	200 ns
Memory capacity (instruction)	1 Kwords
Memory capacity (IRAM)	256 words
Memory capacity (ERAM)	1 Kwords

MB8764 specifications. Each high-speed DSP is completely independent. Parallel buses transfer data between the DSPs. Data can be asynchronously transferred at 1-2 μ s/word via the IRAM (dual port RAM) built into the DSP.

We used parallel processing to achieve a 1 ms cycle. One DSP handles the joint servo operation and the other handles the other operations.

The host computer is not used in real-time operations. The host transfers coordinate values, parameters, and commands to the two DSPs and manages the teaching data. The host computer communicates with the DSPs asynchronously via the dual port RAM.



- | | |
|---|---|
| <p>Coordinate frames</p> <ul style="list-style-type: none"> Σ^R : Reference coordinate frame Σ^H : End effector coordinate frame Σ^W : Working coordinate frame Σ^J : Joint coordinate frame <p>Superscripts</p> <ul style="list-style-type: none"> R : Quantity measured in Σ^R H : Quantity measured in Σ^H W : Quantity measured in Σ^W J : Quantity measured in Σ^J <p>Control elements</p> <ul style="list-style-type: none"> J^{-1} : Inverse Jacobian T_p, R : Transformation matrices S_p : Compliance selection matrix G_f : Compensator in force feedback G_p : Position feedback gain I : Identity matrix | <p>Control signals</p> <ul style="list-style-type: none"> θ_a^J : Desired joint velocity θ_a^J : Desired joint position θ : Current joint position X : End effector current position X_o : End effector desired position X_e : Difference between X_o and X X_s : Position feedback selected by S_p F : Contact force F_o : Desired contact force F_e : Difference between F_o and F F_s : Force feedback selected by $I - S_p$ X_n : Position of constrained surface |
|---|---|

Fig. 4—Hybrid position/force control.

3. Force control

Figure 4 shows the block diagram of the hybrid position/force control. Since it is hard to control the torque of articulated robots using a conventional speed reduction mechanism, the end effector position and the forces acting on the end effector are fed as velocity feedback to the joint servo.

Either hybrid or compliance control can be used to control the feedback of the end effector position and the force acting on the end effector. The type of control that is used depends on whether the selection matrix S_p is used. In hybrid control, the direction of the end effector trajectory and the direction of force on the end effector is separated into

orthogonal components. For the force components, hybrid control enables the force F^R to follow the target force F_o^R . In compliance control, the direction of the end effector trajectory and the direction of the force are not completely separated. The apparent compliance of the end effector can be actively controlled by changing the position feedback gain matrix G_p and the characteristics of the force compensator $G_f(s)$. In the active compliance control mode, setting G_p , target velocity V_o^R , and target force F_o^R to zero places the robot in the direct teaching state. In this state, the robot moves with any force acting on its end effector.

In any mode, the velocity of the end effector is the sum of the velocity generated

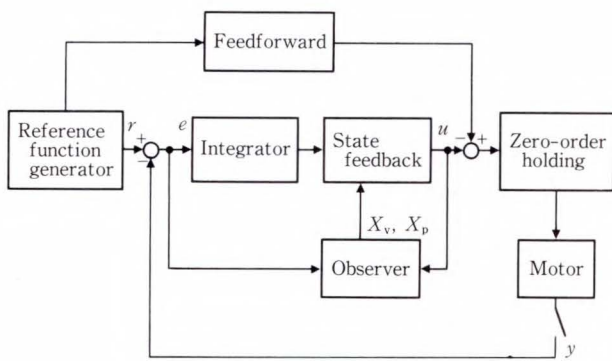


Fig. 5—Servo control.

by the force compensator V_f^R , the velocity generated by the position compensator V_p^R , and the command along the trajectory from the host computer V_o^R . The velocity of the end effector in the orthogonal coordinate is transformed into the joint velocity by the inverse Jacobian matrix J^{-1} .

The joint velocity is sent to the servo control section to control the motors.

4. Servo control

The servo controller was designed using the state-space method and consists of a reference function generator, observer, integrator, and the state feedback. Figure 5 shows the block diagram of the servo controller. The servo controller controls the position and velocity of the joint.

The motor is modeled on the following transfer function because it is driven by a constant current source:

$$G(s) = g/s^2, \dots\dots\dots (1)$$

where g is a constant determined by the motor properties and s is Laplace's operator.

When the velocity X_v and the position X_p of the motor are chosen as the states, Equation (1) can be rewritten as follows:

$$\begin{bmatrix} \dot{X}_v(t) \\ \dot{X}_p(t) \end{bmatrix} = \begin{bmatrix} 0 & 0 \\ 1 & 0 \end{bmatrix} \begin{bmatrix} X_v(t) \\ X_p(t) \end{bmatrix} + \begin{bmatrix} g \\ 0 \end{bmatrix} u(t), \dots\dots\dots (2)$$

where u is the input voltage.

Since Equation (2) is a continuous system, the following discrete state equation is obtained using a zero-order holding of input and sampling

time T .

$$\begin{bmatrix} Z_v(k+1) \\ Z_p(k+1) \end{bmatrix} = \begin{bmatrix} 1 & 0 \\ 1 & 1 \end{bmatrix} \begin{bmatrix} Z_v(k) \\ Z_p(k) \end{bmatrix} + \begin{bmatrix} gT^2 \\ gT^2/2 \end{bmatrix} u(k), \dots\dots\dots (3)$$

where $Z_v = X_v$, $Z_p = X_p$.

We wrote the servo control algorithm using this equation.

The reference function generator receives the velocity command of the joints from the force controller and generates the reference position and reference acceleration signals. The reference acceleration signal α is a feedforward signal which provides the current necessary to accelerate the motor.

The reference position signal r is subtracted from the current position signal of the motor. This error signal drives the feedback loop. The error system decreases the dynamic range of the variable. As a result, we can construct the software control system with little computing error even if a fixed-point processor such as the MB8764 is used.

The observer (also an error system) estimates the velocity and position error signals of the motor to obtain smoother and smaller error signals.

The equation of the observer is given by:

$$\tilde{x}(k) = (A - hcA) \tilde{x}(k-1) + (b - hcb) \times u(k-1) + he(k), \dots\dots\dots (4)$$

where

$$\begin{aligned} \tilde{x} &= [\tilde{X}_v \tilde{X}_p]^T \text{ and is the state to be estimated} \\ h &= [h_1 \ h_2]^T \text{ and is the observer gain} \\ c &= [0 \ 1] \\ A &= \begin{bmatrix} 1 & 0 \\ 1 & 1 \end{bmatrix} \\ b &= [gT^2 \ gT^2/2]^T \\ e &\text{ is the actual position error.} \end{aligned}$$

The observer gain h is determined so that the poles of Equation (4) are those of a second-order Butterworth filter.

An integrator is added to reduce the steady-state positioning error. When the integrator is added, the feedback loop section becomes a third-order system. State feedback control

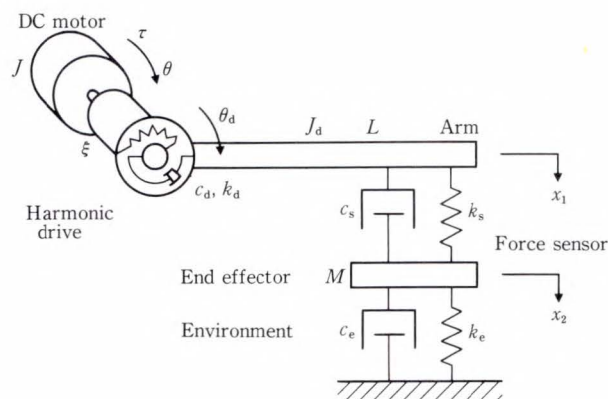


Fig. 6—Arm model with compliant joint.

is performed using three states: the velocity error \tilde{X}_v , the position error \tilde{X}_p , and the integration of the position error X_i . Input to the motor u is determined by the next equation.

$$u(k) = f_1 \tilde{X}_v(k) - f_2 \tilde{X}_p(k) - f_3 X_i(k), \quad (5)$$

where $f = [f_1, f_2, f_3]$ and is the feedback gain. The feedback gain is chosen so that the poles of the feedback loop are those of a third-order Butterworth filter.

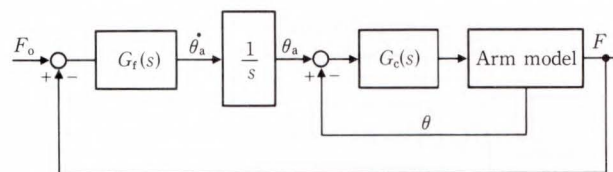
Using these techniques, we constructed a servo controller with a high gain and quick response. As a result, force control can be applied to the articulated robot using speed reduction gears.

5. Force control stability

When the controller shown in Fig. 4 is in the hybrid control mode, the force control sometimes becomes unstable. When analyzing stability (see Fig. 6), we assumed that:

- 1) the robot arm only rotates through θ ,
- 2) the elastic deformation of the speed reduction mechanism (harmonic drive) with θ is approximately linear, and
- 3) the motor, robot arm, force sensors, end effector, and the environment that restricts the end effector are treated as a three-degrees-of-freedom vibration model.

Under these conditions, the model of the mechanism is given by Equation (6).



$$G_f(s) = k_f, \quad G_c(s) = k_i/s + k_p + k_d s$$

$$k_i = \omega^3/g, \quad k_p = 2\omega^2/g, \quad k_d = 2\omega/g$$

($\omega = 2\pi 50$: bandwidth of joint servo)

Fig. 7—Force feedback controller.

$$\tau = J \ddot{\theta} + \{ c_d(z \dot{\theta} - \dot{\theta}_d) + k_d(z \theta - \theta_d) \} z,$$

$$x_1 = L \theta_d,$$

$$J_d \ddot{\theta}_d + \{ c_s(\dot{x}_1 - \dot{x}_2) + k_s(x_1 - x_2) \} L -$$

$$- c_d(z \dot{\theta} - \dot{\theta}_d) - k_d(z \theta - \theta_d) = 0,$$

$$M \ddot{x}_2 + c_e \dot{x}_2 + k_e x_2 + c_s(\dot{x}_2 - \dot{x}_1) +$$

$$+ k_s(x_2 - x_1) = 0, \quad \dots \dots \dots (6)$$

where

- J : moment of inertia of the motor
- J_d : moment of inertia of the arm
- M : mass of the end effector
- c_d : damping of the harmonic drive
- k_d : stiffness of the harmonic drive
- c_s : damping of the force sensor
- k_s : stiffness of the force sensor
- c_e : damping of the environment
- k_e : stiffness of the environment
- θ_d : rotation of the arm
- τ : input torque
- z : inverse of reduction ratio ξ
- L : length of the arm
- x_1 : position of the arm tip
- x_2 : position of the end effector.

The feedback control system including the mechanism represented by this equation is configured as shown in Fig. 7, and the following conditions are set:

- 4) The proportional gain k_f is used as the compensator $G_f(s)$.
- 5) The servo for determining the rotation angle is designed by setting poles in the third-order Butterworth arrangement with a 50 Hz bandwidth.

A closed-loop circuit is formed by adding the joint servo of the motor and the compensator k_f to the mechanism model represented

Table 2. Simulation constants

J	: Motor inertia	$1.68 \times 10^{-4} \text{ kgm}^2$
ξ	: Reduction ratio	78
J_d	: Arm inertia	1.2 kgm^2
L	: Arm length	0.56 m
c_s	: Force sensor damping	116 Ns/m
k_s	: Force sensor stiffness	$1.76 \times 10^5 \text{ N/m}$
M	: Mass of end effector	0.2 kg
c_e	: Environmental damping	100 Ns/m
k_e	: Environmental stiffness	$1.0 \times 10^8 \text{ N/m}$

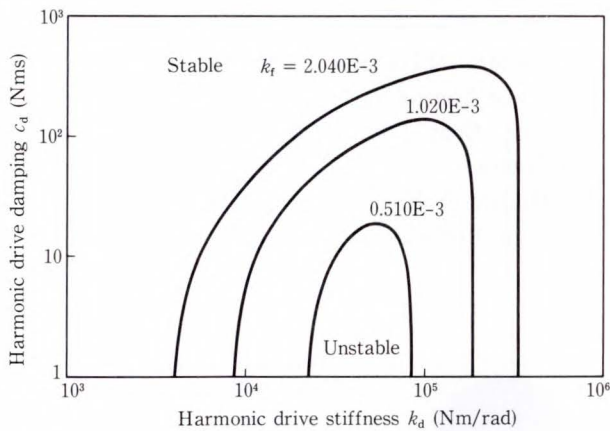


Fig. 8—Stability condition for force feedback gain and harmonic drive stiffness.

by Equation (6).

The characteristic equation of the circuit is given by:

$$D(s) + k_f N(s) = 0, \quad \dots \dots \dots (7)$$

where

$$\begin{aligned}
 N(s) &= J\omega(2s^2 + 2\omega s + \omega^2)(c_d s + k_d) \times \\
 &\quad \times (c_s s + k_s)(Ms^2 + c_e s + k_e), \\
 D(s) &= s [J(s^3 + 2\omega s^2 + 2\omega^2 + \omega^3) \times \\
 &\quad \times \{ (J_d s + c_d s + k_d) \times \\
 &\quad \times (Ms^2 + (c_s + c_e)s + k_s + k_e) + \\
 &\quad + L^2(c_s s + k_s)(Ms^2 + c_e s + k_e) \} + \\
 &\quad + z^2 s(c_d s + k_d) \\
 &\quad \{ (J_d s^2 + L^2 c_s s + L^2 k_s) \times \\
 &\quad \times (Ms^2 + c_e s + k_e) + \\
 &\quad + J_d s^2(c_s s + k_s) \}],
 \end{aligned}$$

$\omega = 2\pi 50$: bandwidth of the joint servo.

We considered the case in which some of the parameters in Equation (7) are fixed (see Table 2). By applying the Routh-Hurwitz

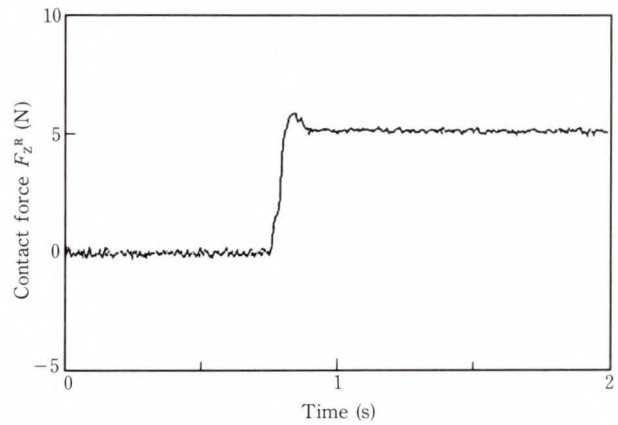


Fig. 9—End effector response to 5 N force step.

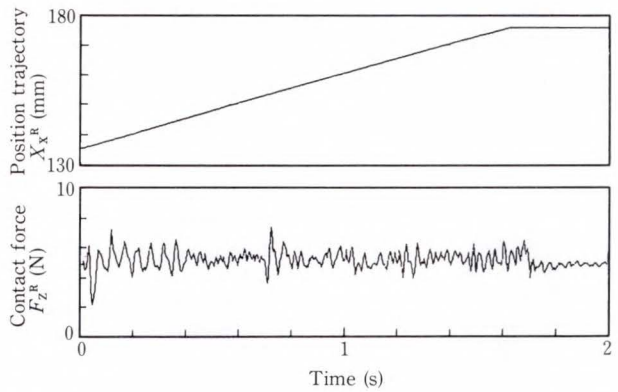


Fig. 10—End effector contact force under hybrid control.

criterion to Equation (7), the stability condition for speed reducer stiffness k_d , the speed reducer damping c_d , and the force feedback gain k_f can be obtained (see Fig. 8). These conditions reveal that there is a stability limit.

6. Experimental investigation

Stability analysis of the force feedback control system has shown that if the mechanism between the motor and force sensor is not rigid, the system is stable only when the force feedback gain is small. This applies to the four-degrees-of-freedom arm of a SCARA robot. Analysis has also shown that a compensator $G_f(s)$ consisting of a PID can only slightly improve stability. We achieved stable force control by setting the gain of the compensator of the hybrid controller (see Fig. 4) to a reasonably small value.

Figure 9 shows the step response of the load F_z^R when the desired force F_{oz}^R is 5 N and is

applied in the negative Z direction to a horizontal aluminum base. Figure 10 shows how load F_z^R follows force F_{oz}^R when the end effector is moved at 25 mm/s in the X direction. These figures show satisfactory results. The slight disturbance in the follow-up (see Fig. 10) may be due to interference between the horizontal and vertical directions of the SCARA arm.

7. Conclusion

We have developed an active force controller to improve the assembly capability of SCARA robots. The controller uses a position/force feedback loop outside the joint servo and is implemented using two Fujitsu MB8764 DSPs in parallel processing. Compliance or hybrid

control worked well with a 1 kHz sampling rate. We analyzed the stability of the force control for joints having a non-rigid arm. The force control can be stabilized by keeping the force feedback gain reasonably small and by using a high sampling rate.

References

- 1) Whitney, D.E.: Force Feedback Control of Manipulator Fine Motions. *ASME J. Dynamic Syst., Meas., Control.*, **98**, pp. 91-97 (1977).
- 2) Raibert, M.H., and Craig, J.J.: Hybrid Position/Force Control of Manipulators. *ASME J. Dynamic Syst., Meas., Control.*, **102**, pp. 126-133 (1981).
- 3) Eppinger, S.D., and Seering, W.P.: On Dynamic Models of Robot Force Control. Proc. IEEE Int. Conf. Robotics Auto., 1986, pp. 29-34.



Yutaka Yoshida

Sensing Technology and Robotics
Laboratory
FUJITSU LABORATORIES, ATSUGI
Bachelor of Mechanical Eng.
Kyoto Institute of Technology 1979
Master of Mechanical Eng.
Kyoto University 1981
Specializing in Control of Robot
Manipulators



Yasuyuki Nakata

Sensing Technology and Robotics
Laboratory
FUJITSU LABORATORIES, ATSUGI
Bachelor of Physical Eng.
Tokyo Institute of Technology 1985
Master of Physical Eng.
Tokyo Institute of Technology 1987
Specializing in Control of Robot
Manipulators



Akihiko Yabuki

Sensing Technology and Robotics
Laboratory
FUJITSU LABORATORIES, ATSUGI
Bachelor of Mechanical Eng.
Doshisha University 1983
Master of Mechanical Eng.
Osaka University 1985
Specializing in Sensors and
Mechanisms of Robots

UDC681.3.06:681.51

Simulator for a Coordinated Two-Arm Robot

• Hiroshi Wada • Mitsuo Kamimura • Sadao Fujii

(Manuscript received January 23, 1990)

Fujitsu is developing a general-purpose assembly robot consisting of two coordinated multi-jointed arms modeled on their human counterpart. Fujitsu is also developing software to deal with assembly problems such as the layout of work, assembly procedures, and path generation; and to deal with operation problems such as representation and implementation of coordinated operation. The robot language TACL: Two Arm Cooperation Language and simulator for the robot was developed to help solve these problems. A task-level robot language ASL: Assembly Sequence Language and a method of generating TACL from ASL have also been developed. This paper describes TACL, the simulator, ASL, and how TACL is generated.

1. Introduction

One arm of the coordinated two-arm robot manipulates an object while the other acts as a jig for support. The arms perform coordinated actions such as assembling or transferring parts and transporting cables and paper without slack. The coordinated two-arm robot performs complex and detailed operations which, up to now, could only be done by humans. This robot eliminates the need to arrange and position mechanisms.

The coordinated two-arm robot presents special problems, for example: how the coordinated operations of the arms can be described, how jobs can be shared between the arms, how the arms can be positioned, how they can be prevented from interfering with each other, and how the teaching time required for complex jobs can be reduced.

To deal with these problems, we developed the robot language TACL; Two-Arm Cooperation Language. TACL describes the parallel and synchronized operations of the two arms as a sequence of hand positions. TACL was developed on a simulator¹⁾ that enables us to check the operations described in TACL. The

coordinated two-arm program was written in SIGLA²⁾, MAL³⁾, AL⁴⁾, and other robot languages. In these languages, only one arm movement is defined in each statement, and each statement is sequentially described. This makes it difficult for the programmer to understand arm coordination. TACL overcomes this difficulty because it defines the movements of both arms on the same statement line. This makes it easier for programmers to define and conceptualize arm coordination.

Because it is very difficult to program the hand positions required for complex work, we developed a new robot language ASL (Assembly Sequence Language). This language describes the work to be done by robots as changes in the status of the assembled objects. We then developed a way to generate TACL from assembly data groups including the ASL (see section 3.1). The generation method we developed enables the robot language programmer to define the task-level language and translate it into a motion-level language.

This paper briefly describes TACL and the assembly data groups including ASL. It then describes the generation of TACL from

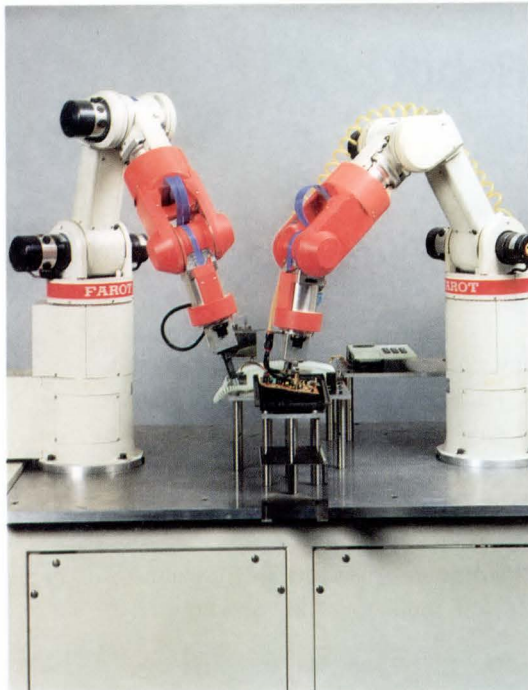


Fig. 1—Coordinated two-arm robot.

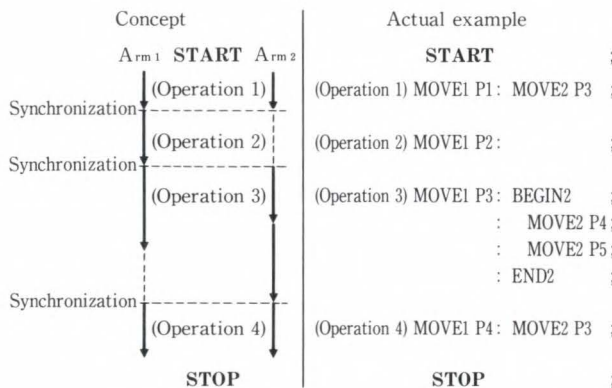


Fig. 2—Concept and example of TACL.

ASL and the verification of TACL by operation simulation using a solid model.

2. Two-Arm Coordinated Robot Language: TACL

The TACL for the coordinated two-arm robot shown in Fig. 1 is described first.

In a conventional language for a single-arm robot, some of the hand positions are defined in three-dimensions. Then, the moving procedures and how the robot hand should move

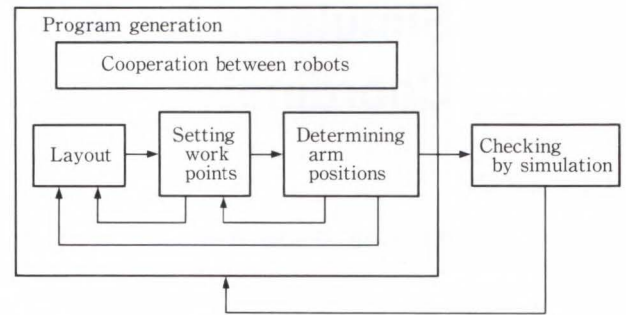


Fig. 3—Programming.

between the positions are described. In TACL, the movements of both arms are described on the same statement line and the arms are synchronized to enable cooperation and work-sharing between the arms. Each move command is synchronized. To synchronize complicated motions, several commands can be combined into one group command using the BEGIN and END statements.

For example (see Fig. 2), if commands for arm 1 and arm 2 are described on the same line, they are executed simultaneously and the commands on the next line are not executed until they terminate. The commands between BEGIN and END are regarded as being on the same line.

3. Assembly data

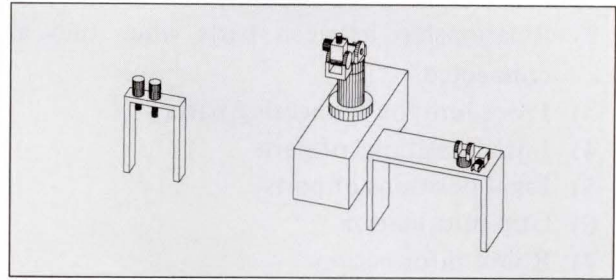
The procedure for manual generation of TACL is as follows (see Fig. 3):

- 1) Determine the layout of the robot and environment, placing stress on operational efficiency
- 2) Define the work points considering the positions of the robot and items in the environment
- 3) Determine how the robot should move to the work points by taking other robots locations and the environment into consideration
- 4) Determine the movement procedures and how the robot hand should move between work points. Also, describe the coordination of the arms.

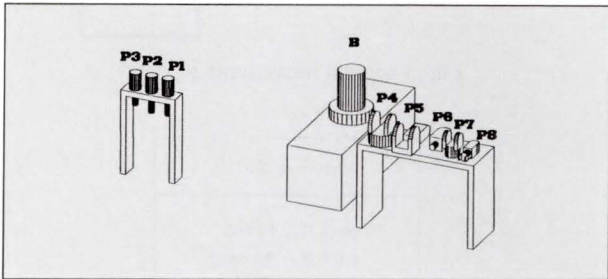
Analysis of the above procedures reveals that data for the following seven factors is required to generate TACL:

FIX part-B
 part-P4 + part-B
 part-P5 + part-P4 (IF part-P4 + part-B)
 part-P6 + part-P5 (IF part-P5 + part-P4)
 part-P7 + part-P6 (IF part-P6 + part-P5)
 part-P8 + part-P7 (IF part-P7 + part-P6)
 part-P1 + part-P4 (FOR part-P5 + part-P4)
 part-P2 + part-P5 (FOR part-P6 + part-P5)
 part-P3 + part-P7 (FOR part-P8 + part-P7)

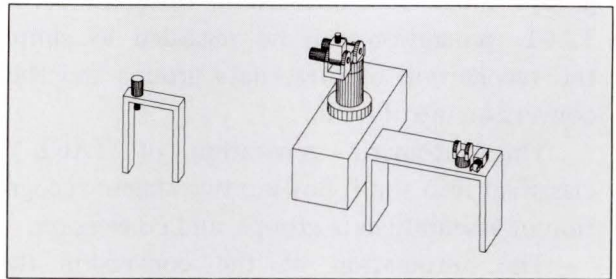
a) ASL



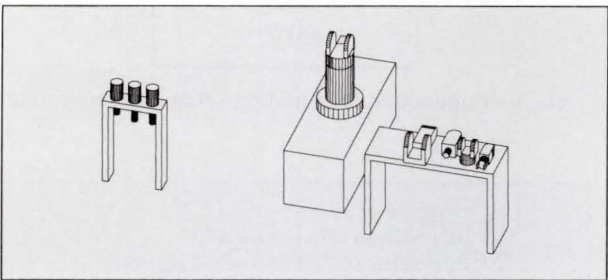
f) After excuting part-p6 + part-p5



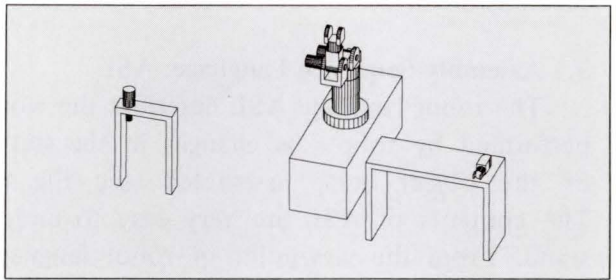
b) Initial status



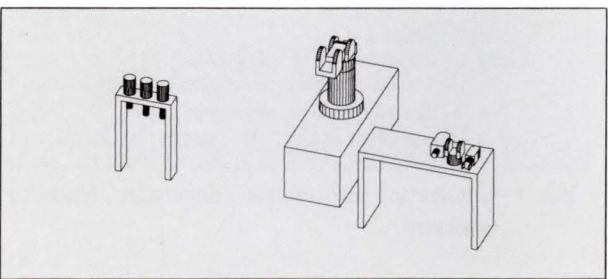
g) After excuting part-p2 + part-p5



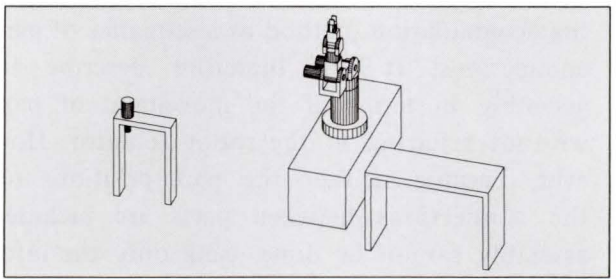
c) After excuting part-p4 + part-B



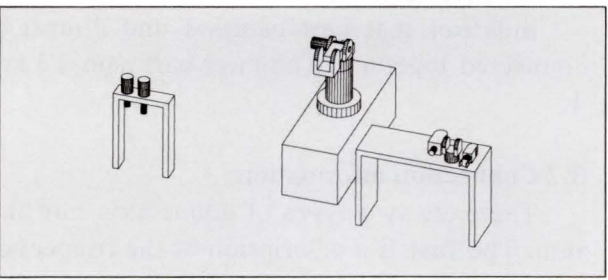
h) After excuting part-p7 + part-p6



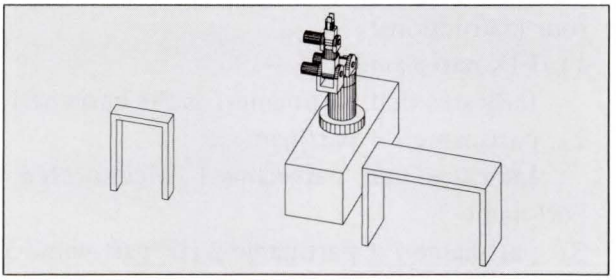
d) After excuting part-p5 + part-p4



i) After excuting part-p8 + part-p7



e) After excuting part-p1 + part-p4



j) After excuting part-p3 + part-p7

Fig. 4—Descriptions of assembly of a miniature robot in ASL.

- 1) Parts required for assembly
- 2) Relationship between parts when they are connected
- 3) Procedure for connecting parts
- 4) Initial positions of parts
- 5) Final positions of parts
- 6) Grip information
- 7) Robot information.

Therefore, to generate TACL, the data groups must be expressed in different forms. TACL generation can be regarded as simply the recognition of these data groups and their conversion into TACL.

The automatic generation of TACL is classified into the following two stages: recognition of assembly data groups, and conversion.

The automation of the conversion that produces TACL from assembly data groups is described below.

3.1 Assembly Sequence Language: ASL

The robot language ASL describes the work performed by robots as changes in the status of the object being assembled (see Fig. 4). The contents of ASL are very easy to understand. From the viewpoint of robot language levels, ASL is equivalent to a task language. ASL describes the assembly procedure of the accumulation method as a sequence of parts connections. It can therefore describe the assembly in terms of the movement of parts without referring to the robot actuator. However, because neither the part positions nor the connections between parts are included, assembly cannot be done using only the information provided by this language.

This language consists of the following four instructions:

- 1) FIX part-name-1
Indicates that part-name-1 is the basic part.
- 2) part-name-1 + part-name-2
Indicates that part-name-1 is connected to part-name-2.
- 3) part-name-1 + part-name-2 (IF part-name-3 + part-name-4)
Indicates that connection of part names 1 and 2 starts after connection of part names 3 and 4 ends.

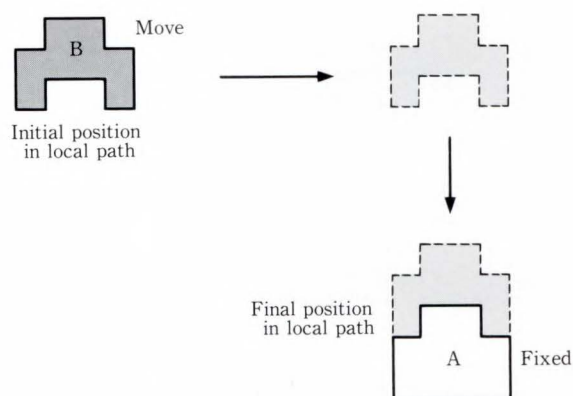


Fig. 5—Local movement of parts.

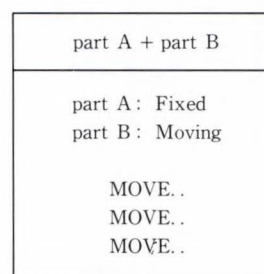


Fig. 6—Connection information related to movement.

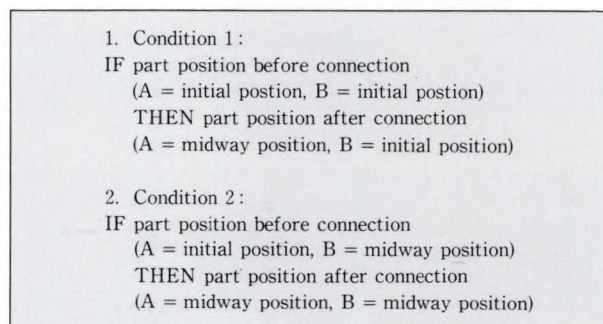


Fig. 7—Connection information concerning change of positions.

- 4) part-name-1 + part-name-2 (FOR part-name-3 + part-name-4)

Indicates that part names 1 and 2 must be connected together to connect part names 3 and 4.

3.2 Connection information

There are two types of connection information. The first is a description of the connection or separation of two parts using the coordinate system of one of the parts. This type applies when the parts are already close together (see Figs. 5 and 6). The second type includes the

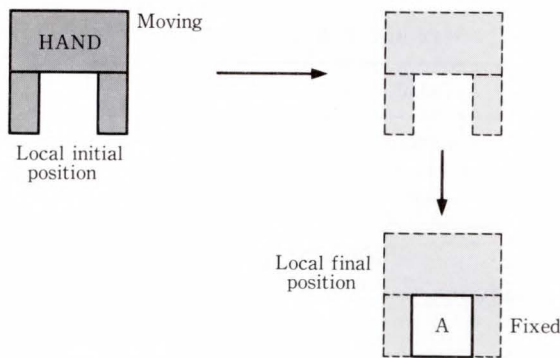


Fig. 8—Local movement of the HAND.

How to grasp part A	
	MOVE..
	MOVE..
	MOVE..
	CLOSE

Fig. 9—Information on how to grasp the part.

	MAIN MOTION	SUB MOTION
1	part P4 + part B	—
2	part P5 + part P4	part P1 + part P4
3	part P6 + part P5	part P2 + part P5
4	part P7 + part P6	—
5	part P8 + part P7	part P3 + part P7

Fig. 10—Example of a connection sequence.

information related to positions of parts from the beginning to the end of connection (see Fig. 7).

3.3 Initial status

Initial positions of parts before assembly and initial connection status.

3.4 Final status

Final positions of parts after assembly.

3.5 Grip information

Parts must be held in the proper way to prevent damage and to prevent them from being dropped. Although it is not done at the moment, the grip information may also describe

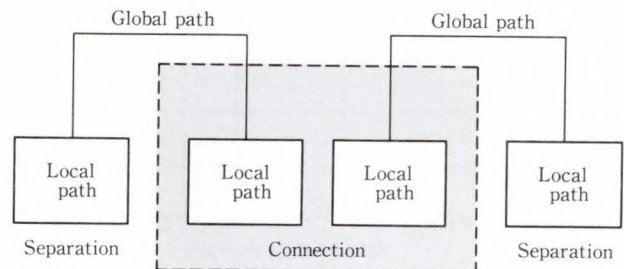


Fig. 11—Global and local paths.

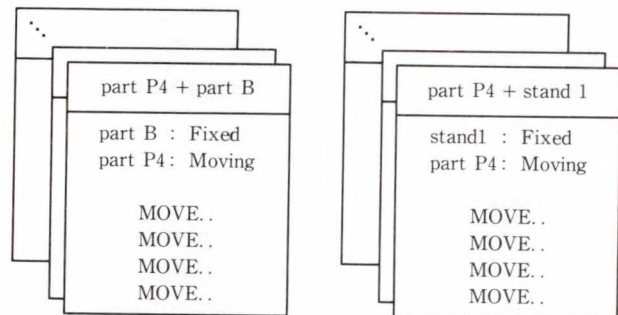


Fig. 12—Local path extracted from connection information.

jigs. Also included in the grip information are instructions on how to grasp the part; that is, how the robot hand makes a local approach to a part in the coordinate system of the subject (see Figs. 8 and 9).

3.6 Robot information

This information includes the robot type, joint length, joint movement range, joint speed, and robot location.

4. TACL generation

This chapter describes the generation of TACL from assembly data groups (ASL, connection information, initial status, final status, grip information, and robot information).

4.1 Procedure 1

The names of the parts required for the assembly and the connection sequence are extracted from the ASL. Figure 10 gives the connection sequence obtained from the ASL in Fig. 4. The parts connections under MAIN MOTION are executed in the order shown in Fig. 10. The SUB MOTION connection is required for the MAIN MOTION connection.

(FIX B)	B	P1	P2	P3	...
Initial	—	○	○	○	○
Midway	—	—	—	—	—
Final	○	—	—	—	—

Status before assembly

Midway status

→

(FIX B)	B	P1	P2	P3	...
Initial	—	—	—	—	—
Midway	—	—	—	—	—
Final	○	○	○	○	○

Status after assembly

Fig. 13—Control of part positions.

4.2 Procedure 2

The local path is extracted from the connection information to separate the connected parts and connect one of them to another part (see Figs. 11 and 12).

4.3 Procedure 3

Because the local path obtained in procedure 2 is defined with respect to the coordinate system of one of the parts, it must be converted to world coordinates. Assuming that the matrix indicating the local path in the world coordinate system is P^W , the matrix indicating the part position in the world coordinate system is POS^W . Also, the matrix indicating the local path in the part coordinate system is P^B .

P^W is obtained using the following equation:
 $P^W = POS^W * P^B$.

Therefore, the positions of parts must be controlled throughout assembly (see Fig. 13). Information about the initial and final positions of parts is required for this procedure.

The positions of two parts that are connected together are determined from the positions of the parts before connection and the condition group described in the connection information. For example, if the positions before connection for “part A + part B” are (part A = initial position, part B = initial position), one of the three positions below can be selected as the part positions after connection.

This selection can be made using connection information concerning changes in position:

- (part A = initial position, part B = midway position)
- (part A = midway position, part B = initial position)
- (part A = midway position, part B = midway position).

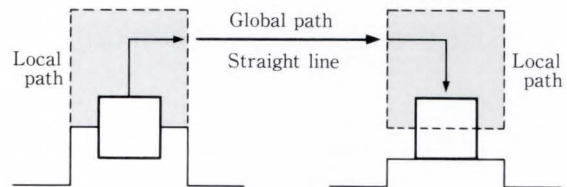


Fig. 14—Generation of the global path.

	MAIN MOTION	SUB MOTION
1	EX 1	—
2	EX 2	EX 6
3	EX 3	EX 7
4	EX 4	—
5	EX 5	EX 8

Fig. 15—Part connection job.

If one of the two connected parts is at the initial or final position, the other part will be positioned relative to it.

4.4 Procedure 4

The global path used to connect each part is obtained. (At present, an almost straight line is used, see Fig. 14.)

4.5 Procedure 5

Job scheduling is performed with on the assumption that one parts connection equals one job. Jobs are then assigned to robots.

4.5.1 Rules for job scheduling

- 1) Jobs in the MAIN MOTION must be executed sequentially without overlap. There can be a wait status between jobs (see Fig. 15).
- 2) The SUB MOTION connection is required

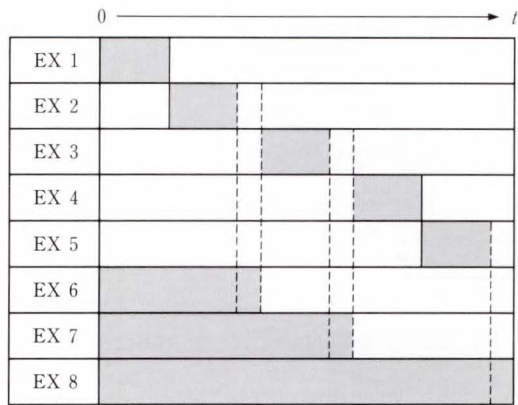


Fig. 16—Job scheduling.

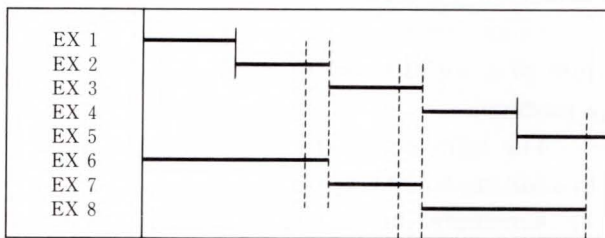


Fig. 17—Robot job assignment.

for the MAIN MOTION connection. The end of a job in MAIN MOTION is synchronized with the end of the global move of the associated job in SUB MOTION. This causes the job in MAIN MOTION to wait until the local move is executed in SUB MOTION. When the job in SUB MOTION ends, the next job in MAIN MOTION starts.

- 3) All SUB MOTION jobs can be started at the same time and can run in parallel.

Figure 16 is an example of a job schedule. The broken lines are synchronization lines.

4.5.2 Rules for job assignment to robots

- 1) If a job is assigned to a robot, the job is not released until the job ends. If a wait follows the assigned job, the job is not released until the wait ends.
- 2) If two parts are to be moved for a connection, two robots are assigned. If one part is to be moved, one robot is assigned.
- 3) Job assignment must ensure that all jobs are properly executed.

Figure 17 shows the job assignment based on Fig. 16. Only one robot is assigned to each job. The broken line indicates the synchronization line.

robot 1	robot 2
EX 1	EX 6
WAITING	
EX 2	EX 7
WAITING	
EX 3	EX 8
WAITING	
EX 4	
EX 5	
WAITING	

Fig. 18—Job assigned to each robot.

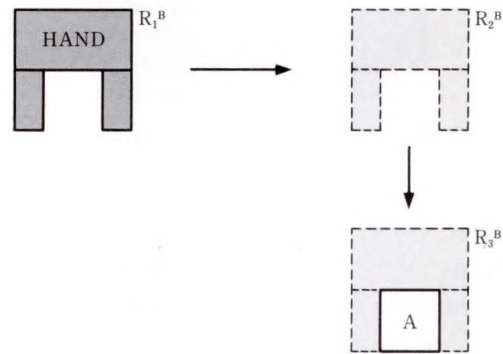


Fig. 19—How to hold the part.

4.6 Procedure 6

Jobs are assigned to robots 1 and 2 (see Fig. 18).

Rules for job assignment to each robot are as follows:

- 1) If a job is assigned to a robot, the job is not released until the job ends. If a wait follows the assigned job, the job is not released until the wait ends.
- 2) The robot must be able to operate in the assigned positions.
- 3) Job assignment must ensure that all jobs are properly executed.

4.7 Procedure 7

TACL is generated. The jobs in Fig. 18 are converted into descriptions of robot hand positions.

When the robot hand positions in parts coordinates are indicated by R_1^B (see Fig. 19), and the part positions in world coordinates are

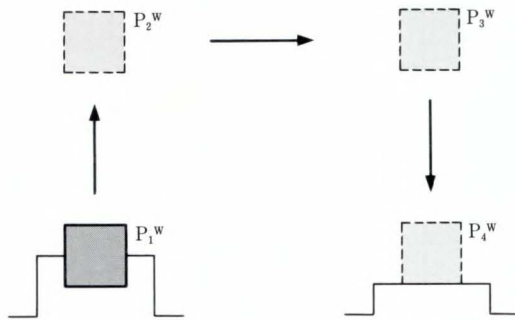


Fig. 20—Moving the part. 1

MOVE	$P_1^W * R_1^B$
MOVE	$P_1^W * R_2^B$
MOVE	$P_1^W * R_3^B$
CLOSE	
MOVE	$P_2^W * R_3^B$
MOVE	$P_3^W * R_3^B$
MOVE	$P_4^W * R_3^B$

Fig. 21—Part of the generated TACL.

indicated by P_1^W (see Fig. 20), the robot hand positions R_1^W in world coordinates can be obtained using the following expression⁵⁾:

$$R_1^W = P_1^W * R_1^B,$$

P_1^W was already obtained in procedures 3 and 4, and R_1^B can be obtained from the grip information. Figure 21 shows part of a TACL program that was generated under the conditions shown in Figs. 19 and 20.

5. Verifying TACL

When the automatically generated TACL is used directly to control the two-arm robot, the TACL program may be incomplete and the robots or a robot and the work, may interfere with or collide with each other. These problems are virtually impossible to prevent, since current robots do not have advanced recognition and judgment ability.

Therefore, it is necessary to check the generated TACL. An effective way of checking the operation is to model robots and their operating environment on a computer and run an assembly animation on the display. Several models can express three-dimensional objects, but the best, from the viewpoints of clarity, interference checks, and recent advances in displays, is the solid model.

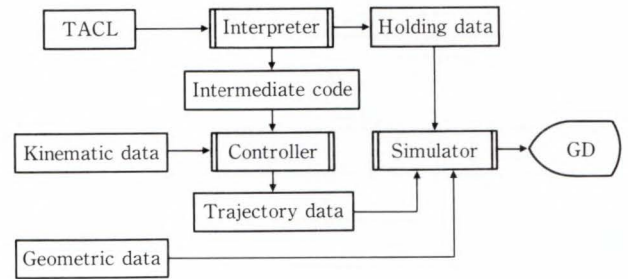


Fig. 22—Coordinated two-arm robot simulator.

Figure 22 shows the configuration of an operation simulation that verifies TACL using modeling. Figure 23 shows parts of an animation of a coordinated two-arm robot assembling a terminal.

The following two kinds of data are required in addition to TACL:

1) Kinematic data

Data concerning the mechanisms; for example, the type, joint ranges, and speed of the robot.

2) Geometric data

Geometric data of the robot and environment as defined in the CSG-type solid model. {We are using the technical information processing system (TIPS)⁶⁾ as the solid modeler.}

Simulation involves the following three processing blocks:

1) Interpreter

Converts the input TACL to intermediate code and holding data.

2) Controller

Converts the intermediate code and kinematic data to robot movement (trajectory) joint data.

3) Simulator

Uses the geometric data, holding data, and joint movement data to display a three-dimensional solid model.

6. Conclusion

This document briefly described TACL and assembly data groups including ASL. It then described how TACL is generated from assembly data groups and how the operation of a robot described in TACL is checked using solid-model animation.

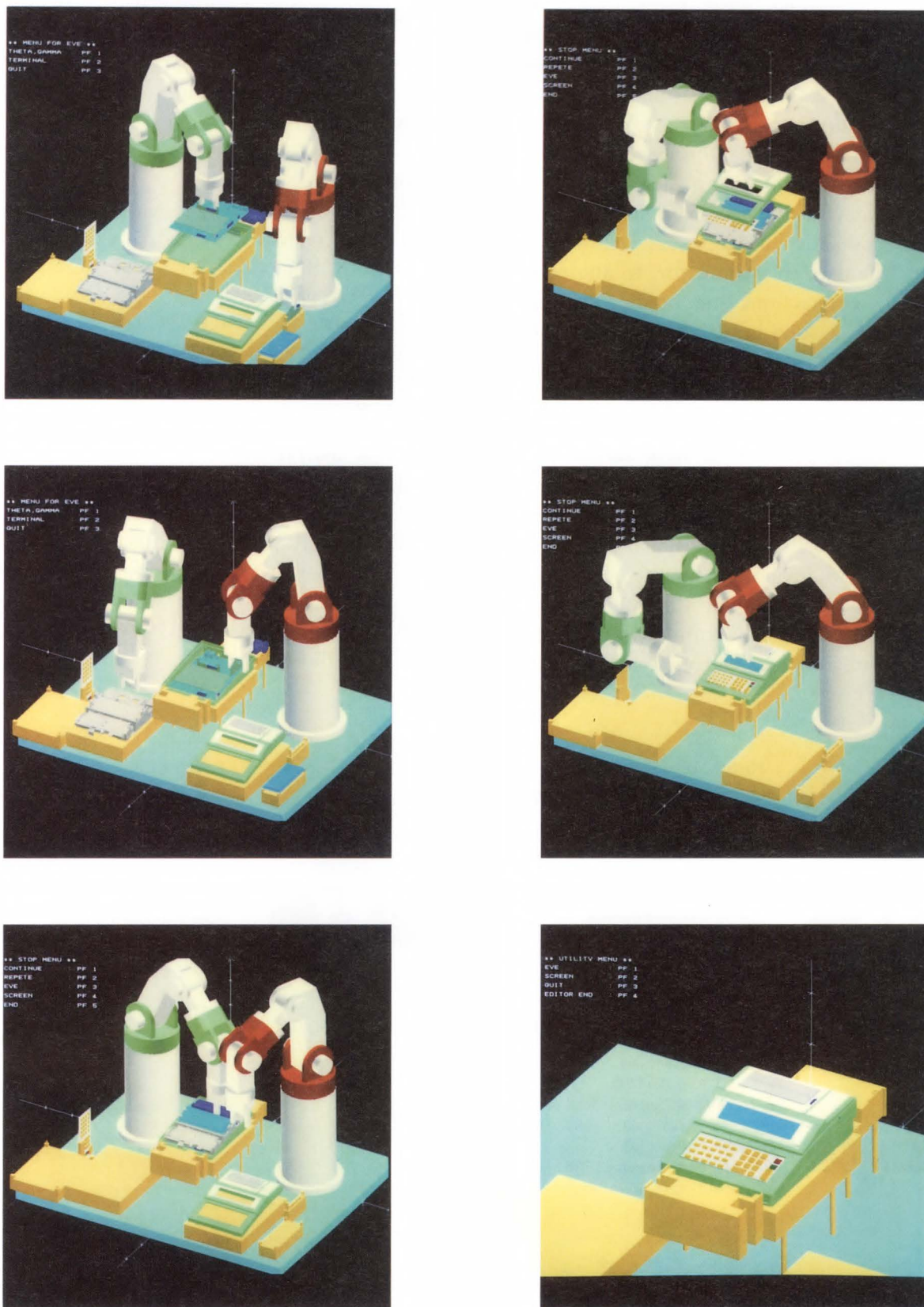


Fig. 23—Animations of the coordinated two-arm robot assembling a terminal.

By developing these technologies, several solutions have been found for problems unique to coordinated two-arm robots, for example, how to express the coordination of two arms.

We now need to make the coordinated two-arm robot easier to use. Future research will aim to develop technologies to achieve the following: to detect data concerning parts layout (parts positions) using visual sensors and to input this data to a simulator, to automatically calculate connections and holding methods of parts using a solid model, and to automatically generate an assembly procedure (ASL) by extracting data related to the assembly structure from assembly drawings produced using CAD.

A major problem is how to compensate for differences between the real world and the computer simulation. These differences are inevitable because of installation errors in the work and robot, parameter errors in the robot, and distortion of the robot body due to work loads. For accurate work that only permits micro-meter errors, we believe that

a touch sensor is more effective than a visual sensor. This is how a human checks the orientation of an object in darkness. We are making every effort to develop robots that have this ability.

References

- 1) WADA, H.: Teaching System for Coordinated Two-Arm Controller. Proc. Int. Sympo. Expos. Robots, Jarvis, R.A., ed., Sydney, Aust. Robot Assoc. Inc., 1988, pp. 983-997.
- 2) Salmon, M.: SIGLA-The Olivetti SIGMA robot programming language. Proc. 8th ISIR., 1978, pp. 358-363.
- 3) Gini, G., et al.: Introducing software system in industrial robots. Proc. 9th ISIR., 1979, pp. 309-321.
- 4) Mujtaba, S., et al.: AL User's Manual. 1st ed., U.S.A., Stanford A. I. Lab., 1979.
- 5) Paul, R.P.: 1. HOMOGENEOUS TRANSFORMATIONS. Robot Manipulators, 1st ed., England, The MIT Press, 1981, pp. 9-40.
- 6) Kinoshita, M. et al.: TIPS-1 '84. 1st ed., Jpn. TIPS working group, 1985, 470p.



Hiroshi Wada

Corporate Production Eng. Group
Production Technology
Development Div.
FUJITSU LIMITED
Bachelor of Precision Machinery
The University of Tokyo 1985
Specializing in Robotics



Sadao Fujii

Corporate Production Eng. Group
Production Technology
Development Div.
FUJITSU LIMITED
Bachelor of Precision Eng.
Hokkaido University 1968
Specializing in Computer Aided Design
Engineering



Mitsuo Kamimura

Corporate Production Eng. Group
Production Technology
Development Div.
FUJITSU LIMITED
Bachelor of Precision Eng.
Hokkaido University 1984
Master of Precision
Hokkaido University 1986
Specializing in Robotics

A Logic State Measurement Technique Using Multi-Stroboscopic Sampling for the Electron Beam Tester

• Akio Ito • Kazuo Okubo • Akifumi Muto

(Manuscript received December 21, 1989)

A multi-stroboscopic sampling (MSS) technique was devised for electron beam tester logic state measurement. In this technique, electron beam pulses are shot and secondary electron signals are sampled m times in each cycle of LSI device operation. In addition, s-curve interpolation (SCI) is combined with MSS for quantitative voltage measurement. Using this combination, the measurement time required for 1 024 logic states was reduced to 1/70 the time required for stroboscopic waveform measurement.

1. Introduction

The electron beam tester is widely used for design verification and failure analysis of LSI devices. Stroboscopic waveform measurement has proven to be a valuable tool for analyzing and localizing LSI memory device failures.

However, stroboscopic waveform measurement is impractical for LSI logic device testing because the low test signal repetition rates make the measurement time prohibitively long¹⁾.

A multi-sampling method was developed²⁾ that reduced the measurement time by a factor of two for signals with low repetition rates by using two multiplexed sampling units. These units are alternately gated by a delay unit. However, this method does not significantly reduce the overall measurement time because only a few units can be sampled at a time and the sample rate (controlled by the delay unit) is limited to about 20 ms.

To overcome these limitations, we have developed a new logic state measurement technique which uses multi-stroboscopic sampling (MSS) and s-curve interpolation (SCI). In MSS, the sampling is synchronized to the clock of the LSI logic device. There are a large number of logic states, and therefore clock

cycles, in a test cycle. However, the sampled digital data for each test cycle is accumulated in a buffer memory and therefore the number of states that can be simultaneously sampled is unlimited. When combined with MSS, SCI enables quantitative voltage measurement at each logic state.

2. Stroboscopic waveform measurement

Figure 1 shows the principle of stroboscopic waveform measurement³⁾ using an electron beam (EB). For quantitative measurement of the voltage V_S applied to the electrodes of the LSI device, the energy of the emitted secondary electron (SE) is analyzed by measuring the retarding voltage V_R using a retarding field energy analyzer. The energy distribution curve obtained by scanning the retarding voltage (the so-called s-curve) undergoes a linear shift when the electrode voltage is varied. Therefore, we can obtain V_{SO} from the shift in the s-curve. This shift is obtained by measuring the variation in the retarding voltage that keeps the detected SE signal constant. This is quantitative voltage measurement using feedback.

In addition, stroboscopic sampling is used to measure the waveform of an electrode at a high

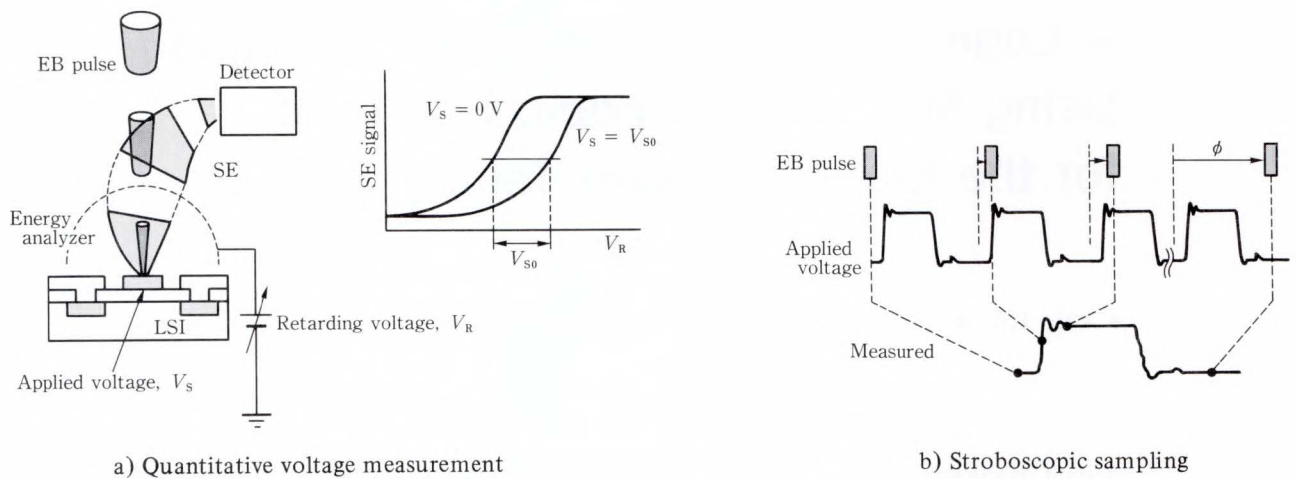


Fig. 1—Principle of stroboscopic waveform measurement.

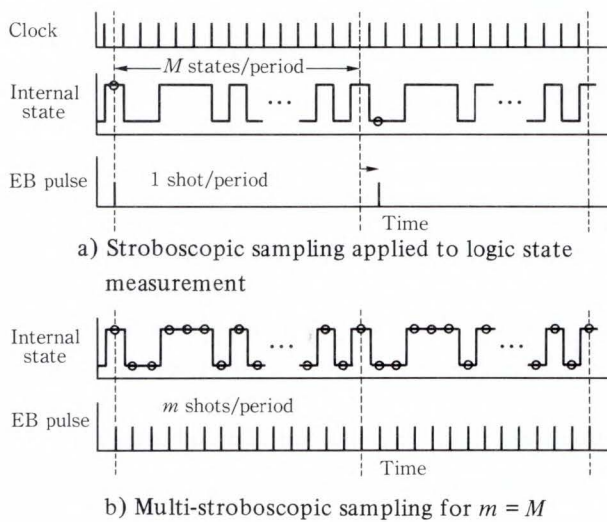


Fig. 2—Multi-stroboscopic sampling (MSS).

time-resolution. Short electron beam pulses are applied to the electrode at the same repetition rate as the electrode signal to be measured. The secondary electrons emitted when these pulses are applied are detected and sampled. SEs are sampled by altering the timing of the electron beam pulse relative to the signal. In this way, the entire waveform is obtained.

3. Multi-stroboscopic sampling (MSS)

To perform an operation, LSI logic devices move through numerous logic states and therefore require a large number of clock cycles. When an LSI logic device is tested by stroboscopic waveform measurement as shown in

Fig. 2 a), the test cycle has a period equal to the number of clock cycles required for the operation and is therefore very long. The stroboscopic sampling measurement time is as follows:

$$T_S = k_1 M^2 / f_c, \dots \dots \dots (1)$$

where k_1 is a factor for signal averaging and quantitative voltage measurement (typically⁴ $k_1 = 2\,300$), M is the number of logic states in one test cycle, and f_c is the clock rate. Since T_S is proportional to the square of M , if $M = 1\,000$ and $f_c = 1\text{ MHz}$, T_S is $2\,300\text{ s}$ and is therefore far too high {see Fig. 2a)}.

Figure 2b) shows the principle of MSS. Electron beam (EB) pulses synchronized to the device clock are shot and SE signals are sampled m times in each test cycle. If the clock rate is above the maximum sampling rate, it must be a multiple of the sampling rate. In this case, the multi-stroboscopic sampling number m is as follows:

$$m = M/N, (N = 1, 2, 3, \dots), \dots \dots (2)$$

where N is the ratio of the clock rate f_c to the sampling rate f_s . Therefore, in MSS, the measurement time T_M' of the SE signals corresponding to the logic states can be expressed as follows:

$$T_M' = k_2' NM / f_c = k_2' M^2 / (mf_c), \dots (3)$$

where k_2' is a factor for signal averaging only. If

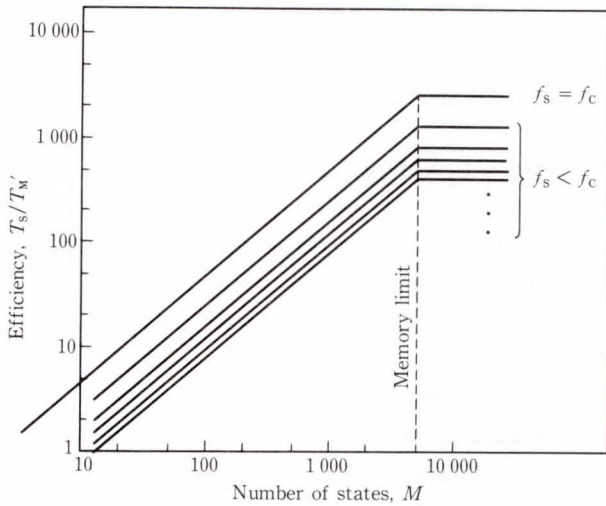


Fig. 3—Estimated efficiency T_s/T_M' of MSS for the number of logic states M in a test cycle.

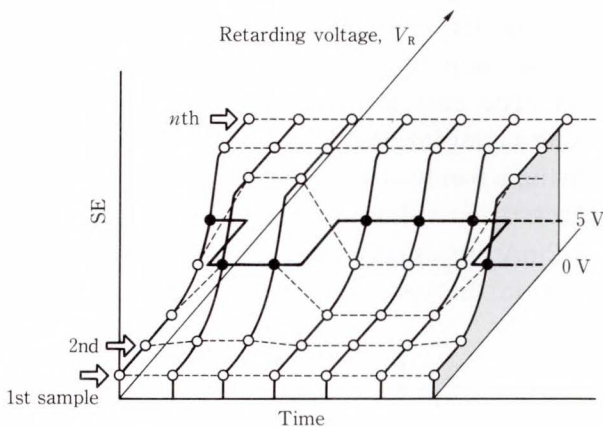


Fig. 4—Principle of s-curve interpolation (SCI) of MSS data.

k_2' is comparable to k_1 , the measurement time T_M can be reduced to about $1/m$ the time required for conventional stroboscopic sampling { see Equations (1) and (3) }. Figure 3 shows the efficiency of the MSS technique T_s/T_M' as a function of the number of logic states M in a test cycle. The efficiency of this technique is limited by the following two factors: The detector bandwidth (which determines the maximum sampling rate), and the size of memory into which the sampled SE data is stored.

The highest efficiency is obtained when $f_s = f_c$. When $f_s < f_c$, the efficiency is reduced by a factor of $N = f_c/f_s$. Because the multi-stroboscopic sampled data must be stored in a buffer

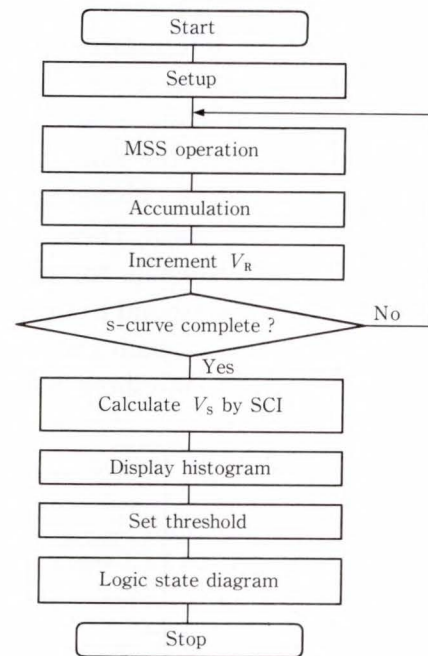


Fig. 5—Logic state measurement flowchart.

memory (see Chap. 5), MSS measurement must be performed in several stages if the number of logic states exceeds the memory size. In this case, there will be no increase in efficiency. The dotted line shows this limitation for a memory sufficient for 5 000 logic states.

4. S-curve interpolation (SCI)

In LSI logic device testing, the size of the logic swing in volts must be considered when setting the thresholds of the logic high and low. Therefore both quantitative voltage measurement and waveform measurement are required in logic state measurement using MSS. However, it is impossible to quantitatively measure the voltage by feeding back the retarding voltage of the energy analyzer. This is because the highly capacitive load of the retarding grid limits the frequency at which the retarding voltage can be varied.

Therefore, for quantitative voltage measurement, s-curve interpolation (SCI) based on an open-loop technique⁵⁾ is combined with MSS. Figure 4 shows the principle of SCI. SE sampling is repeated while the retarding voltage is varied. At each voltage step, the SE signals obtained over the test cycle are stored in the buffer

memory. The s-curves for each logic state are then constructed by interpolating the stored data on the SE- V_R plane as shown in the figure. Finally, the measured voltages for each logic state are calculated from the shift in the interpolated s-curves, and a histogram of the measured voltages is obtained. There are normally two peaks on the histogram for an LSI logic device. These peaks correspond to the logic high and low. A logic state diagram can be quickly obtained by setting the threshold between the

two peaks. Figure 5 shows the logic state measurement procedure using MSS and SCI.

The measurement time is as follows:

$$T_M = k_2 NM/f_c, \dots \dots \dots (4)$$

where k_2 is a factor for signal averaging and quantitative voltage measurement and is several times the value of k_2' in Equation (3).

5. System and performance

Figure 6 shows the block diagram of our electron beam tester⁴⁾. The LSI device is operated by a drive unit which feeds the clock and trigger signals to the MSS controller. The trigger defines the period of the test cycle. The secondary electrons are analyzed by a retarding field energy analyzer⁶⁾ which is directly controlled by a computer in open-loop mode. The retarding voltage step of this analyzer is about 1 V for SCI. The energy-filtered SE signal is detected using a conventional Everhard-Thornley detector having a bandwidth of 3 MHz. An electron beam acceleration voltage of 1 kV and a beam current of 2 nA are usually used. The SE signals at each state in the test cycle are sampled by an A/D

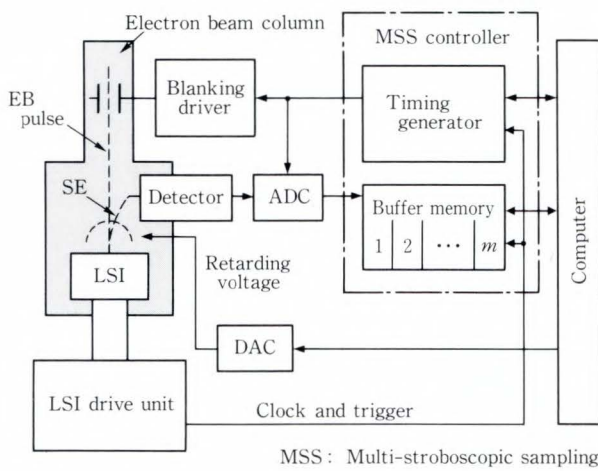
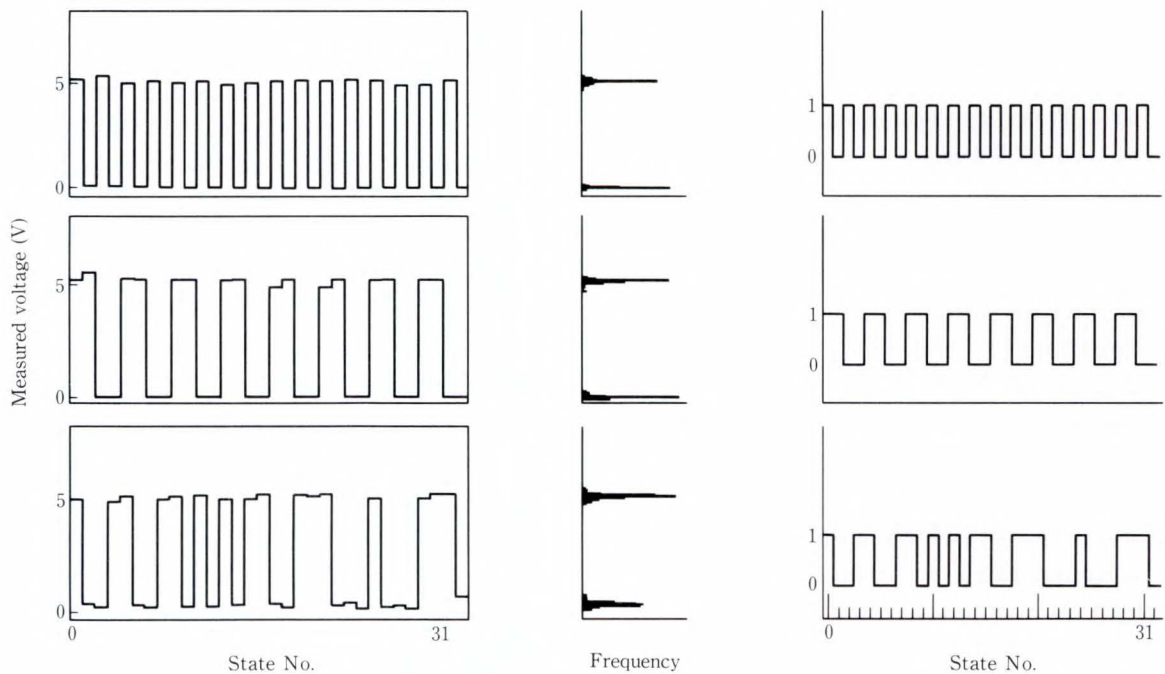


Fig. 6—The electron beam tester.



a) Measured voltage waveform b) Voltage histogram c) Logic diagram of the first 32 states corresponding to a)

Fig. 7—Examples of logic state measurement.

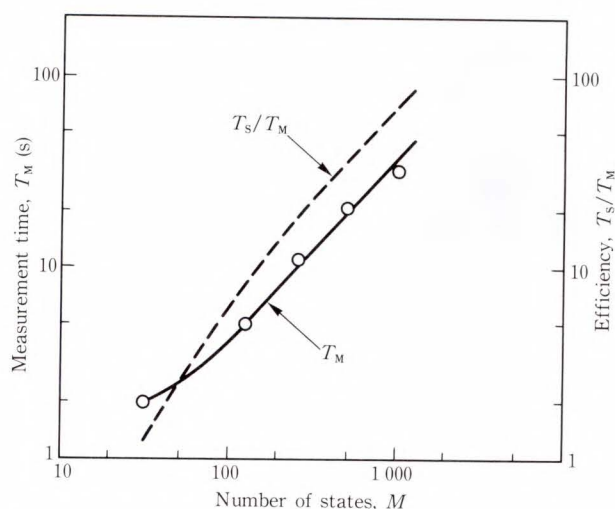


Fig. 8—Measurement time T_M and efficiency T_S/T_M .

converter and then stored in a buffer memory. To increase the signal to noise ratio, the SE data for each logic state is accumulated in the buffer memory during subsequent cycles.

Figures 7 and 8 show the operation of the tester. A 5-volt logic signal is applied to a 5- μ m-wide non-passivated aluminum line. This test signal takes the device through 512 logic states in one test cycle at clock rate of 1 MHz. Figures 7 a) and b) show the quantitatively measured voltage waveform and histogram obtained from logic state measurement of three different lines for which the required voltage resolution was 0.2 V. This histogram contains useful information; for example, whether the logic swing is correct and whether there are any intermediate states caused by a fault. Figure 7 c) shows the final logic state diagrams obtained by setting the threshold between the two peaks of the histogram. The figure shows the first 32 of the 512 logic states.

Figure 8 shows the logic state measurement time T_M versus the number of states M in the test cycle for an experiment in which the clock rate was 1 MHz, the duration of the electron beam pulse was 10 ns, and the required voltage resolution was 0.2 V.

The solid line represents the measurement time. The measurement time required for 1 024 logic states was 30 s. As expected, above $M = 100$ the measurement time was proportional

to M . The deviation below $M = 100$ is due to the processing time of the computer. The broken line represent the efficiency T_S/T_M , where T_S is the measurement time estimated from Equation (1). The efficiency is also proportional to M and is typically 70 for 1 024 logic states. Therefore, the measurement time is 1/70 the time required for stroboscopic waveform measurement.

6. Conclusion

A logic state measurement technique which combines multi-stroboscopic sampling with s-curve interpolation was devised to reduce the measurement time. The measurement time using this technique is typically 30 s when the required voltage resolution is 0.2 V, the time resolution is 10 ns, the number of states is 1 024, and the clock rate is 1 MHz. This is 1/70 the time required for stroboscopic waveform measurement.

References

- 1) Ostrow, M., Menzel, E., Postulka, E., Gorlich, S., and Kubalek, E.: IC-internal Electron Beam Logic State Analysis. *SEM*, **2**, pp. 563-572 (1982).
- 2) Sano, T., Miyoshi, M., Asami, S., and Okumura, K.: A Multi-sampling Waveform Measurement Method in the EB Tester. Proc. 11th Int. Cong. Electron Microscopy, Kyoto, 1986, pp. 633-634.
- 3) Balk, L.J., Feuerbaum, H.P., Kubalek, E. and Menzel, E.: Quantitative Voltage Contrast at High Frequency in the SEM. *SEM*, **1**, pp. 616-624 (1976).
- 4) Furukawa, Y., Goto, Y., Ishizuka, T., Ookubo, K., and Inagaki, T.: Quantitative Voltage Measurement by a Software Closed Loop Technique in Electron Beam Testing. Proc. SPIE, Electron-Beam, X-Ray, & Ion-Beam Techniques for Submicrometer Lithographies V, **632**, pp. 232-236 (1986).
- 5) Fujioka, H., and Ura, K.: An Open-loop Spectroscopy for Quantitative Waveform Measurements with Scanning Electron Microscope. *J. Phys.*, **E**, **18**, pp. 284-285 (1985).
- 6) Ito, A., Ookubo, K., Goto, Y., Furukawa, Y., and Inagaki, T.: Improved Energy Analyzer for Voltage Measurement in Electron Beam Probing for LSI Diagnosis. *J. Vac. Sci. & Technol.* **B**, **3**, pp. 383-385 (1985).



Akio Ito

Sensing Technology and Robotics
Laboratory
FUJITSU LABORATORIES, ATSUGI
Bachelor of Electronic Eng.
Nagoya University 1975
Master of Electronic Eng.
Nagoya University 1977
Specializing in Electron Beam
Technology



Akifumi Muto

Corporate Production Engineering
Group
Production Technology
Development Div.
FUJITSU LIMITED
Bachelor of Electrical Eng.
Kyoto University 1973
Specializing in Electron Beam
Testing



Kazuo Okubo

Sensing Technology and Robotics
Laboratory
FUJITSU LABORATORIES, ATSUGI
Bachelor of Applied Physics
Hokkaido University 1980
Master of Applied Physics
Hokkaido University 1982
Specializing in Electron Beam
Technology

Electron Beam Tester for VLSI Diagnosis

• Masaaki Kawabata • Akifumi Muto • Tetsuya Mukunoki

(Manuscript received January 25, 1990)

An electron beam tester for design verification and fault diagnosis of large-scale high-density ICs was developed.

The tester can measure voltage waveforms of fine electrodes in VLSI circuits by using an electron beam. The measurement time resolution is 100 ps and the voltage resolution is better than 0.1 V.

The electron beam tester is directly connected to an LSI tester to reduce the propagation delay and waveform distortion. It can measure through the insulation film and can test a logic circuit with a long repetition frequency in a short time.

1. Introduction

The number of transistors in a VLSI chip ranges from several hundred thousand to several million¹⁾. However, the number of input and output pins of VLSI does not increase with the number of transistors. Therefore fault diagnosis estimated by the status of input and output pins has been extremely limited.

The electron beam tester shows promise in the direct measurement of internal circuits for design verification and fault diagnosis. The electron beam tester produces a very fine focused beam for high-precision measurement using Scanning Electron Microscope (SEM) techniques. By using stroboscopic sampling, high-speed waveform measurement is also possible²⁾.

For practical use of the electron beam tester, the following must be achieved:

- 1) Steady signal supply without delay or distortion to high speed VLSIs in a vacuum, and quick and easy replacement of the Device Under Test (DUT),
- 2) Measurement through the insulation film protecting the VLSI surface, and
- 3) Short measurement time, especially for logic circuits having a long test cycle.

To solve these problems, a new electron beam tester was developed. This paper presents

an overview of the new tester, and describes the techniques used to develop it and their effects.

2. Overview

Figure 1 shows the new electron beam tester and Table 1 lists its main specifications.

Fujitsu's 16-bit personal computer FM-16 β is used to select the test mode, set parameters, and control the system including chamber evacuation and the stage shift sequence. It also accumulates and edits the results.

The electron beam column and its controller for generating, scanning, and focusing the electron beam were made by modifying a conventional scanning electron microscope. A beam blanker and a hemispherical secondary electron energy analyzer³⁾ are also incorporated. The beam blanker generates 100 ps electron beam pulses using a Mianda electron beam scanner⁴⁾. It provides a measurement time resolution of 100 ps.

We also developed automatic control for focusing, beam alignment, gain and offset of secondary electron signals, and signal averaging. Automatic signal averaging is used to measure at the same accuracy under all operating conditions. The waveform measurement time is

Table 1. Specifications

Item	Contents
Measurement items	Voltage waveform, logic state
Time resolution	100 ps
Voltage accuracy	100 mV
Signal bandwidth	200 MHz
Measurement range	10 μ s from trigger, 1 024 clock in logic state
Special resolution	0.5 μ m (accelerating voltage: 1 kV)
Measurement area	100 mm square
Automatically controlled item	Beam control parameters, working distance, beam alignment, image focus, sampling time
DUT changing time	5 min
Output mode	CRT, X-Y plotter
DUT	input/output pins: 288, packaged

DUT: Device Under Test

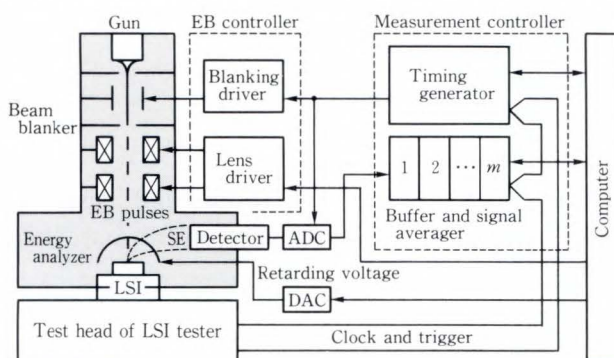


Fig. 1—Electron beam tester and its block diagram.

generally 10 s to 20 s at a 0.1 V resolution and 1 MHz sampling frequency.

These specifications enable the operator to use the electron beam tester in the same way as when probing electrodes using an oscilloscope. Even a circuit designer who is unfamiliar with electron beam devices can use the tester very easily by selecting test points and making decisions based on the test results. These tester

features contribute greatly to efficient and accurate diagnosis.

3. Direct connection with test head of LSI tester

When using the electron beam tester, the DUTs must be in a vacuum. After changing the DUTs, the chamber must be reevacuated which is troublesome and time consuming. Also, because fine 1 μ m wiring patterns must be tested, each image must be enlarged several hundred times to determine the test point. The field of view is 200 μ m to 300 μ m square and must be frequently shifted. We have therefore developed a subchamber through which the DUTs can be supplied to the tester { see Fig. 2 a) } .

To test VLSIs we must supply electrical power and a large number of signals. However, it is difficult to install the test head in the vacuum chamber because the drive circuits are large and generate considerable heat. This means that the signals and power should be supplied from outside the vacuum chamber.

To externally drive the DUT in the vacuum, even when the test head is beside the electron beam tester the signal cables will need to be almost two meters long. This is long enough to cause a propagation delay or signal waveform distortion and therefore hamper the testing of high speed devices. Driving a DUT with numerous input/output pins at high speed (i.e. over several tens of megahertz) requires short signal path lengths and a high performance LSI tester.

We developed the stage mechanism shown in Fig. 2 b) to shift the image field. The test head of the LSI tester is installed outside the vacuum chamber and connected directly to the stage. This reduces the signal path length to about 200 mm, and therefore supplies signals with less distortion. Various ways of directly connecting the test head and DUT are shown in Fig. 3. For the new tester we chose method a) because it allows easy assembly and maintenance of the column.

When the DUT is changed, the entire performance board including the peripheral

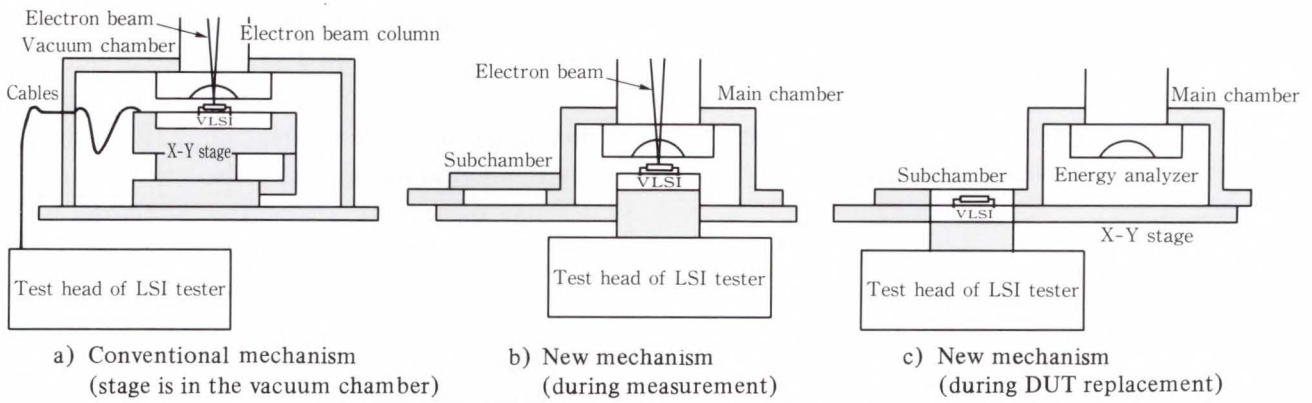


Fig. 2—Outlines of the conventional and new mechanisms.

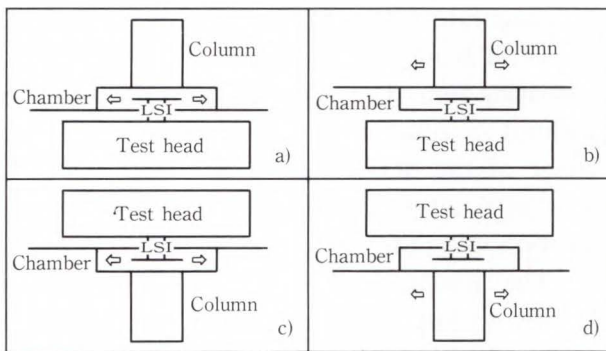


Fig. 3—Ways of connecting an electron beam tester to an LSI tester (⇔ : indicates direction of movement).

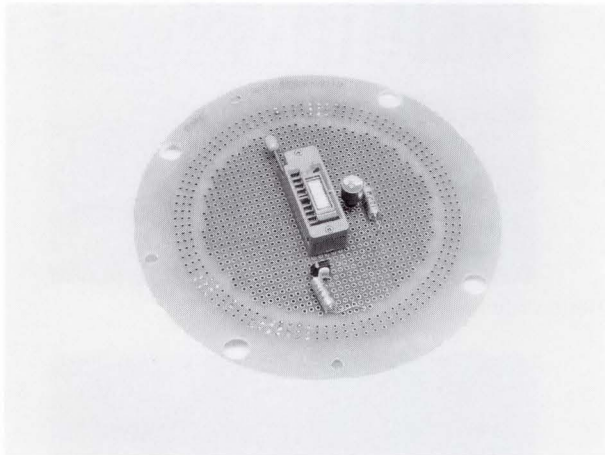


Fig. 4—Example of a performance board.

circuits is replaced. The VLSI's peripheral circuits are made in advance so that the system can be used efficiently by simply replacing the performance board (see Fig. 4).

To reduce the replacement time, we made a subchamber having about 1/30 the volume of the main chamber. This subchamber enables

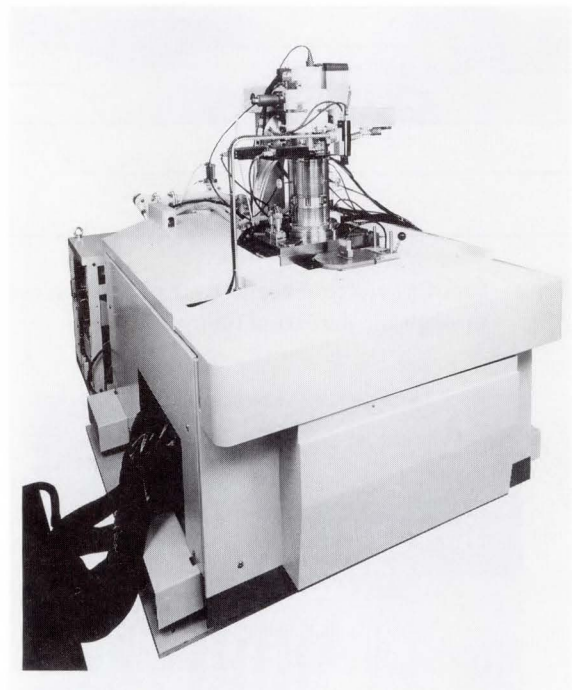


Fig. 5—Electron beam tester mechanism. LSI tester test head is connected under the electron beam column. Cables between tester and test head can be seen on the left side.

the DUT to be replaced by simply releasing the subchamber vacuum while maintaining the vacuum in the electron beam column and main chamber { see Fig. 2 b) } .

After replacing the DUT, the subchamber is quickly re-evacuated to about 1 Pa and the DUT is moved to the main chamber. At this point, the vacuum in the main chamber falls to about 1 Pa but is soon completely recovered.

This system reduces VLSI mounting time to one minute or less and reduces to five

minutes or less the time required to achieve the vacuum of 6.6×10^{-3} Pa needed for testing.

Figure 5 shows the mechanism. The test head of the LSI tester is installed under the stage and is connected to the LSI tester by cables.

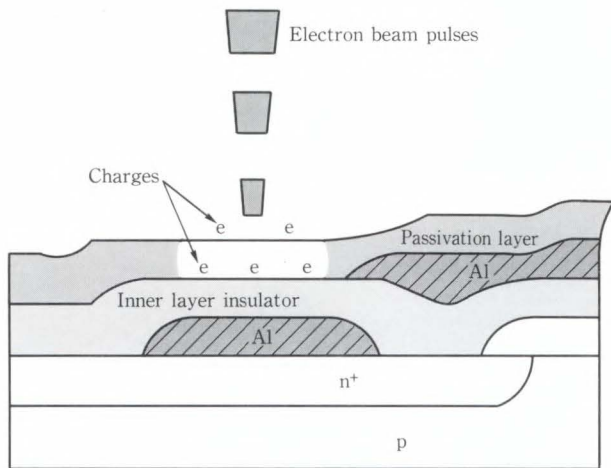


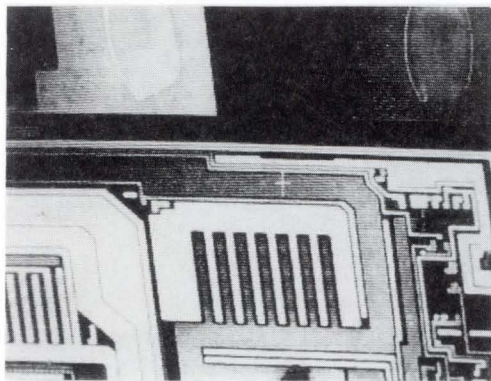
Fig. 6—Shooting electron beams to the LSI electrodes through the insulation film.

4. Measurement through the insulation film

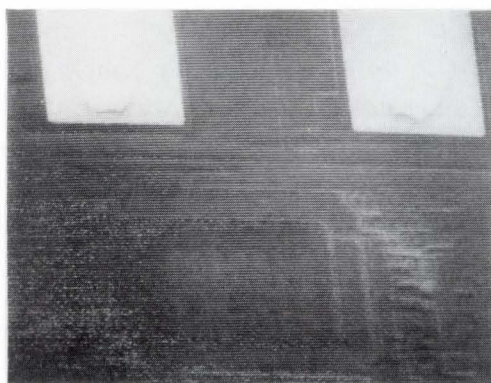
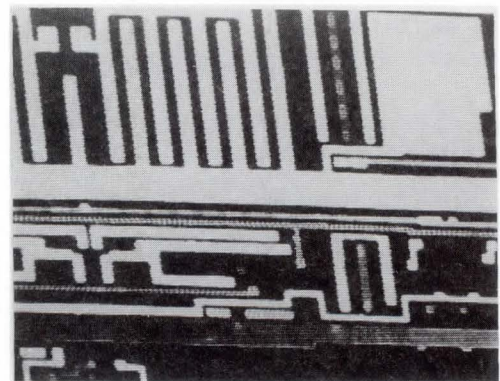
The surface of an LSI chip is covered with a PSG or silicon nitride insulation film (passivation film) to protect it from humidity and other environmental influences. Also, the higher the density of circuit elements, the more likely it is that the wiring will be multi-layered. Therefore the electron beam tester must usually be applied to positions covered by insulation film (see Fig. 6).

When an electron beam is applied to the insulation film, the film is charged and the VLSI's surface potential is changed resulting in inaccurate testing or image display. Figure 7 shows SEM images of devices with and without insulating film. The wiring pattern of the device without a film can be clearly seen. But the image of the device with a film is unclear, and it is difficult to accurately determine the test location using the image.

The insulation film used to be removed before testing by chemical etching, but this



a) Without insulation film



b) With insulation film

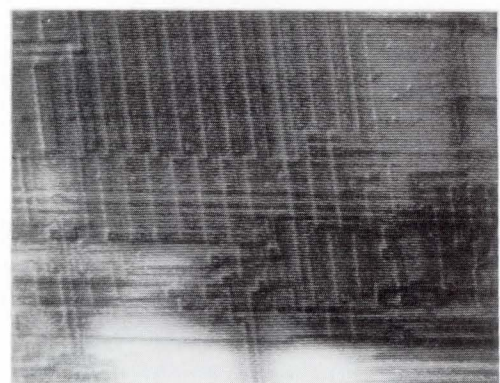


Fig. 7—SEM images of devices with and without insulation film.

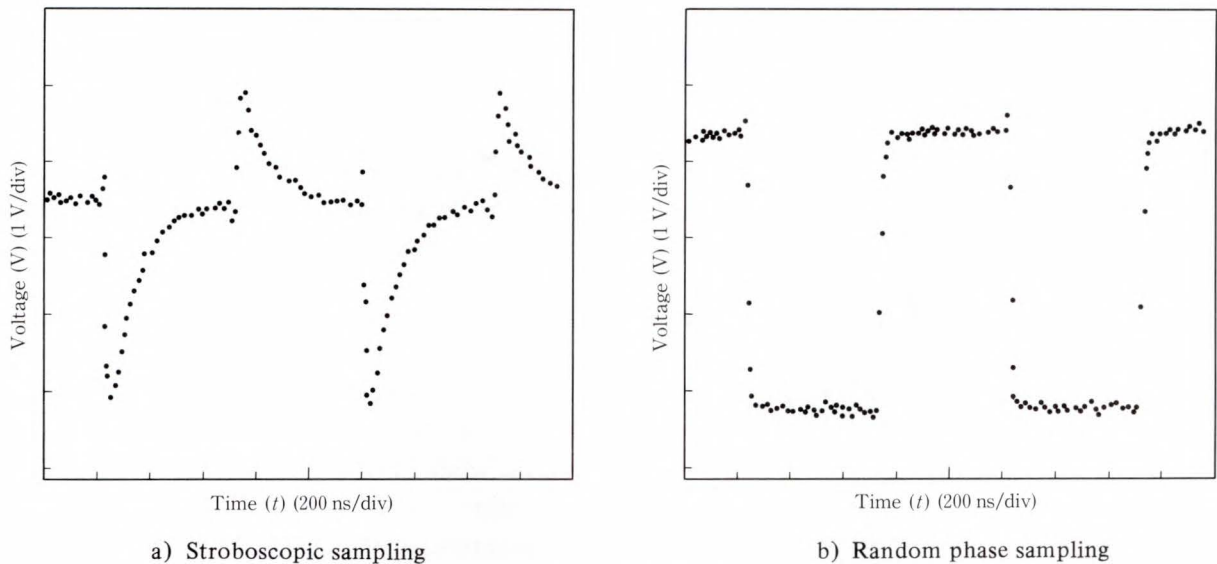
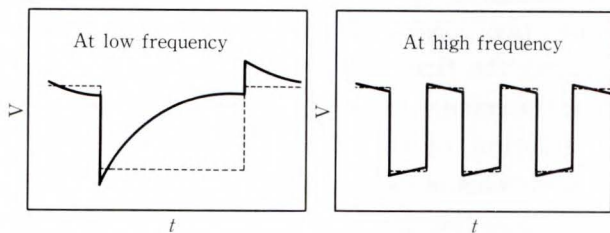
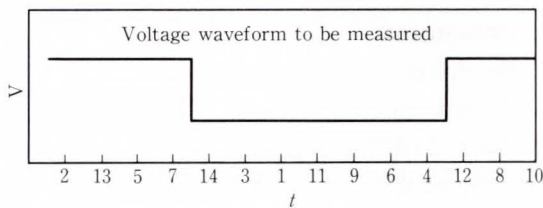


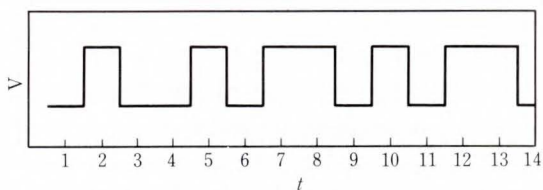
Fig. 8—Measurement through the insulation film. Applied waveform is a square wave.



a) Waveform measured using conventional stroboscopic sampling
At high frequency, low distortion data can be obtained



b) An example sampling sequence of RPS



c) Quasi voltage waveform rearranged in sampling sequence. This looks like a high frequency waveform

Fig. 9—Algorithm of random phase sampling (RPS).

is difficult to do without damaging the wiring pattern.

When a square wave was measured using

conventional stroboscopic sampling without removing the insulation film, a highly distorted differential waveform was observed { see Fig. 8 a) } and accurately testing was not possible.

To observe a SEM image, the alternate phase scanning method⁵⁾ was developed. To measure a waveform with the insulation film intact, the fast phase scanning method^{6),7)} was developed. However, in the fast phase scanning method, control of the electron beam position is complex and the signal processing required for quantitative voltage measurement is difficult to implement.

Considering that a differential waveform can be obtained at low frequency and that low distortion data can be obtained at high frequency by measuring a square wave { see Fig. 9 a) }, we developed the random phase sampling (RPS) technique⁸⁾.

A sampling phase is selected at random in the test range { see Fig. 9 b) } so that testing is not continued at only one level (high or low). Figure 9 c) shows the rearranged quasi waveform. This looks like a high frequency waveform and enables accurate measurement through the insulation film. The data collected at each test phase is accumulated and displayed in phase sequence.

By using this technique an accurate wave-

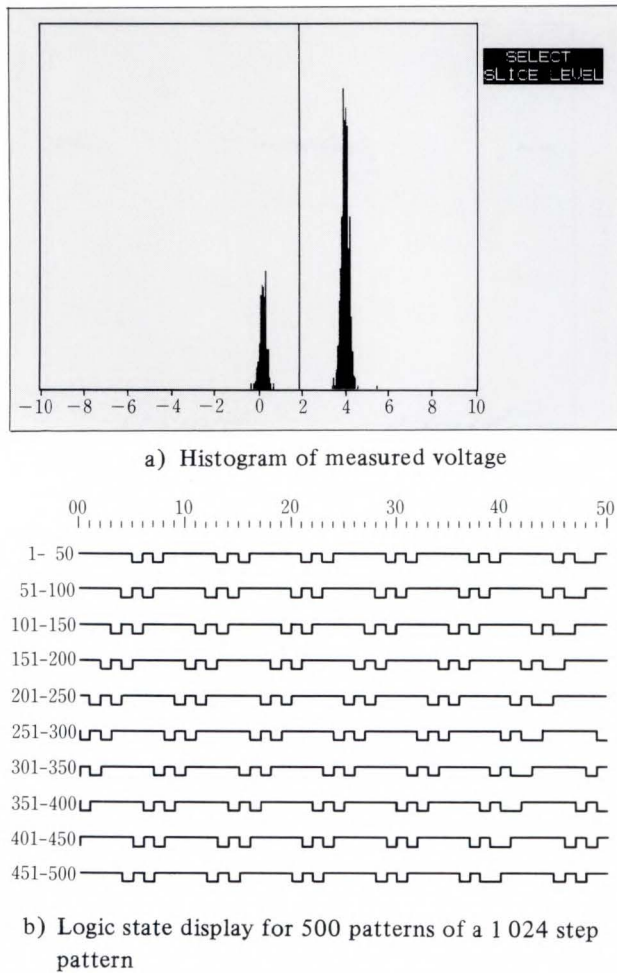


Fig. 10—Sampling measurements.

form is obtained with little distortion { see Fig. 8 b) }. The voltage is reduced by about 25 percent when the insulation film is 1 μm thick and becomes even smaller as the wiring pattern gets thinner. This is probably due to the local field effect and to the electrical field in the insulation film.

5. Short time measurement of logic waveforms

Stroboscopic waveform measurement²⁾ was developed to enable the electron beam tester to measure a rapidly varying periodic voltage waveform. The advantage of this method is that rapid waveform changes can be accurately measured using short electron beam pulses. However, since there is only one sample in each repetition cycle, it takes a long time to measure waveforms having a long period. For example, if 1000 patterns are repeated using

a 1 MHz clock, it takes hundreds to thousands of seconds to measure a logic waveform; which is far from practical.

We developed a multistroboscopic sampling (MSS) technique⁹⁾ that applies numerous electron beam pulses in a single cycle for logic waveform measurement. A waveform is sampled m times in a single cycle pattern string. Theoretically, the measurement time will be reduced to $1/m$, but in practice it may be longer due to the processing time of the computer.

Figure 10 shows the results of MSS measurement when 1024 patterns are repeated using a 1 MHz clock. Sampled data is converted to a quantitative voltage value and the frequency is displayed in a histogram as shown in Fig. 10 a). The logic waveform is obtained by determining a threshold level { perpendicular line between the two peaks in Fig. 10 a) }. Figure 10 b) shows the first 500 of the 1024 patterns. The measurement took about 30 s at a voltage resolution of 0.2 V and a time resolution of 10 ns. This measurement time is about 70 times less than the time required by the conventional stroboscopic waveform measurement technique. The method is explained more fully in another paper in this series.

6. Conclusion

We have developed an electron beam tester connected directly to an LSI tester. A sub-chamber enables easy replacement of DUTs and the tested VLSI can be replaced together with the entire performance board. These developments have reduced sample replacement time to about five minutes. The electron beam control system is automated to simplify diagnostics and to enable testing through the insulation film using a random phase scanning technique. Use of multistroboscopic sampling reduced the logic waveform measurement time to $1/70$ the time required by the conventional method. This tester can be used for VLSI design verification with wires 1 μm or finer. It reduces development times and assists in VLSI performance improvement.

References

- 1) Approaches to the Performance of Microprocessors, Minicomputers, and Mainframes in ULSI Era. (in Japanese), *Nikkei Electronics*, **453**, pp. 95-118 (1988-08-08).
- 2) Plows, G.S. and Nixon, W.C.: Operational Testing of LSI Arrays by Stroboscopic Scanning Electron Microscopy. *Microelectron. Reliab.*, **10**, pp. 317-323 (1971).
- 3) Ito, A., Ookubo, K., Goto, Y., Furukawa, Y. and Inagaki, T.: Improved Energy Analyzer for Voltage Measurement in Electron Beam Probing for LSI Diagnosis. *J. Vacuum Sci. & Technol.* **B3**, 1, pp. 383-385 (1985).
- 4) Ozaki, K., Ito, A., Goto, Y., Furukawa, Y. and Inagaki, T.: Electron Beam Probing System with Ultrahigh Time Resolution. *J. Vacuum Sci. & Technol.*, **B5**, 1, pp. 84-87 (1987).
- 5) Takashima, S.: New Techniques for Stroboscopic Observation of Insulator Coated ICs. (in Japanese), Proc. Sympo. Electron Beam Test., Osaka, 1982, pp. 14-19.
- 6) Todokoro, H. and Fukuhara, S.: Waveform Measurement on Passivated LSI. (in Japanese), Proc. Sympo. Electron Beam Test., Osaka, 1982, pp. 20-25.
- 7) Todokoro, H. and Fukuhara, S.: Low Energy Electron Beam LSI Tester. (in Japanese), Proc. Sympo. Electron Beam Test., Osaka, 1983, pp. 91-96.
- 8) Ookubo, K., Goto, Y., Furukawa, Y. and Inagaki, T.: Quantitative Voltage Waveform Measurement Technique for an Internal Electrode with a Passivation Film. Proc. 11th Int. Cong. Electron Microscopy, Kyoto, 1986, pp. 631-632.
- 9) Ito, A., Ookubo, K., Ishizuka, T., Muto, A. and Goto, Y.: New Logic State Measurement Technique for the Electron Beam Tester. *Proc. SPIE, Integrated Circuit Metrology, Inspection, and Process Control III*, **1087**, pp. 513-518 (1989).



Masaaki Kawabata
Corporate Production Engineering
Group
Production Technology
Development Div.
FUJITSU LIMITED
Bachelor of Electronics
Nagoya Institute of Technology 1971
Specializing in Electron Beam Testing



Tetsuya Mukunoki
Corporate Production Engineering
Group
Production Technology
Development Div.
Bachelor of System and Information
Hiroshima University 1984
Specializing in Electron Beam Testing



Akifumi Muto
Corporate Production Engineering
Group
Production Technology
Development Div.
FUJITSU LIMITED
Bachelor of Electrical Eng.
Kyoto University 1973
Specializing in Electron Beam Testing

Phase-Shifted Gratings for DFB Lasers

• Manabu Matsuda • Shouichi Ogita • Yuji Kotaki

(Manuscript received September 7, 1989)

The introduction of phase shifts in the grating for distributed feedback (DFB) lasers gives additional freedom in DFB laser design to realize various kinds of advanced performance. Here, a technology of fabricating a multiple-phase-shifted grating for long-cavity DFB lasers for coherent optical communication systems has been developed. This new technology is based on a method using a phase-shifting mask. A new phase-shifting mask with three steps in the height has been developed and uniform gratings with the three phase shifts of 0.8π have been fabricated. This method can provide not only an arbitrary phase shift, but also an arbitrary combination of phase shifts at arbitrary locations.

1. Introduction

DFB lasers have been developed for high-speed optical communication systems. One of the most important elements in the DFB structure is the grating to provide distributed feedback. The first DFB laser for optical communication systems used a uniform grating¹⁾.

However, such a DFB laser does not necessarily oscillate in a single mode. Theoretically two-mode oscillation takes place in DFB lasers with a uniform grating and an anti-reflection coating on both facets. This is because of the cancellation between one running wave and the wave being fed back along the cavity due to their phase difference of π close to the Bragg wavelength. There are two modes with the same threshold gain on both sides of the stop band. An elegant way of achieving stable single-mode operation in DFB lasers is to use a π (or $\lambda/4$) phase shift in the grating²⁾. This matches the phase of the two counter running waves and gives single-mode oscillation at the Bragg wavelength. An interesting feature of this π phase shift is that the field intensity is strongly enhanced at the phase shift point. This field enhancement sometimes causes the spatial hole-burning effect and gives undesired multiple-mode operation at high output powers³⁾. However the field enhancement at the phase shift point provides new

freedom in design for advanced DFB laser structures. One example is the dislocation of the phase shift point from the center of the cavity⁴⁾. This gives a higher field intensity at either end of the cavity, increasing the output from a facet. Another example is an introduction of multiple phase shifts in the grating⁵⁾. This provides not only single-mode oscillation near the Bragg wavelength, but also a large freedom in controlling field distribution along the laser cavity. A long-cavity multiple-phase-shifted (MPS) DFB laser for narrow linewidth operation is a typical example. In the MPS-DFB laser, a high field uniformity is realized by the effect of multiple phase shifts to suppress the undesired spatial hole-burning. Thus the introduction of phase shifts in the grating is of great importance for realizing advanced performance of DFB lasers.

Several techniques to fabricate a phase-shifted grating have been developed, for example, use of both positive and negative photoresists^{6), 7)}, use of a phase-shifting mask⁸⁾, use of an EB direct writing⁹⁾ and use of a self-interference grating mask¹⁰⁾. Among them, the method using a phase-shifting mask makes it not only possible to produce an arbitrary phase shift, but also to simplify and to obtain high through-put of grating fabrication.

In this paper, a new method of fabricating a

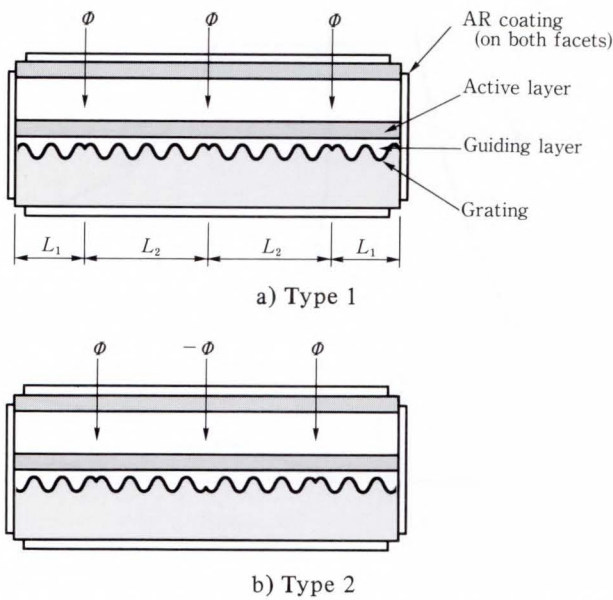


Fig. 1—Structure of multiple-phase-shifted DFB lasers.

multiple-phase-shifted grating using a phase-shifting mask for advanced MPS-DFB lasers is described.

2. Multiple-phase-shifted DFB lasers

Coherent optical fiber communication systems require DFB lasers with very narrow linewidth. The straightforward way to reduce the laser linewidth is to make the cavity longer^{11),12)}. However, in the long-cavity laser, the coupling coefficient κL tends to be large and this causes the spatial hole-burning and resultant mode instability³⁾. It is necessary to make a long-cavity laser with uniform field distribution along the laser cavity. To achieve this, a multiple-phase-shifted grating is introduced in DFB lasers.

So far, two types of long-cavity MPS-DFB lasers have been discussed. These lasers have three phase shifts of Φ with the same signs or opposite signs in the grating as illustrated in Fig. 1. One phase shift is located at the center of the cavity and the other two phase shifts are located symmetrically with respect to the center. Parameter a is introduced to indicate the position of the first and the third phase shifts. The term a is expressed as $a = L_2 / (L_1 + L_2)$. L_1 is the distance between the first or the third phase shift and the end of the cavity, and

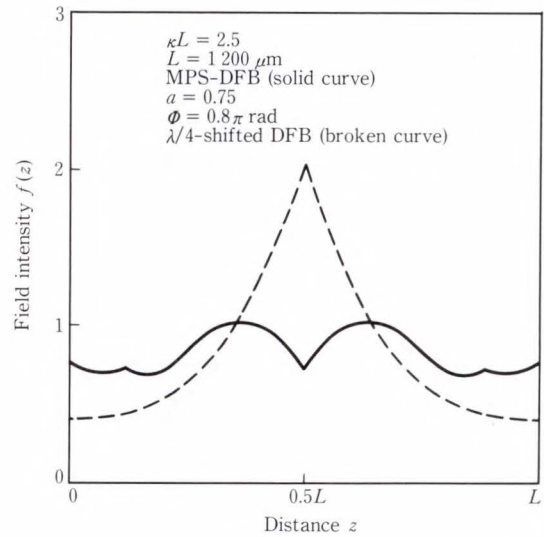


Fig. 2—Comparison of field distribution.

L_2 is the distance between the first or the third and the second (center of the cavity). Theoretically, we can obtain good performance in MPS-DFB lasers when $\Phi = 0.8\pi$ ($\lambda/5$ -shifted) and $a = 0.75$. The comparison of the field distributions of the $\lambda/4$ -shifted DFB laser and the MPS-DFB laser with (Φ, Φ, Φ) grating is shown in Fig. 2. Both lasers have the same coupling coefficient of 2.5 and the same cavity length of 1.2 mm. Obviously, the intense field non-uniformity is suppressed in the MPS-DFB laser, compared with that in the $\lambda/4$ -shifted DFB laser. Here, a new parameter called the flatness factor F is defined, which indicates the flatness of the field intensity along the laser cavity. When a normalized field intensity and its average are expressed as $f(z)$ and f_0 , respectively, F is given by

$$F = \frac{1}{L} \int_0^L \{f(z) - f_0\}^2 dz.$$

Both $(\Phi, -\Phi, \Phi)$ and (Φ, Φ, Φ) grating give almost the same field distribution. Their F is nearly 0.024, while the F for a $\lambda/4$ -shifted DFB laser is nearly 0.32. This uniform field distribution in MPS-DFB lasers suppresses the hole-burning effect and makes it possible to make a long-cavity DFB laser for linewidth narrowing. The threshold gain difference $\Delta\alpha L$

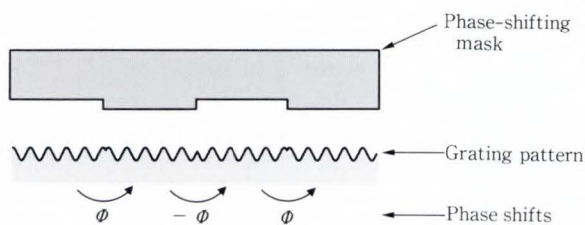


Fig. 3—Conventional phase-shifting mask.

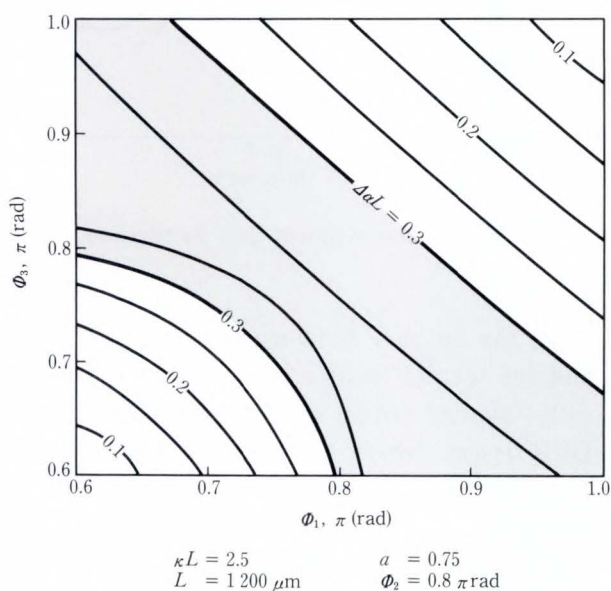


Fig. 4—Mapping of threshold gain difference $\Delta\alpha L$.

of the (Φ, Φ, Φ) grating is 0.34 while the $\Delta\alpha L$ of the $(\Phi, -\Phi, \Phi)$ grating is 0.17. Therefore the (Φ, Φ, Φ) grating is expected to give higher performance.

One of the simplest methods of fabricating a phase-shifted grating is to use a phase-shifting mask, as reported by Shirasaki et al⁸⁾. With this conventional phase-shifting mask, however, it is only possible to make the $(\Phi, -\Phi, \Phi)$ grating as illustrated in Fig. 3. With the $(\Phi, -\Phi, \Phi)$ grating, a very narrow linewidth of 830 kHz has already been achieved in a MPS-DFB laser with a 1.2 mm long cavity¹³⁾. However, much better performance can be expected for the (Φ, Φ, Φ) type MPS-DFB laser. Therefore developing a technology to make the (Φ, Φ, Φ) grating is strongly required. This will not only enable much better performance MPS-DFB lasers to be made but also more advanced DFB lasers by controlling the field distribution.

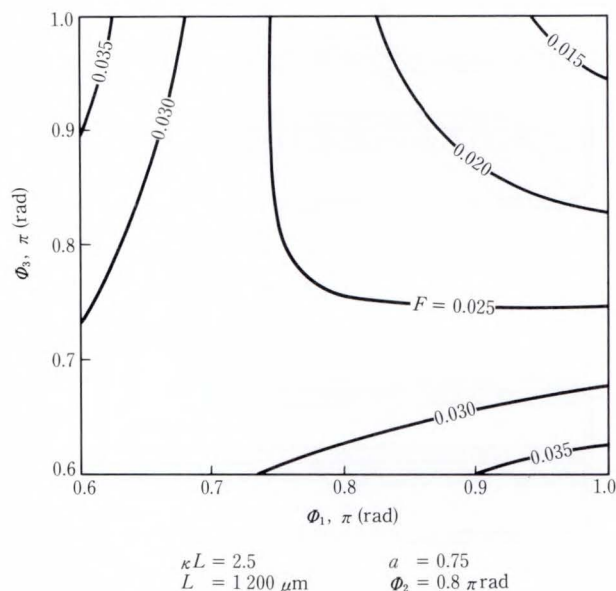


Fig. 5—Mapping of the flatness F .

3. Requirements for multiple-phase-shifted grating

It is important to investigate the requirements for the grating in MPS-DFB lasers. The effect of the variations of phase shifts from 0.8π was theoretically evaluated. Here the three phase shifts are denoted as Φ_1 , Φ_2 , and Φ_3 . The coupling coefficient κL is 2.5 and the parameter a is 0.75. In calculation, Φ_2 was fixed at 0.8π . We evaluated the threshold gain difference $\Delta\alpha L$ when Φ_1 and Φ_3 are varied between 0.6π and 1.0π . Figure 4 shows the mapping of the threshold gain difference $\Delta\alpha L$. The shadowed region shows where $\Delta\alpha L$ is above 0.3, which is enough to maintain single-mode operation¹⁴⁾. We also evaluated the flatness factor F .

Figure 5 shows the mapping of F . In this mapping, F never exceeds 0.04^{15),16)}. So the flatness does not give any limitation to the variations of phase shifts within the range in Fig. 5. Therefore phase shifts in an MPS grating should be required to be in the shadowed region shown in Fig. 4.

4. Principle of generating phase-shifted grating patterns

In addition to the variations in phase shifts, uniformity of the grating over a wafer is also

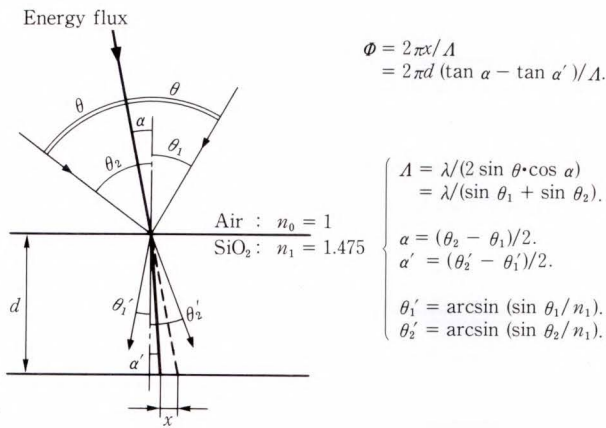


Fig. 6—Principle of generating phase shift.

very important. To realize large, uniform grating, Shirasaki et al. developed a method to fabricate phase-shifted gratings using a phase-shifting mask on the basis of the interference lithography technique⁸⁾. In this technique, a phase-shifting mask with a step is used. The two laser beams for interference lithography are tilted differently from the normal as illustrated in Fig. 6.

The period Λ of the first order grating is determined by the wavelength of incident laser λ and the two incident angles θ_1 and θ_2 as follows:

$$\Lambda = \lambda / (\sin\theta_1 + \sin\theta_2).$$

When the two incident angles are the same, θ , Λ is given by

$$\Lambda = \lambda / (2 \sin\theta).$$

This corresponds to the grating period of conventional interference lithography. The interference grating pattern propagates along the path of energy flux, which is along the line bisecting the angle between the two incident beams. Then, the path should be shifted if the two beams have different incident angle toward some kind of dielectric material as illustrated in Fig. 6. Hence, the amount of lateral shift x is written as follows:

$$x = d [\tan\{(\theta_2 - \theta_1)/2\} - \tan\{(\theta_2' - \theta_1')/2\}].$$

Here d is the step height of dielectric material

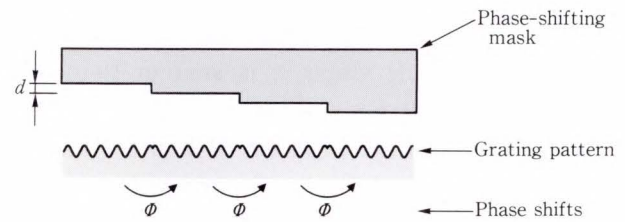


Fig. 7—Multiple-phase-shifting mask.

and θ_1' and θ_2' are the angles after refraction obtained from Snell's law:

$$n \sin\theta_1' = \sin\theta_1,$$

and

$$n \sin\theta_2' = \sin\theta_2.$$

The term n is the refractive index of the dielectric material. The phase shift Φ can be controlled by adjusting the incident angles of the two laser beams in holographic exposure. Thus the Φ is given by

$$\begin{aligned} \Phi &= 2 \pi x / \Lambda \\ &= 2 \pi d [\tan\{(\theta_2 - \theta_1)/2\} - \tan\{(\theta_2' - \theta_1')/2\}] / \Lambda. \end{aligned}$$

A phase-shifting mask has been developed on the basis of this idea.

5. Multiple-phase-shifted grating

5.1 Design of MPS mask

A new phase-shifting mask with three steps is shown in Fig. 7. Different step heights, d_1 , d_2 , and d_3 , on a mask produce different phase shifts of Φ_1 , Φ_2 and Φ_3 , respectively, and it enables the sign of the phase shifts to be made all positive. With $d_1 = d_2 = d_3$, it is possible to obtain the phase shifts (Φ , Φ , Φ) for MPS-DFB lasers as illustrated in this figure. Fused quartz was chosen for the dielectric material because it has low absorption at 325 nm, the wavelength of the incident He-Cd laser used for holographic exposure. The height d was designed as 2.15 μm and the asymmetric angle α as 5.48 degrees. If d is small, α will be larger than ten degrees. Then it is impossible to get an anti-reflection coating below two percent to suppress multiple reflections between the two surfaces of the mask and

also between the mask and the substrate⁸⁾. On the other hand, when α is smaller than three degrees, d will be more than $3\ \mu\text{m}$. The large step will cause the problem of contact between the substrate and the mask, and will also make the fabrication of a uniform mask more difficult. Thus we designed d to be $2.15\ \mu\text{m}$ and α to be 5.48 degrees.

Next the step widths were designed, considering that the $(-\Phi, -\Phi, -\Phi)$ type MPS-DFB laser is equivalent to the (Φ, Φ, Φ) laser. The mask was designed so that the phase shifts (Φ, Φ, Φ) and $(-\Phi, -\Phi, -\Phi)$ repeat alternatively, considering the application for $1.2\ \text{mm}$ long MPS-DFB lasers as illustrated in Fig. 1 with $a = 0.75$. By cleaving a wafer with a multiple-phase-shifted grating at the positions where both the center of the lowest shelf and that of the top shelf of the steps are located, a number of both (Φ, Φ, Φ) type and $(-\Phi, -\Phi, -\Phi)$ type MPS-DFB lasers are fabricated at once. Therefore, the lowest (the 0th) shelf of the steps was $300\ \mu\text{m}$ wide because L_1 was $150\ \mu\text{m}$. Both the first and the second shelves were $450\ \mu\text{m}$ wide because L_2 was $450\ \mu\text{m}$. And the top (the third) shelf was $300\ \mu\text{m}$ wide because L_1 was $150\ \mu\text{m}$.

5.2 Fabrication of MPS mask

Figure 8 shows the fabrication process for this mask. Basically, it is a modification of the manner for the conventional one⁸⁾. The mask was $64 \times 64\ \text{mm}^2$ and $2\ \text{mm}$ thick. The efficient area was $40 \times 40\ \text{mm}^2$. First, thin aluminum film was patterned by the lift-off technique onto a fused quartz substrate with optically polished surfaces. This pattern was $300\ \mu\text{m}$ wide. Next, the first SiO_2 film of $2.15\ \mu\text{m}$ was deposited onto it by sputtering. Both the deposition rate and uniformity were controlled. These procedures were repeated until three aluminum layers were embedded in SiO_2 . The second pattern was $1.2\ \text{mm}$ wide and the third was $2.1\ \text{mm}$ wide. Then, aluminum film was patterned reverse to the third layer by the lift-off technique. This pattern was $300\ \mu\text{m}$ wide. The third SiO_2 film was etched off by reactive ion etching with CF_4 gas. The etching stopped

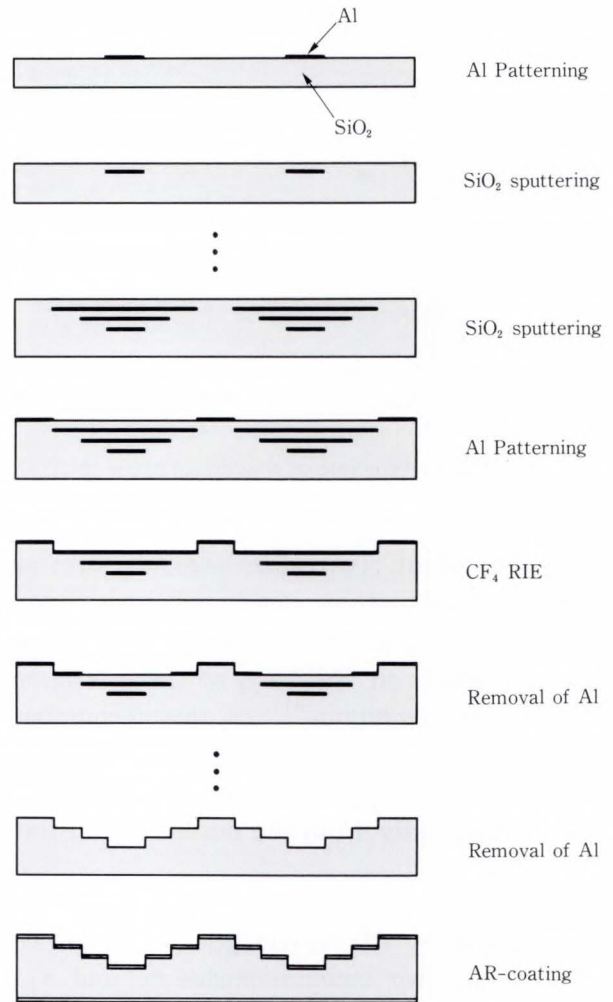


Fig. 8—Mask fabrication.

Table 1. Measured heights and expected phase shifts

Step	Height (μm)	Phase shift (rad)
1	2.16 ± 0.05	$0.78\pi \pm 0.03$
2	2.18 ± 0.04	$0.80\pi \pm 0.02$
3	2.23 ± 0.04	$0.82\pi \pm 0.02$

automatically when it reached the third aluminum film. Then the naked aluminum film was removed with acid. These procedures were repeated two more times and a new phase-shifting mask of three pairs of steps was obtained. Then an anti-reflection coating below two percent was formed on both surfaces of this mask.

5.3 Evaluation of MPS mask

Table 1 shows the measured step heights and

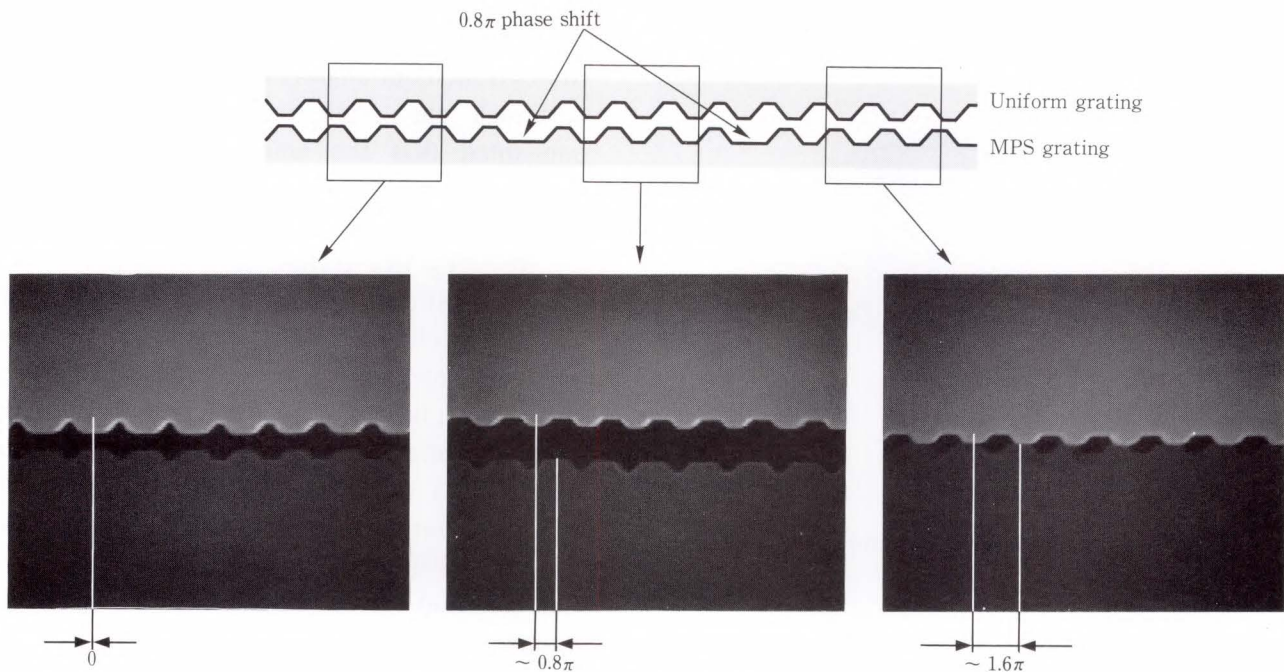


Fig. 9—SEM photographs of MPS grating.

expected phase shifts with their deviations over a $30 \times 30 \text{ mm}^2$ area in this $64 \times 64 \text{ mm}^2$ mask. Suppose the Φ_2 at the center is 0.8π , Φ_1 and Φ_3 are calculated to be 0.78π and 0.82π , respectively from the measured d_1 and d_3 . As shown in Table 1, high uniformity was attained over the $30 \times 30 \text{ mm}^2$ region. Expected phase shifts corresponding to the heights satisfied the requirement for the threshold gain difference $\Delta\alpha L$ above 0.3, as shown in Fig. 4. Consequently, it is confirmed that the fabricated multiple-phase-shifting mask should offer good multiple-phase-shifted gratings.

Next the reflectance from the two surfaces of this mask was measured against incident angles between 35 degrees and 50 degrees by detecting the reflected He-Cd laser power. The reflectance for the two incident angles is below two percent which is enough to suppress multiple reflections between the two surfaces of the mask and between the mask and the substrate.

5.4 Fabrication and evaluation of MPS grating

Multiple-phase-shifted gratings were fabricated using the new mask and interference lithography. First, positive photoresist was

coated on InP substrate. The mask surface with the steps was brought into contact with the photoresist and the photoresist was exposed by the two He-Cd beams with the incident angles of 36.9 degrees and 48.5 degrees. Then the photoresist was developed and the pattern was printed onto an InP substrate by wet etching. The photoresist was removed and finally a multiple-phase-shifted grating was fabricated. In the interference lithography process, the thickness of the photoresist was adjusted so that the reflectance was below two percent for the two incident angles of 36.9 degrees and 48.5 degrees. This is because it is necessary to suppress the fringe pattern due to multiple reflections.

Figure 9 shows the scanning electron microscope photographs of the gratings. To evaluate the phase shifts, two gratings, both having exactly the same period, were put face to face. The lower grating has multiple phase shifts of 0.8π , while the upper has no phase shifts. On the left, they have the same phase. In the middle, the lower has a phase shift of nearly 0.8π against the upper. And on the right, the lower has a phase shift of nearly 1.6π against the upper.

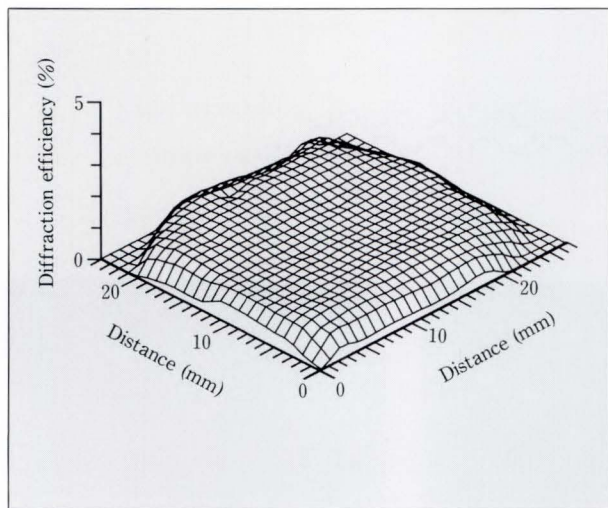


Fig. 10—Distribution of diffraction efficiency.

The uniformity of the grating depth was also evaluated. Figure 10 shows the distribution of diffraction efficiency by measuring the diffracted He-Cd laser power over the substrate of $27 \times 24 \text{ mm}^2$. The diffraction efficiency is determined by the depth and the shape of the grating. When a shallow grating is fabricated, its shape becomes trapezoidal. So, diffraction efficiency is almost directly proportional to the grating depth. Thus the distribution of diffraction efficiency is assumed as the distribution of the grating depth. This uniform distribution of diffraction efficiency shows the very uniform depth over the entire grating. On the other hand, the phase-shifting mask did not harm the uniformity of the grating. This is because if the mask surface is abraded and the light is scattered, uniform grating will never be fabricated.

6. Discussion and conclusion

In the case of conventional $\lambda/4$ -shifted DFB lasers, the phase shift can be evaluated from their spontaneous emission spectra of the laser because the phase shift determines where the oscillation mode is located between the two submodes on both sides of the stop band. However, this technique cannot be used for MPS-DFB lasers because spontaneous emission spectra of MPS-DFB lasers are much more complicated than conventional $\lambda/4$ -shifted DFB

lasers. In this paper, the phase shifts are only evaluated indirectly from the step heights and the two incident angles in holographic exposure. Although the evaluation was indirect, it is confirmed that the uniform step heights and fairly small variances of phase shifts over an area of $30 \times 30 \text{ mm}^2$ were obtained.

By using this technique, a very good multiple-phase-shifting mask which satisfied the design was obtained. This was due to controlling the SiO_2 deposition and the successful fabricating process. In this paper, the mask was designed only for fabricating the grating with multiple phase shifts of the same value and symmetric location along the cavity. This is because it is for MPS-DFB lasers. However, an application of this method gives more freedom in device design, since it enables fabricating a mask to make necessary phase shifts at necessary positions. It is believed that it will become one of the highly advanced technologies for fabricating more complicated device structures in the future.

In conclusion, a multiple-phase-shifting mask to form a multiple-phase-shifted grating has been developed. And the uniform multiple-phase-shifted grating for MPS-DFB lasers was fabricated by this new technique.

References

- 1) Kogelnik, H., and Shank, C.V.: Coupled-wave theory of distributed feedback lasers. *J. Appl. Phys.*, **43**, pp. 2327-2335 (1972).
- 2) Haus, H.A., and Shank, C.V.: Antisymmetric taper of distributed feedback lasers. *IEEE J. Quantum Electron.*, **QE-12**, pp. 532-539 (1976).
- 3) Soda, H., Kotaki, Y., Ishikawa, H., and Imai, H.: Mode analysis of $\lambda/4$ shifted GaInAsP/InP DFB lasers considering a refractive index change due to a spatial hole burning along a laser axis. (in Japanese), *IECE, Jpn., Tech. Group Meeting, OQE86-7*, pp. 49-56 (1986).
- 4) Kotaki, Y., Soda, H., Wakao, K., Ishikawa, H., Yamakoshi, S., and Imai, H.: High-efficiency operation of phase-adjusted DFB laser by asymmetric structure. *Electron. Lett.*, **22**, 9, pp. 462-463 (1986).
- 5) Ogita, S., Kotaki, Y., Ishikawa, H., and Imai, H.: Optimum design for multiple-phase-shift distributed

- feedback laser. *Electron. Lett.*, **24**, pp. 731-732 (1986).
- 6) Utaka, K., Akiba, S., Sakai, K., and Matsushima, Y.: $\lambda/4$ -shifted InGaAsP/InP DFB lasers by simultaneous holographic exposure of positive and negative photoresists. *Electron. Lett.*, **20**, pp. 1008-1010 (1984).
 - 7) Okai, M., Tsuji, S., Hirao, M., and Matsumura, H.: New high-resolution positive and negative photoresist method for $\lambda/4$ -shifted DFB lasers. *Electron. Lett.*, **23**, 8, pp. 370-371 (1987).
 - 8) Shirasaki, M., Soda, H., Yamakoshi, S., and Nakajima, H.: $\lambda/4$ -shifted DFB-LD corrugation formed by a novel spatial modulating mask. Tech. Digest IOOC-ECOC '85, pp. 25-28 (1985).
 - 9) Fice, M.J., and Ahmed, H.: Fabrication of first-order gratings for 1.5 μm DFB lasers by high-voltage electron-beam lithography. *Electron. Lett.*, **23**, 11, pp. 590-592 (1987).
 - 10) Okai, M., Chinone, N., Taira, H., and Harada, T.: Corrugation-pitch-modulated phase-shifted DFB laser. Tech. Digest IOOC '89, 21D3-3, pp. 102-103 (1989).
 - 11) Liou, K.Y., Dutta, N.K., and Burrus, C.A.: Linewidth-narrowed distributed feedback injection lasers with long cavity length and detuned Bragg wavelength. *Appl. Phys. Lett.*, **49**, pp. 366-368 (1986).
 - 12) Ogita, S., Kotaki, Y., Kihara, K., Matsuda, M., Ishikawa, H., and Imai, H.: Dependence of spectral linewidth on cavity length and coupling coefficient in DFB lasers. *Electron. Lett.*, **24**, pp. 613-614 (1988).
 - 13) Ogita, S., Kotaki, Y., Matsuda, M., Kuwahara, Y., and Ishikawa, H.: Characteristics of long cavity multiple phase-shift (MPS) DFB laser. (in Japanese), *IECE, Jpn., Tech. Group Meeting*, **OQE89-42**, pp. 37-42 (1989).
 - 14) Soda, H., Kotaki, Y., Sudo, H., Ishikawa, H., Yamakoshi, S., and Imai, H.: Stability in single longitudinal mode operation in GaInAsP/InP phase-adjusted DFB laser. *IEEE J. Quantum Electron.*, **QE-23**, pp. 804-814 (1987).
 - 15) Ishikawa, H., Soda, H., Wakao, K., Kihara, K., Kamite, K., Kotaki, Y., Matsuda, M., Sudo, H., Yamakoshi, S., Isozumi, S., and Imai, H.: Distributed feedback laser emitting at 1.3 μm for gigabit communications systems. *IEEE J. Lightwave Technol.*, **LT-5**, 6, pp. 848-855 (1987).
 - 16) Ishikawa, H., Yamakoshi, S., and Isozumi, S.: Distributed Feedback Laser Emitting at 1.3 μm for High-Bit-Rate Systems. *FUJITSU Sci. Tech. J.*, **22**, 5, pp. 451-460 (1986).



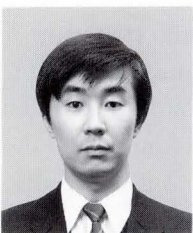
Manabu Matsuda

Optical Semiconductor Devices Laboratory
FUJITSU LABORATORIES, ATSUGI
Bachelor of Science
Kanazawa University 1983
Specializing in Optical Semiconductor
Devices



Yuji Kotaki

Optical Semiconductor Devices Laboratory
FUJITSU LABORATORIES, ATSUGI
Bachelor of Electronic Eng.
Tokyo Institute of Technology 1982
Master of Electronic Eng.
Tokyo Institute of Technology 1984
Specializing in Optical Semiconductor
Devices



Shouichi Ogita

Optical Semiconductor Devices Laboratory
FUJITSU LABORATORIES, ATSUGI
Bachelor of Electrical Eng.
Kanazawa University 1983
Master of Electrical Eng.
Kanazawa University 1985
Specializing in Optical Semiconductor
Devices

Overview of an Experimental Reflective Programming System: ExReps

• Jiro Tanaka • Yukiko Ohta • Fumio Matono

(Manuscript received September 19, 1989)

This paper presents an overview of an experimental reflective programming system (ExReps). ExReps is an environment in which one can input programs and execute goals. It consists of two layers: the abstract machine layer and the execution system layer. Both layers are based on an enhanced metacall mechanism. Reflective operations are implemented on these metacalls. This paper shows examples of program execution on ExReps and examples of reflective programming.

1. Introduction

Recently, various parallel logic languages have been proposed. PARLOG¹⁾, Concurrent prolong²⁾ and GHC³⁾ are examples of such languages. Because these languages embody the concept of processes and synchronization inside a language, it is natural to try to describe an operating system in these languages.

In fact, various work has been done for systems programming from the very beginning of parallel logic languages^{4),5)}. PPS (PARLOG Programming System)⁶⁾ and Logix⁷⁾ are examples of such systems. However, the resulting systems consist of huge amounts of codes and their overall structures are unclear.

Unlike conventional programming languages, problem solving in GHC consists of two parts, i.e. a program and a goal. The goal corresponds to the initial query and the program is the collection of rewriting rules. GHC program execution is performed by consecutively applying GHC programs to the given goal until it becomes empty.

A parallel programming system can be defined as a system that supports this type of problem solving in a parallel logic language. It is a system in which one can load programs and execute goals.

The objectives of our research are as follows: First, we want to design a simple programming

system that is totally written in a parallel logic language and that is written in a more structured manner⁸⁾. Second, we would like to test advanced features of a programming system such as reflective operations^{9),10)}.

We have built a new programming system called ExReps "Experimental Reflective Programming System"¹¹⁾ in GHC. We chose GHC because it had syntactic simplicity and semantic cleanliness. One feature of ExReps is the reflective capability it provides. This capability allows the user process to catch the current state of the system, modify it, and then return it to the system. This feature makes it possible to design a powerful programming system in a simple manner. In this paper, we present an overview of the ExReps system.

The organization of this paper is as follows: Chapter 2 describes the overall structure of ExReps. Chapter 3 describes metacalls which provide the bases for our programming system. ExReps consists of two layers: the distributed abstract machine layer and the execution system layer. The distributed abstract machine layer is described in Chap. 4. The execution system layer is described in Chap. 5. Examples of application program execution are shown in Chap. 6. Examples of reflective programming are shown in Chap. 7.

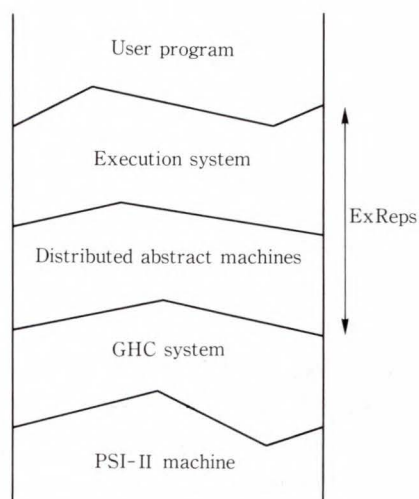


Fig. 1—Overview structure of ExReps.

2. Overall structure of ExReps

ExReps is totally written in GHC. Because GHC is a parallel language, it is quite natural to implement it on parallel hardware. In fact, various kinds of multi-micro distributed computers are becoming popular. Though we expect ExReps to be adaptable to such distributed hardware, we implemented ExReps on the PSI-II sequential Prolong machine¹²⁾ as a first step.

The overall structure of ExReps is shown in Fig. 1. Because the current version of PSI-II only understands ESP¹³⁾ (the object-oriented dialect of Prolong), we installed the GHC system first. This GHC system is a slightly modified version of Ueda's GHC run-time system¹⁴⁾ and it executes the compiled GHC programs.

ExReps is constructed on top of the GHC system. ExReps consists of two layers: the distributed abstract machine layer and the execution system layer. The distributed abstract machine layer¹⁵⁾ simulates the behavior of distributed hardware in which multiple processors are interconnected. Because ExReps has this abstract machine layer, the change from PSI-II to parallel hardware is not too difficult.

The execution system layer loads user programs and executes user goals. It is constructed on top of the abstract machine layer.

3. Stepwise enhancement of metacalls

User programs can be executed on a programming system. However, the programming system must not fail even if a user program fails. The metacall mechanism⁴⁾ works as a basic unit of execution control and protection in the programming system.

A metacall tries to execute, in an interpretive manner, the goals that are given as an argument. We can separate the metacall into two levels: the meta-level, in which ordinary execution is performed; and the object-level, in which goal execution is simulated inside the metacall.

Various kinds of metacalls have already been discussed. Here, we briefly review how they work.

The simplest metacall is the following single-argument metacall:

exec (G).

This metacall simply executes the given goal "G" inside "exec" and the computation result is exactly the same as the direct execution of "G". This form of metacall does not help much because the execution result is always the same as the direct execution.

The first extension is the following three-argument metacall⁴⁾:

exec (G, In, Out).

Here, "In" is called the input stream and is used for communication from the system to the metacall. "Out" is called the output stream and is used for communication from the metacall. Goal execution can be suspended, resumed, or aborted by instantiating "In" to "[suspend |In]", "[resume |In]" or "abort |In>".

If the execution of the metacall finishes successfully, "Out" is instantiated to "[success]". If it fails, "Out" is instantiated to "[failure(R)]" (where "R" is instantiated to the message showing the cause of the failure). This metacall itself never fails, i.e. it has failure protection.

Although this extension of the metacall aims at obtaining object-level information for the meta-level world, there is another direc-

tion for extending the metacall. The other direction is realizing reflective capability^{9),10)}, in which the object-level goal can obtain meta-level information.

Reflective operations work as wires which connect the meta-level and object-level. The object-level world can obtain meta-level information through these wires. The user can write object-level programs which handle meta-level information, and the modified meta-level information can be reflected back to the meta-level.

The extension of metacall depends on the resources to be controlled. Because it is useful to manage processes dynamically, we explicitly introduce a scheduling queue in our metacall. This scheduling queue contains the list of active processes. Initially the user goal is enqueued to the scheduling queue. The goal execution is performed in cycles of dequeuing a process from the queue, and then applying the program to the process and enqueueing the new sub-goals to the queue.

The enhanced metacall becomes as follows:

exec (H, T, In, Out).

The first two arguments express the scheduling queue in difference list form. The use of the difference list to express the scheduling queue was originally proposed by Shapiro²⁾.

Next, we introduce a reduction count¹⁶⁾ in the metacall. Reduction count expresses how many times transformation rules are applied to the given goal. It corresponds to the computation time in conventional systems. We also add two more arguments, "MaxRC" and "RC", in the metacall:

exec (H, T, In, Out, MaxRC, RC).

Here, "MaxRC" shows the maximum reduction count allowed in "exec", and "RC" shows the current reduction count.

Once we obtain the enhanced metacalls, object-level goals are able to handle the enhanced information from the metacalls. This is because it has already been explicit in the metacalls. We have prepared two kinds

of reflective operations: "get" operations to obtain meta-level information and "put" operations to return the information to the meta-level.

We have a reified scheduling queue and a reduction count in our enhanced metacalls. We have considered four kinds of reflective operations that object-level program can use: "get_rc", "put_rc", "get_q", and "put_q".

The meaning of each operation is as follows: "get_rc (MaxRC, RC)" gets "MaxRC" and "RC" from the meta-level, "put_rc (MaxRC)" resets "MaxRC" to the given argument, "get_q (H, T)" gets the current scheduling queue in difference list form, and "put_q (H, T)" resets the current scheduling queue to the given arguments.

In the programming system, this enhanced metacall is used in two ways. Because this metacall has an i/o stream, a scheduling queue, and a reduction counter, it can be regarded as an abstract machine. An abstract machine receives a goal from the input stream, executes it while containing computed sub-goals in the scheduling queue, and produces the output from the output stream. Therefore, the enhanced metacall can be used to express an abstract machine at the distributed abstract machine layer.

The other way of using enhanced metacalls is by expressing the user process at the execution system layer. Because the enhanced metacall provides the unit of execution control and protection, we can use it for user process management.

Although we have omitted the implementation details of these extended metacalls, they can easily be implemented by enhancing simple GHC metacall implementation¹⁷⁾. Implementing various reflective operations is also quite straightforward, once we get the enhanced metacalls.

4. Abstract machine layer

In this chapter, we first describe the conceptual image of the abstract machine layer. Then we describe the actual implementation of the abstract machine layer.

4.1 Conceptual image of the abstract machine layer

We construct distributed abstract machines on top of the GHC system. At this layer, abstract machines are connected by a network and each machine executes GHC goals.

For example, we can define the following ring-connected distributed machines by using “exec” and “nm”; where each “exec” is the one described in the previous chapter, and “nm” is the network manager.

```
d_machine:-true|
  nm (Nm4, Nm1, In1, Out1),
  exec (T1, T1, In1, Out1, _, 0),
  nm (Nm1, Nm2, In2, Out2),
  exec (T2, T2, In2, Out2, _, 0),
  nm (Nm2, Nm3, In3, Out3),
  exec (T3, T3, In3, Out3, _, 0),
  nm (Nm3, Nm4, In4, Out4),
  exec (T4, T4, In4, Out4, _, 0).
```

When this program is executed, four network managers and four abstract machines are generated. The network manager “nm” has four arguments. The first arguments is the input to the network manager. The second is the output from the network manager. The output of one network manager is connected to the input of the other. Therefore, four “nm” processes are connected to the uni-directional ring. The third and fourth arguments of “nm” are used for input and output to the “exec”, that is attached to each “nm”. The scheduling queue of “exec” is initially empty.

The ordinary GHC program runs inside each “exec”. User goals can be entered in “exec” from the input stream. Each “exec” can throw goals that have a pragma¹⁸⁾ to another “exec” through the output stream. A pragma specifies where the goal is to be thrown: Goal “A”, which has pragma “@P”, is expressed as goal “A@P”. Note that this definition allows multiple use of pragma for the given goal. For example, “A@P1@P2” is a legal goal and pragmas are interpreted from the outermost level. The kind of pragma that is used depends on the topology of abstract machines. We assume that the pragma “@forward” is used for a uni-directional

ring.

Each “nm” delivers goals. If a goal has a pragma, “nm” simply peels off the outermost pragma and sends the remaining part to the next “nm”. A goal having no pragma is dropped to the “exec” connected to the “nm”. Therefore, goal “A@forward@forward” will be dropped to “exec” located two ahead.

However, these distributed GHC machines are isolated from the external world. We need to input user goals from the input device and display the output to the window. Therefore, the program of distributed machines with i/o must be as follows:

```
d_machine:-true|
  window (O),
  keyboard (O1, I),
  nm (Nm4', Nm1, In1, Out1),
  exec (T1, T1, In1', Out1, _, 0),
  nm (Nm1, Nm2, In2, Out2),
  exec (T2, T2, In2, Out2, _, 0),
  nm (Nm2, Nm3, In3, Out3),
  exec (T3, T3, In3, Out3, _, 0),
  nm (Nm3, Nm4, In4, Out4),
  exec (T4, T4, In4, Out4, _, 0),
  dist (Nm4, Nm4', O2),
  merge (I, In1, In1'),
  merge (O1, O2, O).
```

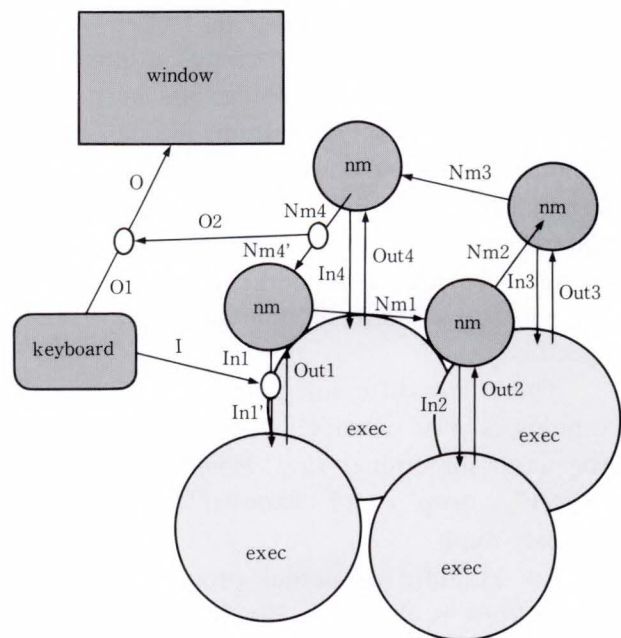


Fig. 2—Distributed abstract machines.

The overall structure of this distributed machine is shown in Fig. 2. A window and a keyboard controller are added to the previous program for interface to the outside world. The window handles all input and outputs at the abstract machine layer level. They keyboard controller is used to generate the read request so that we can input goals from the window. Two “merge” processes are added to join “I” to “In”, and “O1” to “O2”.

As explained before, the scheduling queue of each “exec” is initially empty. The execution starts when a user goal is entered from the window. The user goal goes through the keyboard controller and enters the “exec”. The user goal is computed inside the “exec”. However, computed sub-goals are thrown out if they contain pragmas. The goals move through the network managers and drop to the specified “exec”. The i/o operations are also expressed as goal “A@io”. We assume that this goal simply passes through “nm” and is captured by “dist” to be sent to the window.

4.2 Actual implementation of abstract machine layer

Although we have shown the conceptual images of the distributed abstract machine layer as a GHC program “d_machine”, the actual implementation of this layer on ExReps is more complicated. In the “d_machine” program, the topology of abstract machines has been fixed. However, in the actual system, we can specify various distributed abstract machines. We can dynamically construct a linear array, ring, cube, square mesh, triangular mesh, hexagonal mesh, or tree. The size of network, i.e. the number of processors we want to construct, can also be specified.

There are different pragmas for different topologies. For example, “@forward” was used for a uni-directional ring. However, “@right”, “@left”, “@up”, and “@down” are used for a square mesh.

An example of actual program execution on ExReps is shown in Fig. 3. After installing the GHC system, we execute the abstract machine construction program. This program

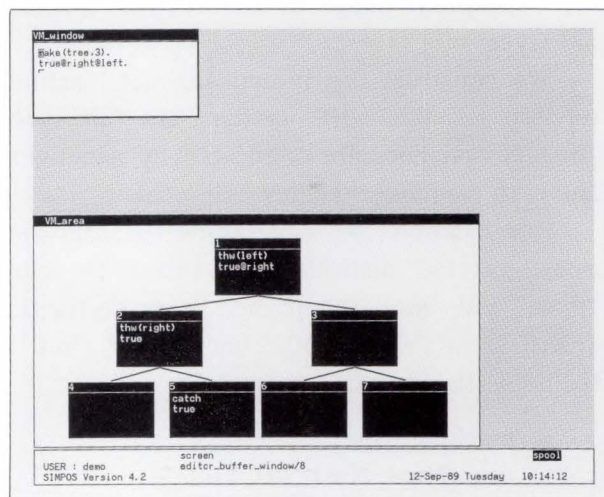


Fig. 3—Abstract machine construction on ExReps.

dynamically creates the network of abstract GHC machines following the user input and opens the “VM_window” in the PSI-II display (upper-left corner). We can specify the topology and size of the network from this “VM_window”.

In this example, we typed in “make (tree, 3)”, which dynamically created a tree network of size 3. The structures of abstract machines will be displayed in the “VM_area” window (lower-left corner). This window is used to display the execution state of each abstract machine. Each abstract machine (shown as a black square), is also a window, and the executing goals are displayed through these windows.

When the abstract machines are constructed, the “VM_window” is connected to the GHC machine #1. We need to use pragmas to throw goals to other abstract machines. Therefore, if “true@right@left” is typed in, that goal will be carried to the GHC machine #5 through network managers. (Note that goal “true” corresponds to “noop” in conventional languages, and pragmas are peeled off from the outermost level.)

5. Execution system layer

The execution system layer loads the user programs and executes user goals. In this chapter, we first describe the outline of the execution system layer. Then we describe the

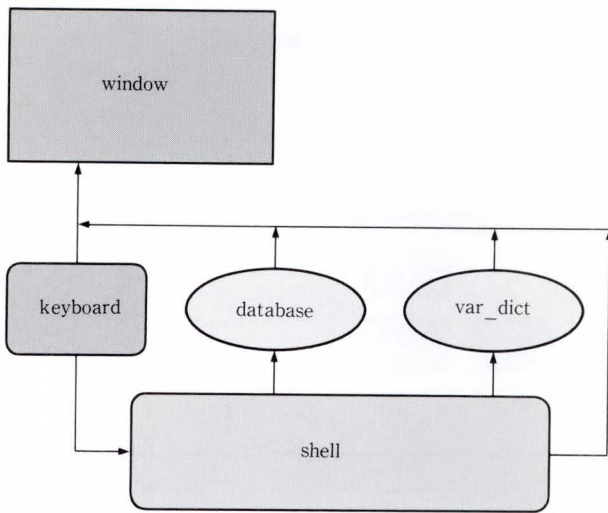


Fig. 4—Execution system layer.

shell that accepts message from the user. The actual implementation of the execution system is also described.

5.1 Outline of the execution system

It is possible to execute an application program directly on top of the abstract machine layer. However, application programs are usually executed on the operating system. The execution system layer operates such an operating system and enables the user to enter user programs and have execution control. The structures of the execution system are illustrated in Fig. 4.

The execution system layer consists of a window, keyboard controller, shell, database server, and a variable dictionary. Each element of the execution system layer is realized as a GHC process. Arrows in the figure show the flow of messages between processes. The window is the system window of the execution system. It takes care of all system inputs and outputs. The keyboard controller always generates the read request to the system window. Therefore, we can always input goals or commands from the system window. The shell generates the user processes depending on the inputs from the user. The shell will be explained in the next section. The database server contains the user program. We can add, delete, and check the user program definitions.

The variable dictionary provides facilities for defining the macro. It can internally memorize the values of variables and replace user's queries with these values.

5.2 Shell

Depending on messages from the user, the shell creates the user task, accesses the database server, or sends messages to the variable dictionary. The shell plays a central role in the execution system.

The program for the shell is as follows:

```

shell ([ ], Val, Db, MaxRC, Out):-true |
    Val = [ ], Db = [ ], Out = [ ].
shell ([goal(Goal)|In], Val, Db, MaxRC, Out)
:-true |
    Val = [record_dict(Goal, NGoal)|Val1],
    window (WOut),
    keyboard (KOut, EIn),
    exec_server(run, NGoal, EIn, EOut, I, O),
    exec ([NGoal|T], T, I, O, MaxRC, O),
    shell (In, Val1, Db, MaxRC, Out),
    merge (KOut, EOut, WOut).
shell([db(Message)|In], Val, Db, MaxRC,
Out):-true |
    Db = [Message|Db1],
    shell (In, Val, Db1, MaxRC, Out).
shell([binding (Message)|In], Val, Db,
MaxRC, Out):-true |
    Val = [Message|Val1],
    shell (In, Val1, Db, MaxRC, Out).
  
```

The “shell” has five arguments: the first is the input stream, the second is the stream to the variable dictionary, the third is the stream to the database server, the fourth is the internal state which specifies the maximum reduction count allowed for the user process, and the fifth is the output stream.

This program works as follows:

- 1) If the input stream of “shell” is “[]”, it means the end of input. All streams will be closed in this case.
- 2) If “goal (Goal)” is in the input stream, “Goal” is sent to the variable dictionary. The variable dictionary checks the bindings of every variable in “Goal” and creates “NGoal” in which all variables are bound

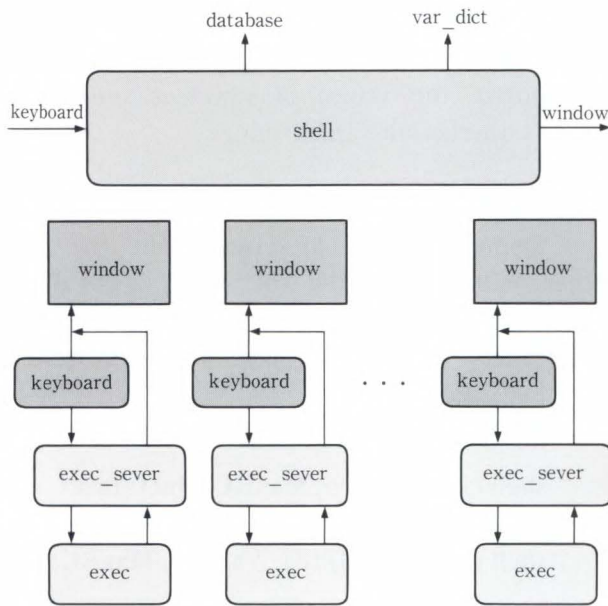


Fig. 5—Creation of processes in shell.

to the current bindings. Then a user process consisting of “**window**”, “**keyboard**”, “**exec**” and “**exec_server**” are created. The “**exec_server**” works as a backend process of “**exec**” and provides the users with various kinds of services.

- 3) If “**db (Message)**” or “**binding (Message)**” is in the input stream, “**Message**” is sent to the appropriate stream. Actually, an application program can be registered in the database server by message “**db (assert (Program))**”. “**binding (Message)**” is used to register and check the current bindings of variables.

Figure 5 shows the snapshot in which user processes are created according to the user input. Each user process has its own window and keyboard. Once created, it runs independently from the shell. Our design policy is that the shell is only responsible for the creation of user processes. Therefore, commands to the user process must be entered from its user window.

5.3 Implementation of the execution system layer

In the actual ExReps system, the execution system is created by typing in “**ps**” from the “**VM_window**”. When created, “**PS_window**” is also opened. We can input user programs and

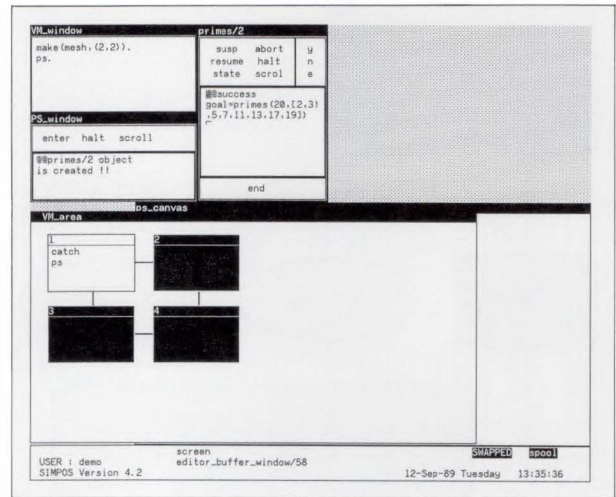


Fig. 6—Execution of user program on ExReps.

goals from the “**PS_window**”.

A program execution example is shown in Fig. 6. In this example, we created abstract machines with a 2 by 2 mesh and installed a primes program which computes the list of prime numbers lower than a given number.

User process “**primes/2**” is created by typing in “**primes (20, X)**” from the “**PS_window**”. It has its own user window “**primes/2**”; and we can suspend, abort, or resume the process dynamically by sending appropriate messages from the window. We can execute other commands such as “**halt**”, “**state**”, and “**scrol**”. “**halt**” closes the user window, “**state**” shows the current variable bindings of the input goal, and “**scrol**” scrolls the i/o window up or down. The computation result is shown in the i/o subwindow of “**primes/2**” as the bindings of the input goal.

6. Application program execution on ExReps

In this chapter, we show two examples of application program execution. The first is the four queens problem. This example shows the distributed execution of a user program on abstract machines. The second is an odd-number-learning example. This example shows the interactive execution capabilities of ExReps.

6.1 Four queens program

As mentioned before, we can execute

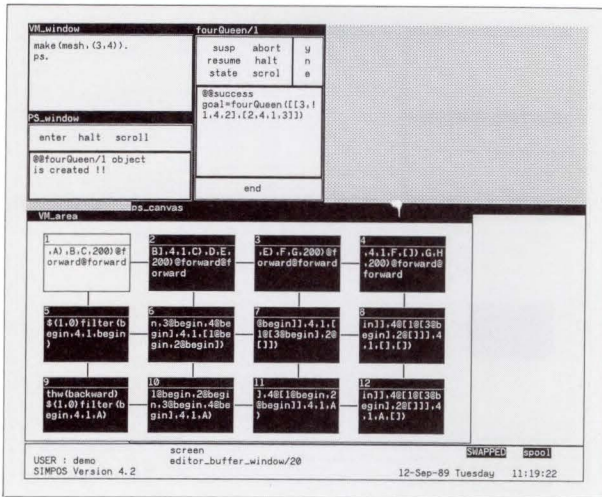


Fig. 7—Execution of four queens program on ExReps.

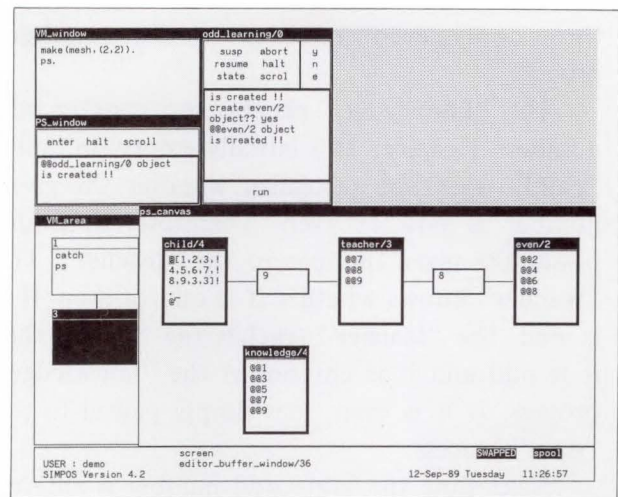


Fig. 8—Odd-number-learning example.

a user program in a distributed manner by adding pragmas to the application program. As an example, we chose the well-known n queens problem. This problem is concerned with the location of n queens non-overlapping with vertical, horizontal, and diagonal directions in an n by n grid.

We tried to execute the four queens problem in a distributed manner. Our solution was to generate 4 by 4 processes which correspond to a 4 by 4 grid and to solve the problem by stream communications between processes.

The actual program execution is shown in Fig. 7. In this example we created 4 by 3 grid abstract machines.

The reason we created such 4 by 3 machines was to show the folding capabilities of abstract machines. Although this program creates 4 by 4 processes, they must be folded into the 4 by 3 abstract machines. Folding is realized by extending the interpretation of pragma to the opposite direction. In this case, pragma “@down” at the bottom row of the grid is interpreted as “up”.

There are two solutions to the four queens problem and the computation result is shown in “fourQueen/1” window.

6.2 Odd-number-learning

The other application is an odd-number-learning example. This program was made to demonstrate the interactive program execution

capabilities of ExReps.

As explained before, we can suspend, abort, and resume the execution of a user program from the user window. However, we sometimes need more fine-grain execution control.

The GHC program embodies the concept of processes and streams. (A process is regarded as a tail-recursive goal. A stream is regarded as a gradually instantiated variable.) Therefore, we would like to control the execution of each process or each stream.

Our approach is as follows: We declare processes and streams explicitly in the user program to distinguish them from ordinary goals and variables. When a process or a stream is created, the system dynamically asks whether the user wants to open a window in “ps_canvas”. If the answer is yes, a process or stream window will be created. We can see and control the current state of a process or a stream from the window. (Here, the “ps_canvas” window is regarded as a blackboard upon which we can freely write figures and communicate.)

The odd-number-learning example is shown in Fig. 8.

This example consists of four processes: “child”, “knowledge”, “teacher”, and “even” processes.

We can input integer numbers from the “child” process. The “child” process can access

the “knowledge” process and is expected to throw only even numbers to the “teacher” process.

The “knowledge” process can contain odd numbers. However, it is initially empty. Initially, “child” does not recognize whether the given number is odd or even. Therefore, it simply passes the given number to the “teacher”. The “teacher” knows whether it is odd or even. If it is odd, the “teacher” teaches the “child” that it is odd and it is entered in the “knowledge” process. If it is even, it is simply passed to the “even” process.

Next time the same odd number is entered from the “child” process, the child can recognize that the number is odd by consulting the knowledge process and does not pass it to the “teacher”.

This odd-number-learning example is an interactive system which models the learning processes of a child at a very superficial level.

In Fig. 8, four processes and two streams are explicitly declared and windows corresponding to those processes and streams are opened. We can see the current state of processes or streams from these windows. The execution of processes and streams can be separately suspended, aborted, or resumed by entering commands from these windows.

7. Reflective programming on ExReps

We can write reflective programs by using the reflective operations described in Chap. 3. In this chapter, we show two examples of reflective programming. The first example is a load balancing program, the second is a dynamic reduction count control program.

7.1 Load balancing

The first example is a load balancing program that is executed directly on top of abstract machines. This load balancing program can be written as a reflective program by using reflective operations.

Reflective operations must be executed urgently. Therefore, we introduce the concept of express goals, which have the form “G@exp”. We assume that express goals are executed

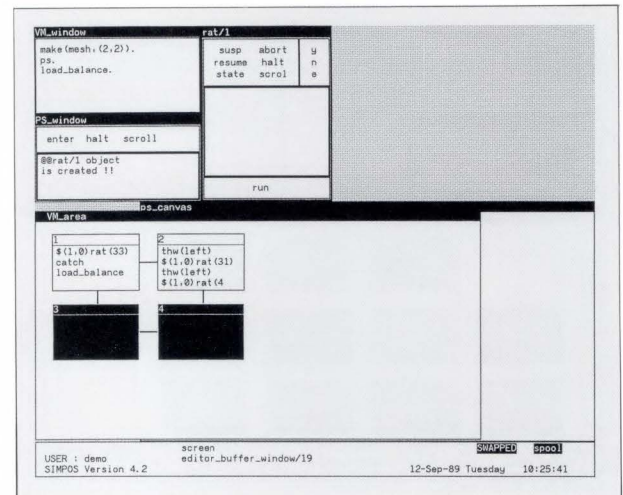


Fig. 9—Execution snapshot of load balancing program.

urgently in “exec”. While express goals are being processed, the normal execution of goals is frozen. When express goals are decomposed to subgoals, they are also processed as express goals.

The load balancing program is shown below. If we enter “load_balance@exp” as a goal executed on the abstract machine, it automatically moves among abstract machines and performs load balancing.

```
load_balance:-true|
    get_q (H, T),
    length (H, T, N),
    balance (N, H, T).
balance (N, H, T):-N>100|
    N1:=N-100,
    separate (N1, H, T, NH, NT, X),
    goals (X) @exp@down,
    load_balance@exp@right,
    put_q (NH, NT).
balance (N, H, T):-N<=100|
    load_balance@exp@right.
```

When “load_balance@exp” is executed inside an abstract machine, it goes into the express state. The current scheduling queue of the abstract machine is taken out and the length of the queue is computed. If it is longer than 100, “N1” excessive goals are separated from the scheduling queue and thrown out. The “load_balance@exp” goal is also thrown out to the

right to invoke load balancing on other abstract machines. (If the abstract machine is at the right end, it is thrown to the left.) If the queue is shorter than 100, it simply throws the “**load_balance@exp**” goal to the right (or left) abstract machines.

Figure 9 shows a snapshot of the execution of this load balancing program.

We assumed 2 by 2 mesh abstract machines. This load balancing program is entered from the “**VM_window**”. This means that this program is executed in parallel with the execution system program. As a user program, we only execute rat programs on machine #1 and #2. These rat programs produce children incessantly and the load of abstract machines increases with time. The load balancing program is also moving machines #1 and #2. When the load of machines #1 and #2 exceeds their limitations, the excessive goals are thrown out to machines #3 and #4.

7.2 Dynamic reduction count control

The second example is the dynamic reduction count control program which is executed at the user program level. The following program shows how to define the “**check_rc**” predicate, which asks the user whether to change the remaining reduction count of the user task.

```

check_rc:-true|
  get_rc (MaxRC, RC),
  RestRC:=MaxRC-RC,
  output ([rc_rest=, RestRC]) @io,
  input ([change_rc??], Ans) @io,
  check (Ans, MaxRC, RC).
check (yes, MaxRC, RC):-true|
  input ([add_rc>>], AddRC) @io,
  NMaxRC:=MaxRC + AddRC,
  put_rc (NMaxRC).
check (no, _, _):-true| true.
    
```

We assume that input and output operations have the format of “**input (Message_list, X)**” and “**output (Message_list)**”, respectively. In the case of the input, “**Message_list**” is printed and then the user’s input is instantiated to “**X**”.

We insert this “**check_re@exp**” goal in the application program. Whenever this goal is ex-

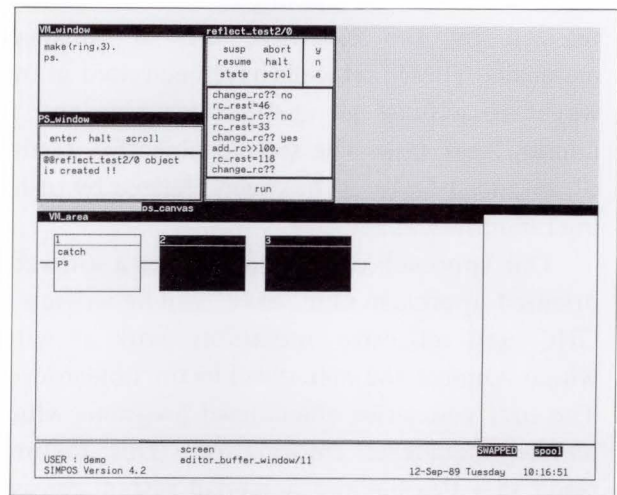


Fig. 10—Dynamic reduction count control example.

ecuted, it gets “**MaxRC**” and “**RC**” and computes the remaining reduction count. After displaying the remaining reduction count, it asks whether to change the reduction count. If the answer is “**yes**”, it asks how much the reduction count is to be increased. It then computes the new maximum reduction count and stores it as the new “**MaxRC**” of the user task.

If the answer is “**no**”, it does nothing.

An execution snapshot of this program is shown in Fig. 10.

Although we created ring abstract machines of size 3, the structure of abstract machines is irrelevant. In this example, the current remaining reduction count is gradually decreasing. When it became “**33**”, we added “**100**”. However, because we consume the reduction count before we come across the next “**check_rc@exp**” goal, the next display of the remaining reduction count is “**118**”.

8. Conclusion

We have presented an overview of the ExReps system. After describing the enhanced metacall mechanism, we described the abstract machine layer and execution system layer of the ExReps system. Program execution examples and reflective programming examples were also presented.

In the introduction, we described two of our research objectives. The first objective, construc-

tion of a simple programming system, has been realized by the extensive use of enhanced metacalls. These metacalls have been used in two ways: to express an abstract machine and to manage user task. The second objective, testing of advanced features, has been realized by utilizing reflective capabilities.

Our approach can be classified as a software-oriented approach. Our "exec" can be written in GHC, and reflective operations work as wires which connect the meta-level to the object-level. The user can write object-level programs which handle meta-level information. This features result in a flexible and powerful system consisting of small a core.

In contrast, PIMOS¹⁹⁾ tries to implement its "exec" directly as a built-in predicate. PIMOS tries to realize various features of a distributed operating system using a machine-dependent hard-wired approach. We believe that such an approach may result in an overly complex system, especially in the case of parallel implementation.

In this paper, reflective operations have been defined in an ad hoc fashion. Other resources, such as a variable environment, can also be controlled in a similar manner¹⁷⁾. A more sophisticated way to define reflective operations may also be possible^{9), 20)}.

Note that the programs shown here are extremely simplified versions. A more complete version of ExReps, running on PSI-II, has already been demonstrated at FGCS'88¹¹⁾.

Information on this version is available from the authors.

9. Acknowledgement

This research has been carried out as a part of the Fifth Generation Computer Project in Japan. The authors would like to express our thanks to Mr. K. Furukawa, Deputy Director of ICOT, for his discussions and encouragements.

References

- 1) Clark, K. and Gregory, S.: PARLOG, Parallel Programming in Logic. Research Report DOC 84/4, Department of Computing, Imperial College of Science and Technology, Revised 1985.
- 2) Shapiro, E.: A Subset of Concurrent Prolog and Its Interpreter. *ICOT Tech. Rep.*, TR-003, 1983.
- 3) Ueda, K.: Guarded Horn Clauses. *ICOT Tech. Rep.*, TR-103, 1985.
- 4) Clark, K. and Gregory, S.: Notes on Systems Programming in Parlog. Proc. In. Con. Fifth Gen. Comput. Syst. 1984, ICOT, 1984, pp.299-306.
- 5) Shapiro, E.: Systems Programming in Concurrent Prolog. Proc. 11th Annual ACM Symp. Principles of Programming Languages, ACM, 1984, pp. 93-105.
- 6) Foster, I.: The Parlog Programming System (PPS). Version 0.2, Imperial College of Science and Technology, 1986.
- 7) Silverman, W., Hirsch, M., Hourri, A. and Shapiro, E.: The Logix System User Manual. Version 1.21, Weizmann Institute, Israel, 1986.
- 8) Tanaka, J.: A Simple Programming System Written in GHC and Its Reflective Operations. Proc. Logic Programming Conf. '88. ICOT, Tokyo, 1988, pp. 143-149.
- 9) Smith, B.C.: Reflection and Semantics in Lisp. Proc. 11th Annual ACM Symp. Principles of Programming Languages, ACM, 1984, pp. 23-35.
- 10) Maes, P.: Reflection in an Object-Oriented Language. Preprints of the Workshop on Metalevel Architectures and Reflection, Alghero-Sardinia, 1986.
- 11) Tanaka, J.: Experimental Reflective Programming System "ExReps". Demonstration material of the Int. Conf. Fifth Gen. Comput. Syst. 1988, ICOT, 1988.
- 12) Nakashima, H. and Nakajima, K.: Hardware Architecture of the Sequential Inference Machine: PSI-II. Proc. 1987 Symp. Logic Programming, San Francisco, 1987, pp. 104-113.
- 13) Chikayama, T.: Unique Features of ESP. Proc. Int. Conf. Fifth Gen. Comput. Syst. 1984, pp. 292-298.
- 14) Ueda, K. and Chikayama, T.: Concurrent Prolog Compiler on Top of Prolog. Proc. 1985 Symp. Logic Programming, Boston, 1985, pp. 119-126.
- 15) Taylor, S., Av-Ron, E. and Shapiro, E.: "A Layered Method for Process and Code Mapping". *Concurrent Prolog: collected papers*, Shapiro, E., ed., The MIT Press, 1987, pp. 78-100.
- 16) Foster, I.: Logic Operating Systems: Design Issues. Proc. Fourth Int. Conf. Logic Programming, 2, The MIT Press, 1987, pp. 910-926.
- 17) Tanaka, J.: Meta-interpreters and Reflective Operations in GHC. Proc. Int. Conf. Fifth Gen. Comput. Syst. 1988, ICOT, 1988, pp. 774-783.
- 18) Shapiro, E.: Systolic programming: A paradigm of parallel processing. Proc. Int. Conf. Fifth Gen.

Comput. Syst. 1984, ICOT, 1984, pp. 458-471.

- 19) Chikayama, T., Sato, H. and Miyazaki, T.: Overview of the parallel inference machine operating system (PIMOS). Proc. Int. Conf. Fifth Gen. Comput. Syst. 1988, ICOT, 1988, pp. 230-251.

- 20) Watanabe, T. and Yonezawa, A.: Reflection in an Object-Oriented Concurrent Language. Proc. ACM CON. Object-Oriented Programming Systems, Languages and Applications, San Diego, 1988, pp. 306-315.



Jiro Tanaka

International Institute for Advanced
Study of Social Information Science,
FUJITSU LIMITED
Bachelor of Science
The University of Tokyo 1975
Ph. D. in Computer Science
University of Utah 1984
Specializing in Parallel Processing,
Logic Programming



Fumio Matono

Development Dept.
FUJITSU SOCIAL SCIENCE
LABORATORY LIMITED
Bachelor of Arts
Tokyo International University 1986
Specializing in Logic Programming



Yukiko Ohta

Development Dept.
FUJITSU SOCIAL SCIENCE
LABORATORY LIMITED
Bachelor of Arts
Rikkyo University 1985
Specializing in Logic Programming

Unified Hardware Description Language (UHDL) and Its Support Tools

• Masahiro Fujita • Hisanori Fujisawa • Nobuaki Kawato

(Manuscript received September 29, 1989)

A lot of effort has been devoted to improving the efficiency of designing ASICs, and many new hardware description languages have been developed. However they have serious drawbacks. They are designed for use only in limited areas, and their semantics are constructed in rather an *ad hoc* manner. To overcome these drawbacks, UHDL, which has a multiple view mechanism and whose semantics are based on mathematical logic, is being developed. Using UHDL realizes high-quality synthesis, and there is no ambiguity in the interpretation of design descriptions. This paper summarizes the important features of UHDL and its support tools.

1. Introduction

ASICs (application specific ICs) are increasing in popularity. Since only a limited amount of time is allowed for their design, the quality of available CAD tools determines the quality of hardware design. A lot of effort has been devoted to improving the efficiency of the design process, and many new tools have been developed. New hardware description languages (HDLs) are the most important of these. Tools for assisting in implementation design, such as placement and routing, have been successfully developed and there are now many commercial software programs available. These allow design data to be easily transferred from one site to another^{1),2)}. Many HDLs for higher level design stages and their tools have also been developed to assist in higher level design. Even though they have useful mechanisms for certain purposes, such as automata³⁾, the mechanism of hierarchical description⁴⁾, and multiple-view design⁵⁾, they are not yet practical for all logic design purposes. Some may have limited success in certain areas, such as simulation.

They cannot be used as an HDL in a total CAD system for higher level design stages because they have at least one of the following

drawbacks:

- 1) They are designed for use only in limited areas. Little attention is paid to efficient synthesis from high-level descriptions.
- 2) Their semantics are constructed in rather an *ad hoc* manner, and they lack a rigid mathematical background. This can become a serious problem especially for asynchronous designs, if designers attach different meanings to the same design descriptions.

To overcome these drawbacks, Artificial Intelligence Laboratory researchers are developing the Unified Hardware Description Language (UHDL). UHDL has two important features. The first feature is having multiple views, like VHDL⁵⁾, which enables designers to see their designs from their own viewpoints, such as structure, behavior, interface, and datapath. As a result, UHDL can be used for most purposes. In particular, designers can specify a datapath in their high-level design descriptions so that the synthesis results will be what they expect. Without specifying a datapath, satisfactory results of synthesis cannot be obtained from high-level design description.

The second important feature is that the semantics are based on a mathematical logic

called Interval Temporal Logic (ITL)⁶⁾, and behavior is described in terms of intervals. One can easily check one's understanding of the meanings of a description by referring to the model of the mathematical logic. Moreover, it is possible to describe synchronous and asynchronous behavior in the same manner using intervals, which is necessary for the design of ASIC chips.

This paper summarizes the important features of UHDL and its support tools. A basic knowledge of HDLs such as Digital System Design Language (DDL)³⁾ is assumed.

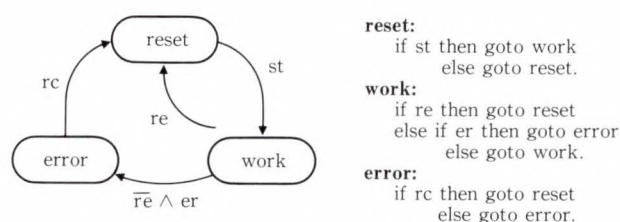
2. Features of UHDL

The important features of UHDL are presented in the following subsections. The most important feature is that the behavior description of UHDL is based on a mathematical logic called ITL⁶⁾. Another feature is that it has multiple views.

2.1 Interval Temporal Logic (ITL) and UHDL

Although many HDLs have been developed for high-level design descriptions, their semantics are defined in rather an *ad hoc* way, i.e. they do not have any mathematical models. This can lead to a situation where developers and users have different interpretations of the design descriptions, thus causing many problems.

Clear semantics are required and UHDL is based on the ITL, which is a time-extended mathematical logic. At present, the most popular way to describe the synchronous behavior of hardware is to use automaton or state transition representation. An example of a (synchronous) state transition diagram and its description in HDL is shown in Fig. 1. State transitions are activated during each clock cycle. This representation is easy to understand and is convenient for mechanical handling, because it has a clear mathematical model, the automaton. However, when asynchronous behavior is encountered, the representation used in Fig. 1 cannot be directly applied. Although most automaton-based HDLs have some extension to represent asynchronous behavior, they have no formal models and are defined in rather an *ad hoc* manner.



a) Example of a state diagram b) HDL description of a)

Fig. 1—State diagram and HDL description.

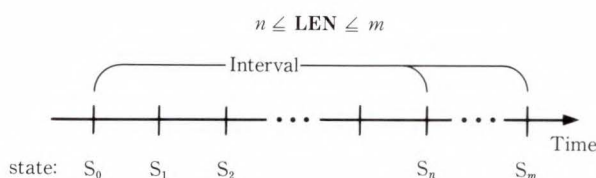


Fig. 2—States and an interval.

In UHDL, intervals of ITL⁶⁾, which are extensions of states in DDL, are introduced to uniformly describe both synchronous and asynchronous behaviors. The semantics of UHDL descriptions are based on ITL. An interval is a collection of consecutive states, as shown in Fig. 2, and is activated and terminated just like DDL state transition statements. The only difference between states and intervals is the length; states have a fixed length, whereas intervals have various lengths, as shown in Fig. 2.

ITL is briefly reviewed before presenting the features of UHDL. ITL is a kind of temporal logic which is time-extended to classical logic. Classical logic can only express properties of a single state, and the values of variables cannot be changed. This means sequential circuits cannot be directly described using classical logic. Thus temporal logic is proposed as an extension of classical logic to enable the dynamic properties of hardware to be described. In temporal logic, the values of variables are defined at each state, so they can be changed as time advances. These changes are controlled by temporal operators. ITL has two temporal operators, chop and next, and is defined over intervals. The chop operator divides an interval into two sub-intervals; the former and the latter. The next operator specifies the properties of the

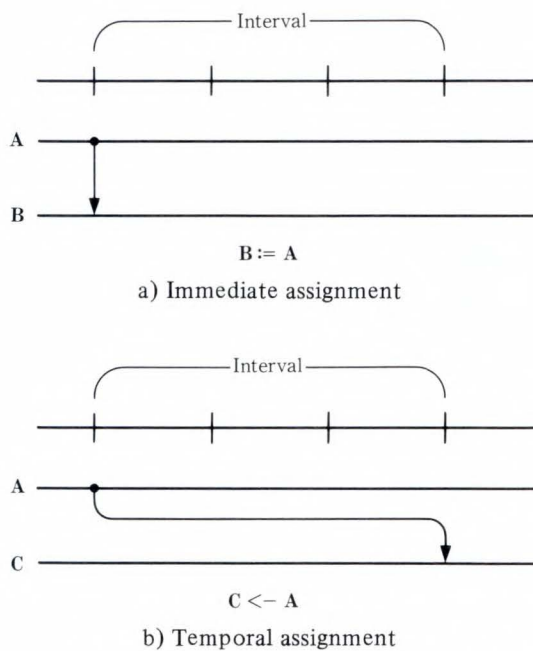


Fig. 3—Assignment statements of UHDL.

next states. The meanings of these two temporal operators are strictly defined in terms of intervals. Therefore it is possible to strictly define the dynamic behavior of hardware in terms of intervals using these temporal operators. The most important points are that UHDL is based on ITL and that all UHDL statements can be defined in terms of chop and next operators. This means the semantics of UHDL is strictly defined.

ITL intervals provide a very flexible mechanism for describing the behavior of hardware. In describing synchronous behavior, intervals are terminated on some clock timing, whereas in describing asynchronous behavior, intervals are terminated on any signal timing.

An interval description has the following form:

interval-name (clock-name):
action-statements;

'interval-name' is the name of that interval, and 'clock-name' enclosed in parentheses shows which clock is used to terminate that interval. If no 'clock-name' is given, the default clock is used. 'action-statements' are collections of behavior statements such as arithmetic or logical assignments, conditional statements, and

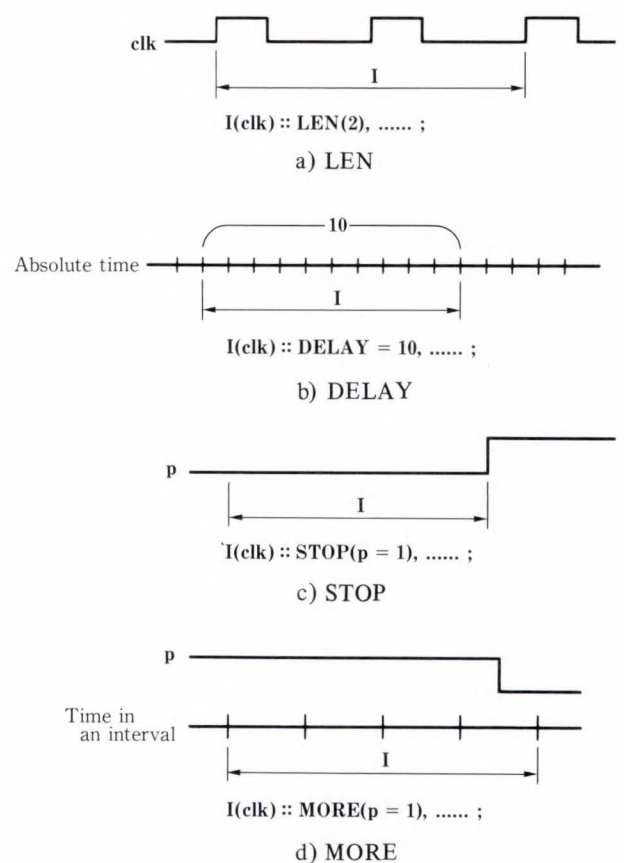


Fig. 4—Length of intervals.

statements relating to controlling the sequence of intervals. Each action-statement is separated by a comma, and is executed in parallel just like DDL³⁾ which is the semantics of ITL.

There are two ways to assign the resulting values of arithmetic and logical operations to variables, immediate assignment (':=') and temporal assignment ('<-'). For immediate assignment, a value is assigned to a variable at that time, i.e. there is no delay in assignment. For temporal assignment, the present value of the right hand side of a temporal assignment statement is transferred to the left hand side at the end of the interval, i.e. there is a time delay of the length of the interval. Immediate and temporal assignments are shown in Fig. 3. Immediate assignment corresponds to combinational circuit descriptions, and temporal assignment corresponds to data transfer between registers, which is a natural extension of assignments in DDL.

There are several action-statements which

relate to the length of intervals, **LEN**, **DELAY**, **STOP**, **MORE**, etc., which are also defined in terms of chop and next operators of ITL. **LEN** specifies the length of an interval by the clock. It is used in describing synchronous behavior, as shown in Fig. 4 a). **DELAY** specifies the absolute length of an interval in nanoseconds, picoseconds, etc. It is used in describing asynchronous behavior, as shown in Fig. 4 b). **STOP** controls the timing of interval termination. **STOP** ($p = 1$) means that if p becomes active, then that interval must be terminated, as shown in Fig. 4 c). Clearly, this **STOP** statement can be used to describe asynchronous behavior. The reverse of **STOP** is **MORE**. **MORE** ($p = 1$) means that if p is active, then the interval cannot be terminated at that time, and the length of the interval is extended at least one more clock as shown Fig. 4 d). Using these statements, synchronous and asynchronous behavior can be described uniformly.

Since UHDL is based on ITL, function or subroutine calls are available. Many functions can be defined, and they are activated and deactivated by 'call' and 'return' statements. Although many automata can also be defined in DDL, which corresponds to the function of UHDL, there is no way to activate and deactivate those automata. In other words, all automata are activated all the time. For example, the UHDL description of Fig. 5 a) expresses the

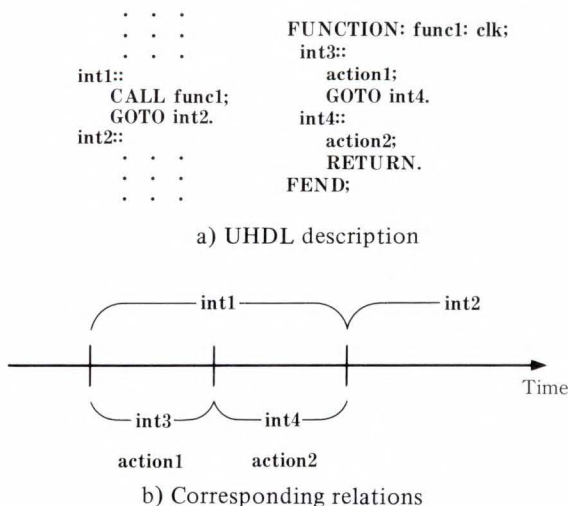


Fig. 5—Activation and deactivation of functions.

relationship of Fig. 5 b). As can be seen, an interval can be decomposed in several different ways by calling functions. This provides a powerful and useful way to describe complex timing, such as pipeline executions. There are several pipeline stages in the pipeline execution sequence, and each state is not necessarily activated at all times. This means one pipeline stage can be directly described by one function of UHDL, not by one automaton of DDL.

UHDL provides another powerful statement, the **KEEP** statement, to describe parallel actions. This is also defined in terms of the chop and next operators of ITL. **KEEP** (**action-statement**) means that 'action-statement' is executed at all the intervals except the last time. By using the **KEEP** statement together with the function call statement and conditional statement, behavior which is difficult to describe in other HDLs can be easily described without any loops. This includes activation of initial pipeline stages.

The most important point is that all the statements of UHDL are based on ITL and have mathematical models. This means there is no ambiguity in the semantics.

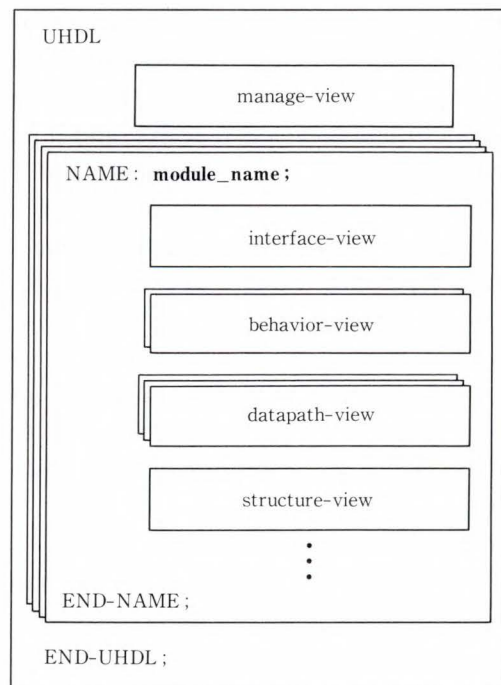


Fig. 6—Organization of UHDL description.

2.2 Multiple views

UHDL allows designers to see and describe their designs from various points of view, such as management, interface, behavior, structure, and datapath. Although this mechanism of multiple views is already introduced into VHDL⁵⁾, UHDL has a special view of datapath for efficient synthesis, which is not included in other HDLs. The general structure of UHDL descriptions is shown in Fig. 6. In UHDL, hardware systems are described with a collection of modules, which are interconnected with each other and form a hierarchical structure. The management view contains data to manage all the design descriptions of a hardware system. These include the name of the hardware system being designed, the name of the design leader, the date the design is described, etc. The other views are described for each module and explained below with the emphasis on the datapath view.

2.2.1 Interface view

An interface view contains all information about external terminals of the module, such as names and bit widths. There are three types of external terminals, input, output, and bus, which can be used as both input and output. A bit width and polarity are assigned to each terminal. The polarity specifies the active value of that terminal. I.e., if the polarity is positive (specified as '+terminal name'), then the value 1 of that terminal means it is active, and if polarity is negative (specified as '-terminal name'), then the value 0 of that terminal means it is active. (All external terminals are distinguished from internal terminals by prefixing their name with a period.) An example of the interface view is shown in Fig. 7. In this example the inputs, data, and reset have positive polarity and the output, out, and the bus, extbus have negative polarity. All external terminals are 16 bits wide, ranging from 0 to 15.

2.2.2 Behavior view

In this view, the behavior of the hardware module being designed is described with intervals, which were explained in the previous section. A behavior view can be a collection of related functions. Since the concept of inter-

```

INTERFACE-VIEW : Sakura4F;
PURPOSE : example;
REVISION : 007;
DATE : 89/09/18;
DESIGNER : Kawato;
INPUTS : +.data(0:15), +.reset(0:15);
OUTPUTS : -.out(0:15);
BUSES : -.extbus(0:15);
END-VIEW ;

```

Fig. 7—Example of interface view description.

vals provides powerful methods for describing complex timing relations, complex hardware designs such as pipeline processors can be easily described. Moreover, as an interval is a natural extension of state in DDL and the basic syntax of UHDL has a high similarity to DDL, designers who are familiar with DDL or similar HDLs can easily make use of the behavior view of UHDL.

2.2.3 Structure view

A structure view describes one level of a circuit structure. It describes which modules exist and are interconnected within a module. For example, the circuit structure shown in Fig. 8a) is described as shown in Fig. 8b). A structure view is composed of management sentences, external terminal sentences, type sentences, and net sentences. External terminal sentences specify inputs, outputs, and buses for the module. A type sentence describes which kind of modules are used internally. External terminal sentences and type sentences are connected by net sentences.

A type sentence has the following form:

```

TYPES;
module type: module name, ...;
...
END TYPES;

```

'module-type' is the name of the type being used, such as adder or multiplexer, and 'module name' is the name of the module being used internally.

A net sentence has the form:

```

net-name: output-terminal, input-terminal 1,
input-terminal 2, ...;

```

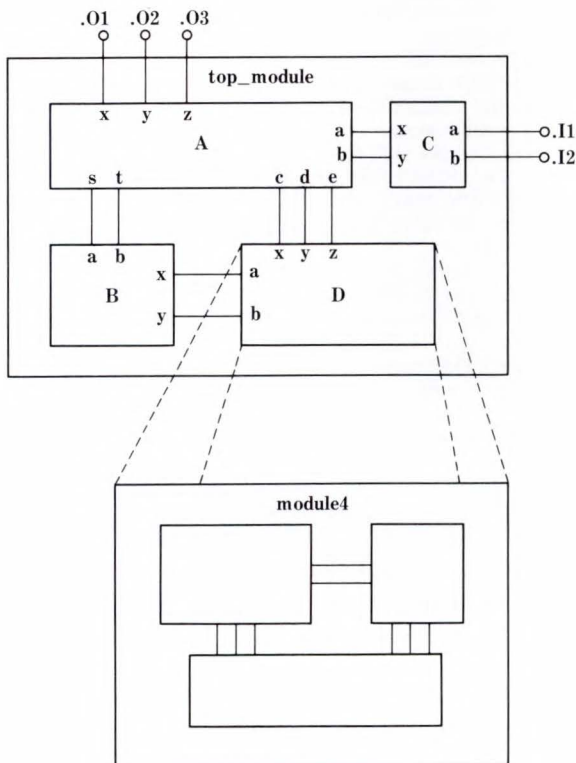
'net name' is the name of the net which connects 'output-terminal' and 'input-terminal 1', 'input terminal 2', etc.

2.2.4 Datapath view

There has been a lot of work done for high-level synthesis, i.e. synthesis from the behavior level. There are not yet any practical programs which can economically synthesize large systems with reasonable quality⁷⁾. Logic synthesis, that is, synthesis from Boolean expressions, has recently been very successful in real hardware design. The difference between high-level synthesis and logic synthesis is that high-level synthesis includes the extremely difficult problem of datapath generation. High-level synthesis without datapath information may result in the synthesized datapath being completely different from what the designers expect. This means designers cannot easily change synthesized datapaths, although it is often required due to implementation problems. Moreover, when designs are modified, the synthesized datapaths may be completely

different from the original ones, even if only a small part of the behavior is modified. Therefore, a realistic solution to the problem of high-level synthesis is that designers supply datapaths as well as behavior descriptions. This is not so difficult, because designers usually have an image of the datapath from the very beginning of the design process, or designs are usually similar to previous designs.

In UHDL, designers can supply datapath information with a datapath view, and the synthesis procedures can make the most use of that datapath description for efficient synthesis. That is, if a datapath has no conflict, the synthesis procedure generates only the control logic for the datapath and behavior description. A high-quality circuit is then automatically



a) Example of a circuit

```

STRUCTURE-VIEW: top_module;
PURPOSE: EXAMPLE;
REVISION: 007;
DATE: 88/11/22;
DESIGNER: James;

INPUTS: .I1, .I2;
OUTPUTS: .O1, .O2, .O3;

TYPES;
    module1 : A;
    module2 : B;
    module3 : C;
    module4 : D;
END-TYPES;

NETS;
    N01 : .I1, C.a;
    N02 : .I2, C.b;
    N03 : C.x, A.a;
    N04 : C.y, A.b;
    N05 : D.x, A.c;
    N06 : D.y, A.d;
    N07 : D.z, A.e;
    N08 : B.x, D.a;
    N09 : B.y, D.b;
    N10 : A.s, B.a;
    N11 : A.t, B.b;
    N12 : A.x, .O1;
    N13 : A.y, .O2;
    N14 : A.z, .O3;
END-NETS;
END-VIEW;
    
```

b) Corresponding structure view

Fig. 8—Example of a structure view.

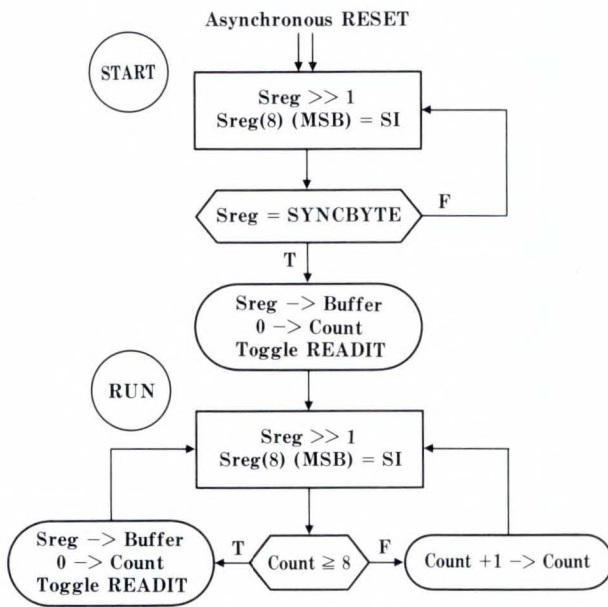


Fig. 9—ASM chart for a serial-parallel data converter.

synthesized from that control logic, using the increasingly popular advanced logic synthesizers. A datapath view defines the hardware facilities which are used in behavior descriptions and describes the datapath among them. In the definition part of a datapath view, the type and name of each hardware facility being used in the module is specified. There are two types, system and user-defined. A system type is a hardware facility which is already defined by the system supporters, such as REGISTER and ALU, and a user-defined type is a hardware facility which is defined by the designer. The details of a user-defined facility are described as a module in UHDL. Any module description of UHDL can be a user-defined type. The datapaths among hardware facilities are expressed as nets among them and are described in the same way as a structure view.

3. Example of Description

A UHDL description is shown for a serial-parallel data converter which converts serial data into 9-bit parallel data. The behavior description in ASM chart⁸⁾ for the converter is shown in Fig. 9, and the corresponding UHDL description is shown in Fig. 10. There is a special bit pattern, SYNCBYTE, to indicate the beginning of serial data. Also, converted data

```

UHDL;

MANAGE-VIEW: Kawato;
SYSTEM: SYS1;
REVISION: 01;
DATE: 88/02/02;
DESIGNER: Drunken_Piper;
END-VIEW;

NAME: S2P-CONVERTER;

INTERFACE-VIEW: Kakuda;
PURPOSE: EXAMPLE;
REVISION: 01;
DATE: 88/02/02;
DESIGNER: Drunken_Piper;
INPUTS: .RESET, .SI;
OUTPUTS: .PO(9), .READIT;
END-VIEW;

DATAPATH-VIEW: Fujita;
PURPOSE: EXAMPLE;
REVISION: 01;
DATE: 88/02/02;
DESIGNER: Drunken_Piper;
TYPES;
    REGISTER(9): Sreg, Buf;
    COMP(9): SyncComp, CntComp;
    COUNTER(4): Count;
END-TYPES;
NETS;
    N0 = FROM(.SI) TO(Sreg.IN8);
    N1 = FROM(Sreg.OUT) TO(Buf.IN, SyncComp.IN);
    N2 = FROM(Buf.OUT) TO(.SPBYTE);
    N3 = FROM(Count.OUT) TO(CntComp.IN);
END-NETS;
END-VIEW;

BEHAVIOR-VIEW: Matsunaga;
PURPOSE: EXAMPLE;
REVISION: 01;
DATE: 88/02/02;
DESIGNER: Drunken_Piper;
DEFINE: SYNCBYTE = X'A5';
% for example
BOOLEAN: .READIT = myReadIt, .PO = Buf;
CLOCK: SPCLK(100000, 50000);
FUNCTION: MAIN: SPCLK;
LOGIC:: IF .RESET THEN (GOTO START);
START:
    Sreg <- (.SI || Sreg) >> 1,
    IF (Sreg = SYNCBYTE)
    THEN (Buf <- Sreg, Count <- 0, myReadIt <- ~myReadIt, GOTO RUN);
    RUN:
    Sreg <- (.SI || Sreg) >> 1,
    IF (Count >= 8)
    THEN (Count <- 0, myReadIt <- ~myReadIt, Buf <- Sreg, GOTO RUN)
    ELSE (Count <- Count + 1, GOTO RUN);
    FEND;

END-VIEW;
END-NAME;
END-UHDL;
    
```

Fig. 10—UHDL description corresponding to Fig. 9.

is stored into the internal register and output to the external terminal, PO, every eight cycles. The output terminal, READIT, toggles its values indicating when the data of the output terminal, PO, is significant.

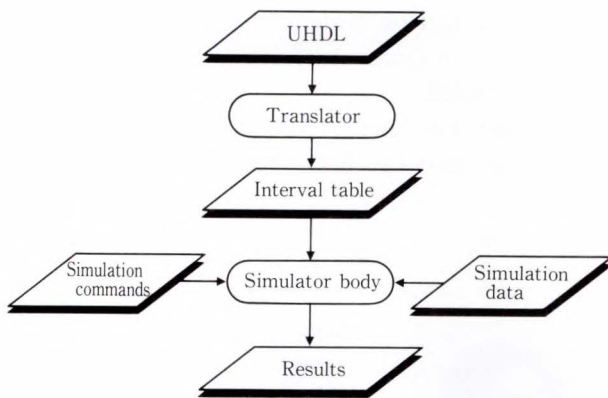


Fig. 11—Organization of the UHDL simulator.

4. UHDL Tools

Currently two types of tools for UHDL are under development: a simulator and a translator for synthesis. The simulator can simulate a full set of behavior view UHDL descriptions. It first converts UHDL descriptions into an **interval table** as shown in Fig. 11. In an interval table, all conditions appearing in UHDL descriptions are rearranged according to each interval, by which the simulator can refer and store different kinds of data quickly. The **simulator body** then refers to the interval tables to obtain data for simulation. **Simulation commands** are supplied to control simulation sequences, such as to initialize variables and to stop simulation at certain conditions. The simulator can be used both in the batch mode and in the interactive mode. In the interactive mode, there are many useful commands such as step execution, modification of variables' values, and a trace of variables.

To show the performance of the simulator, consider a UHDL description for the 8251, a microprocessor peripheral chip. The original behavior description in UHDL contains about 150 lines, which are converted into about 300 lines of an interval table. It takes 53.4 on the SUN 3/50 to simulate 1 000 clock cycles of the 8251 chip, which means the simulation speed is 53 ms per clock cycle. The required memory for this simulation is about 32 Kbytes.

The translator translates behavior descriptions in UHDL into state transition tables. It can only handle a subset of the behavior view of

UHDL, because it is extremely difficult to synthesize asynchronous circuits, although the full set is necessary for simulation purposes. Two types of outputs are generated by the translator, control logic and net list of macro modules. Both these outputs are technology-independent; they only express logical relations and have no information of implementation details. The generated control logic is directly transferred to logic synthesizers and is automatically minimized and converted into technology-dependent circuits, i.e. circuits for CMOS gate arrays. The net list generated by the translator from datapath description is transferred to macro module expanders which are usually rule-based systems, because the expansion process is a rather straightforward one. Since powerful logic synthesizers and macro expanders are both currently available, we can expect very high-quality synthesis results.

5. Conclusion

This paper presents UHDL and HDL for all aspects of hardware logic design processes. UHDL has two important features: it has multiple view mechanism and its semantics are based on a mathematical logic, which distinguish UHDL from other HDLs. A simulator and a translator for synthesis are being developed. The output of the translator will be connected to a logic synthesis system.

References

- 1) Marx, E.R.: EDIF: The Standard for Workstation Interconnection. *IEEE Micro*, 5, 5, pp. 68-75 (1985).
- 2) van Cleemput, W.M.: A Structural Design Language for Computer Aided Design of Digital Systems. Stanford Univ., Comp. Sys. Lab., Tech. Rep., 136, 1977, 27p.
- 3) Duley, J.R., and Dietmeyer, D. L.: A Digital System Design Language (DDL). *IEEE Trans. Comput.*, C-17, 9, pp. 850-861 (1968).
- 4) Cory, W.E.: Symbolic Simulation for Functional Verification with ADLIB and SDL. Proc. ACM IEEE 18th Design Autom. Conf., Nashville, 1981, pp. 82-89.

- 5) Coelho, D.R.: The VHDL Handbook. Boston, Kluwer Academic, 1989, 389p.
- 6) Moszkowski, B.: A Temporal Logic for Multilevel Reasoning about Hardware. *IEEE Comput.*, **18**, 2, pp. 10-19 (1985).
- 7) McFarland, M.C., Parker, A.C., and Camposano, R.: Tutorial on High-Level Synthesis. Proc. ACM IEEE 25th Design Autom. Conf., Las Vegas, 1988, pp. 330-336.
- 8) Prosser, F.P., and Winkel, D.E.: The Art of Digital Design. 2nd ed., N.J., Prentice-Hall, 1987, 525p.



Masahiro Fujita

Artificial Intelligence Laboratory
FUJITSU LABORATORIES,
KAWASAKI
Bachelor of Electrical Eng.
The University of Tokyo, 1980
Dr. of Information Eng.
The University of Tokyo, 1985
Specializing in Computer-Aided Design



Nobuaki Kawato

Artificial Intelligence Laboratory
FUJITSU LABORATORIES,
KAWASAKI
Bachelor of Electronic Eng.
The University of Tokyo, 1971
Dr. of Electronic Eng.
The University of Tokyo, 1976
Specializing in Computer-Aided Design
and Artificial Intelligence



Hisanori Fujisawa

Artificial Intelligence Laboratory
FUJITSU LABORATORIES,
KAWASAKI
Bachelor of Applied Physics
The University of Tokyo, 1985
Master of Applied Physics
The University of Tokyo, 1987
Specializing in Computer-Aided Design

Approximation for the Rate of Short Circuit in Electronic Devices Caused by Whisker Growth on Zn Electroplated Steel

• Takeshi Nagai • Katsuhide Natori • Takashi Furusawa

(Manuscript received September 1, 1989)

Specimens of electroplated cold-rolled steel plate were exposed for approximately six years. Nucleation and growth of Zn whisker on specimens were observed, and the number of days before whiskers were detected was recorded. A correlation was found between the number of days before whisker detection and the macro internal stress measured using the bending strain method.

The number and length of whiskers was counted and measured, and an approximation for the projected rate of short circuit caused by whiskers was obtained.

An approximate rate of short circuit by whisker growth was of about nine fit was obtained.

1. Introduction

The spontaneous formation of metal whiskers on electroplated tin, zinc, and cadmium finishes of electronic components was first reported in 1946. Since then, they have been observed in a wide variety of electronic components¹⁾⁻³⁾. Several explanations of the nucleation and growth mechanisms of whiskers have been proposed using dislocation theory⁴⁾⁻⁶⁾.

Zinc electroplating is commonly used as a finish for steel parts, for example on shelf and cover plates of electronic appliances. In the past, there was a space of more than 3 mm between the electroplated part and the IC leads or terminals. This space was adequate to avoid short circuits caused by whisker. Also, because the voltage between the electroplated part and the component or terminal was usually between 12 V and 24 V, whisker growth was not a problem. However, in the future, packaging density will increase and the voltage will be reduced to 5 V. Therefore, whiskers may then occasionally cause short circuits. Short whisker growth is

therefore an important technical problem and requires attention.

Lindborg et al.^{7),8)} have investigated the relationship between macrostress and zinc whisker growth rate using transmission microscopy, evaluation from X-ray line broadening⁹⁾, and the dilatometric method. From their investigations, it was found that whisker growth from zinc electroplate mainly depends on the internal macrostress that is placed on the plate during electrodeposition. The growth rate was found to be a steeply varying function of macrostress. There is slow growth or no growth at all below 45 MPa, a mixed region at 45 MPa to 55 MPa, and a rapid growth above 55 MPa.

Lindborg¹⁰⁾ has proposed an explanation of nucleation and the growth mechanism of whiskers.

This mechanism is as follows:

- 1) Compressive macrostress occurs in a zinc electroplated layer because of H₂ gas absorption during zinc electroplating.
- 2) Columnar (cylindrical) grains in zinc electro-

plate having Bardeen-Herring sources¹¹⁾ at the bottom of the grain become whisker nuclei. These sources occur unintentionally at the same time as the compressive macrostress mentioned in step 1) above.

- 3) When compressive macrostress is applied to Bardeen-Herring sources, new loops occur.
- 4) Interstitials are absorbed and vacancies are emitted as the loops expand laterally by climb. Interstitials are structured loops, in which vacancies are transported away from the loop.
- 5) The loops reach the full size of the columnar grain and start to glide upwards. Further loops are generated by the Bardeen-Herring sources, and these loops start to expand.
- 6) Whiskers grow by a repetition of steps 1) to 5) above.

Observation by scanning electron microscope has supported this explanation.

Sugiarto et al.¹²⁾ have conducted an experiment in which a large number of specimens were electroplated using bright zinc electrodeposits under a wide range of conditions. The specimens were exposed for 240 days, and whiskers were observed on every specimen. However, no whiskers were detected on specimens electroplated with dull zinc without organic brightener.

In this study, 15 specimens were triple-electroplated with zinc. They were then exposed and checked for whisker growth. The specimens were examined by X-ray diffraction, the microstrain was measured using the Hall plot⁹⁾, and the macrostress was measured using the X-ray and bending strain methods. The number and length of whiskers on three specimens selected from the first batch were counted and measured using an optical microscope. An approximation for the rate of short circuit caused by whisker growth was then obtained.

2. Experimental procedure

The soft steel specimens were 50 mm square and 1 mm thick. Fifteen specimens were triple-electroplated with zinc under the 15 different conditions shown in Table 1. The electroplating was $7 \mu\text{m} \pm 2 \mu\text{m}$ thick. The electroplated specimens were exposed and checked by naked

Table 1. Type of bath, and suppliers of Zn electroplate, brightening compound, and chromate treatment reagents

Specimen	Bath	Brightener	Chromate
A	Acid	Schering	Schering
B	Cyanide	Rohco	Dipsol
C	Cyanide	Okuno	Okuno
D	Cyanide	Rohco	Rohco
E	Cyanide	Jasco	Jasco
F	Cyanide	Dipsol	Dipsol
G	Cyanide	Jasco	Rohco
H	Cyanide	Dipsol	Dipsol
I	Cyanide	Rohco	Rohco
J	Cyanide	Rohco	Rohco
K	Alkaline	Japan Metal	Japan Metal
L	Cyanide	Japan Metal	Japan Metal
M	Alkaline	Japan Metal	Japan Metal
N	Cyanide	Rohco, Dipsol	Taiho
O	Alkaline	Jasco	Asahimate

eye every ten days. The interval from the date the specimens were electroplated to the date whiskers were detected was recorded. Three batches of specimens were prepared and then exposed. The first batch was examined by X-ray diffraction. The microstrain of the first batch was measured using the Hall plot, and the macrostress was measured using the X-ray and bending strain methods.

Specimens other than those in the first and second batches were measured using the bending strain method. A substrate of 130 mm × 10 mm × 0.2 mm cold rolled steel was used to measure the macrostress. One side of the steel substrate was insulated and the other side was zinc electroplated under the conditions shown in Table 1. Each specimen was held by a 30 mm plastic holder. After electroplating and rinsing, the bending strain δ of the specimens was measured. The macrostress σ was calculated using following equation:

$$\sigma = l^3 \cdot E \cdot \delta / 2l^2 \cdot x \cdot (t + x),$$

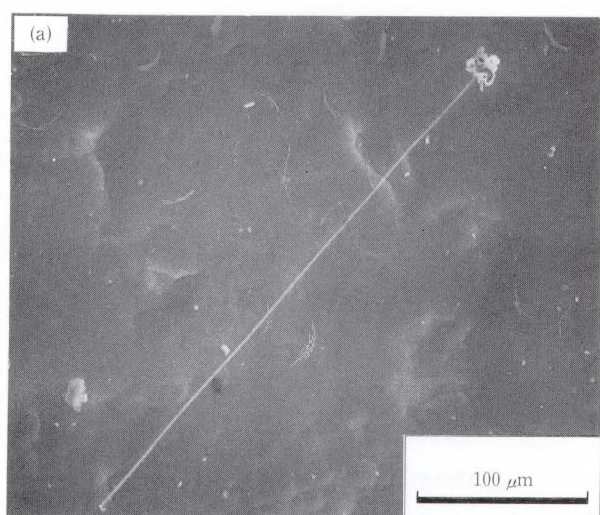
where l : Length of specimen minus the 30 mm holding section

δ : Bending strain caused by electroplate

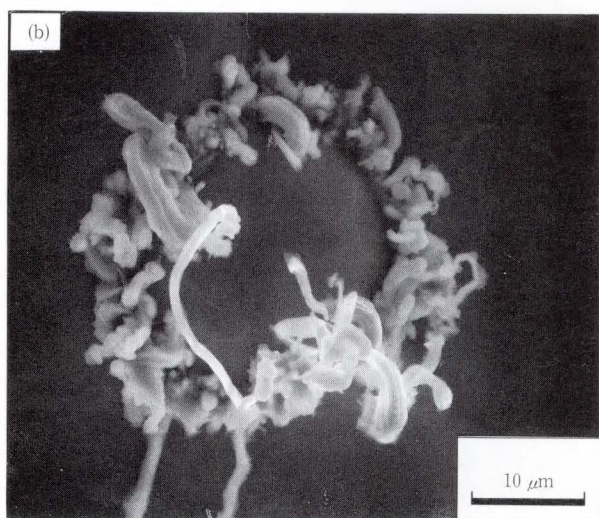
E : Young's modulus

x : Thickness of zinc electroplate.

Two types of whiskers were observed using a scanning electron microscope. These are shown



a) Needle-like whisker



b) Protuberances

Fig. 1—The two types of whiskers observed under a scanning electron microscope.

in Fig. 1. The first type are needle-like (normal) whiskers and can be observed by the naked eye. The second type are rounded protuberances and appear as powder to the naked eye. Because these protuberances are unlikely to cause short circuits, the appearance of the needle-like whiskers was used to determine the interval between specimen preparation and whisker detection. The number and length of whiskers on three specimens from the first batch were counted and measured three times using an optical microscope (Wild, West Germany). This was done after 730, 1834, and 2307 days of exposure. An approximation for the rate of short circuit caused by whiskers was then obtained.

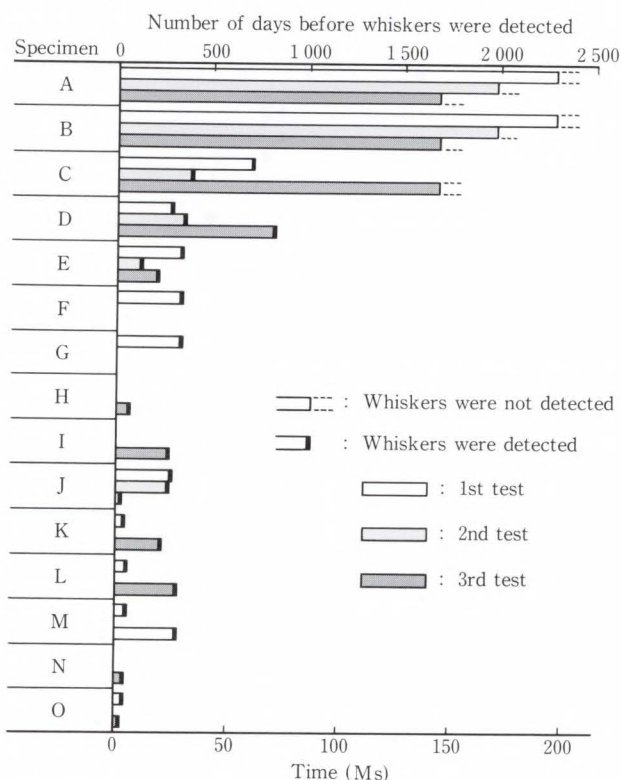


Fig. 2—Number of days before whiskers were detected.

Table 2. Intensity of X-ray diffraction peaks of Zn electroplates

Specimen	(002)	(100)	(101)	(102)	(110)	(112)	(200)	(201)
A	6	100	8	0	100	11	9	5
B	0	76	55	0	100	8	4	15
C	13	100	100	0	13	6	21	65
D	0	9	5	0	100	4	1	1
E	0	10	12	0	100	10	0	3
F	3	100	55	0	32	24	6	26
G	11	100	63	0	14	0	15	86
J	4	100	52	0	61	12	5	39
K	0	20	15	0	100	14	3	20
L	0	0	3	0	100	5	0	0
M	0	19	6	0	100	22	2	2
O	32	20	65	0	100	47	4	5
Powder	43	25	100	18	18	28	18	11

3. Results

3.1 Relationship between whisker growth and parameters of zinc electrodeposits

Figure 2 shows the number of days before whiskers were detected on 15 specimens that were exposed three times. No whiskers were detected on the triple-exposed specimens A

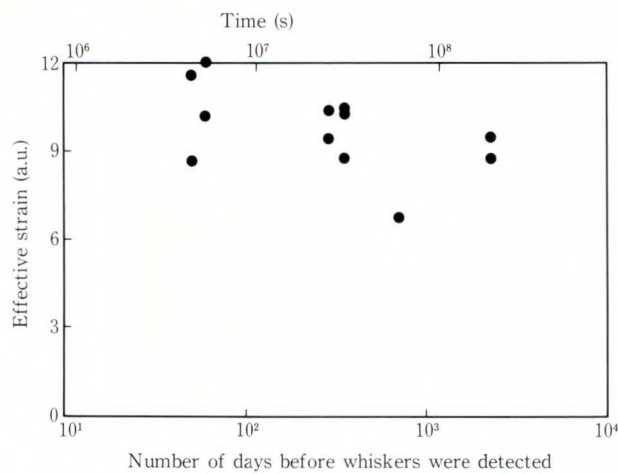


Fig. 3—Relationship between effective strain obtained by Hall plot and the number of days before whiskers were detected.

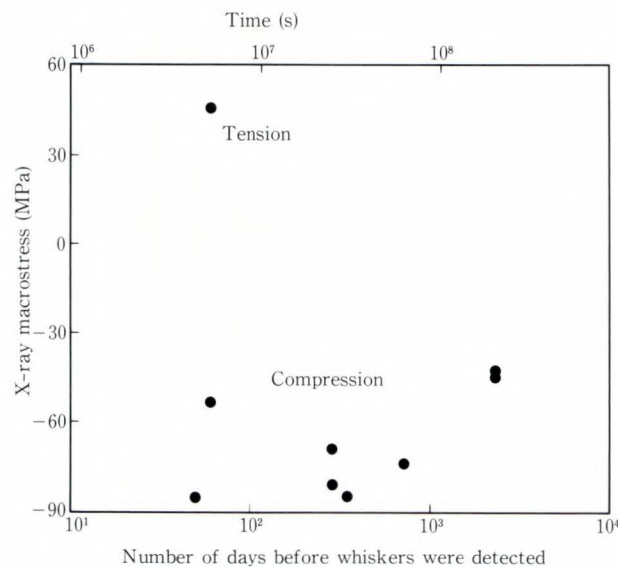


Fig. 4—Relationship between macrostress measured by X-ray method and the number of days before whiskers were detected.

and B. All other specimens eventually developed whiskers. The specimens are listed in decreasing order of electroplating effectiveness. It has been confirmed by further (or three times) experiments that A and B do not grow whiskers. Table 2 shows the relative intensity of X-ray diffraction patterns on the first batch of specimens. The bottom line is the X-ray diffraction pattern of zinc powder. Compared to zinc powder, it is clear that zinc electrodeposits have a much stronger preferred orientation. Eight specimens

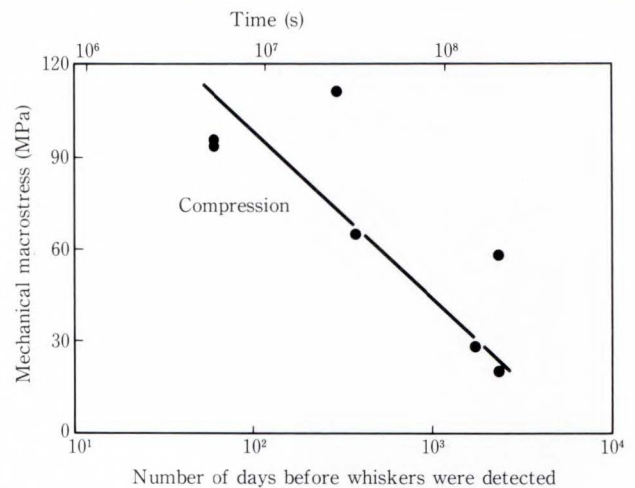


Fig. 5—Relationship between macrostress measured by bending strain and the number of days before whiskers were detected.

had (110) preferred orientation, and five specimens had (100). There is no relationship between the number of days before whiskers were detected and the preferred orientation.

Figure 3 shows the relationship between the effective strain obtained by Hall plot and the number of days before whiskers were detected. The effective strain originates from the dislocation density of zinc electrodeposits. Effective strain had no effect on the number of days before whiskers were detected, and there is no relationship between microstress and whisker growth.

Because macrostress causes lattice compression, the X-ray macrostress can be obtained by measuring lattice compression. Figure 4 shows the relationship between X-ray macrostress and the number of days before whisker were detected. The points are scattered and there is no relationship between whisker growth on zinc electroplate and X-ray macrostress. As shown in Table 2, because zinc electrodeposits have a strong preferred orientation, the $2\theta\text{-sin}^2\psi$ curves¹³⁾ of zinc electrodeposits are non-linear. The X-ray macrostress was obtained at high ψ points; therefore, the values of X-ray macrostress that were obtained are not reliable. For this reason, whisker growth rate was not estimated using X-ray macrostress.

Figure 5 shows the relationship between

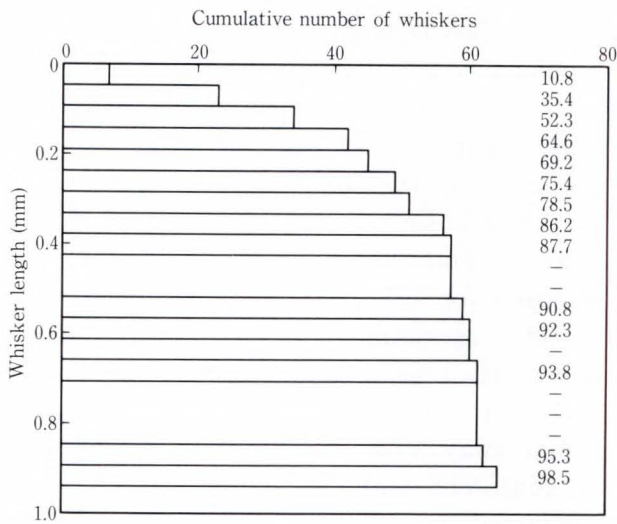


Fig. 6—Cumulative distribution of whisker growth after exposure for 730 days.

macrostress measured using the bending strain method and the number of days before whiskers were detected. Although the points here are also scattered, this method shows the relationship much clearer than the X-ray macrostress measurement. The macrostresses of three specimens (A, B, and C) is less than 60 MPa. No whiskers were detected in the triple-exposed specimens A and B (see Fig. 2). During the first and second exposure, specimen C grew whiskers after day 400 and 720. But in the third exposure, specimen C did not grow whiskers after day 1 800. The smaller the macrostress measured using the bending strain method, the larger the number of days before whiskers were detected. The results shown in Fig. 5 are consistent with the results of Lindborg⁸).

3.2 Approximation for the rate of short circuit in electronic devices caused by whiskers

Figure 6 shows a cumulative histogram of the number and length of whiskers observed on three specimen after exposure for 730, 1 834, and 2 307 days. Figures on the right-hand side of Fig. 6 indicate the cumulative distribution.

Figure 7 is the logarithmic normal probability plot¹⁴ of whisker length vs the cumulative number of whiskers after exposure for 730, 1 834, and 2 307 days. The most probable

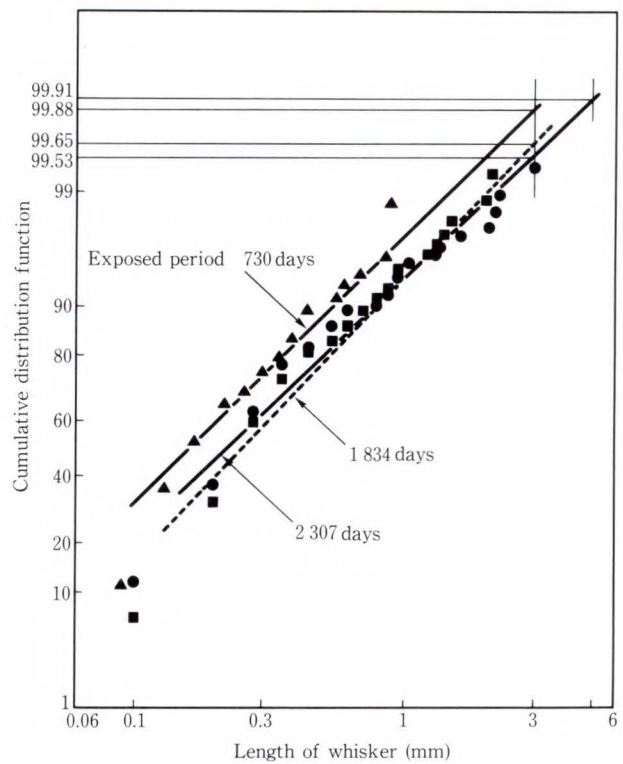


Fig. 7—Logarithmic normal probability plot of length vs. the cumulative number of whiskers after exposure for 730, 1 834, and 2 307 days.

normal distribution of whisker length versus the number of whiskers after exposure for 730, 1 834, and 2 307 days appears as a line on a cumulative distribution function plot¹⁴).

Figure 7 shows that the cumulative distribution function for a whisker length of 3 mm is 99.88 percent for an exposure of 730 days. This indicates a strong growth probability of whiskers shorter than 3 mm after exposure for 730 days. The growth probability of whiskers longer than 3 mm is 0.12 percent (100-99.88) after exposure for 730 days.

The number of short circuits occurring over a certain number of days in electronic devices having a 3 mm space between zinc-electroplated parts and IC leads and terminals will be approximately equal to the number of whiskers in this study that grew beyond 3 mm in the same period.

Approximation for the rate of short circuit = rate of formation and growth in this study of whiskers longer than 3 mm × number of

Table 3. Approximation for the rate of short circuit by 3 mm whiskers after exposure for 730, 1 834, and 2 307 days

Number of days of exposure	730 (63.1 Ms)	1 834 (158.5 Ms)	2 307 (199.3 Ms)
Probability of 3 mm whisker growth in a 75 cm ² area	1.2×10^{-3}	3.5×10^{-3}	4.7×10^{-3}
Number of whisker	64	138	163
Growth direction distribution coefficient	0.1	0.1	0.1
Conduction probability	0.5	0.5	0.5
Approximation for the rate of short circuit (h ⁻¹ · cm ⁻²) (s ⁻¹ · m ⁻²)	2.9×10^{-9} 8.1×10^{-9}	7.4×10^{-9} 20.3×10^{-9}	9.2×10^{-9} 25.6×10^{-9}

$$\begin{aligned} & \text{whiskers}/(\text{area of specimen} \times \text{exposure} \\ & \text{time} \times \text{growth direction distribution coef-} \\ & \text{ficient} \times \text{conduction probability}) \\ & = 0.12 \times 10^{-2} \times 64 / (75 \times 730 \times 24 \times 0.1 \times 0.5) \\ & = 2.9 \times 10^{-9} \text{ (piece/h} \cdot \text{cm}^2 \text{)}. \end{aligned}$$

Where, number of whiskers = number of whiskers shown in Table 3 for the three specimens after exposure for 730, 1 834, and 2 370 days. The surface area of specimens is 25 cm² × 3. The growth direction distribution coefficient is the rate of vertically grown whiskers in the random grown whiskers, and is 0.1 from observation. If whiskers contact IC leads or terminals, the conduct probability is 0.5, because fifty percent of whisker do not conduct because of contamination etc.

We calculated that the rate of short circuit caused by whisker growth would be approximately 2.9×10^{-9} (piece/h · cm²) after 730 days.

From Fig. 7, the rate of growth of whiskers longer than 3 mm after exposure for 1 834 days was calculated to be 3.5×10^{-3} , and an approximate rate of short circuit of 7.4×10^{-9} (piece/h · cm²) was obtained. From Fig. 7, the rate of growth of whiskers longer than 3 mm after exposure for 2 307 days was calculated to be 4.7×10^{-3} , and an approximate rate of short circuit of 9.2×10^{-9} (piece/h · cm²) was ob-

tained. Also from Fig. 7, the rate of growth of whiskers longer than 5 mm after exposure for 2 307 days was calculated to be 9×10^{-4} and an approximate rate of short circuit of 1.8×10^{-9} (piece/h · cm²) was obtained.

Table 3 shows an approximation for the rate of short circuit by 3 mm whiskers after exposure for 730, 1 834, and 2 307 days.

Our approximation for rate of whisker short circuit for a device having a total area of 1 cm² in which zinc electroplated parts are 3 mm away from the IC leads and terminals is consistent with the failure rates (fit) encountered in reliability engineering. Table 3 clearly shows that the rate of short circuit caused by whisker growth on zinc electroplate will increase with exposure time. The specimens that grew whiskers the earliest now have a very large number of whiskers.

4. Conclusion

4.1 Relationship between whisker growth and parameters of zinc electroplating

One side of the steel substrates was insulated and electroplated, and the macrostress was measured using the bending strains of the substrates. A large number of whiskers grew on specimens having a macrostress of more than 60 MPa. The bending strain method is inexpensive and therefore a favoured method. A method of decreasing macrostress have been reported¹⁵⁾. The following processes were used: baking at 180 °C and zinc electroplating without brighteners.

4.2 Approximation for the rate of short circuit caused by whiskers in electronic devices

An approximation was obtained for the rate of whisker short circuit for a device having a total area of 1 cm² in which zinc electroplated parts are 3 mm away from the IC leads and terminals. This rate was 9.2×10^{-9} (piece/h · cm²) which is consistent with reliability figures for such devices as coils, capacitors, and switches. The rate of short circuit caused by whisker growth was very low but not zero.

References

- 1) Compton, K.G., Mendizza, A., and Arnold, S.M.: Filamentary Growth on Metal Surfaces, Whiskers. *Corrosion*, **7**, 4, pp. 327-334 (1951).
- 2) Koonce, S.E., and Arnold, S.M.: Growth of metal whiskers. *J. Appl. Phys.*, **24**, 4, pp. 365-366 (1953).
- 3) Fisher, R.M., Darken, L.S., and Carroll, K.G.: Accelerated growth of tin whiskers. *Acta Met.*, **2**, 5, pp. 368-373 (1954).
- 4) Eshelby, J.D.: A tentative theory of metallic whisker growth. *Phys. Rev.*, **91**, 9, pp. 755-756 (1953).
- 5) Franks, J.: Growth of whiskers in the solid phase. *Acta Met.*, **6**, 2, pp. 103-109 (1958).
- 6) Furuta, N., and Hamamura, K.: Growth mechanism of proper tin-whisker. *Jpn. J. Appl. Phys.*, **8**, 12, pp. 1404-1410 (1969).
- 7) Lindborg, U., Ramsin, S., Lind, L., and Revay, L.: Microstructure and metallurgical properties of some zinc electroplates. *Plating*, **61**, 12, pp. 1111-1116 (1974).
- 8) Lindborg, U.: Observations on the growth of whisker crystals from zinc electroplate. *Met. Trans.*, **6A**, 8, pp. 1581-1586 (1975).
- 9) Hall, W.H.: X-ray line broadening in metals. *Proc. Phys. Soc. (London)*, **62A**, pp. 741-743 (1949).
- 10) Lindborg, U.: A model for the spontaneous growth of zinc, cadmium and tin whiskers. *Acta Met.*, **24**, 2, pp. 181-186 (1976).
- 11) Hirth, J.P., and Lothe, J.: "Diffusive glide and climb process". *Theory of Dislocations*, NY., McGraw Hill, 1968, pp. 506-517.
- 12) Sugiarto, H., Christie, I.R., and Richard, B.P.: Studies of zinc whiskers formation and growth from bright zinc electrodeposits. *Trans. Inst. Metal Finishing*, **62**, 3, pp. 92-97 (1984).
- 13) Yoshioka, Y.: "Principle of X-ray macrostress measurement". *How to measure macrostress using X-ray diffraction*, Soc. Mater. Sci., Jpn., ed. 2nd ed., Tokyo, Yohkendo, 1981, pp. 54-62.
- 14) Shiomi, H.: "Reliability Mathematics". *Elementary Reliability Engineering*, (in Japanese), Tokyo, Tokyo Denki University, 1972, pp. 35.
- 15) Itoh, S., and Hayashi, O.: Whisker from zinc electroplating. (in Japanese), *Practical Metal Finishing*, **34**, 4, pp. 112-118 (1987).



Takeshi Nagai

Atsugi Administration Dept.
FUJITSU LABORATORIES, ATSUGI
Bachelor of Metallurgical Eng.
Waseda University 1961
Dr. of Metallurgical Eng.
Waseda University 1976
Specializing in Metallic Materials
Engineering



Takashi Furusawa

Development Dept.
Fujitsu Sinter Limited
Tsurumi Technical High School (1956)
Specializing in Metal Sintering
Technology



Katsuhide Natori

Electronics Packaging Laboratory
FUJITSU LABORATORIES, ATSUGI
Fujitsu Technical College 1968
Specializing in Electronics Packaging
Engineering

Overseas Offices

Abu Dhabi Office

8th Floor, A1 Masaad Tower,
P.O. Box 322, Abu Dhabi, U.A.E.
Telephone: (971-2)-333440
FAX: (971-2)-333436

Algiers Office

6, Boulevard Colonel,
Amirouche, Alger, Algeria
Telephone: (213)-2-78-5542
Telex: 408-67522

Amman Office

P.O. Box 5420, Ammán, Jordan
Telephone: (962)-6-66241
FAX: (962)-6-662417

Bangkok Office

Room 405, 4th Floor, Dusit
Thani Bldg., 1-3, Rama IV,
Bangkok, Thailand
Telephone: (66-2)-236-7930
FAX: (66-2)-238-3666

Beijing Office

Room 1601, Scite Tower
Jiangoumen-wai Dajie, Beijing,
People's Republic of China
Telephone: (86-1)-512-3610
FAX: (86-1)-512-9041

Bogotá Office

Cra. 13 No. 27-50,
Edificio Centro Internacional
Tequendama, Oficina No. 326.
Bogotá, D.E. Colombia
Telephone: (57-1)-296-8258
FAX: (57-1)-286-7148

Brussels Office

Avenue Louise 176, Bte 2
1050 Brussels, Belgium
Telephone: (32-2)-648-7622
FAX: (32-2)-648-68676

Hawaii Branch

6660 Hawaii Kai Drive, Honolulu,
HI 96825, U.S.A.
Telephone: (1-808)-395-2314
FAX: (1-808)-396-0059

Indonesia Project Office

16th Floor, Skyline Bldg.,
Jalan M.H. Thamrin No. 9,
Jakarta, Indonesia
Telephone: (62-21)-3105981
FAX: (62-21)-3105983

Jakarta Office

16th Floor, Skyline Bldg.,
Jalan M.H. Thamrin No. 9,
Jakarta, Indonesia
Telephone: (62-21)-333245
FAX: (62-21)-327904

Kuala Lumpur Office

Letter Box No. 47, 22nd Floor,
UBN Tower No. 10, Jalan P.
Ramlee, 50250, Kuala Lumpur,
Malaysia
Telephone: (60-3)-238-4870
FAX: (60-3)-238-4869

London Office

2, Longwalk Road, Stockley Park,
Uxbridge, Middlesex, UB11 1AB,
England
Telephone: (44-1)-573-4444
FAX: (44-1)-573-2643

Munich Office

c/o D V18 Siemens AG, Otto-
Hahn-Ring 6, D-8000, München
83, F.R. Germany
Telephone: (49-89)-636-3244
FAX: (49-89)-636-45345

New Delhi Office

Flat No. 517-B, 5th Floor, World
Trade Centre, Barakhamba Lane,
New Delhi, 110001, India
Telephone: (91-11)-331-1311
FAX: (91-11)-332-1321

New York Office

680 Fifth Avenue, New York,
N.Y. 10019, U.S.A.
Telephone: (1-212)-265-5360
FAX: (1-212)-541-9071

Paris Office

Batiment Aristote,
Rue Olof Palme 94006,
Creteil Cedex, France
Telephone: (33-1)-4-399-0897
FAX: (33-1)-4-399-0700

Shanghai Office

Room 1504 Ruijin Bldg.,
205 Maoming Road South,
Shanghai, People's Republic
of China
Telephone: (86-21)-336-462
FAX: (86-21)-336-480

Taipei Office

Sunglow Bldg. 66, Sung Chiang
Road, Taipei, Taiwan
Telephone: (886-2)-561-7715
FAX: (886-2)-536-7454

Washington Office

Republic Place, 1776 Eye Street,
N.W. Washington D.C., U.S.A.

Overseas Subsidiaries

		Telephone	Fax
FKL Dong-Hwa Ltd.	338-13, Daehong-Ri, Sunghwan-Eub, Chunwon-Gun, Chungnam, Republic of Korea	(82-417)-4-3660	(82-417)-63-3671
Fujian Fujitsu Communications Software Ltd.	Wuliting Fuma Road, Fuzhou, Fujian, People's Republic of China	(86-591)-560070	(86-591)-56-0022
Fujitsu America, Inc.	3055 Orchard Drive, San Jose, CA 95134-2017, USA	(1-408)-432-1300	(1-408)-432-1318
Fujitsu Australia Ltd.	475 Victoria Ave., Chatswood, NSW 2067, Australia	(61-2)-410-4555	(61-2)-411-8603
Fujitsu Australia Software Technology Pty. Ltd.	1st Floor, Techway House, Forest Corporate Park, 18 Rodborough Road, Frenchs Forest, N.S.W. 2086, Australia	(61-2)-975-2922	(61-2)-975-2899
Fujitsu Business Communication System, Inc. (Sales Headquarter)	3190 Mira Loma Ave., Anaheim, CA 92806-1906, USA	(1-714)-630-7721	(1-714)-630-7660
Fujitsu Canada, Inc.	2411 West 14th Street, Tempe, AZ 85281, USA	(1-602)-921-5900	(1-602)-921-5999
Fujitsu Component (Malaysia) Sdn. Bhd.	6280 Northwest Drive, Mississauga, Ontario, Canada L4V 1J7 No. 1, Lorong Satu, Kawasan Perindustrian Parit Raja, 86400 Batu Pahat, Johor, Malaysia	(1-416)-673-8666 (60-7)-482111	(1-416)-673-8677 (1-408)-727-0355
Fujitsu Component of America, Inc.	3320 Scott Boulevard, Santa Clara, CA 95054-3197, USA	(1-408)-562-1000	(1-408)-748-7655 or (1-408)-727-0355
Fujitsu Customer Service of America, Inc.	12670 High Bluff Drive, San Diego, CA 92130-2013, USA	(1-619)-481-4004	(1-619)-481-5175
Fujitsu Deutschland GmbH	Frankfurter Ring 211, 8000 München 40, F.R. Germany	(49-89)-323-780	(49-89)-323-78100
Fujitsu do Brasil Ltda.	Rua Manoel de Nóbrega, 1280, 2 ^o Andar, C.E.P. 04001, São Paulo, SP, Brazil	(55-11)-885-7099	(55-11)-885-9132
Fujitsu España, S.A.	Edificio Torre Europa 5 ^a , Paseo de la Castellana, 95, 28046 Madrid, Spain	(34-1)-581-8000	(34-1)-581-8300
Fujitsu Europe Ltd.	2, Longwalk Road, Stockley Park, Uxbridge, Middlesex, UB11 1AB, England	(44-1)-573-4444	(44-1)-573-2643
Fujitsu Finance (U.K.) PLC	2, Longwalk Road, Stockley Park, Uxbridge, Middlesex, UB11 1AB, England	(44-1)-573-4444	(44-1)-573-2643
Fujitsu Hong Kong Ltd.	Room 2521, Sun Hung Kai Centre, 30 Harbour Road, Hong Kong	(852)-8915780	(852)-721724 or (852)-8383630
Fujitsu Imaging Systems of America, Inc.	3 Corporate Drive, Commerce Park, Danbury, CT 06810, USA	(1-203)-796-5400	(1-203)-796-5665 or (1-203)-796-5723
Fujitsu International Finance (Netherlands) B.V.	Officia 1, De Boelelaan 7, 1083 HJ Amsterdam, The Netherlands	-	-
Fujitsu Italia S.p.A.	Via Melchiorre, Gioia No. 8, 20124 Milano, Italy	(39-2)-657-2741	(39-2)-657-2257
Fujitsu Korea Ltd.	9th Floor, Korean Reinsurance Bldg., 80, Susong-Dong, Chongro-Gu, Seoul Special City, Republic of Korea	(82-2)-739-3281	(82)-417-63-3671
Fujitsu Microelectronics Asia Pte. Ltd.	No. 2, Second Chin Bee Road, Jurong Town, Singapore 2261, Singapore	(65)-265-6511	(65)-265-6275
Fujitsu Microelectronics, Inc.	3545 North First Street, San Jose, CA 95134-1804, USA	(1-408)-922-9000	(1-408)-432-9044
Fujitsu Microelectronics Ireland Limited	Greenhills Centre, Greenhills Rd., Tallaght, Dublin 24, Ireland	(353-1)-520744	(353-1)-520539
Fujitsu Microelectronics Italia S.r.l.	Centro Direzionale, Milanofiori, Strada No. 4-Palazzo A2, 20090 Assago-Milano, Italy	(39-2)-824-6170	(39-2)-824-6189
Fujitsu Microelectronics Limited	Hargrave House, Belmont Road, Maidenhead, Berkshire SL6 6NE, U.K.	(44-628)-76100	(44)-628-781484
Fujitsu Microelectronics (Malaysia) Sdn. Bhd.	Pesiaran Kuala Selangor, Seksyen 26, 40000 Shah Alam, Selangor Darul Ehsan, Malaysia	(60-3)-511-1155	(60-3)-511-1227
Fujitsu Microelectronics Pacific Asia Limited	Rooms 616-617, Tower B, New Mandarin Plaza, 14 Science Museum Road, Tsimshatsui East, Kowloon, Hong Kong	(852-3)-723-0393	(852-3)-721-6555
Fujitsu Microsystems of America, Inc.	3025 Orchard Parkway, San Jose, CA 95134-2017, USA	(1-408)-434-1160	(1-408)-434-0359
Fujitsu Mikroelektronik GmbH	Lyoner Strasse 44-48, Arabella Centre 9, OG/A, 6000 Frankfurt/Niederrad 71, F.R. Germany	(49-69)-66320	(49-69)-6632122
Fujitsu Network Switching of America, Inc.	4403 Bland Road, Somerset Park, Raleigh, NC 27609, USA	(1-919)-790-2211	(1-919)-790-8376
Fujitsu New Zealand Ltd.	6th Floor, National Insurance House, 119-123 Featherston Street, Wellington, New Zealand	(64-4) 733-420	(64-4)-733-429
Fujitsu Nordic AB	Torggatan 8, S-171 54 Solna, Sweden	(46-8)-764-7690	(46-8)-28-0345
Fujitsu Philippines, Inc.	2nd Floor, United Life Bldg., Pasay Road, Legaspi Village, Makati, Metro Manila, Philippines	(63-2)-85-49-51	(63-2)-817-7576
Fujitsu (Singapore) Pte. Ltd.	200, Cantonment Road, #11-01 South Point, Singapore 0208, Singapore	(65)-224-0159	(65)-225-5075
Fujitsu Systems Engineering of America, Inc.	2986 Oakmead Village Court, Santa Clara, CA 95054, USA	(1-408)-988-8012	(1-408)-492-1982
Fujitsu Systems of America, Inc.	12670 High Bluff Drive, San Diego, CA 92130-2013, USA	(1-619)-481-4004	(1-619)-481-4093
Fujitsu (Thailand) Co., Ltd.	3rd Floor, Olympia Thai Bldg., 444 (3rd Floor), Rachadaphisek Road, Bangkok 10310, Thailand	(662-512)-1736	(662-513)-2574
Fujitsu Vitória Computadores e Serviços Ltda.	Avenida Nossa, Senhora da Penha, 570, 8 ^o Andar, Praia do Canto-Vitória-Espirito Santo, Brazil	(55-27)-225-0355	(55-27)-225-0954
Information Switching Technology Pty. Ltd.	Level 32, 200 Queen Street, Melbourne 3000, Australia	(61-3)-670-4755	-
Intellistor, Inc.	2120 Miller Drive, Longmont, CO 80501, USA	(1-303)-678-0697	-
Tatung-Fujitsu Co., Ltd.	5 Floor Tatung Bldg., 225, Nanking East Road 3rd Section, Taipei, Taiwan	(886-2)-713-5396	(886-2)-717-4644

FUJITSU LIMITED

6-1, Marunouchi 1-chome, Chiyoda-ku, Tokyo 100, Japan

Phone: National (03) 216-3211 International (Int'l Prefix) 81-3-216-3211 Telex: J22833 Cable: "FUJITSULIMITED TOKYO"